Imperial College London

Cellular Automata Simulations of Field-Scale Flaming and Smouldering Wildfires in Peatlands

A thesis submitted in partial fulfilment of the

requirements for the degree of

Doctor of Philosophy

in

Mechanical Engineering

by

Dwi Marhaendro Jati Purnomo

2022

Supervised by Prof. Guillermo Rein

Declaration of Originality

I declare that this thesis and the work described within have been completed solely by myself under the supervision of Prof. Guillermo Rein. Where others have contributed or other sources are quoted, full references are given.

Dwi Marhaendro Jati Purnomo

2022

Copyright Declaration

Imagination is more important than knowledge. Knowledge is limited.
Imagination encircles the world.
Albert Einstein

To my beloved parents.

Abstract

Cellular Automata Simulations of Field-Scale Flaming and Smouldering Wildfires in Peatlands

by

Dwi Marhaendro Jati Purnomo

Doctor of Philosophy in Mechanical Engineering

Imperial College London, 2022

Supervised by Prof. Guillermo Rein

In peatland wildfires, flaming vegetation can initiate a smouldering fire by igniting the peat underneath, thus, creating a positive feedback to climate change by releasing the carbon that cannot be reabsorbed by the ecosystem. Currently, there are very few models of peatland wildfires at the field-scale, hindering the development of effective mitigation strategies. This lack of models is mainly caused by the complexity of the phenomena, which involves 3-D spread and km-scale domains, and the very large computational resources required. This thesis aims to understand field-scale peatland wildfires, considering flaming and smouldering, via cellular automata, discrete models that use simple rules. Five multidimensional models were developed: two laboratory-scale models for smouldering, BARA and BARAPPY, and three field-scale models for flaming and smouldering, KAPAS, KAPAS II, and SUBALI. The models were validated against laboratory experiments and field data. BARA accurately simulates smouldering of peat with realistic moisture distributions and predicts the formation of unburned patches. BARAPPY brings physics into BARA and predicts the depth of burn profile, but needs 240 times more computational resources. KAPAS showed that the smouldering burnt area decreases exponentially with higher peat moisture content. KAPAS II integrates daily temporal variation of moisture content, and revealed that the omission of this temporal variation significantly underestimates the smouldering burnt area in the long term. SUBALI, the ultimate model of the thesis, integrates KAPAS II with BARA and considers

the ground water table to predict the carbon emission of peatland wildfires. Applying SUBALI to Indonesia, it predicts that in El Niño years, 0.40 Gt-C in 2015 (literature said 0.23 to 0.51 Gt-C) and 0.16 Gt-C in 2019 were released, and 75% of the emission is from smouldering. This thesis provides knowledge and models to understand the spread of flaming and smouldering wildfires in peatlands, which can contribute to efforts to minimise the negative impacts of peatland wildfires on people and the environment, through faster-than-real-time simulations, to find the optimum firefighting strategy and to assess the vulnerability of peatland in the event of wildfires.

Acknowledgements

I would like to thank my supervisor, Prof. Guillermo Rein for his professional guidance, expertise, and generosity during this PhD. His kindness and supports have been amazing, making my PhD life enjoyable and I am deeply grateful for that. It has been a pleasure to have a chance to work with him, with all the supports and encouragement.

Many collaborators have contributed to this work, who I would like to thank. Prof Nieves Fernandez-Anez and Prof Michel Bechtold have been kind enough to allow me to have extensive discussion about my research and result in several papers. Not to mention, the helps from and discussions with Hafiz Amin, Agung Santoso, Han Yuan, Eirik Christensen, Matthew Bonner, Wuquan Cui, Samaneh Moafi, Parwati Sofan, Rory Hadden, and Sebastian Apers.

I want to say thank you to Imperial Hazelab. It is a great honour to be part of a wonderful group of diverse people with excellent professionalism and personality. I would like to thank Prof Ravi Vaidyanathan and Prof Yulianto Nugroho for their professional and personal guidance. Special thanks to Wuquan Cui, my lab buddy and top-tier conference companion and guide. Immeasurable gratitude to all Hazelab members Franz, Francesco, Yuqi, Guoxiang, Zhenwen, Xuanze, Francesca, Simona, Rik, Nik, Ben, Harry, Edmund, Heidari and Tatenda for all their help whether big or small. All of you made this journey so much fun and easier.

This work would have not been possible without the generous support of the Indonesian Endowment Fund for Education (LPDP), the European Research Council, and the Department of Mechanical Engineering, Imperial College London.

The biggest thanks go to my parents and friends, who even made it possible for me to stand, fight, and survive in Britain. Thank you for your consistent support, encouragement, and love.

Dwi Marhaendro Jati Purnomo

London, UK

June, 2022

Table of Contents

Nomenclature

Z	pre-exponential factor (1/s)
c	solid specific heat capacity (J/kg-K)
C	gas specific heat capacity (J/kg-K)
D	mass diffusivity (m^2/s)
E	activation energy (kJ/mol)
$\bar{h}$	specific enthalpy (J/kg)
h_c	convective coefficient (W/m^2-k)
h_m	mass-transfer coefficient (kg/m^2-s)
R	universal gas constant (m^3-Pa/K-mol)
ΔH	change in enthalpy (MJ/kg)
k	thermal conductivity (W/m-k)
I_T	thermal inertia (W^2-s/m^4-K^2)
m	mass (kg)
$\dot{m}''$	mass flux (kg/m^2-s)
n	reaction order (-)
p	pressure (Pa)
t	time (s)
T	temperature (^{o}C)
X	volume fraction (-)
Y	mass fraction (-)
L	length of reactor (mm or m)
d	thickness of reactor (mm or m)
S_d	in-depth spread rate (mm/min)
P_s	CA smouldering probability (-)
U	CA intrinsic value (-)
t_s	CA smouldering time (s)

Greeks

ε	emissivity (-)
κ	permeability (m^2)

$\bar{\rho}$	bulk density (kg/m^3)
ν	viscosity/stoichiometry (-)
ψ	porosity (-)
$\dot{\omega}'''$	volumetric reaction rate (kg/m^3-s)
τ	tortuosity (-)
σ	Stefan-Boltzmann constant (W/m^2-K^4)
γ	radiative conductivity constant (m)
Θ	CA smouldering threshold (-)
φ	CA heat transfer coefficient (-)

Subscripts

s	solid
f	formation
d	destruction
g	gas
i	solid species number
j	gaseous species number
N	nitrogen
O	oxygen
a	ambient
o	organic
D	diffusion
G	generation

Abbreviation

CA	cellular automata
MC	moisture content (%)
IC	inorganic content (%)
DOB	depth of burn (m)
GWT	ground water table (m)
EF	emission factor (-)

Preface

This thesis contains 10 chapters with Chapter 1 presenting the background, aims, and methodology of this thesis. Each Chapter 2-9 is a journal manuscript as listed below for reference, and Chapter 10 is the conclusion of this thesis and potential future works.

Chapter 2 is based on:

> Dwi M J Purnomo, Hafiz M F Amin, Wuquan Cui, and Guillermo Rein, 2022. **Can Infrared Emissions Distinguish Flaming and Smouldering Wildfires? A Laboratory Study to Assist Remote Sensing**. *Fire Technology*, (submitted).

Chapter 3 is based on:

> Dwi M J Purnomo, Nieves Fernandez-Anez, Guillermo Rein, 2022. **Cellular Automata Models of Wildfire Spread**. *Progress in Energy and Combustion Science*, (to be submitted).

Chapter 4 is based on:

> Dwi M J Purnomo, Eirik G Christensen, Nieves Fernandez-Anez, Guillermo Rein, 2022. **BARA: Three Dimensional Simulation of Smouldering Fire of Peat with Horizontally Heterogeneous Moisture**. *International Journal of Wildland Fire*, (revisions).

Chapter 5 is based on:

> Dwi M J Purnomo, Han Yuan, Muhammad A Santoso, Guillermo Rein, 2022. **BARAPPY: Hybrid model of Cellular Automata and Physics-Based to Simulate Three Dimensional Smouldering Fire**. *Fire Technology,* (to be submitted).

Chapter 6 is based on:

> Dwi M J Purnomo, Matthew Bonner, Samaneh Moafi, Guillermo Rein, 2021. **Using Cellular Automata to Simulate Field-Scale Flaming and Smouldering Wildfires in Tropical Peatlands**. *Proceeding of Combustion Institute*, 38(3), pp. 5119–5127.

Chapter 7 is based on:

> Dwi M J Purnomo, Sebastian Apers, Michel Bechtold, Parwati Sofan, Guillermo Rein, 2022. **Integrating Cellular Automata and Remote Sensing to Model Field-Scale**

Peatland Wildfires with Transient Soil Moisture. *International Journal of Wildland Fire*, (submitted).

Chapter 8 is based on:

Dwi M J Purnomo and Guillermo Rein, 2022. **The Relevant Rules and Complexity in Cellular Automata for Smouldering Fire Modelling**. (to be submitted).

Chapter 9 is based on:

Dwi M J Purnomo, Sebastian Apers, Michel Bechtold, Parwati Sofan, Guillermo Rein, 2022. **Estimation of Burnt Area and Carbon Emission of Indonesian Smouldering Wildfires from 2015 to 2019**. (to be submitted).

Chapter 1 – Introduction to Peatland Wildfires

1.1. Peatland Wildfires and Its Impact

Wildfires happen all around the globe, from tropical to arctic landscapes (Quah and Johnston, 2001; Sullivan, 2009b; Kolden and Rogan, 2013), in various ecosystem: savannah, grassland, bushland, rainforest, and peatland (Urbanski, 2014). When a wildfire happens in a peatland ecosystem, it releases carbon that cannot be reabsorbed by ecosystem, facilitating a positive feedback mechanism to climate change (Johnston *et al.*, 2012; Rein, 2013; Turetsky *et al.*, 2015; Rein and Huang, 2021). This positive feedback is facilitated because such wildfire can burn peat, the carbon-rich organic soil underneath the surface vegetation (Rein, 2016). Figure 1.1 shows an example of a peatland ecosystem in New Island, The Falkland Island, where both the surface vegetation and the peat soil underneath are flammable. Peat is decomposed dead vegetation, which has been accumulated for years (ranging from a few years to thousands of years depending on the depth of peat layer) under very wet conditions (Page *et al.*, 2004; Packalen and Finkelstein, 2014; Turetsky *et al.*, 2015). Similar to fossil fuel, when peat burns, it releases carbon that cannot be reabsorbed by the ecosystem, such as from the regrowth process of vegetation, thus, it warms the Earth, and causes more favourable conditions (drier and hotter) for wildfires to happen more frequently and severely (Turetsky *et al.*, 2015). This feedback mechanism has been proven by the prevalence of peatland wildfires in Southeast Asia, Southern Africa, Northern Europe, North America, and even in the Arctic, and the higher frequency and severity of the wildfires (Page *et al.*, 2002; Rein, 2013; Grundling *et al.*, 2019; Scholten *et al.*, 2021). The fact that peatland ecosystem contains 25% of the world's soil carbon, although its area is only 2 – 3% of the Earth's land surface, means peatland wildfire is alarming for the climate change (Yu, 2012).

Figure 1.1. Photo of a peatland ecosystem in New Island, The Falkland Island in 2018. Photo was taken by Wuquan Cui.

Peatland wildfires are the largest fires on Earth in term of fuel consumption (Hu *et al.*, 2018), causing these wildfires to release enormous emission that deteriorate human's health (Rein, 2013; Rein and Huang, 2021). In 1997, peatland wildfires in Southeast Asia emitted 0.8 – 2.56 Gt-C to the atmosphere, which is equivalent to 13 – 40% of the global man-made carbon emission from that year (Page *et al.*, 2002). These incidents are responsible for the 110,000 premature deaths caused by diseases inflicted because of the wildfires, such as respiratory and cardiovascular diseases (Johnston *et al.*, 2012). The disease infliction is encouraged by the behaviour of the smoke that stays in a low altitude and lingers as a haze often near population (Rein, 2013; Rein and Huang, 2021).

1.2. Ignition and Spread of Peatland Wildfires

Peatland wildfires typically start with flaming combustion that burns the surface vegetation (Noble *et al.*, 2018). The flaming vegetation can ignite the peat underneath, and nucleate smouldering hotspots (ignition of smouldering peat at randomly distributed locations). The smouldering peat remains active, and grows (due to smouldering spread), for weeks to months even after the flaming has been extinguished. Smouldering is a flameless type of combustion, which has almost half the temperature of flaming (450°C – 700°C), and spreads two order of magnitude slower than flaming (~0.5 mm/min; Rein, 2016; Christensen, Fernandez-Anez and Rein, 2020). However, smouldering is the most persistent fire on Earth and releases greater emissions than flaming in both gas and

particulate emissions (Rein, 2013). Smouldering also spreads in a three-dimensional (3-D) direction, two-dimensional (2-D) horizontal spread and a one-dimensional (1-D) vertical spread, which is commonly known as in-depth spread (Christensen, Fernandez-Anez and Rein, 2020). Meanwhile, flaming can be assumed to spread only in a 2-D horizontal direction, especially, if the canopy of vegetation is not significant (Finney, 1998). Figure 1.2 compares flaming and smouldering wildfires at the field-scale. While flaming locations can be clearly seen through its naked flame signature, the locations of smouldering are unclear as it only shows a smoke signature. However, the smouldering is active, consume the peat, and continuously releases emissions.

Figure 1.2. Comparison between flaming and smouldering wildfires. These photos are from a field-scale experiment of flaming and smouldering wildfires on peatland (Santoso, 2021). Photos taken by Wuquan Cui.

Although both flaming and smouldering combustion are present, smouldering is the most prominent carbon emitter in peatland wildfires (Huang, Rein and Chen, 2015). In the 1997 South East Asia peatland wildfires, of the 0.8 – 2.56 Gt-C that was released to the atmosphere, only ~0.1 Gt-C was from flaming vegetation (Page *et al.*, 2002). Smouldering is also always an unwanted type of combustion, since sometimes, flaming wildfires are intentional such as for forest management where wildfire is encouraged to avoid the accumulation of fuel that could initiate very large wildfires (Malamud, Morein and Turcotte, 1998; Block *et al.*, 2016; Waldrop and Goodrick, 2018).

Smouldering ignition, spread, and extinction significantly depend on the moisture content (MC, in this thesis referred to as gravimetric MC if not stated differently), inorganic content (IC), and bulk density of peat (in that order; Rein, 2016; Christensen, Fernandez-Anez and Rein, 2020). Of these three properties, peat MC varies significantly both spatially and temporally in natural peatland, apart from being the single most important of the properties that affect smouldering dynamics (Harris and Bryant, 2009;

Meingast *et al.*, 2014; Prat-Guitart *et al.*, 2016a, 2017; Bechtold *et al.*, 2018; Burdun *et al.*, 2020). Spatially, peat MC varies both horizontally and vertically, where vertically, peat has higher MC in-depth, whereas horizontally, the peat MC variation is significantly more complex (see Figure 1.3 of horizontal MC variation in an Ireland peatland) and depends on many factors such as topography and surface vegetation (Prat-Guitart *et al.*, 2017). The spatial variation is caused by topography and surface vegetation, whereas the temporal variation is due to hydrological processes, weather conditions, seasonal change and climate change (Dettmann and Bechtold, 2016; Prat-Guitart *et al.*, 2016a, 2017; Asmuß, Bechtold and Tiemeyer, 2019; Bechtold *et al.*, 2020).

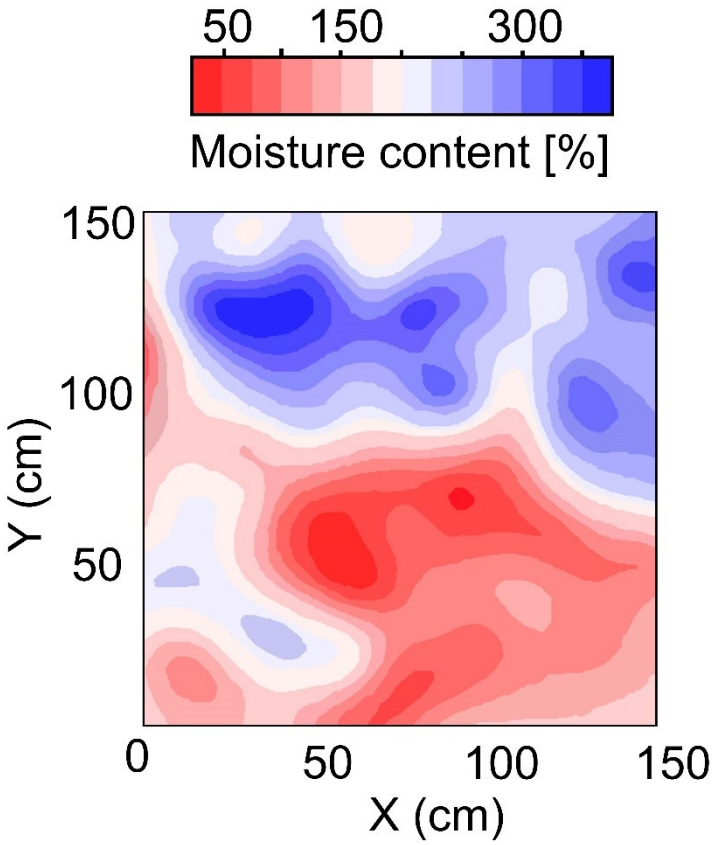

Figure 1.3. The moisture content profile of natural peatland in Ireland. This moisture content profile is extracted following the measurement of Prat-Guitart et al. (2017).

Smouldering peat is unlikely to happen if the peat MC is higher than the critical MC (~150%, gravimetric and dry-basis), but once the peat MC is below the critical MC, smouldering can start although the peat is still relatively wet (Frandsen, 1987, 1997; Huang, Rein and Chen, 2015). When the peat is smouldering at a relatively high MC, subsurface smouldering can emerge, which is difficult to detect and can facilitate smouldering across seasons (Amin, Hu and Rein, 2020; Scholten *et al.*, 2021). Smouldering that spreads underground is not significantly affected by ambient conditions,

thus, this fire becomes very robust and can sustain in a very unfavourable conditions such as in winter seasons (Scholten *et al.*, 2021). The smouldering survives the winter season by lurking underground, when the surface is covered in snow, and when spring starts, it melts this snow cover, and smouldering resurfaces, rekindling the flaming fire and starting a new wildfire (Scholten *et al.*, 2021). Therefore, without new and independent sources of ignition, peatland wildfires can happen every year.

The nucleation and growth of smouldering hotspots in peatland wildfires were revealed by Grundling *et al.* (2019) and Santoso (2021) who conducted experiments on peatland wildfires at the field-scale. In these works, flaming was initiated on peatland and the ignited smouldering hotspots were observed and monitored (Grundling *et al.*, 2019; Santoso, 2021). These works show that the smouldering hotspots were not created uniformly on the entire flaming burnt area, instead, they are created at randomly distributed locations (see Figure 1.4), which then spread to become bigger (Grundling *et al.*, 2019; Santoso, 2021).

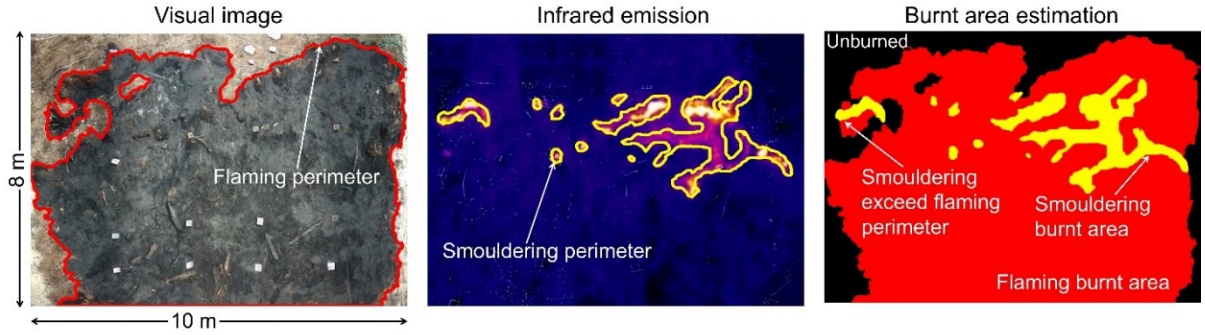

Figure 1.4. Comparison between flaming and smouldering burnt area in the same location where the smouldering is initiated by flaming. The flaming burnt scar is obtained from a visual image, whereas the smouldering burnt scar is obtained from infrared emissions. The visual image and infrared emissions were obtained from field-scale experiments of flaming and smouldering fires on peatland on day five after the flaming was initiated (Santoso, 2021).

In Figure 1.4, the smouldering was only initiated at the top of the plot, which has drier peat (48% gravimetric MC) compared to the bottom (155% gravimetric MC), which also confirms with the spatial nonuniformity of peat MC in natural peatlands (Prat-Guitart *et al.*, 2017). Although the peat at the top part has relatively similar MC, the ignition of smouldering is nonuniform, which also confirms the finding of Grundling *et al.* (2019). At the beginning, the smouldering burnt area is smaller than the flaming burnt area, whereas at the end of the smouldering lifespan, its burnt area could be smaller, larger, or similar to the flaming burnt area, depending on the spread rate of smouldering. Figure 1.4 shows several regions that contain smouldering that spreads beyond the

flaming burnt area perimeter, thus, indicating the possibility that the smouldering burnt area can exceed the flaming burnt area if the smouldering lifespan is sufficient.

1.3. Detection and Emission of Peatland Wildfires

The current literature on peatland wildfires (at the field-scale and considering both flaming and smouldering) is dominated by detection and estimation of carbon emission (Page *et al.*, 2002; Elvidge *et al.*, 2015; Huijnen *et al.*, 2016; Sofan *et al.*, 2020). Recent technologies for the detection and monitoring of wildfires are via remote sensing (Burke *et al.*, 2019). In the remote sensing works for detection and monitoring purposes, infrared emissions that are emitted by the Earth's surface are analysed, and the difference in their values is used to categorise the object (see Figure 1.5), such as vegetation, fire, water, cloud, etc. (Kramer, 1996; ESA, 2015; Cao *et al.*, 2017; USGS, 2019; NASA, 2020). This categorisation is based on the combination of infrared emissions at different wavelengths (such as short wave (SWIR), mid wave (MWIR), and long wave (LWIR) infrared), in which different objects emit different infrared signal values for each wavelength (Dozier, 1981; Siegert *et al.*, 2004; Elvidge *et al.*, 2013, 2015; Atwood *et al.*, 2016; Giglio, Schroeder and Justice, 2016; Sofan *et al.*, 2020). The differentiation between fire and non-fire objects, however, is performed after the masking processes to omit the undesirable noises such as from cloud. Therefore, the infrared signals from cloud are analysed and used to remove the location at which the clouds are predicted to be present, after which the infrared signals at the remaining locations are analysed to differentiate between fire and non-fire objects (Giglio, Schroeder and Justice, 2016). The detection of wildfires is very important, for instance, to alert the authorities the wildfires that might be happening in the remote area, and help in strategizing the mitigation attempts (Giglio, Schroeder and Justice, 2016).

The detection of wildfires via remote sensing that use infrared emissions obtained by satellites, can also be used to estimate carbon emission from wildfires, since this method can be implemented at any time, by using the data from the past and present (Page *et al.*, 2002; Huijnen *et al.*, 2016). The remote sensing of wildfires that result in the estimation of burnt area (see Figure 1.5) can be combined with the emission factor to estimate the carbon emissions (Urbanski, 2014). The emission factor is the amount of a product generated per unit amount of an activity that generates the product (Urbanski, 2014). While this method is a bottom-up approach, there are also top-down approaches (see Figure 1.5), where the remote sensing is dedicated to tracing the carbon emissions directly (Huijnen *et al.*, 2016). By estimating the carbon emissions released by the

wildfires, the impact of these fires on climate change can be approximated, and better mitigation can be proposed.

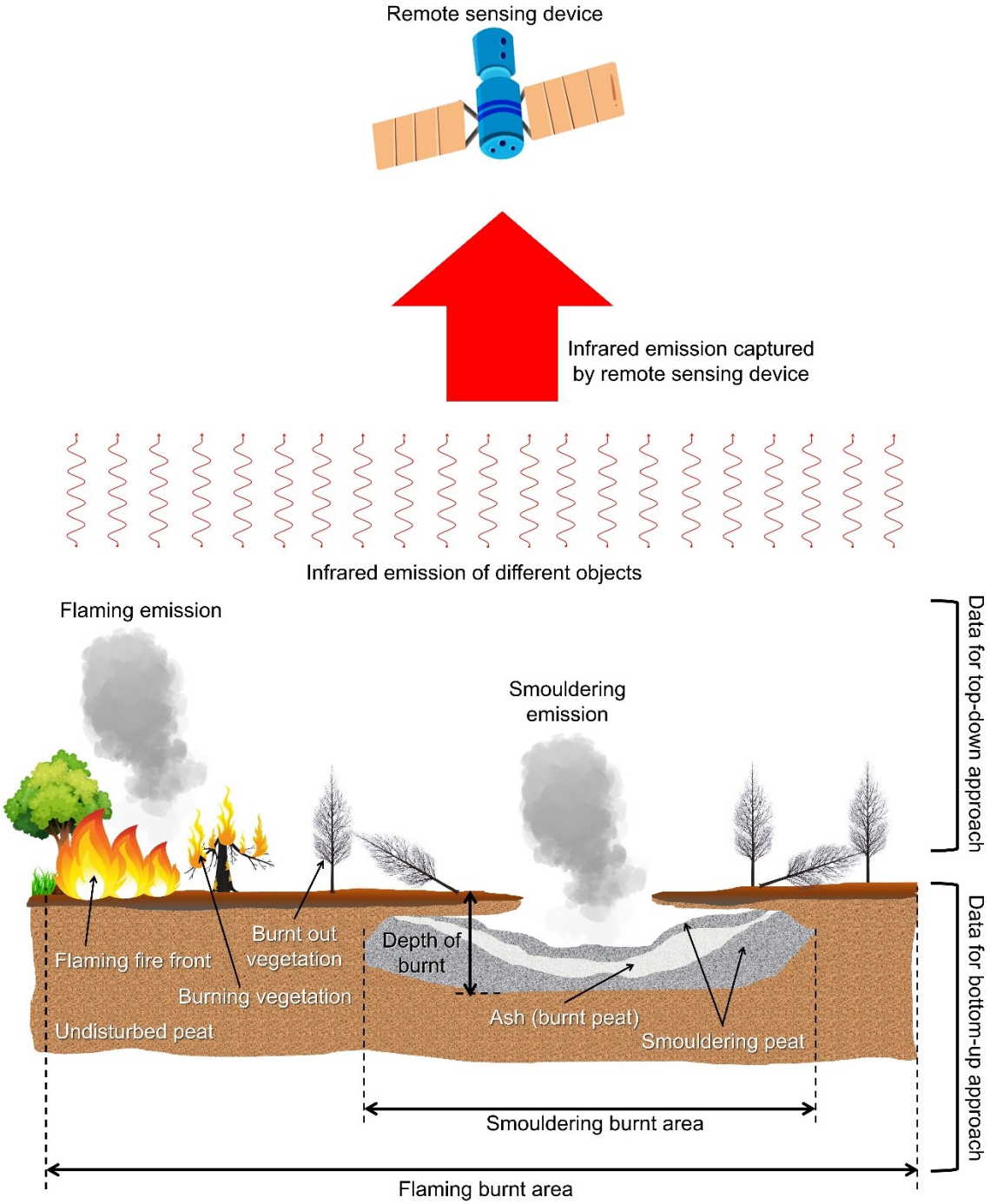

Figure 1.5. Remote sensing application for detection and carbon emission estimation of peatland wildfires. Different objects emit different infrared signals that can be used to distinguish the objects. The bottom-up approach for carbon emission estimation uses data of flaming and smouldering burnt areas and depth of burn, whereas the top-down approach uses data of released gas of flaming and smouldering, which all are obtained by using remote sensing devices.

The emissions from flaming and smouldering wildfires can be estimated based on the product of mass of fuel burnt and an emission factor (Hu *et al.*, 2018). For flaming wildfires, the mass of fuel burnt can be estimated by using the burnt area and the amount, type, and density of the vegetation per unit area, which depend on the type of ecosystem in which the wildfire happens (Urbanski, 2014; see Figure 1.5). This differentiation stems from the fact that the vegetation in different ecosystem is different, thus, the carbon content of the vegetation is also different (Urbanski, 2014). For smouldering wildfires, its burnt area and depth of burn (DOB) are required to estimate the volume of peat loss (Hu *et al.*, 2018; see Figure 1.5), and then the mass of peat burnt can be estimated by the product of this volume with the peat bulk density. Due to the 3-D spread nature of smouldering, the depth of burn is potentially nonuniform, increasing the difficulty of the emission estimation. The approximation of emissions from smouldering, especially at the field-scale, however, can be performed by assuming a uniform depth of burn (see Figure 1.5), in which the volume of peat loss is its product with the smouldering burnt area and the emissions are the product of this volume with the corresponding emission factor (Page *et al.*, 2002).

The detection and carbon emission estimation of peatland wildfires suffer from the difficulty to accurately detect smouldering (Elvidge *et al.*, 2015). While flaming wildfires can be detected with a reasonable accuracy, due to the lower temperature of smouldering, the radiation from smouldering wildfires is significantly weaker than from flaming wildfires, causing the detection of smouldering to become challenging (Elvidge *et al.*, 2015). The weak radiation of smouldering causes its infrared signals to be similar to other non-fire objects, or objects which are slightly heated by the sunlight; thus, some studies discuss the usage of night-time infrared data to detect smouldering (Elvidge *et al.*, 2015). When the subsurface smouldering emerges, the weak radiation of smouldering is weakened even further since it is hindered by non-burning objects above the smouldering peat. Therefore, while it is already challenging to detect smouldering at the surface, subsurface smouldering significantly increases detection difficulty. This difficulty means there is the possibility of false alarms in which the authorities are informed that wildfires have been successfully extinguished, but smouldering hotspots remain active, lurking, and reanimate flaming when the environment and weather are favourable (Scholten *et al.*, 2021), or vice versa, which make the firefighting attempts and resources are wasted (the former is more important than the latter).

In emission studies, especially the bottom-up approach, the difficulty of detecting smouldering means that there must be assumptions made to estimate the emissions from

smouldering peat which are independent of emissions from flaming vegetation. This separation is important since flaming vegetation releases carbon that can be directly reabsorbed, such as via vegetation regrowth post wildfires, whereas smouldering peat releases carbon that cannot be directly reabsorbed by the ecosystem (Rein, 2013; Turetsky *et al.*, 2015). The commonly used assumption is by assuming that the burnt area of flaming and smouldering are equal; thus, the emissions from smouldering are simply the product of the flaming burnt area with DOB and the smouldering emission factor, which is different from the flaming emission factor (Page *et al.*, 2002; Hu *et al.*, 2018). This assumption can cause inaccuracy in the carbon emission estimation, since the smouldering burnt area is different from the flaming burnt area (Grundling *et al.*, 2019; Santoso, 2021; see Figure 1.4). Therefore, models for peatland wildfires are needed to overcome these limitations (see Figure 1.6).

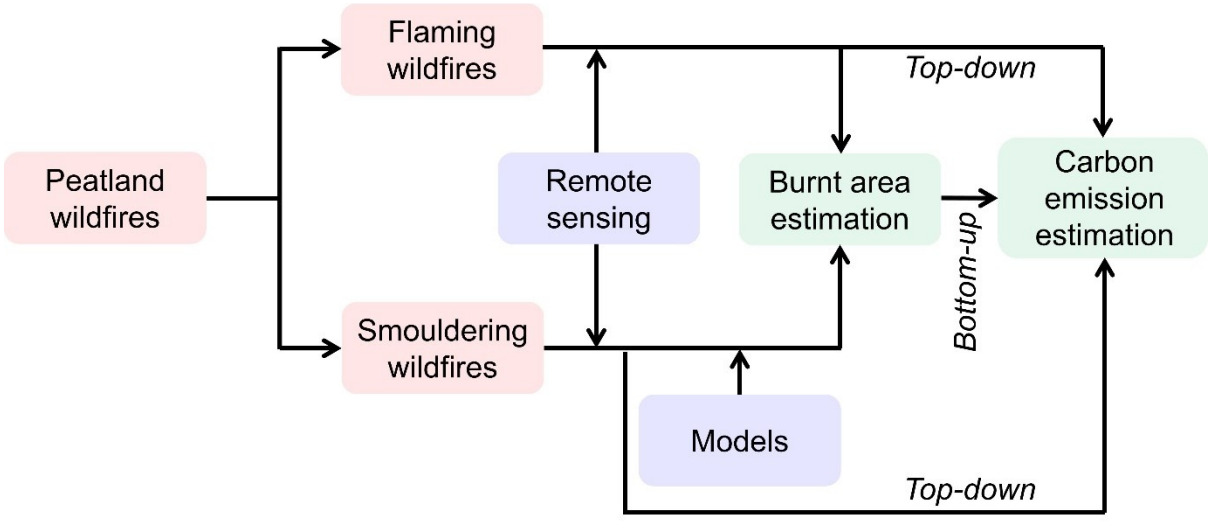

Figure 1.6. Schematic of the use of the models for the studies of peatland wildfires. The red shade represents phenomena, blue shade represents methods, and green shade represent output.

1.4. Aims of the Research

The dynamics of peatland wildfires, starting from ignition, spread, and emission are poorly understood. Previous works, which consist of laboratory and field-scale studies, have not fully captured the phenomena, where the smouldering and flaming parts of peatland wildfires are studied separately and the integration of the two fire types are rarely considered (Frandsen, 1987; Perry, 1998; Finney *et al.*, 2015; Huang, Rein and Chen, 2015). While the studies of flaming have considered the phenomena at the field-scale (Perry, 1998; Sullivan, 2009c), field-scale smouldering studies are rare (Grundling *et al.*, 2019; Santoso, 2021). Studies of emissions from peatland wildfires, although limited, are available both bottom-up (Page *et al.*, 2002) and top-down (Huijnen *et al.*, 2016)

approaches. However, in the bottom-up approach, significant assumptions on the smouldering part are considered, whereas in the top-down approach, the dynamics and the source of emissions (from flaming vegetation or from smouldering peat) are disregarded. Moreover, the period of time of active flaming and smouldering are significantly different, causing top-down approach to have uncertainty on the time considered for collecting data, especially for carbon emissions from smouldering.

This thesis aims to scientifically understand peatland wildfires based on the dynamics of flaming and smouldering across scales and provide the tools to estimate their spread behaviour and carbon emissions for mitigation purposes (such as firefighting attempts). This thesis provides practitioners with the knowledge and tools to approximate the ignition and spread of flaming and smouldering in peatland wildfires, in various environmental conditions and fire scenario, with faster-than-real-time simulations. This can help the practitioners to develop optimum strategy for the mitigation of peatland wildfires, for instance, the deployment of the firefighters based on the fire front location predicted by the simulation, and the management of peatland in general, such as the assessment of peatland vulnerability in the event of wildfires to develop the preventive measures (e.g., surface vegetation type and density management and peat rewetting).

This thesis also provides knowledge and tools to estimate the emissions from peatland wildfires that considers the distinction between flaming and smouldering carbon emissions. Therefore, the peatland management (e.g., the development of measures to minimise the negative impacts of peatland wildfires) can be improved since the source of emissions is known and the measures that have highest benefit can be explored (e.g., either focusing the resources on surface vegetation or peat management), resulting in better mitigation of climate change.

1.5. Methodology of the Research

1.5.1. Peatland wildfires modelling and cellular automata

Investigating peatland wildfires means investigating field-scale phenomena (thousands of hectares), which involve flaming and smouldering combustion, and are affected by environmental factors (surface vegetation, wind, peat MC) that vary spatially and temporally. The smouldering part also requires understanding of its 3-D spread that lead to many important phenomena. While experimental studies can be conducted at the small scale, the investigation of peatland wildfires at their actual scale can be prohibitively expensive in a comprehensive manner. Computational models are, therefore, the most promising route to investigate field-scale peatland wildfires.

The current literature on the modelling of peatland wildfires is concentrated on field-scale flaming wildfire models and small-scale smouldering wildfire models, but without the integration of the two, which is the emerging phenomenon in peatland wildfires. Many models have been developed to simulate flaming wildfires at the field-scale, which use different approaches (Perry, 1998; Sullivan, 2009c). By using different approaches, many phenomena in wildfires have been simulated, such as crown fire and firebrand (Finney, 1998; Pastor *et al.*, 2003; D'Ambrosio *et al.*, 2006). These models have been prevalently used by practitioners and authorities to help with wildfire mitigation and forest management (Finney, 1998). Flaming wildfire models are commonly based on Geographic Information System (GIS) data, which are used to determine the input parameters in the model, such as vegetation type and density (Perry, 1998; Sullivan, 2009c). The GIS data are input into such models to estimate the spread rate of the flaming, which mostly follow the semi-physical approach of Rothermel (1972). The estimation of the spread rate also depends on the weather conditions (obtained, for example, from weather stations) such as rain and wind dynamics (Rothermel, 1972; Alexandridis *et al.*, 2011). This spread rate is only at 1-D direction, a downwind direction which is the direction of the maximum spread rate, thus, another approach is required to estimate the spread rate at over 360^{o} direction. The spread rate of the flaming wildfire over 360^{o} direction is most commonly estimated by using the elliptical model of Alexander (1985); Finney (1998). Once the spread rate at any direction is determined, the model can visualize the flaming fire front and burnt scar at any time, while considering the environmental (e.g., fuel type and density) and weather (e.g., wind and rain) effects (Perry, 1998; Sullivan, 2009c).

The current literature in smouldering computational studies is rich in fundamental investigation of the sustainability and spread of smouldering at different conditions (Huang and Rein, 2015, 2017; Huang, Rein and Chen, 2015; Huang *et al.*, 2016; Yuan, Restuccia and Rein, 2021). Sustainability studies focus on the ability of smouldering to ignite and preserve fire when the MC and IC, the two most important factors in smouldering, are varied (Rein and Huang, 2021), which results in the critical MC and IC of self-sustained smouldering. Meanwhile, spread studies aim to understand the spread behaviour, such as spread rate and the fire front shape, of smouldering, and the factors that affect them (Huang, Rein and Chen, 2015; Huang and Rein, 2017). These studies also discuss the fundamental process involved in smouldering such as drying and pyrolysis (Huang and Rein, 2015, 2017; Huang, Rein and Chen, 2015). Most of the smouldering models use physics-based approaches and all of these are at the small scale

(cm-scale; Huang and Rein, 2015, 2017; Huang, Rein and Chen, 2015; Huang *et al.*, 2016; Yuan, Restuccia and Rein, 2021).

The behaviour of flaming and smouldering are significantly different; thus, the existing field-scale wildfire models, which only consider flaming, are inadequate to study peatland wildfires. These flaming wildfire models need to be integrated with the smouldering wildfire models, which should consider the field-scale phenomena prior to the integration. Therefore, there are two main gaps in the literatures for the modelling of peatland wildfires: field-scale modelling of smouldering and the integration of this model with the flaming wildfire models.

Previous computational studies on flaming wildfires have used many different approaches including physics-based, semi-physical, and empirical approaches (Perry, 1998; Sullivan, 2009c); however, computational studies of smouldering have only considered a physics-based approach (Huang and Rein, 2015, 2017; Huang, Rein and Chen, 2015; Huang *et al.*, 2016; Yuan, Restuccia and Rein, 2021). While the physics-based approach is a powerful tool with high level of details and accuracy, this approach is unsuitable for modelling field-scale peatland wildfires due to the very high computational demand. The large scale of the phenomena presents a significant computational burden. Even using high performance computers, the computational time required to complete the model is too long, and therefore, the model cannot be used for immediate mitigation such as during firefighting. This argument was the consideration that drove the development of non-physics-based approach for flaming wildfire models. The main reason for the development of these alternative models is their ability to simulate the phenomena at near real time (Perry, 1998; Sullivan, 2009c). Other benefits of using alternative models are its ability to cope with incomplete understanding on the fundamental of physics and chemistry, in which while physics-based models will be unable to perform simulation due to this incomplete understanding, the alternative models can still perform the simulation (Perry, 1998; Sullivan, 2009c). The development of physics-based models is still very important to understand fundamental phenomena; however, once the practicality of the model for field-scale mitigation is considered, alternative models have the upper hand.

There have been alternative models for simulating flaming wildfires: fire propagation in arrays (Weber, 1990), Markov chains (Catchpole, Hatton and Catchpole, 1989), percolation model (von Niessen and Blumen, 1986), and cellular automata (Clarke, Brass and Riggan, 1994; Karafyllidis and Thanailakis, 1997; Hargrove *et al.*, 2000). The aim of the alternatives is mainly to improve the practicability of the models, therefore, the models can be used to aid the mitigation more effectively, for instance,

computationally light models enable real time simulations to support firefighting attempts. Fire propagation in arrays simulates the propagation of fire based on the cells that are inside a certain geometry derived from the experiments (Weber, 1990). Markov chains determine the spread of the fire based on the time delay, which is obtained from the spread rate calculation (Catchpole, Hatton and Catchpole, 1989). Percolation model allows the spread of the fire from one cell to another with a certain probability (von Niessen and Blumen, 1986). Meanwhile, cellular automata (CA) do not have specific restrictions on the rules to be used, thus, fire propagation in arrays, Markov chains, percolation model, and many other concepts can be implemented in CA, while other alternative models do not have this flexibility. For example, fire propagation in arrays is similar to the CA model of Trunfio *et al.* (2011), Markov chains concept is similar to the CA model of Porterie *et al.* (2007), and the percolation model is similar to the CA model of Hargrove *et al.* (2000). This characteristic means that CA have all the benefits of the other alternative models, and their drawbacks can be minimised using the combination of different approaches; drawbacks from an approach can be compensated by using different approaches, for instance, deterministic concept that cannot simulate firebrand can be integrated with probabilistic concept to simulate the firebrand in CA. The other alternatives do not have these characteristics, thus, their benefits are limited to the benefits of one concept and their drawbacks cannot be resolved with the same method (i.e., concepts integration). Compared to other alternative models, CA do not have relative drawbacks (benefits that the other models have but CA do not have) since CA can implement other alternative models; CA have relative drawbacks when compared to physics-based model, i.e., lower level of detail and lack of physics consideration. CA also have basic limitations, e.g., non-flexible rules and neighbourhood, static structure, and inability to accommodate external events (Muzy *et al.*, 2005a, 2006).

Peatland wildfires involve many phenomena, which are affected by many factors that vary temporally and spatially, thus, of many different alternative approaches, this thesis focuses on the development of CA, discrete computational models that use simple rules (von Neumann, 1967; Wolfram, 1984; see detail description of CA in Chapter 3.1). Since the rules that can be implemented in CA are not limited to a certain approach (von Neumann, 1967; Wolfram, 1984), this method has limitless potential and is suitable for the modelling of field-scale peatland wildfires. The limitless potential stems from the adjustability of the implemented rules, thus, when one set of rules are unable to model certain phenomena, different rules can be implemented, which also means that a hybrid

of different set of rules are also possible, and optimum rules that are accurate and within a reasonable computational cost can be selected.

Cellular automata (CA) have been extensively used for the flaming wildfire models (Clarke, Brass and Riggan, 1994; Karafyllidis and Thanailakis, 1997; Collin, Bernardin and Sero-Guillaume, 2011; Trunfio *et al.*, 2011; Ntinas *et al.*, 2017). Its compatibility with GIS data and its high computational efficiency are the main reasons for the extensive use (Clarke, Brass and Riggan, 1994; Karafyllidis and Thanailakis, 1997; Collin, Bernardin and Sero-Guillaume, 2011; Trunfio *et al.*, 2011; Ntinas *et al.*, 2017). The ability of CA to embrace many different approaches and their combinations mean CA stand out from other alternative models. For example, probabilistic approach is needed to model firebrand phenomenon, where embers are flown, carried by the wind during wildfires and ignite new hotspots distant from the fire front, since this phenomenon is unlikely to be deterministic (Pastor *et al.*, 2003; Alexandridis *et al.*, 2011). CA can use semiphysical approach to simulate the flaming wildfire spread, and also integrate a probabilistic approach to simulate the firebrand (Alexandridis *et al.*, 2011). Therefore, CA offer limitless potential for modelling many phenomena in wildfires that cannot be modelled by using conventional approaches. There are several works of smouldering model that use CA (Belcher *et al.*, 2010; Fernandez-Anez, Christensen and Rein, 2017; Fernandez-Anez *et al.*, 2019); however, these works are all at the small scale. CA is proven to be able to simulate fingering, a very complex phenomenon in smouldering where the burnt scar shaped like fingers that the physics-based models cannot simulate (Fernandez-Anez *et al.*, 2019).

Peatland wildfires modelling means integrating the flaming models with the smouldering models. Since all the smouldering models are still at the small-scale, an upscale of these models are required prior to this integration. There are only two pioneering works that have successfully simulated peatland wildfires at the field-scale (Purnomo *et al.*, 2021; Widyastuti *et al.*, 2021). The work of Widyastuti *et al.* (2021) used agent-based model to simulate peatland wildfires. This agent-based model stems from the attribution of each cell in the domain to a specific set of values (Widyastuti *et al.*, 2021). Each cell in the domain is considered an agent, in which agent of different states (e.g., unburned, burning) has different attributes (e.g., probability of flaming spread, probability of smouldering ignition) which also depends on the environment (e.g., fuel) and weather (e.g., wind) conditions (Widyastuti *et al.*, 2021). The determination of variables of the model in this work, however, is statistical; the values of the variables are selected based on the combination, which makes the model has a good agreement with

the burnt scar data of flaming wildfire (Widyastuti *et al.*, 2021). This method leads to an issue of generality, in which the model is accurate only for the burnt scar data it is calibrated against. To improve the generality of the model, a significant number of burnt scar data from different wildfires is required, which consequently significantly increase the resources required. The work of Purnomo *et al.* (2021) uses CA that implement the semiphysical model of Rothermel (1972) to calculate the flaming spread rate and experiments on smouldering to estimate the smouldering spread rate; thus, the generality problem is minimised. However, the models in Purnomo *et al.* (2021) and Widyastuti *et al.* (2021) did not consider actual conditions in nature sufficiently, especially in the smouldering part, for instance, neither model considered the peat MC variation. Figure 1.7 summarizes the phenomena involved in peatland wildfires and the phenomena that have been considered in previous models.

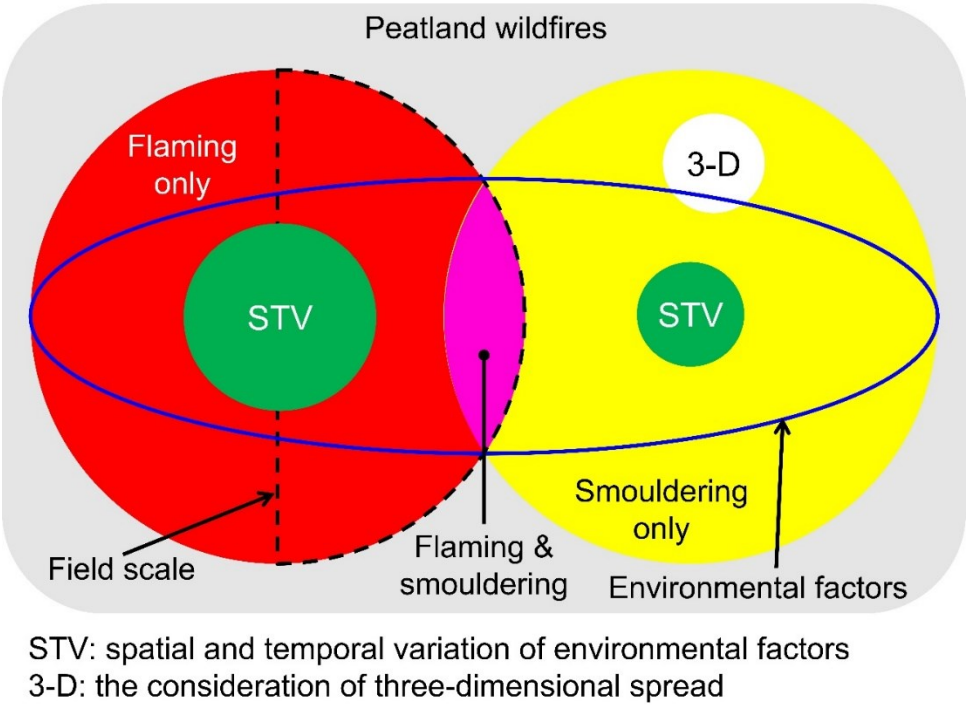

Figure 1.7. The phenomena involved in peatland wildfires and the phenomena that have been addressed in the previous models. The red represents flaming models, yellow represents smouldering models, and magenta represents the integration of flaming and smouldering models. The region encapsulated by the black dashed line corresponds to field-scale models, whereas outside this line corresponds to small scale models. The region encapsulated by the blue line corresponds to the models that consider environmental factors such as vegetation type and density of flaming and peat moisture content for smouldering, and the green represents the consideration of spatial and temporal variation (STV) for the environmental factors. White represents the consideration of 3-D spread. The larger size of the geometry, either independent or intersected geometry, correspond to more models that were developed.

The optimum peatland wildfire model is formed when the magenta region (integration of flaming and smouldering at the field-scale) intersects with green (environmental factors that considers its spatial and temporal variation) and white (3-D spread of smouldering) regions, which is the ultimate model that will be developed in this thesis. The specific aim of this thesis is therefore to develop a 3-D CA model of field-scale peatland wildfires that considers flaming and smouldering, and incorporates actual conditions in nature with its spatial and temporal variations, while remaining computationally feasible.

1.5.2. Upscaling and integration

The main problem in the modelling across scale is the different domain configuration required, i.e., different temporal or spatial resolution. When the cm-scale is upscale to km-scale, the resolution of the domain needs to be significantly courser. Otherwise, the computer will fail to complete the simulation due to insufficient resources, even when using high performing computers. The coarsening process of the domain introduces inherent issue such as the interaction within one entity (cell) in the domain that is a few orders of magnitude larger in size than in the small-scale domain (see Figure 1.8a). The small-scale model that is dedicated to the cm-scale domain, requires additional treatments to be implemented for the km-scale domain. Without these treatments, the model would be inaccurate since the process within one cell in the larger domain is the accumulation of the processes in many cells in the smaller domain (see Figure 1.8a). For example, if in the smaller domain one cell represent a 1-mm × 1-mm square and in the larger domain it is 1-m × 1-m square, then the process within one cell in the larger scale is the accumulation of the processes in 1 million cells in the smaller scale.

The field-scale models for flaming in the literature do not consider the upscaling process from the small scale, but instead directly use the large scale domain (Perry, 1998; Sullivan, 2009c). This thesis follows this approach for the flaming model; however, for the smouldering, since there are no field-scale models and field-scale experimental data are very limited in previous studies, the model is developed from the small scale and continued with the upscaling process. This thesis proposes multi-scale calibration for the upscaling from the small to field-scale models (see Figure 1.8b). The multi-scale calibration stems from the introduction of a resolution variable that contains information on the temporal and spatial resolutions of the domain. The other variables that govern the models are functions of this resolution variable. In the small-scale calibration, this resolution variable is set constant. Once the small-scale model is calibrated, the effect of

the resolution variable is activated, and the models are recalibrated with different value of the resolution variable (thus different domain resolution). This process is repeated with many different values of the resolution variable (see Figure 1.8b), thus, the models are accurate in many different domain resolutions and can be used across scales.

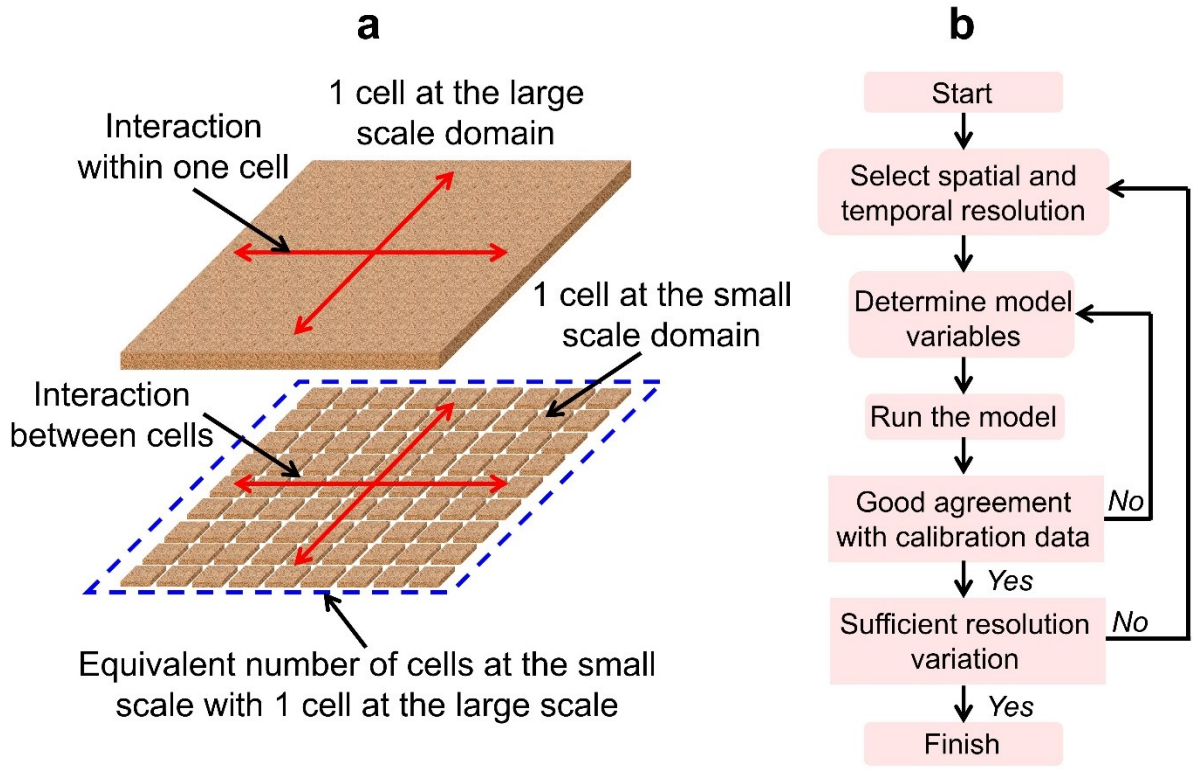

Figure 1.8. (a) Illustration of the upscaling from small scale domain to larger scale domain. (b) Schematic of the multi-scale calibration of the model.

The integration of flaming and smouldering models is novel and an area which has rarely been touched on. This integration is very important to understand the behaviour of peatland wildfires. The complexity of each combustion type, the limited studies on how the two fires affect each other, the different timescale between them, and the lack of availability of the data to validate the models are a few of the reasons for the lack of studies on this topic. The complexity of each combustion type stems from the many phenomena that should be considered and the factors that influence them, which are spatially nonuniform and vary temporally. Once these phenomena and factors are considered, to develop the integrated model, the interaction between smouldering and flaming during peatland wildfires become an issue; the smouldering of peat that is initiated by the flaming of vegetation, with both have different environmental factors, need to be investigated. Once the smouldering initiation issues are solved, the significantly different timescale (two order of magnitude) between flaming and smouldering spread requires comprehensive consideration when the two fires are

integrated. Although if the integrated models are successfully developed, the fidelity of the models need to be validated. However, only a very limited validation data are available, especially experimental studies at the field-scale that consider flaming and smouldering combustion (Grundling *et al.*, 2019; Santoso, 2021).

This thesis proposes separated computational domain for flaming and smouldering, which run independently (see Figure 1.9). The two domains, however, interact when the initiation of smouldering from flaming happens (see Figure 1.9). By using two independent domains, flaming that is affected by factors such as vegetation type and wind dynamics and smouldering that is affected by factors such as peat MC can be modelled independently, and the interaction between the domains only happen when instructed (see details in Chapter 6.1.2). This method, however, still requires both the domains to have the same spatial and temporal resolutions; thus, multi-scale calibration on the model with different resolution variables need to be performed on both flaming and smouldering. The different timescales between flaming and smouldering is an important issue; however, this issue can be solved with a selection of the domain's temporal and spatial resolutions that satisfy stability criteria. Since the model is calibration-based, the model's variables (including the variables that govern the initiation of smouldering by flaming) are optimised against the available laboratory-controlled experiments. Once the variables are calibrated, the upscaling process is performed and the model is validated against field-scale data, which is explained in Chapter 1.5.3.

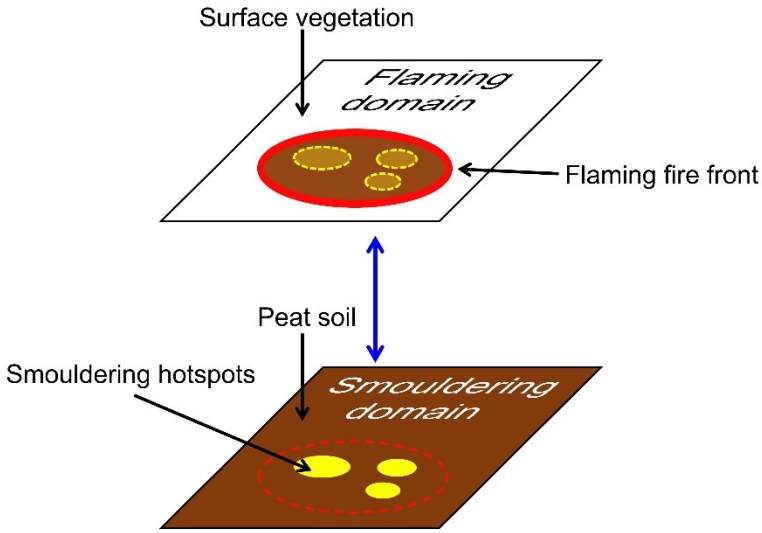

Figure 1.9 Illustration of multi-domain approach, where flaming and smouldering domains are separated. The white represents surface vegetation, brown represents peat soil, red represents flaming, and yellow represents smouldering. The dashed lines represent the projection across domains and the solid blue arrow represents the reciprocal interaction between the two domains.

1.5.3. Validation and extrapolation

The experimental data on peatland wildfires at the field-scale are very limited (Grundling *et al.*, 2019; Santoso, 2021); thus, validating the models against field-scale peatland wildfires experiments is not always possible. Due to this limitation, an alternative to acquire the validation data is required. Most of studies on peatland wildfires are done through observation of real wildfires either currently, or of historical fires, which is mostly via remote sensing (Page *et al.*, 2002; Elvidge *et al.*, 2015; Huijnen *et al.*, 2016). Since the satellites record the radiation data continuously, the analysis of wildfires can be performed either during the incident (real time) or in the past. This method provides tools to analyse peatland wildfires (at any location) more thoroughly based on past and current events, thus, the remote sensing data can be used to validate the models at the field-scale. While the use of remote sensing data to validate the wildfire models has been commonly performed for flaming wildfire models (Alexandridis *et al.*, 2008), it has not been used to validate smouldering wildfire models, mainly due to the limited remote sensing data of smouldering wildfires (see Chapter 1.3). In this thesis, both the flaming and smouldering components of the field-scale models are validated against corresponding remote sensing data, either obtained from the raw remote sensing data or through algorithm implemented on the raw remote sensing data.

A validation based on remote sensing relies heavily on the goodness of the remote sensing data. If the remote sensing data are insufficiently accurate, the model would not be valid although if it has good agreement with the validation data. Therefore, the assessment of the goodness of the remote sensing data is of utmost important. The traditional way of assessing this goodness is by comparing the generated remote sensing data, via algorithms, with the ground observation. This method validates the algorithm results on the locations of flaming and smouldering with the actual location of the fires that are determined from the ground observation. The accuracy of the algorithms is derived from this comparison, in which if accuracy is high, then the algorithm provides a powerful tool for wildfires detection; otherwise, the algorithm needs improvement.

While this method is robust and straightforward, it is expensive and suffers from the black box problem. Collecting the data from ground observation require comprehensive understanding on the accessibility and the resources needed. Most of the peatlands are in rural area, and are hard to access, and consequently require significant amount of resources. Although if this issue is resolved, the scale and uncertainties of the data collected from the ground observations causes its comparison with algorithm results is difficult, especially for smouldering. The scale of the satellite data is around few

hundred meters per one pixel, whereas within a square of few hundred meters per one pixel, there are many possibilities (see Figure 1.10): entirely flaming, entirely smouldering, combination of flaming and smouldering, intact, partly smouldering, etc. (Sofan *et al.*, 2020). While flaming wildfires are apparent and give strong radiation to the satellite, determining smouldering is difficult, even in ground observations, and its radiation is significantly weaker (Elvidge *et al.*, 2015). The effect of atmospheric obstacles such as cloud make this to be more difficult (see Figure 1.10). Once this issue is resolved, without understanding the typical radiation from flaming and smouldering, the values used in the algorithm to determine the categorization of the pixel (whether it is flaming, smouldering, or intact) have insufficient generality. This insufficiency means that the algorithm has a good accuracy for the data used in the comparison but inaccurate in other data. The algorithm is treated like a black box, where the fundamental knowledge of physics in the algorithm is not present and the accuracy of the algorithm is volatile. The accuracy and generality of the algorithm can be improved by assessing the algorithm against as many ground observation data as possible, similar to those in machine learning. However, this approach leads to the issue of resources availability.

This thesis proposes to use laboratory-controlled experiments to assess the goodness of remote sensing of flaming and smouldering. This method has been used repeatedly for flaming fire (Sun *et al.*, 2006; Boulet *et al.*, 2009, 2011); however, none of the studies consider smouldering peat, especially when both fire types are discussed. By using laboratory-controlled experiments, the resources required to conduct the experiments are significantly lower and the noise level in the experiments is minimal (see Figure 1.10). The detail of dynamics of the fire and the different conditions of the sample can be investigated without significant additional required resources. The main drawback of the laboratory-controlled experiment is the need for adjustment when the results are applied to a field-scale remote sensing. However, the adjustment for smouldering can adapt the adjustment from flaming (the noise level at the same location is similar between flaming and smouldering), which are more readily available (Wooster, Zhukov and Oertel, 2003). The aim of this method is to investigate the typical value of radiation from flaming and smouldering, resolving the black box problem, which then can be used to assess the goodness of remote sensing data and assist with the improvement of remote sensing of peatland wildfires. The improved remote sensing of peatland wildfires can then be used to obtain accurate validation data for models.

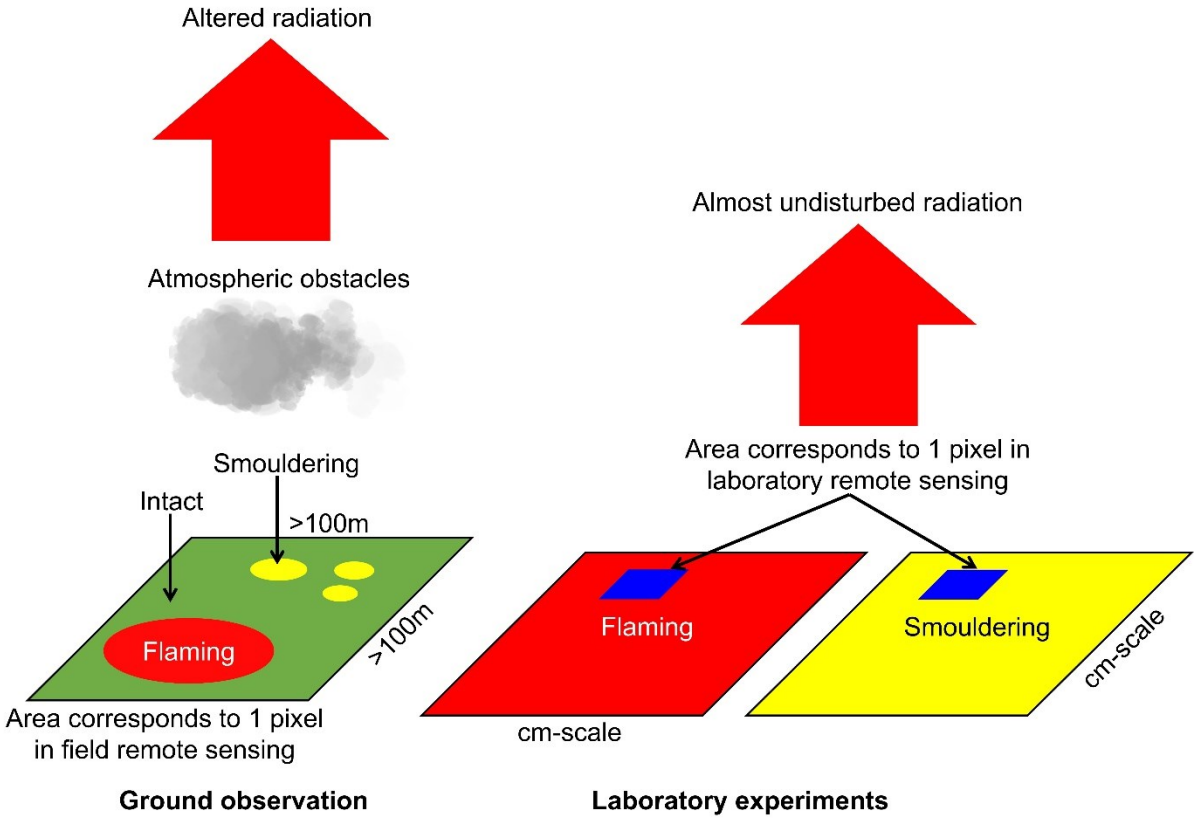

Figure 1.10. Comparison between ground observation and laboratory-controlled experiments to assess the goodness of remote sensing application.

Validated models provide practitioners with robust tools to approximate the behaviour of peatland wildfires, such as how they start and spread, and help strategize mitigation attempts. This usability means that the model can also be used to simulate peatland wildfires in many different scenarios, not only wildfires that are happening or have happened in the past, thus, the effect of variables that might influence peatland wildfires can be investigated and quantified. For example, by varying the peat MC, the effect of different peat MC in the ignition and spread of smouldering can be studied and the critical value at which the peatland wildfires become significant threats can be quantified. With this understanding, the mitigation of peatland wildfires will become more effective since, for instance, the information on the required resources can be estimated more accurately. The extrapolation use of the model provides the practitioners with more knowledge and data to consider when developing mitigation strategies.

This thesis proposes extrapolation usage of the models to estimate the smouldering area given the same flaming conditions, by varying the peat conditions. Therefore, the ratio between flaming and smouldering area is investigated in different conditions of peat. This investigation is important for two reasons: smouldering is the always unwanted wildfires (Turetsky *et al.*, 2015) and smouldering is still difficult to detect via state-of-the-

art technologies (Elvidge *et al.*, 2015). Flaming wildfires are sometimes intentional and desirable, such as for prescribed fires to avoid large wildfires by minimising the fuel accumulation (Malamud, Morein and Turcotte, 1998; Block *et al.*, 2016; Waldrop and Goodrick, 2018), whereas smouldering is the unwanted side effect of these fires; flaming vegetation accidentally ignites the soil underneath when flaming occurs on peatland ecosystem (Turetsky *et al.*, 2015). Therefore, in the event of prescribed fires in peatland, when the flaming is under control the only concern is the ignition and spread of smouldering (in the event of unwanted flaming wildfires on peatland, both flaming and smouldering are of concern). While current technologies are able to detect flaming with a high level of confidence, the detection of smouldering remains scientific challenge. Therefore, model can help in estimating the ignition and spread of smouldering which current technologies might fail to detect. With the help of the model, the ratio between flaming and smouldering area can be investigated, and many important variables such as carbon emissions can be estimated.

1.6. Thesis Outline

The outline of the thesis is as follows.

Chapter 1: In this chapter, the impacts and phenomena present in peatland wildfires are discussed. The literatures studying this topic are reviewed and the gaps exist from the literatures are identified and used to derive the aims and methodology of this thesis.

The goodness of remote sensing to provide data for validating the model is investigated. Chapter 2 is dedicated to this task and investigate the following.

Chapter 2: In this chapter, the radiation of flaming and smouldering are investigated in laboratory-controlled experiments. This investigation aims to distinguish the radiation of flaming and smouldering at a detailed level, which will be used in subsequent chapters. A good set of validation data provide a pillar for the development of a high-fidelity model for peatland wildfires.

Since there are many different approaches can be used for cellular automata, the existing approaches for wildfire modelling are reviewed. Chapter 3 is dedicated to this task.

Chapter 3: In this chapter, the existing cellular automata models for wildfires are reviewed. This review aims to understand the existing approaches in the literatures, implemented to cellular automata for wildfires modelling and investigate their usability,

benefits, and drawbacks. A good understanding on the approaches used in the literatures provide a strong foundation to develop the model.

Based on the knowledge from the previous chapters, the cellular automata model for 3-D spread of smouldering is developed at the lab-scale. Chapter 4 and 5 are dedicated to this task and investigate the following.

Chapter 4: In this chapter, a 3-D cellular automata model for smouldering at the lab-scale is developed. This model considered the spatial non-uniformities of the sample. This chapter investigates the spread of smouldering in non-uniform condition, which will be used as the basic model for subsequent chapters of field-scale cases.

Chapter 5: In this chapter, cellular automata and physics-based models for smouldering at the lab-scale are compared and combined. The comparison aims to investigate the benefits and drawbacks of each model and assess their suitability for field-scale modelling. The combination aims to increase the level of detail the model in Chapter 4 can provide.

Cellular automata models for field-scale peatland wildfires at the field-scale are developed. Chapter 6 – 9 are dedicated to this task and investigate the following.

Chapter 6: In this chapter, a 2-D field-scale model of peatland wildfires on spatially and temporally uniform peat soil condition is developed. This chapter aims to investigate the initiation of smouldering by flaming and its spread behaviour.

Chapter 7: In this chapter, a 2-D field-scale model of peatland wildfires on temporally vary peat soil is developed, improving the model in chapter 6. This chapter aims to investigate the ignition and spread of smouldering when the peat soil condition change over time, which is the actual condition in the nature.

Chapter 8: In this chapter, the existing cellular automata models for smouldering in the literatures are compared. This chapter aims to investigate the benefits, drawbacks, and usability of the models, especially when applied across scales, with significantly more details than in Chapter 3. This helps to determine the optimum approach to be used for the field-scale peatland wildfires model.

Chapter 9: In this chapter, the knowledge from chapter 4 – 8 are used to develop 3-D cellular automata model for field-scale peatland wildfires, which is the ultimate model in this thesis. This chapter aims to investigate the emission from peatland wildfires that also consider the source of emission, either flaming or smouldering. The emission of peatland wildfires in Indonesia in the recent years are estimated and their impact on climate change are discussed.

Chapter 2 – Can Infrared Emissions Distinguish Flaming and Smouldering Wildfires? A Laboratory Study to Assist Remote Sensing

Summary[1]

This chapter investigated the suitability of infrared-based remote sensing to distinguish between flaming and smouldering wildfires. The investigation is based on laboratory-controlled experiments of flaming pine needle and smouldering peat that are monitored by using infrared (IR) cameras. The infrared emissions seen from the top-view of the burning samples were measured at eight different wavelengths: 1.6 μm, 2.2 μm, 3.5 μm, 4 μm, 4.5 μm, 8 μm, 10 μm, and 12 μm, which are the most commonly used wavelengths in satellite remote sensing. The spectral intensity of flaming and smouldering at different wavelengths were investigated and the detection of subsurface smouldering was also discussed. The spectral intensity of flaming is 2 – 7 times higher than smouldering at any wavelength considered. The flaming to smouldering spectral intensity ratio peaks at 3.5 – 4.5 μm wavelength range, and these wavelengths are recommended for the monitoring of peatland wildfires. The integration of spectral intensities within a sufficiently wide range of wavelengths (emissive power) is required to strengthen the emissions from subsurface smouldering, to enable its detection. These findings indicate that the current technology of satellite remote sensing can distinguish flaming from smouldering, but is unable to detect subsurface smouldering. This chapter provides a novel analysis on using infrared to distinguish smouldering and flaming fires and help improve the remote sensing of peatland wildfires.

2.1. Introduction to Wildfire Detection

Many methods have been developed for the detection and monitoring of wildfires, using both conventional or modern technologies (see Figure 2.1). The conventional method

[1] This chapter is based on "Dwi M J Purnomo, Hafiz M F Amin, Wuquan Cui, and Guillermo Rein, 2022. Can Infrared Emissions Distinguish Flaming and Smouldering Wildfires? A Laboratory Study to Assist Remote Sensing. *International Journal of Wildland Fire*, (submitted)."

involves observing smoke plumes during the day and flame at night, either an in-situ or on top of a firewatch tower. Presently, wildfire detection and monitoring are mostly performed by using remote sensing, due to its large coverage area and near real-time detection (Burke *et al.*, 2019). The use of remote sensing also allows the estimation of carbon emission from wildfires, either via bottom-up approach (Page *et al.*, 2002) or top-down approach (Huijnen *et al.*, 2016). Many different aerial machines have been used for remote sensing purposes: satellites that are placed in the space and follow a certain orbit, aircraft that fly over the wildfires, autopiloted drones that fly over the wildfires at a lower altitude than aircraft, and stratospheric unmanned aerial vehicle (UAV) that fly in the stratosphere of the Earth and can remain on one mission for a long time (weeks). The satellites in wildfire detection are mostly sun-synchronous (in an orbit at which in one year the satellite revolve the sun) or geo-synchronous (match with the rotation of the Earth).

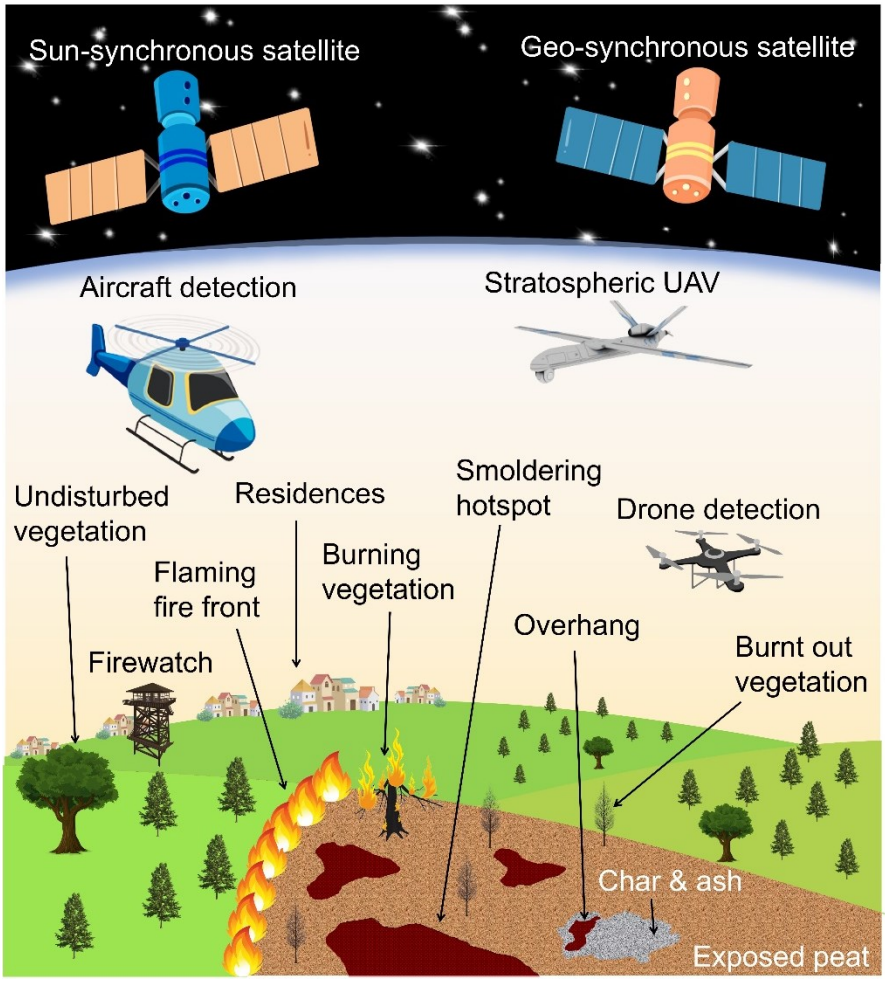

Figure 2.1. The methods have been developed for wildfires detection both conventional (Firewatch and alarm from residents) and modern technologies (aircraft, drones, satellites). The phenomena to be detected in peatland wildfires are flaming, surface smouldering, and subsurface smouldering (overhang).

Most of current technologies in remote sensing of wildfires use infrared sensors (Elvidge *et al.*, 2015) that are equipped in one of the aerial machines. In the detection and monitoring of peatland wildfires, these sensors are used to detect and distinguish the infrared emissions in different state of the surface of the Earth: undisturbed vegetation, flaming fire, exposed soil, burning vegetation, burnt out vegetation, surface smouldering fire, and subsurface smouldering fire. However, while these sensors can accurately detect and monitor flaming wildfires (flaming fire and burning vegetation) and non-active fire (undisturbed vegetation, exposed soil, and burnt out vegetation), the detection and monitoring of smouldering wildfires remain a scientific challenge, especially in subsurface smouldering fire (Elvidge *et al.*, 2015; Burke *et al.*, 2019). The detection and monitoring challenges are caused by the lower temperature of smouldering, which sometimes cannot be distinguished from the non-burning objects.

A recent example of detection failure of smouldering wildfire was the Deurnsche Peel peatland wildfire in the Netherlands in 2020. In this fire event, a large wildfire started on 20 April 2020, in the Deurnsche Peel nature reserve (Hermans, 2021). The glowing region in top-left of Figure 2.2a shows flaming wildfires that were visible in the satellite image, which burned the surface vegetation. After five days and four nights of intensive firefighting, flaming wildfires were successfully extinguished (Hermans, 2021). However, although there were no longer any visible flames or large fires on the surface, the peat soil remained burning via smouldering for a very long time (Hermans, 2021). Smouldering peat could reappear with warm temperatures or strong winds even after they were confirmed to extinguish (Hermans, 2021). The smouldering peat was finally contained after 2 months of intensive firefighting (50 m^3/h water spray) and several heavy rains (Hermans, 2021).

Although it was reported that the smouldering wildfires remained active for two months, satellites failed to capture the smouldering (Hermans, 2021). The satellites were only able to capture the flaming wildfires for five days out of two months. Figure 2.2a shows the satellite data from the same location on different days from two different satellites, the Sentinel-2 and the NASA Earth Observing System Data and Information System (EOSDIS) that provides data from Terra and Aqua satellites (used for MODIS). On the day when the wildfire started, both the satellites successfully captured the flaming wildfires (yellow glowing area in Sentinel-2 and red dots in EOSDIS NASA). One week after the start of the fire, both Sentinel-2 and EOSDIS NASA did not detect any active fire, even though, based on the field observations, the fires remained active via

smouldering (Hermans, 2021). Therefore, satellite remote sensing has not been robust to detect smouldering wildfires, which is mainly due to the insufficiency of the data.

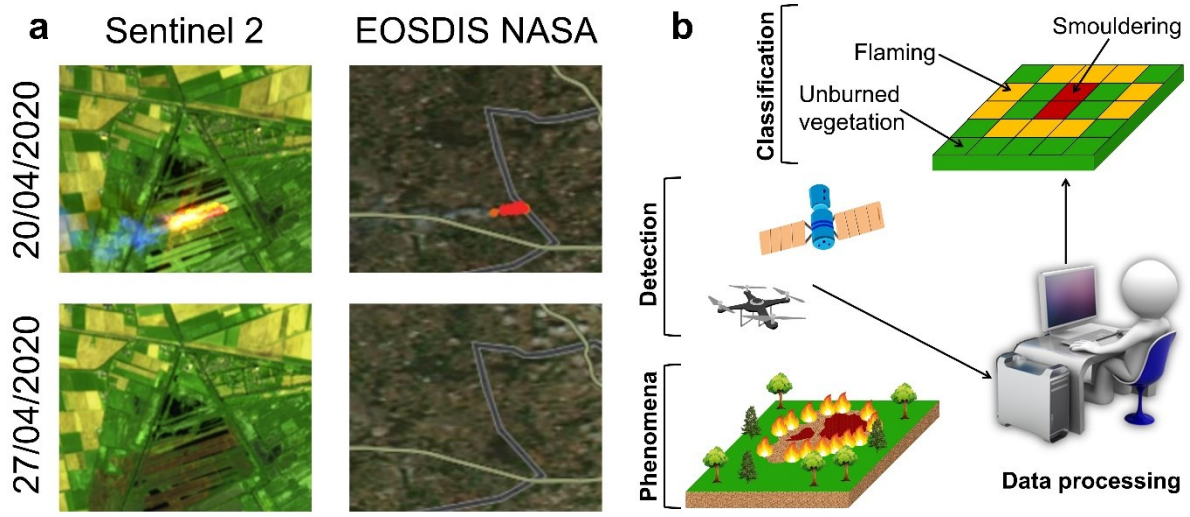

Figure 2.2. (a) Satellite images of a peatland wildfire in Deurnsche Peel nature reserve in the Netherlands (51.401°N, 5.811°E) on 20 and 27 April 2020. The pictures on the left were obtained from the Sentinel-2 satellite, whereas the right pictures are from EOSDIS NASA. The glowing region in the left image and red dots in the right image represent active fires successfully captured by the satellite. (b) The process involved in remote sensing of wildfires. The phenomena are observed by the detection devices which then processed through a certain algorithm and results in the classification of the cells in the grid.

The detection failure in remote sensing applications corresponds to misclassification of the states of the cells in the grid (see Figure 2.2b). In remote sensing, the phenomena observed by the sensors are transferred to the computer for data processing, which then result in the classification of the cells in the grid; thus, misclassification is either caused by either equipment issues, data processing issues, or both (Wooster *et al.*, 2021). The failure in the equipment can be caused by the quality and capability of the sensors. For example, as infrared has a wide range of wavelengths, if the sensors are not sensitive to the wavelength at which the fire can be detected, the data that are transferred to the computer will contain false information on the active fire state. The resolution of the sensors is also important since with course resolution, the radiation of a very small fraction (below 0.01%) of fire in one cell will not be strong enough to be classified as active fire (Wooster, Zhukov and Oertel, 2003; Ichoku *et al.*, 2016; Wooster *et al.*, 2021). Failure in data processing is caused by the poor selection of data and mathematical operation in the algorithm used to classify the cells in the grid. To obtain a good classification, i.e., avoiding both false positive and false negative, the quality and

capability of the sensors and the goodness of the algorithm must be ensured (Wooster *et al.*, 2021).

2.2. Remote Sensing on Flaming and Smouldering

In remote sensing applications, wildfires are mostly detected and monitored by satellites. This selection stems from the simplicity and resources required for the detection and monitoring of wildfires (Elvidge *et al.*, 2015). By using satellites, the only resources required are satellite data and computer to process these data for classification, whereas using other machines such as drones and aircraft, requires sophisticated and expensive setup, for instance, the purchase or rental of machines and the permission to operate these machines. The main disadvantageous of using satellites is the inflexibility of using the sensors, as the sensors equipped in satellites are fixed and cannot be changed at will, unlike those in drones and aircrafts (Nowzad, 2019). Satellites only use band sensors, the sensors that capture infrared emissions within a narrow wavelength (ideally at one exact wavelength to capture the spectral intensity), with a limited number of wavelengths. Moreover, no satellite that covers the whole range of infrared wavelengths, i.e., from short wave (SWIR), mid wave (MWIR), to long wave (LWIR) infrareds (see Figure 2.3). This limitation combined with the spatial and temporal (frequency of data collections) resolutions of the satellites are the main reasons that have caused scientific community to explore alternative options (Nowzad, 2019); for instance, by using drones that have adjustable spatial and temporal resolutions and can be equipped with band or broad (capture infrared emission over a wide wavelength) wavelength sensors (Figure 2.4c; Burke *et al.*, 2019; Nowzad, 2019). However, satellites are still the most developed methods for remote sensing of wildfires and continue to be improved both in terms of sensors and algorithms (Dozier, 1981; Siegert *et al.*, 2004; Elvidge *et al.*, 2013, 2015; Atwood *et al.*, 2016; Giglio, Schroeder and Justice, 2016; Sofan *et al.*, 2019, 2020).

Of many satellites available, those extensively used for wildfires detection are Landsat 8, Sentinel-2, NASA Tera & Aqua, Suomi NPP, NOAA, BIRD, and TET-1, which are equipped with instruments (sensors system) of OLI & TIRS, MSI, MODIS, VIIRS, AVHRR, HSRS, and BIROS respectively (see Table S2.1 for the acronym; Kramer, 1996; ESA, 2015; Cao *et al.*, 2017; USGS, 2019; NASA, 2020). These satellites have significantly different spatial and temporal resolutions and have been used to detect and monitor both flaming and smouldering wildfires either with or without distinction between flaming and smouldering (see Table 2.1). In Table 2.1, the detection and monitoring of flaming and smouldering wildfires without distinction is referred to as hotspots, which means the

hotspots can be either flaming or smouldering without additional information on which type of combustion.

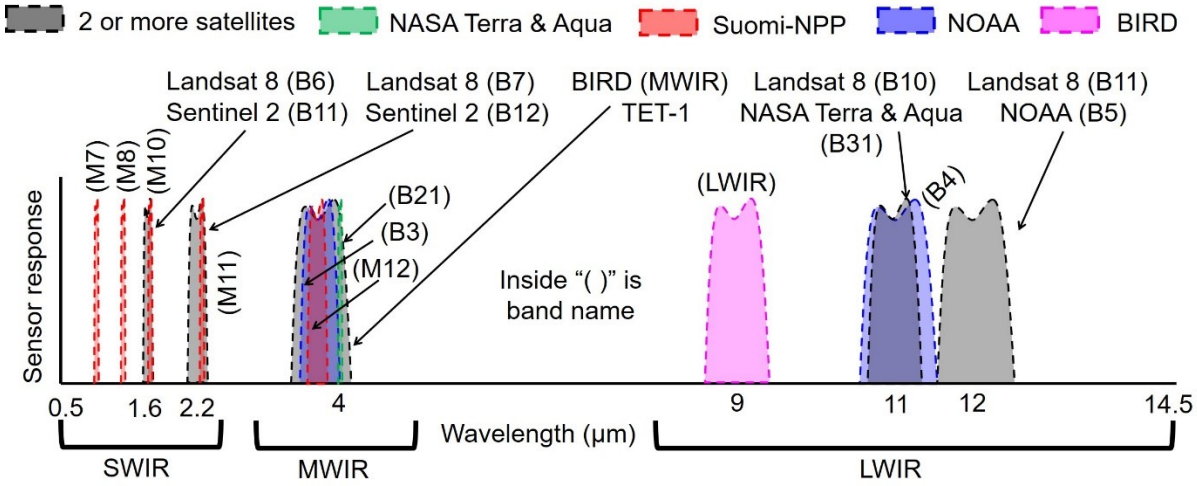

Figure 2.3. Illustration of central wavelength and its width of instruments from different satellites. The band names in brackets correspond to the channel nomenclature of the satellite and are associated with Table 2.1.

In peatland wildfires, number of phenomena are involved as shown in Figure 2.4a, thus, different infrared emissions are radiated. All the objects involved in peatland wildfires radiate infrared emissions, but with different intensities that correspond to the phase and temperature of the object. These differences can be quantified by using wavelength and spectral intensity (see Figure 2.4b). Both flaming and smouldering combustion radiate with spectral intensities following Planck's curve, which represent solid phase radiation, however, smouldering radiation is theoretically lower than flaming at any wavelength due to its lower temperature. The combustion products (mainly CO_2, CO, and H_2O) also radiate infrareds, however, while solid objects have broad wavelength radiation, gas substances have band radiation, and their spectral intensities peak at a narrow wavelength, while it is near zero at other wavelengths (see Figure 2.4b; Boulet *et al.*, 2011; Rein, 2016; Hu *et al.*, 2018). Another infrared emission is radiated by the subsurface smouldering, which is weaker than flaming and surface smouldering; thus, the detection and monitoring of this fire is difficult since its radiation can be indistinctive from the background (undisturbed soil, unburned vegetation, and burnt out vegetation). In actual wildfires, although the spectral intensity profiles of the objects in Figure 2.4a deviate from the theoretical profiles in Figure 2.4b, their profiles are expected to be proportional, for instance, the spectral intensity of flaming vegetation is expected to be higher than smouldering peat at any wavelength, and their peaks are at different wavelengths. Therefore, when there are differences in spectral intensity found in the

actual remote sensing of peatland wildfires, the theoretical understanding presented in Figure 2.4b can be used to distinguish between flaming, smouldering and other objects. However, when flaming vegetation is active on top of active smouldering peat, their distinction can be elusive; this distinction is investigated in this chapter.

In flaming wildfire detection and monitoring, MWIR is commonly used since the gas phase products of flaming combustion radiate the infrared in a narrow range of wavelengths (band) within the range of MWIR, and the flaming vegetation radiation also peak at the range of MWIR (Sun *et al.*, 2006; Boulet *et al.*, 2009, 2011). Moreover, MWIR radiation is less sensitive to the atmospheric noises such as cloud and atmospheric moisture and smoke (Giglio, Schroeder and Justice, 2016). Therefore, the flaming wildfire can be detected and separated from other objects. However, many satellites (e.g., Landsat 8, Sentinel-2) are not equipped with MWIR sensors. Only satellites that have missions of wildfires monitoring (e.g., NASA Terra & Aqua) are equipped with MWIR sensors, most of which have coarser spatial and temporal resolutions, which then affect the accuracy of fire detection (Burke *et al.*, 2019). Due to these issues, for the development of algorithms in remote sensing for wildfires detection and monitoring, researchers start using SWIR data that are available in most satellites (Sofan *et al.*, 2020). However, what SWIR actually detects has not been confirmed, and its usability to detect smouldering wildfires is still unknown.

Table 2.1. List of satellites that have been used for monitoring wildfires. The central wavelength and its band width are shown in Figure 2.3. The temporal resolution represents the frequency of the data collection. The hotspot detection does not distinguish flaming and smouldering, whereas flaming & smouldering detection attempt to distinguish them.

Satellite (Instrument)	Spatial resolution (m)	Temporal resolution (days)	Monitoring application (channel name)
Landsat 8 (OLI & TIRS; USGS, 2019)	30	16	Flaming & smouldering (B6; Elvidge *et al.*, 2015; Sofan *et al.*, 2019)
	30	16	Flaming & smouldering (B7; Elvidge *et al.*, 2015; Sofan *et al.*, 2019)
	30	16	Flaming & smouldering (B10; Elvidge *et al.*, 2015; Sofan *et al.*, 2019)
	30	16	Smouldering (B11; Elvidge *et al.*, 2015)
Sentinel-2 (MSI; ESA, 2015)	20	5	Flaming & Smouldering (B11; Sofan *et al.*, 2020)
	20	5	Flaming & Smouldering (B12; Sofan *et al.*, 2020)
NASA Tera & Aqua (MODIS; NASA, 2020)	500	8	Hotspots (B21) (Giglio, Schroeder and Justice, 2016)
	500	8	Hotspots (B31; Giglio, Schroeder and Justice, 2016)
Suomi-NPP (VIIRS; Cao *et al.*, 2017)	750	1	Hotspots (M7; Elvidge *et al.*, 2013)
	750	1	Hotspots (M8; Elvidge *et al.*, 2013)
	750	1	Hotspots (M10; Elvidge *et al.*, 2013)
	750	1	Hotspots (M11; Elvidge *et al.*, 2013)
	750	1	Hotspots (M12; Elvidge *et al.*, 2013)
NOAA (AVHRR; Cao *et al.*, 2017)	1100	16	Hotspots (B3; Dozier, 1981)
	1100	16	Hotspots (B4; Dozier, 1981)
	1100	16	Hotspots (B5; Dozier, 1981)
BIRD (HSRS; Kramer, 1996)	372	15	Hotspots (MWIR; Siegert *et al.*, 2004)
	372	15	Hotspots (LWIR; Siegert *et al.*, 2004)
TET-1 (BIROS; Kramer, 1996)	160	3	Hotspots (Atwood *et al.*, 2016)

In smouldering fire detection, LWIR is mostly used to separate the smouldering from flaming, since from the Planck's law, smouldering that has lower temperature has infrared emissions peaking within the LWIR range (Elvidge *et al.*, 2015). LWIR can also detect the subsurface smouldering; however, this detection used an infrared camera that has broad wavelength sensitivity (8 – 14 μm), which is mounted on a drone (Burke *et al.*, 2019), unlike those of satellites that have narrow wavelength sensitivity.

Previous studies leave the following gaps in the knowledge on the detection and monitoring of peatland wildfires: (i) can infrared emissions distinguish between flaming and smouldering wildfires, and (ii) how does the infrareds respond to subsurface smouldering. This chapter addresses and discusses these questions by investigating the infrared radiation of smouldering and flaming of natural fuels in the laboratory-controlled experiments, and for the first time, assess the suitability of infrared to distinguish flaming and smouldering for remote sensing of peatland wildfires. Laboratory-controlled experiments were conducted on peat and pine needle samples for smouldering and flaming experiments respectively. Peat samples with five different MC and pine needle with five different fuel bed size were considered. An infrared camera was placed on top of the burning samples to mimic the application of remote sensing, unlike other lab-scale experiments that viewed the sample from the side (Sun *et al.*, 2006; Boulet *et al.*, 2009, 2011). Different optical filters were mounted in front of the infrared camera to capture the infrared emissions at different wavelengths.

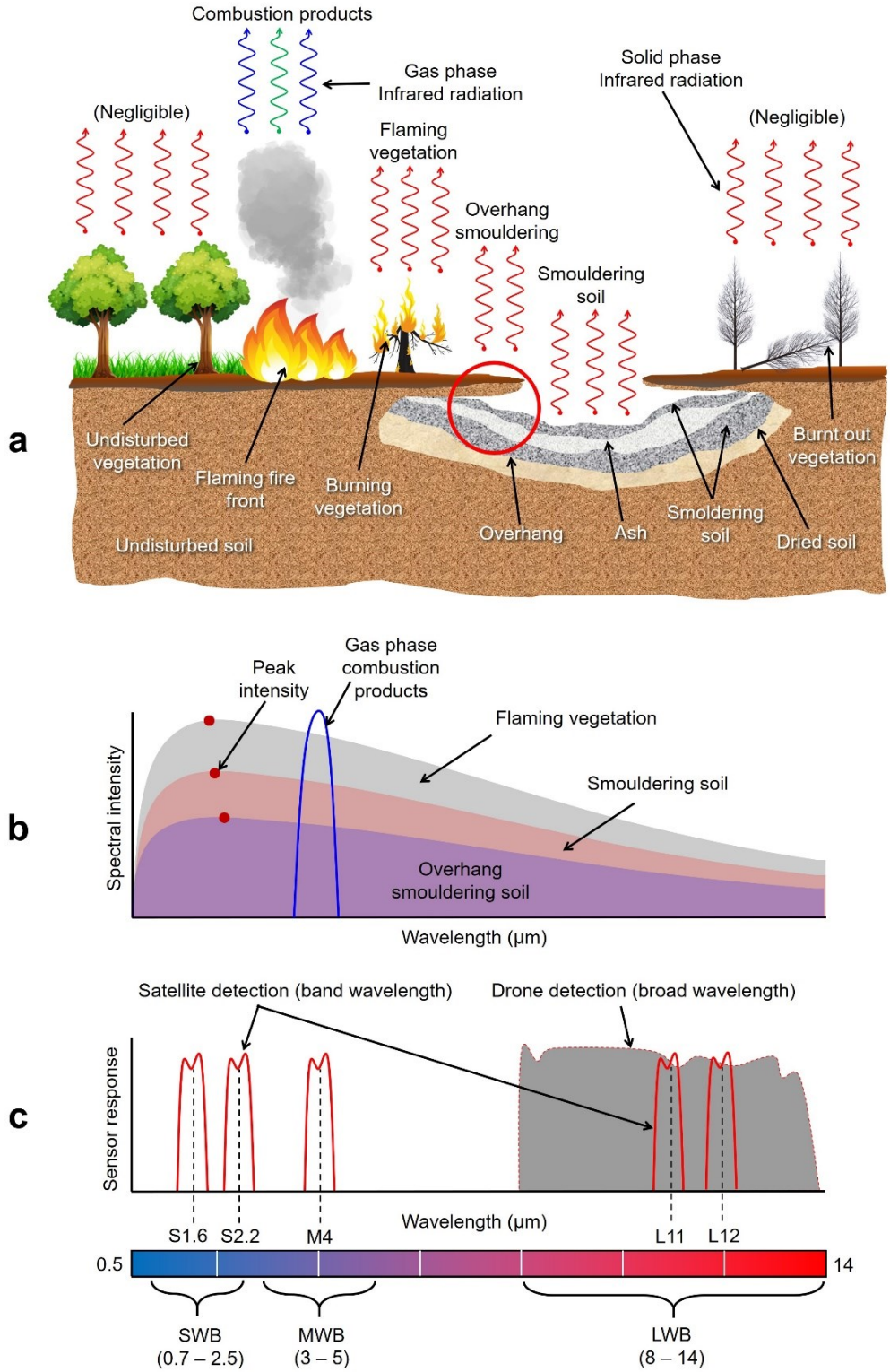

Figure 2.4. (a) Schematic of the phenomena that present in peatland wildfires and the infrared radiations they emit. The red, blue, and green twisted lines are solid, gas, and soot & PM radiation respectively. (b) The corresponding spectral intensities of the radiations in (a). (c) The detection of the radiation in (b) by remote sensing apparatus.

2.3. Materials and Methods

Laboratory scale experiments were conducted on an open-top reactor made of insulating ceramic boards (k = 0.7 W.m^{-1}K^{-1}, ρ = 310 kg.m^{-3}, c_p = 1090 J.kg^{-1}K^{-1}) with internal dimensions of 20 × 20 × 10 cm (Figure 2.5) for both flaming and smouldering experiments. Pine needles were used for the flaming experiments and commercial milled Irish Sphagnum peat (Shamrock Irish Moss Peat, Bord na Mona Horticulture) were used for the smouldering experiments, due to their batch consistent properties in the long term, ease of accessibility, and frequent use in scientific literatures (Valdivieso and Rivera, 2014; Huang *et al.*, 2016; Huang and Rein, 2017; Wang *et al.*, 2017; Hu *et al.*, 2019).

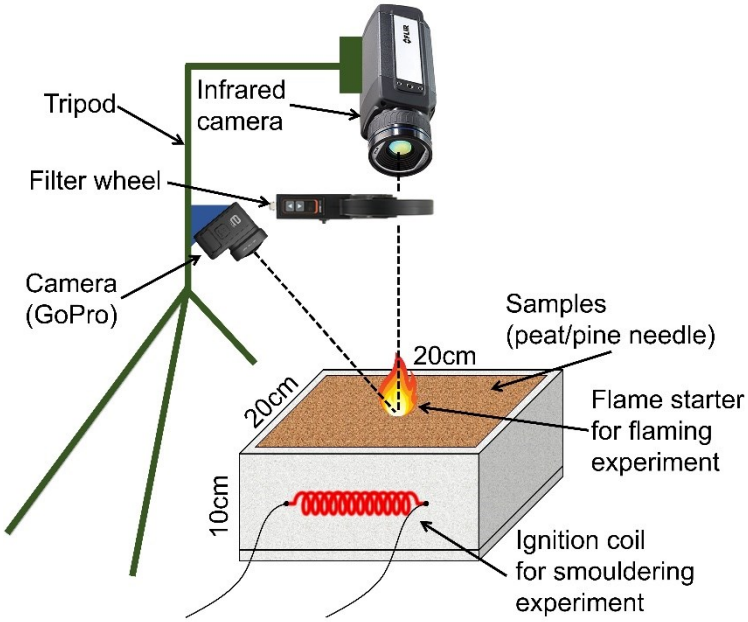

Figure 2.5. The schematic of the laboratory experiment on smouldering of peat and flaming of pine needles. The flaming experiments were initiated at the centre of the reactor, whereas the smouldering experiments were initiated the edge of the reactor. A visual camera (GoPro) and infrared cameras were used to monitor flaming and smouldering experiments.

Before conditioning, samples were dried in an oven at 80°C for 48h (Restuccia, Huang and Rein, 2017; Hu *et al.*, 2019). The selection of 80°C instead of 100°C was to avoid thermal degradation (pyrolysis) of the sample (Huang and Rein, 2017), whereas the selection of 48h drying time was to ensure that there is no longer mass change of the sample when the drying is longer. The fuel bed size of pine needle samples is varied: 6g, 8g, 10g, 12g, and 15g, whereas the variation on peat samples is provided on their MC: 5%, 25%, 35%, 45%, and 65% on dry basis. The selection of fuel bed size of pine needles was based on the range of mass that sustain flaming but only at a reasonable flame height for safety reason. The selection of peat MC was based on the time required to finish the

experiment where with MC higher than 65%, the experiments remained active for more than 8h. The pine needle samples were ignited at the centre of the reactor using a lighter to initiate the flaming fire. The peat samples were ignited at the edge of the reactor using a helical coil, 18 cm long, with a diameter of 1 cm, and made of a 0.5 mm thick nichrome wire. 100 W was supplied to the sample through the coil for 30 min (Hu *et al.*, 2019). The use of ignition coil was because control of aspects like the power provided and the ignition duration are straightforward, thus, the ignition protocol can be standardized and the effect of its variation on the experiment can be minimised. Although in the actual peatland wildfires smouldering peat is initiated by flaming vegetation, the use of ignition coil still provides relevant data, since once the ignition period is over and smouldering is self-sustained, the ignition protocol does not significantly affect the smouldering dynamics.

Both the flaming and smouldering experiments were monitored by using a visual camera (GoPro) and two different infrared (IR) cameras: FLIR X6900sc for SWIR and MWIR experiments, and FLIR A655sc for LWIR experiments, which are mounted as shown in Figure 2.5. The technical specification of the infrared cameras that were used in this chapter is summarized in Table 2.2.

Table 2.2. The technical specification of the infrared cameras used in the experiments.

	FLIR X6900sc	FLIR A655sc
Spectral range (μm)	1.5 - 5	7.5 – 14
Resolution	640 x 512	640 x 480
Maximum frame rate (Hz)	1000	200
Dynamic range (bit)	14	16

The infrared cameras were dedicated to observe the top view of the burning samples to mimic the application of remote sensing, whereas the visual camera was used to aid the observation of infrared camera in showing phenomena involved in the experiments if they were observed by the naked eye. In SWIR experiments, filters with central wavelength of 1.6 and 2.2 μm were placed in front of the infrared camera lens. In MWIR experiments, filters with central wavelength of 3.5, 4, and 4.5 μm were used, whereas in LWIR experiments, filters with central wavelength of 8, 10, and 12 μm were used. These filters were selected based on the central wavelengths that are commonly used in satellite remote sensing for wildfire detection (see Figure 2.3). While the filters in SWIR and MWIR experiments were placed directly in front of the camera lens, in LWIR experiments, a filter wheel (Thorlab FW102C) was placed in front of the camera to carry and change the filters (see Figure 2.5). The usage of filter wheel speeded up the filter

replacement process and minimise the disturbance to the camera position through slight movements caused by manual filter replacement. However, due to experimental constraints for the FLIR X6900sc camera, using filter wheel in SWIR and MWIR experiments was not possible.

In flaming experiments, each combination of fuel bed size and filter wavelength requires an independent experiment, thus, there were in total 40 flaming experiments. The reduction of number of flaming experiments was not possible due to its rapid progression in which an independent experiment only took averagely two minutes. Therefore, changing the filter during a flaming experiment created a mismatch between the infrared emissions from different filters, which was not encountered in smouldering experiments. Meanwhile, in smouldering experiments, an independent experiment was only required when the MC of the sample was changed, however, due to the usage of two different infrared cameras, the smouldering experiments were split into two stages: SWIR and MWIR set of experiments and LWIR set of experiments. Therefore, there were in total 10 independent experiments of smouldering.

Experiments not using filters were also considered, in which the radiation captured by the infrared camera is the broad type. This consideration added 15 independent flaming experiments, however, no additional independent smouldering experiment was needed since the broad infrared measurement can be performed in the same independent experiment as the band infrared measurement. Therefore, the experiments cover both broad and band wavelength radiation in three different spectral range categories (SWIR, MWIR, and LWIR) for flaming and smouldering combustion. Table 2.3 summarizes the channels that are used to address the camera and filters for the experiments. The flaming experiments were recorded at the frequency of 25 frame per second to avoid blurring due to the fast movement of the flame, whereas the smouldering experiments were recorded at the frequency of 1 frame per minute to minimise the memory consumption due to the slow spread of smouldering.

Table 2.3. Channels used in the experiments. Integrated gain is the integration of intensity gain in Figure 2.6 over wavelength.

Channel	Wavelength (μm)	Centre ± band width (nm)	Integrated gain (μm)
S1.6	1.6	1640 ± 25	0.018
S2.2	2.2	2192 ± 10	0.015
M3.5	3.5	3505 ± 42	0.034
M4	4	4080 ± 80	0.075
M4.5	4.5	4515 ± 90	0.067
L8	8	8224 ± 240	0.212
L10	10	10400 ± 300	0.222
L12	12	12290 ± 492	0.252
SWB	1.5 – 2.6 (broad)	N/A	0.833
MWB	3 – 5 (broad)	N/A	1.754
LWB	8 – 14 (broad)	N/A	4.743

In this chapter, the spectral intensities of the smouldering and flaming at different wavelengths were compared. To remove the equipment effects in the experiments, the intensity gain from the cameras and filters responses were considered. The two main features of the intensity gain are centre wavelength and band width; thus, the intensity reading (I) obtained by the camera is the integration of spectral intensity (B) multiplied by the intensity gain (ρ) over wavelength (λ) as shown in Eq. 2.1, in which, outside the band width, the intensity gain is 0. The average spectral intensity ($\bar{B}$) at each channel can be estimated as in Eq. 2.2, since the band width of each channel is very narrow. Figure 2.6 shows the schematic of intensity gain as a function of wavelength of each channel both narrow and broad band. The integral function in Eq. 2.2 corresponds to the integration of the region under each curve in Figure 2.6, which in this chapter, were solved numerically, and its results are listed in the integrated gain column in Table 2.3. Meanwhile, the theoretical spectral intensity of blackbody radiation at a certain temperature and wavelength ($B(T,\lambda)$) follows the Planck's law (Eq. 2.3). In Eq. 2.3, h is Planck constant (6.625×10^{-34} $m^2.kg/s$), c is speed of light (3×10^8 m/s), κ is Boltzmann constant (1.38×10^{-23} $m^2.kg/s^2.K$), and T is temperature.

$$I = \int_0^\infty B(\lambda)\rho(\lambda)d\lambda \tag{2.1}$$

$$\bar{B}(\lambda) \cong I / \int_0^{\infty} \rho(\lambda) d\lambda \tag{2.2}$$

$$B(T, \lambda) = 2hc^2 / \lambda^5 \left(exp\left(\frac{hc}{\kappa T \lambda}\right) - 1 \right) \tag{2.3}$$

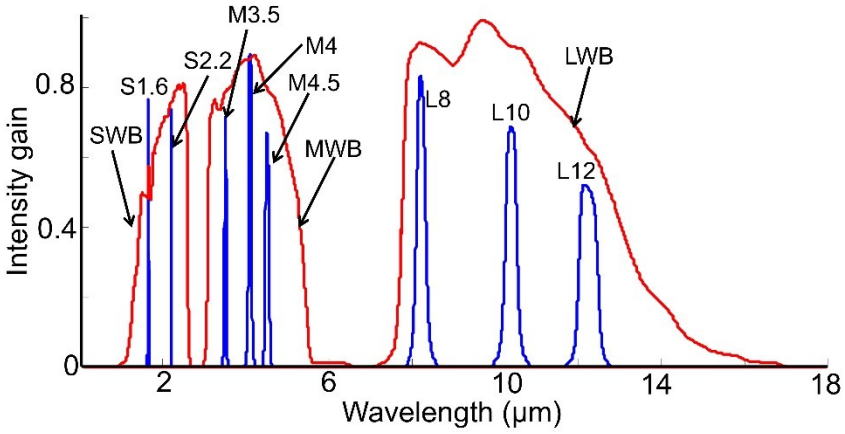

Figure 2.6. The intensity gain of different channels used in this work. The blue lines are for narrow band channels, whereas the red lines are for broad band channels. This scheme corresponds to Table 2.3.

2.4. Results and Discussions

2.4.1. Distinction of smouldering and flaming fires

The infrared cameras with any channel (see Table 2.3) successfully detect the fire, either flaming or smouldering (see Figure 2.7 and Figure 2.8). Figure 2.7b and Figure 2.8b show that although the smouldering and flaming can be detected at any wavelength, the spectral intensity at different wavelengths differ significantly. In smouldering experiments, the highest spectral intensity was obtained with MWIR channels (0.12 – 0.15 W.cm^{-2}.sr^{-1}.μm^{-1}), followed by SWIR channels (0.05 – 0.08 W.cm^{-2}.sr^{-1}.μm^{-1}), and the weakest was obtained with LWIR channels (0.01 – 0.02 W.cm^{-2}.sr^{-1}.μm^{-1}). This pattern also prevailed in the flaming experiments where the spectral intensity in MWIR channels were 0.28 – 0.46 W.cm^{-2}.sr^{-1}.μm^{-1}, SWIR were 0.19 – 0.28 W.cm^{-2}.sr^{-1}.μm^{-1}, and LWIR were 0.02 – 0.06 W.cm^{-2}.sr^{-1}.μm^{-1}. These patterns followed the pattern in the Planck's curve (see Figure 2.9a) of blackbody radiation (Eq. 2.3), and the values fell within the expected temperature of flaming and smouldering (600K – 1200K). The peak spectral intensity in the experiments also confirmed with the Planck's law, where the peak shifts to the longer wavelength when the temperature is lower (smouldering temperature), causing the peak spectral intensity of smouldering were at M4.5 (0.15 W.cm^{-2}.sr^{-1}.μm^{-1}) and flaming at M4 (0.46 W.cm^{-2}.sr^{-1}.μm^{-1}).

The MC of peat and fuel bed size of pine needle did not significantly affect the spectral intensity of the smouldering and flaming respectively, as shown by the negligible error bar in Figure 2.9a. This negligible effect indicates that the temperature (the main factor that affects spectral intensity) of the flaming and smouldering were not significantly affected by the fuel bed size and MC respectively, which confirmed with Huang and Rein (2017). The fuel bed size and MC had only significant effects on the time required to reach the temperature that corresponds to the spread rate of the fire.

In the flaming experiments, there was another important characteristic where the object that is detected was different when using different channels. When using M4.5, the maximum spectral intensity was obtained from the naked flame (0.61 $W.cm^{-2}.sr^{-1}.\mu m^{-1}$), instead of burning vegetation like those in M4 (see Figure 2.8a). This phenomenon was caused by the radiation from participating media (gas phase objects) that have the nature of band radiation, peak at a narrow wavelength and very weak at other wavelengths (see Figure 2.9b). These findings concur with the selection of the wavelength (MWIR) in remote sensing to monitor wildfire (Giglio, Schroeder and Justice, 2016), and comply with the results on the lab-scale experiments (Boulet *et al.*, 2011). The flaming spectral intensity in Figure 2.9a was obtained from the burning vegetation, thus, its value in M4.5 channel was lower than from naked flame.

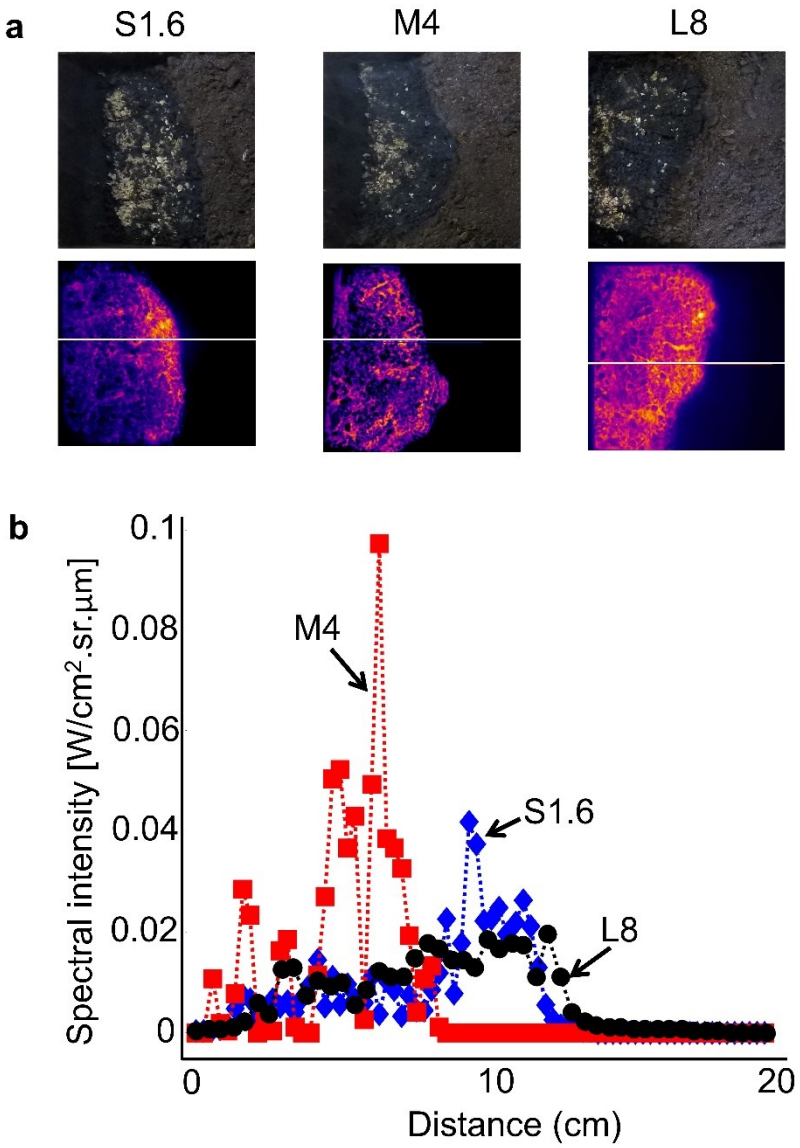

Figure 2.7. (a) Signatures of smouldering peat from visual and infrared cameras with three different channels: S1.6, M4, and L8. (b) Spectral intensity of smouldering in 3 different channels (S1.6, M4, and L8) that correspond to the white lines in (a).

The smouldering could be distinguished from flaming from its lower spectral intensity at any wavelength (with ratio of 1.8 – 6.5 as shown in Figure 2.9b), which is expected since the temperature in smouldering is almost half the flaming temperature (Rein, 2016). The intensity ratio was calculated as the division of flaming vegetation spectral intensity by smouldering peat spectral intensity. The intensity ratio peaked at M4.5 (ratio of 6.5), therefore, M4.5 is the best channel to distinguish between flaming and smouldering. The intensity ratio at M3.5 and M4 were also relatively high (6.2 and 4.4 respectively). Therefore, the range of wavelength recommended to distinguish between flaming and smouldering is between 3.5 – 4.5 µm (i.e., MWIR). Moreover, since within

this range the effect of the atmospheric noises are minimum (Giglio, Schroeder and Justice, 2016), MWIR is the optimum in general cases of detection and monitoring of peatland wildfires. The intensity ratio within SWIR range (M1.6 and M2.2) was relatively high (6.3 and 3.4 respectively), thus, the usage of channels within SWIR range also makes it possible to distinguish between flaming and smouldering, although MWIR is still better than SWIR in term of both intensity ratio and spectral intensity results. LWIR was found to have a relatively low intensity ratio (1.8 –3.1), thus, the usage of LWIR is not recommended since it could reduce the accuracy of attempts to distinguish between flaming and smouldering, which is also coupled with its weak spectral intensity. Although no repeat was performed on each independent experiment, the maximum spectral intensity at different times, which is selected at the early stage (shortly after the ignition period is over), middle stage, and late stage of the experiment, were within 20% difference. Therefore, the experimental uncertainty when the experiment is repeated is expected to be of similar value, and the results presented here prevail.

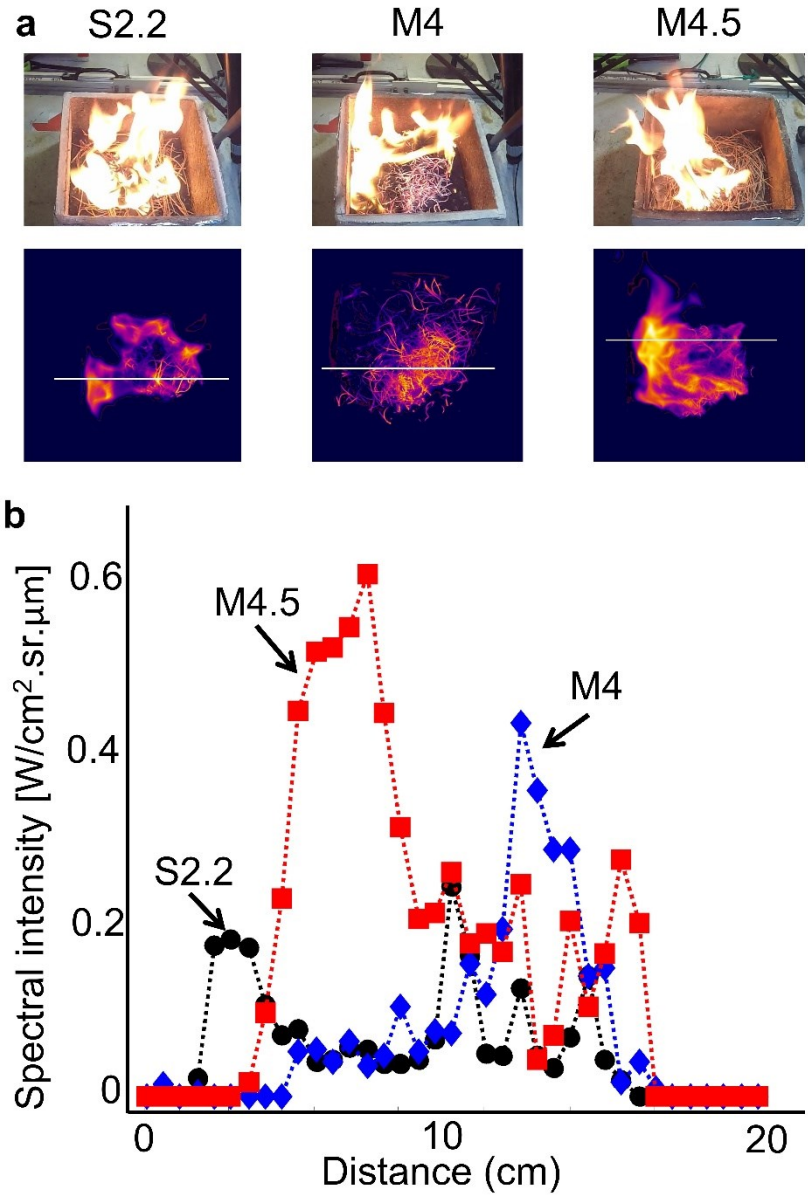

Figure 2.8. (a) Signatures of flaming pine needles from the visual camera and infrared camera with three different filters (S2.2, M4, and M4.5). (b) Spectral intensity of the flaming from three different filters (S2.2, M4, and M4.5), which correspond to the white lines in (a).

Based on these findings, SWIR as a replacement for MWIR in remote sensing of peatland wildfires due to the widely available data (Sofan *et al.*, 2020), could be considered, since SWIR was able to detect both flaming and smouldering, although its spectral intensity and intensity ratio are lower than MWIR. The usage of LWIR to detect smouldering (Sofan *et al.*, 2019), on the other hand, requires sophisticated analysis, due to its significantly lower spectral intensity and intensity ratio than other wavelength ranges and without apparent benefits. The findings in Sofan *et al.* (2019) also show that the radiation from flaming and smouldering within the LWIR range was similar, although

flaming radiation was slightly stronger, whereas in the SWIR range, the flaming radiation was significantly stronger.

These recommendations comply with the findings for when flaming and smouldering fires coexist, which is a commonly observed phenomenon in actual peatland wildfires (Sofan *et al.*, 2020). Figure 2.10 compares the spectral intensities of flaming vegetation and smouldering peat when they coexist. This figure was obtained by scaling the range of spectral intensity in which the range cover the minimum and maximum value in the smouldering and flaming radiation respectively. Therefore, the values correspond to the colour within one channel in Figure 2.10a are linearly proportional. However, the range of spectral intensity is different between different channels to ensure the clarity of the figures. Visually, the radiation from flaming and smouldering can be distinguished by using channel S1.6 and M4, where the flaming radiation (orange) was significantly stronger than smouldering radiation (blue). The use of L12 was ineffective to distinguish between flaming and smouldering since both combustion types have similar radiation strength (both are similarly of a magenta colour). These visual differences confirm with the corresponding spectral intensities, as shown in Figure 2.10b, where the smouldering and flaming spectral intensities in L12 (black circle) are similar, whereas the other two channels have significantly different spectral intensities between flaming and smouldering. The result from M4 channel is the optimum, since the segregation between background, smouldering, and flaming is significantly clearer than in S1.6. The lower clarity in S1.6 is caused by its weaker smouldering radiation that is almost similar to the background when flaming and smouldering coexist (see Figure 2.10b).

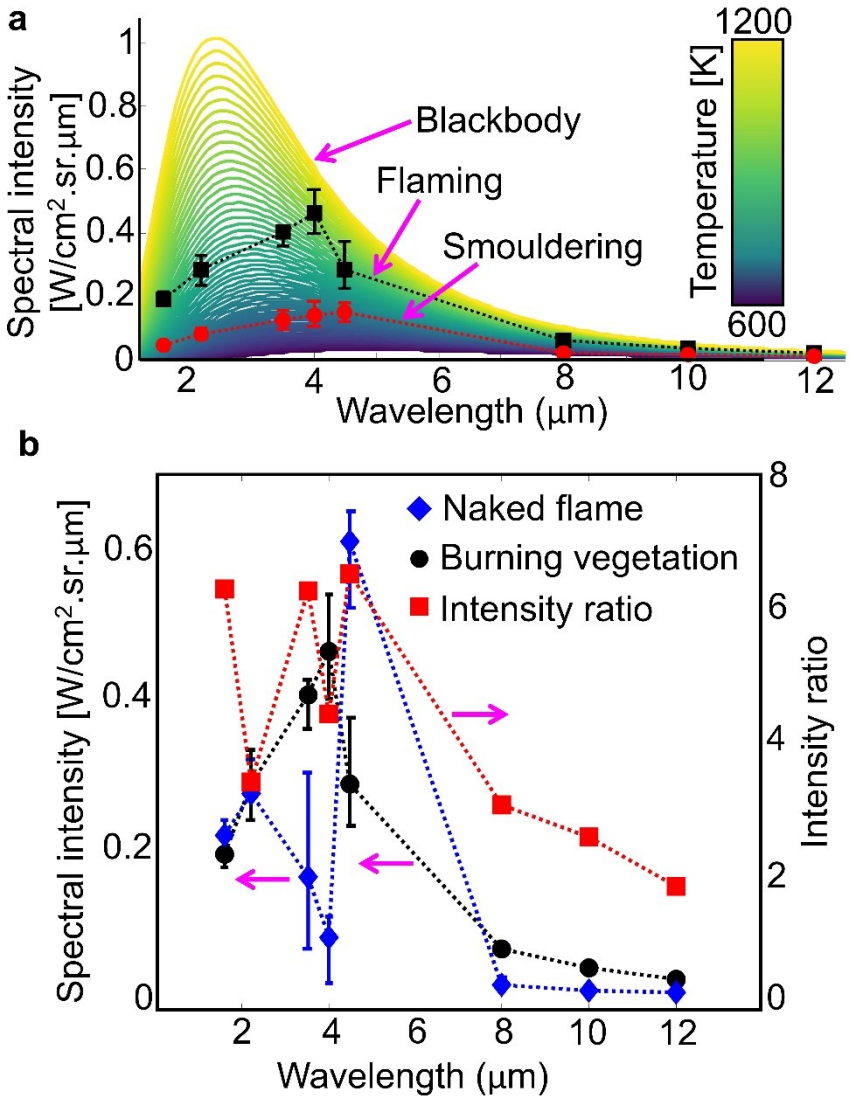

Figure 2.9. (a) Maximum spectral intensity of the smouldering peat and flaming pine needle at different wavelengths and their comparison with the spectral intensity of blackbody radiation at different temperatures. The error bar in (a) represents the variation of maximum spectral intensity from experiments with different moisture contents and fuel bed size for smouldering peat and flaming pine needle respectively. (b) Comparison of spectral intensity between burning vegetation and naked flame in the flaming experiments (left axis) and the intensity ratio between burning vegetation and smouldering peat (right axis) at different wavelengths. The error bar in (b) represent the variation in maximum spectral intensity from flaming experiments with different fuel bed size.

The radiation difference between fires has been used to determine the wildfire hotspots in remote sensing applications (Giglio, Schroeder and Justice, 2016). These findings infer that there are two extreme conditions that need to be considered to distinguish flaming and smouldering wildfires: the radiation difference between smouldering and flaming radiation and the radiation difference between smouldering

radiation and radiation from background, in which the separation of radiation difference between flaming, smouldering, and background confirms with Wooster, Zhukov and Oertel (2003). These findings and recommendations can be used to determine the expected radiation differences between flaming, smouldering, and background in the real application of remote sensing of peatland wildfires; thus, can improve its detection and monitoring when both flaming and smouldering wildfires are present and coexist.

Another important phenomenon to be considered in differentiating flaming and smouldering wildfires is the overlap between the two fire types (Sofan *et al.*, 2019). Another post-processing of the infrared emissions was performed, where the flaming infrared emissions were placed on top of the smouldering infrared emissions. From this post-processing, the smouldering radiation was completely shut off by the flaming radiation. This finding indicates that when flaming and smouldering wildfires overlap, where flaming vegetation is always on top of the smouldering peat, the distinction between flaming and smouldering is not possible. Therefore, the classification of flaming-smouldering state in the algorithm developed in Sofan *et al.* (2019, 2020) requires further investigation. This flaming-smouldering classification could stem from the flaming vegetation that starts cooling down (Wooster, Zhukov and Oertel, 2003). However, this overlapping phenomenon only happens at the beginning of the soil ignition by flaming vegetation. The flaming vegetation occupy a certain location, ignite the soil, and spread quickly while the ignited soil spreads two orders of magnitude slower via smouldering, and therefore, this overlapping phenomenon is only instantaneous. Moreover, when both smouldering and flaming wildfires are present at the same location, the most concerning type of wildfire is flaming due to its higher hazard (e.g., higher spread rate and power). Therefore, the recommendation of using MWIR infrared emissions still prevail despite its ineffectiveness in distinguishing in the event of overlap between flaming and smouldering.

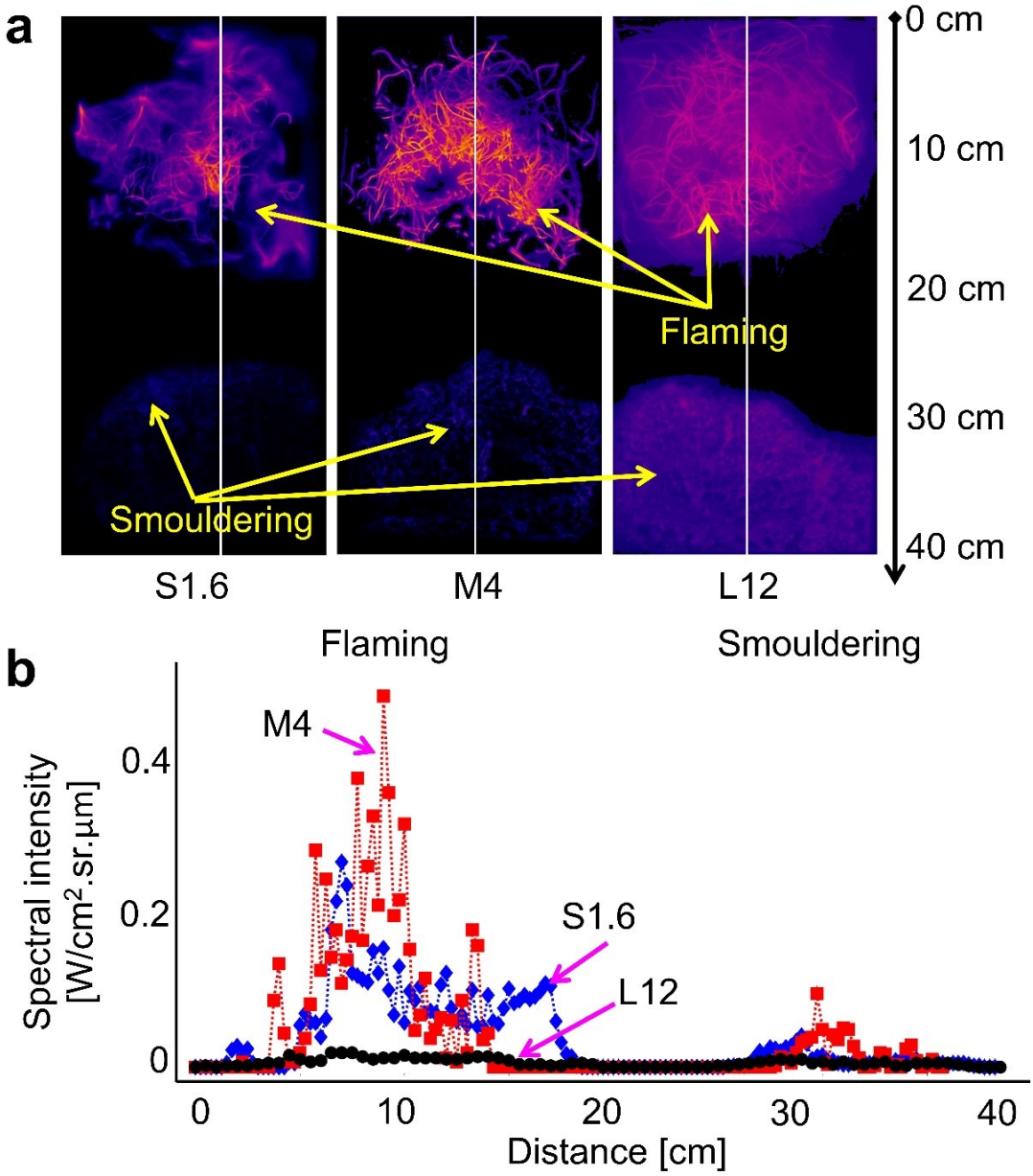

Figure 2.10. (a) Visual comparison between flaming vegetation and smouldering peat when they coexist, using three different channels: S1.6, M4, and L12. (b) The corresponding spectral intensity of the infrared emissions correspond to white lines in (a).

Fire detection in remote sensing uses different algorithms in different products, although the satellite and instrument are the same, for instance, MODIS has many different algorithms to detect wildfires such as Collection 4, Collection 5, and Collection 6 (Giglio, Schroeder and Justice, 2016). The algorithms use different procedures and thresholds to determine the location of wildfires. However, these thresholds are determined empirically and are validated against field observation, thus, the thresholds between different products cannot be compared. Fire Radiative Power (FRP) provides a

method to compare the detection of wildfire between different algorithms, for example, the average FRP of active fire in MODIS Collection 6 is only 16% lower than in MODIS Collection 5 (Giglio, Schroeder and Justice, 2016), whereas the FRP from MODIS and BIRD are within 20% of each other (Wooster, Zhukov and Oertel, 2003). In the earlier version of the remote sensing products, FRP is a function of brightness temperature, a theoretical temperature if the surface were blackbody given the spectral intensity (Giglio, Schroeder and Justice, 2016). This brightness temperature can be calculated from spectral intensity, however, the calculation is sophisticated and requires an optimization process (Giglio, Schroeder and Justice, 2016). In recent products (e.g., MODIS Collection 6), FRP is calculated directly based on the spectral intensity (Giglio, Schroeder and Justice, 2016).

FRP method was used to translate the findings in this chapter into satellite remote sensing application and assess their capability to distinguish between flaming and smouldering wildfires. To simplify the use of FRP method, the formulation in MODIS Collection 6 was used, where FRP is linearly proportional to the spectral intensity (Giglio, Schroeder and Justice, 2016). However, this FRP value is dependent on the sensor characteristics (Giglio, Schroeder and Justice, 2016); thus, the comparison of FRP ratios between flaming and smouldering was used instead of the comparison of FRP values between the two combustion types.

From 240,000 detected wildfires in MODIS, the FRP of the fire ranges from 5 MW to 9000 MW (Giglio, Schroeder and Justice, 2016). In this range, the most frequent value of FRP of active fires ranges from 20 MW to 50 MW with more than 100,000 active fires found within this FRP range (Giglio, Schroeder and Justice, 2016). These values are obtained from the 4 μm channel of MODIS instruments. By using the channel with the same wavelength (M4) and assuming that the flaming wildfires typically have FRPs within the range of 20 MW to 50 MW, smouldering wildfires would have FRPs from 4.5 MW to 11.4 MW (ratio of 4.4). This smouldering FRP range is still within the range of active fires that can be detected by MODIS. This finding also confirms with Wooster, Zhukov and Oertel (2003), where the FRP per unit area of pixel of smouldering is 8.1 kW/m^2 and flaming is 59.7 kW/m^2, a 7.4 ratio, which is similar to the result of M4.5. Although the smouldering in Wooster, Zhukov and Oertel (2003) was from the residual burning (of surface vegetation) instead of peat, the same order of magnitude of smouldering temperature indicates that the FRP of smouldering of peat and surface vegetation are expected to be similar.

Flaming and smouldering wildfires can potentially be differentiated by using current technologies in remote sensing, however, another consideration is that the lower FRP of smouldering could be from the flaming vegetation that has cooled down (Wooster, Zhukov and Oertel, 2003). The cooling down flaming vegetation has been considered by using lower FRP than smouldering (0.42 kW/m^2), but higher than background (Wooster, Zhukov and Oertel, 2003). This method is powerful, however, the uncertainties in the remote sensing (Ichoku *et al.*, 2016) pose difficulty to implement this method accurately. For instance, the cooling flaming vegetation that still has high temperature (thus, high FRP, even higher than smouldering) or smouldering peat that is at the ground level (Wooster, Zhukov and Oertel, 2003) and can spread underground (thus, low FRP, even lower than cooling flaming vegetation).

The fact that smouldering peat remains active although flaming has propagated relatively distant, can be used to overcome these detection and monitoring limitations. Therefore, to determine whether an active fire pixel is smouldering or flaming, firstly, its FRP is checked. If its FRP is around the smouldering or cooling flaming vegetation threshold, then the surrounding region of this active fire pixel is checked to find other active fire pixels which have FRP corresponds to flaming wildfire. If both checks are confirmed, the active fire pixel can be considered a smouldering wildfire. This procedure can return a false signal when the flaming wildfire is extinguished but the smouldering wildfire remains, or when the flaming wildfire exist but the pixel with smouldering FRP is a noise such as shiny objects. To tackle these issues, time series of the FRPs are required, where the FRP data of the landscapes are collected on many different times. For the first issue of the extinguished flaming, the time series data of FRP of the landscape can help find the start and the end of flaming wildfire. If the start and the end of the flaming wildfire are far from the time of the smouldering FRP is detected, then this could be a false signal of smouldering. The data on burnt scar can also be used to find the start and the end of flaming wildfire, since the cloud and other atmospheric noises could conceal the flaming wildfire when it happens. Once the start and end of the flaming wildfire is determined, the presence of shiny objects can then be identified. If objects with smouldering FRP are detected prior to the start of flaming wildfire, then these objects are most likely not smouldering, but noises, such as shiny objects. If the smouldering FRP objects are detected after the start of flaming wildfire, these objects could potentially be smouldering hotspots. Clouds could become noises in this category, however, there are algorithms to minimise clouds effect in remote sensing which are found in the literatures

(Giglio, Schroeder and Justice, 2016). These findings and recommendations can be used to help distinguishing flaming and smouldering in remote sensing of peatland wildfires.

2.4.2. Detection of subsurface smouldering

Another commonly observed phenomenon in peatland wildfires is subsurface smouldering (Huang and Rein, 2017). This phenomenon happens when the smouldering consumes relatively wet peat, and makes the fire favours to spread subsurface (Huang and Rein, 2017). The subsurface spread can only be detected by using broad wavelength (see Figure 2.11a), since weakened smouldering radiation due to subsurface spread could be amplified by integrating the radiation from a wide range of wavelengths (emissive power). The use of band filter at any wavelength fails to detect this subsurface smouldering; thus, satellite remote sensing will likely fail to detect the subsurface smouldering since they use band wavelength. This finding complies with the work of Burke *et al.* (2019) who also use broad wavelength infrared (which is similar to LWB channel) to detect subsurface smouldering. In Burke *et al.* (2019), a drone is equipped with an infrared camera that has spectral range of 8 – 14 μm to detect smouldering coal covered by soil. The infrared camera successfully detected the buried smouldering coal within a certain range of drone altitude.

However, not all spectral range categories are able to detect subsurface smouldering. Figure 2.11b shows that SWB fails to detect subsurface smouldering. This finding can be explained by the total radiation intensity received by the channels (Eq. 2.1). The intensity received by the channels can be considered going through two steps: at the surface of the sample and in front of the sensors. At the surface of the sample, the energy to be emitted is equal regardless of the channel, consequently the initial intensity (I_o) is also equal. This initial intensity pass through the camera lens and filters, and lose some of its energy depending on the camera and filters used. Therefore, the final intensity (I) received by the channel is only a fraction of the initial intensity.

Eq. 2.1 shows the formulation of the final intensity, which can be written as $I = \alpha I_o$, with α the coefficient corresponding to channels. I_o is equal for all channels, but different between surface and subsurface smouldering. The I of subsurface smouldering is the product of α with I_o at the subsurface that is lower than I_o at the surface, thus, the ratio of I of subsurface smouldering on different channels is equal to the ratio of α at different channels, which is the same in both surface and subsurface smouldering. The value of α can be estimated by the product of integrated gain in Table 2.3 with the average spectral intensity at the surface of each channel (see Figure 2.9a). By using this method,

the α of SWB, MWB, and LWB were found to be 0.04, 0.24, and 0.08, respectively. This finding indicates that although the LWIR has weaker radiation at each wavelength, since it is integrated over wide range of wavelength (8 – 14 µm), its α is sufficiently high and the channel (LWB) can detect subsurface smouldering. On the other hand, SWB that has α half of LWB, although it has higher spectral intensity than in LWIR at any wavelength, fails to detect subsurface smouldering. This finding confirms with the α of band channels that peak at M4 with α of 0.01 and cannot detect subsurface smouldering. Therefore, for the first time, the infrared emissions with potential to detect subsurface smouldering were characterised, which can explain the successful detection of subsurface smouldering in Burke *et al.* (2019), and determine the sensors and algorithms that can be used for this detection.

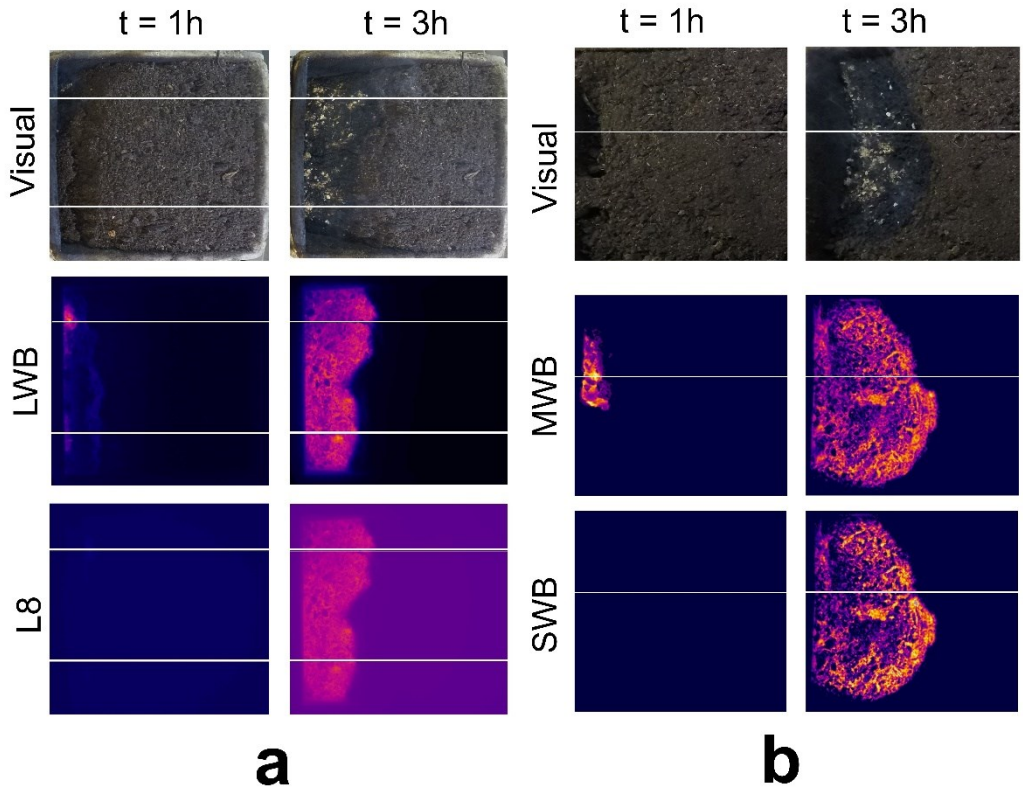

Figure 2.11. (a) The visual images and broad (LWB) and band (L8) infrared emissions of smouldering when subsurface smouldering was observed (at t = 1h after ignition protocol) and the emissions after the smouldering reaches the surface (at t = 3h after ignition protocol). The white lines indicate the same location. (b) The visual images and broad infrared emissions (SWB and MWB) of smouldering when subsurface smouldering was observed (at t = 1h after ignition protocol) and the signatures after the smouldering reaches the surface (at t = 3h after ignition protocol). The white lines indicate the same location.

The capability of satellite remote sensing, which uses band infrared emissions, to detect subsurface smouldering, was further assessed by using two post processing methods: discrete integration and an adjustment factor. In discrete integration method, the spectral intensities from several different band infrareds were summed (e.g., spectral intensities from M3.5, M4, and M4.5 were summed), thus, this method was similar with using broad infrared. However, while broad infrared sums the spectral intensity of all wavelengths within a certain range, the discrete integration method only used finite number of wavelengths within the same range. In the adjustment factor method, the spectral intensity from a band infrared was multiplied by a factor, thus, the weakened radiation of subsurface smouldering is amplified. These post-processing methods are analogous to the use of algorithms in the remote sensing products.

Figure 2.12 shows the infrared emissions after post-processing compared with the emission of LWB. The discrete integration method (labelled as A1 in Figure 2.12) sums the spectral intensity of L8, L10, and L12, whereas the adjustment factor method (labelled as A2 in Figure 2.12) was implemented on L8 with the factor of 30. The LWIR range was used in this post-processing analysis because the infrared camera for SWIR and MWIR experiments (X6900sc) split the spectral intensity range into significantly narrower range than the infrared camera for LWIR experiments. For example, if the LWIR camera can read from 0.2 to 0.8 $W.cm^{-2}.sr^{-1}.\mu m^{-1}$, the camera for SWIR and MWIR splits this range into 0.2 – 0.4 $W.cm^{-2}.sr^{-1}.\mu m^{-1}$, 0.4 – 0.6 $W.cm^{-2}.sr^{-1}.\mu m^{-1}$, and 0.6 – 0.8 $W.cm^{-2}.sr^{-1}.\mu m^{-1}$. This split means that if the maximum spectral intensity in the experiment is, for instance, 0.5 $W.cm^{-2}.sr^{-1}.\mu m^{-1}$, then the range of 0.4 – 0.6 W.cm-2.sr-1.μm^{-1} must be used, and the pixels that have spectral intensity lower than 0.4 W.cm-2.$sr^{-1}.\mu m^{-1}$ will be read as 0.4 $W.cm^{-2}.sr^{-1}.\mu m^{-1}$, which is incorrect. Therefore, post-processing analysis could be limited due to the cut-off process from the camera. Figure 2.12a shows half bottom of Figure 2.11a after post-processing is performed and Figure 2.12b shows corresponding spectral intensity of the magenta line in Figure 2.12a. The half bottom of Figure 2.11a was selected because this part is the region at which subsurface smouldering was observed.

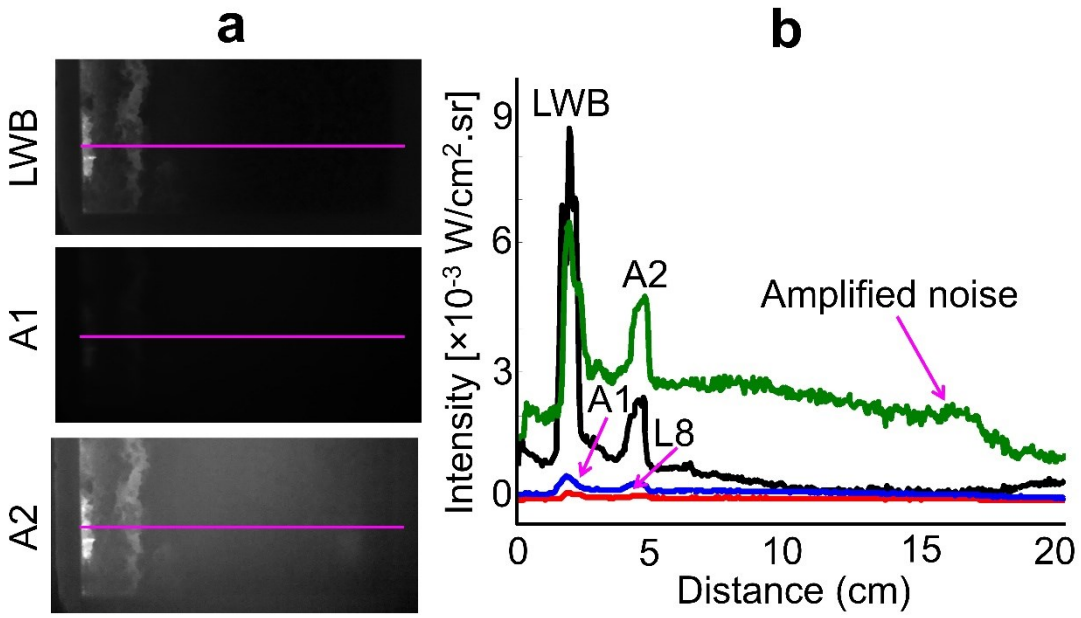

Figure 2.12. (a) Infrared emissions of subsurface smouldering of LWB, discrete integration method (A1), and adjustment factor method (A2). These results only show half bottom of Figure 2.11a where the subsurface smouldering is observed. (b) The corresponding intensity of the magenta line in (a).

Although the discrete integration method (A1) indeed strengthens the weakened infrared emissions of subsurface smouldering (see Figure 2.12b), this method failed to detect subsurface smouldering. This failure stems from the estimation of the total α of this method ($\alpha = 0.02$), which is still lower than α of SWB. This finding also indicates that if more band channels are included, the discrete integration method can potentially detect subsurface smouldering.

This potential is strengthened by the result of adjustment factor method (A2), which successfully detects subsurface smouldering (see Figure 2.12a). However, this successful detection is accompanied by the amplified noise (see Figure 2.12b). While implementing the adjustment factor, the noise of non-smouldering objects is also amplified. Since the background noise is non-uniform, even in the controlled environment, the noise can be amplified and causing false signal. This noise is even more significant in the actual wildfires; thus, while the post-processing has the potential to enable current remote sensing technologies, which mostly use band channel, to detect subsurface smouldering, the noise reduction is of utmost importance. These findings can help in selecting the optimum infrared sensors and filters and the suitable algorithms (such as the mathematical operation and the adjustment factors in the algorithm) for the detection of subsurface smouldering in remote sensing.

2.5. Conclusions

This chapter investigated, for the first time, the suitability of infrareds to distinguish flaming from smouldering fire to assist the remote sensing of peatland wildfires. Laboratory-controlled experiments of remote sensing were conducted on smouldering of peat (with five different MCs) and flaming of pine needles (with five different fuel bed sizes), by using infrareds with eight different wavelengths in three spectral range categories (short-wave, mid-wave, and long-wave). Flaming and smouldering can be detected by infrared in the eight wavelengths that were considered, and both can be distinguished by using the spectral intensity comparison where the intensity of smouldering is one-seventh to half of flaming regardless of the MC of peat and the fuel bed size of pine needles. This lower intensity of smouldering fire applies for the three spectral range categories where the spectral intensity of smouldering in short-wave is 0.05 – 0.08 $W.cm^{-2}.sr^{-1}.\mu m^{-1}$, mid-wave is 0.12 – 0.15 $W.cm^{-2}.sr^{-1}.\mu m^{-1}$, and long-wave is 0.01 – 0.02 $W.cm^{-2}.sr^{-1}.\mu m^{-1}$. The highest intensity ratio between flaming and smouldering was found at mid wave range (with a ratio between 4.4 and 6.5). Based on these findings – that relatively high spectral intensity at mid wave range, and the fact that within this range the radiation from atmospheric noises is minimal – mid-wave infrareds are argued to be the optimum choice in general for the monitoring of peatland wildfires. This choice of wavelength is also recommended when both flaming and smouldering coexist due to the clear separation of spectral intensity between flaming, smouldering, and background radiation; thus, in the real application of remote sensing, flaming, smouldering, and background pixels are expected to have distinct colours or intensities, for instance, yellow, red, and green respectively. However, none of these wavelengths could detect subsurface smouldering. The detection of subsurface smouldering can potentially be performed by integrating the spectral intensity of a sufficiently wide range of wavelengths (emissive power). This integration amplified the weakened radiation of subsurface smouldering and successfully detect the fire, which complies with Burke *et al.* (2019) and improves the understanding on the subsurface smouldering detection. These findings provide the knowledge to select the optimum infrared wavelength and assess the utilisation of remote sensing data for the development of algorithms to detect and monitor smouldering and flaming wildfires in peatlands, thus, can help improve the remote sensing of peatland wildfires.

Chapter 3 – Cellular Automata Models of Wildfires

Summary[2]

Wildfires consist of numerous physical phenomena which lead to multi-facet problems for modelling. Due to the low computational cost of cellular automata, these methods offer solution for the complexity of wildfires modelling. This chapter reviews the existing scientific literature on cellular automata dedicated to wildfires study, which are used to model a number of applications of wildfires from laboratory to field scales. Since many concepts have been used to obtained the rules in the cellular automata, this review emphasizes the discussion on the concepts that are used and how these concepts are improved to tackle the emerging problems in wildfire modelling. Seven main concepts have been found: discrete physical event, wave propagation, heat accumulation, linguistic, diffusion limited aggregation, bond percolation, and site percolation. Cellular automata have successfully modelled several emerging phenomena in wildfires, for instance, the transition from surface fire to crown fire. However, many physical phenomena remains scientific challenges for cellular automata due to a lack of available data and incomplete fundamental understanding. Hybrid methods compensate these issues, by combining other models with cellular automata. However, maintaining low computational cost become an emerging issue. This review provides extensive and comprehensive understanding of cellular automata modelling for wildfires, and identifies gaps in the knowledge and opportunities going forward.

3.1. Introduction to Wildfire Spread Models

Wildfires are natural phenomena which can kill people, damage property and environment, and release smoke and carbon that harms human health and affects the atmosphere. However, they are important for many Earth ecosystems (Block *et al.*, 2016). A single event of wildfire can kill dozens of people and impose billion dollars of economical loss (Gibbons *et al.*, 2012; Maranghides *et al.*, 2013). The occurrence of wildfires are forecast to increase all over the world due to population changes, land use changes, and

[2] This chapter is based on "Dwi M J Purnomo, Nieves Fernandez-Anez, Guillermo Rein, 2022. Cellular Automata Models of Wildfire Spread. *Progress in Energy and Combustion Science*, (to be submitted)."

climate change (Gibbons *et al.*, 2012). Although posing threats to humankind, fires are needed by forest ecosystem for rejuvenation and renewal processes (Block *et al.*, 2016; Waldrop and Goodrick, 2018), and also to regulate atmospheric oxygen, carbon cycles, and climate (Watson, Lovelock and Margulis, 1978; Bowman, 2009). Therefore, it is important in forest management to understand the behaviour of wildfires and how to effectively mitigate them if needed.

Wildfires are affected by many factors including environment, topography, and weather. Figure 3.1 shows a real event of wildfire where nonuniform environment conditions, topography, and wind effects are present. There are several fuel types in this incident: grass, shrubs, and trees, while the fire could also spread to the residences and feed on the flammable materials in the houses (e.g., furniture). The effects of wind dynamics and landscape topography are also present in this wildfire, for instance, the flames lean in an uphill direction showing the buoyancy effect on the flames, which could affect its spread behaviour.

Figure 3.1. Photo of a wildfire in Anaheim Hills, California in 2017. This wildfire shows several parameters need to be considered in mitigating the fire: wind dynamics, topography, and fuel type. This photo was taken by Aarti Kalyani and permission was granted.

Mitigation of wildfires relies on the understanding of the flame spread that consumes the fuel bed. Once ignited, the flame initiates a succession of ignitions to the adjacent fuel which causes the flame to spread (Finney *et al.*, 2015). This spread is affected by heat transfer: convection, radiation, and flame contact, as shown in Figure 3.2, in which the radiation and flame contact (caused by buoyant instabilities) are the prominent causes of the ignition of the adjacent fuel (Finney *et al.*, 2015). The ignition of the adjacent fuel could also be encouraged by the presence of firebrand, flying embers (burning solid fuels) that can travel further and at different direction from the flaming front (see Figure 3.2). The dynamics of flame spread highly depend on environmental conditions (e.g., topography, fuel characteristic) and weather (e.g., wind, ambient air temperature, humidity) conditions (Perry, 1998).

Computational modelling predicts the behaviour of the fire spread over a period of time. There are two main techniques for wildfires simulation: vector-based and raster-based (Perry, 1998; Sullivan, 2009c). The vector-based technique simulates fire spread using spatially continuous geometry, whereas the raster-based technique uses discrete cells generated from the gridding of the computational domain (Perry, 1998; Sullivan, 2009c). The vector-based technique benefits from the accuracy of the fire shape that can be obtained, whereas raster-based technique benefits from lower required computational resources than vector-based (Peterson *et al.*, 2009; Sullivan, 2009c). Modelling of wildfires offers great potential to understand the spread behaviour of fire for forest management, which can be used, for example, to assess the vulnerability of the forest based on vegetation or to strategize a safe prescribed fire. In terms of mitigation of undesirable wildfires, computational models can give insights for firefighting strategy, therefore, the mitigation can be performed more effectively. For instance, faster-than-real-time simulations of the wildfire spread can be performed to determine the optimum deployment of the firefighters and the evacuation route prior to actual mitigation.

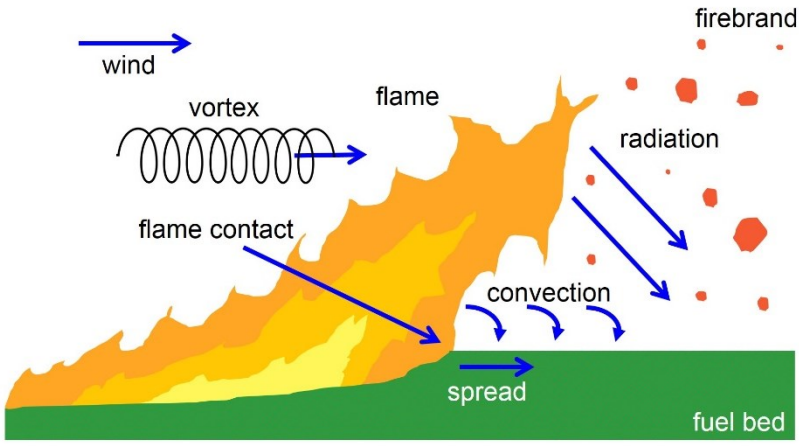

Figure 3.2. Illustration of flame spread in fuel bed of fine particles. The mode for heat transfer are convection, radiation, and flame contact which is caused by buoyant instabilities that lead to fuel ignition (Finney et al., 2015). Modified from Rothermel (1972).

There are three main approaches for wildfire modelling: physical, semiphysical, and empirical (Perry, 1998; Pastor *et al.*, 2003). The physical approach uses fundamental laws of physics and chemistry, whereas empirical approach uses experimental results or statistics of historical fires (Perry, 1998; Pastor *et al.*, 2003; Sullivan, 2009c). The semiphysical approach lies between empirical and physical approaches (Perry, 1998; Pastor *et al.*, 2003). The physical approach can be reliably used across scales, however, this approach is computationally expensive and unable to model certain phenomena due to incomplete understanding of fundamental laws, for instance, the lack of knowledge on how the crown fire starts and behaves (Perry, 1998; Pastor *et al.*, 2003). The empirical approach is very simple and computationally cheap although not reliable outside the conditions of the data used. The semiphysical approach tackles the problems in physical approach (e.g., incomplete understanding of fundamental laws) by adopting findings from experiments and historical fires (Perry, 1998; Pastor *et al.*, 2003). However, compromising the fundamental laws with empirical approaches limits the details of the phenomena that can be captured by the models.

There have been alternatives for wildfire modelling (see Chapter 1.5.1), and of the alternatives, CA have been extensively used for wildfire modelling because the rules in CA can be developed from many different models, in which the other models do not have this flexibility; thus, optimum rules can be selected for specific phenomena (Wolfram, 1984). CA are discrete computational models (raster-based) that use simple rules and limit the execution of its rules only within small area around the point of interest (Wolfram, 1984). These models were first introduced by von Neumann (1967) and since then has been systematically explored by Wolfram (1984, 2002). The main features of

cellular automata are discreteness, neighbourhood, and governing rules (Wolfram, 1984). Cellular automata use discrete states in addition to discrete time (finite time-steps) and space (grid of cells). The discrete states correspond to finite number of states e.g., unburned, burning, and burnt which is different from continuous states such as temperatures. For example, referring to Figure 3.1, there are only three states present: unburned, which are the fuels in front of the fire; burning, which is the flaming vegetation; and burnt out, which is the burnt fuel behind the flaming front. Cellular automata use rules to determine the simulation behaviour and these rules can be adapted from physical, semiphysical, empirical, and novel non-physics (e.g., fuzzy logic) approaches. These rules, however, only affect a specific number of cells, which are determined based on the neighbourhood. For instance, the flame in Figure 3.1 only affect the grass in front of it, and the effects of the flame on the relatively distant houses (such as radiation) are neglected.

This chapter reviews the development of cellular automata modelling for wildfires and find the gaps in the literatures. The development from the first cellular automata used for wildfires in 1971 until present are discussed.

3.2. Introduction to Cellular Automata in Wildfire Modelling

Cellular automata have been used to model wildfires by using different computational domain (cell shape and neighbourhood), environmental conditions (weather, topography, and fuel characteristic), and rules. Table 3.1 lists, chronologically, the previous works on cellular automata modelling for wildfires from 1971 until present. Cellular automata have been used to model both single event, unique wildfires that happen at a certain time, and multiple event wildfires, which means numerous different wildfires over long periods of time (hundreds of years). Single event wildfire modelling aims to predict the detail behaviour of a corresponding wildfire, whereas multiple event wildfire modelling aims to forecast the inherent behaviour of wildfires, e.g., patchiness of forest landscape post wildfires, which could be observed in any wildfires regardless the location and environmental conditions.

Figure 3.3 shows various cell shape and neighbourhood which have been used in previous works. Triangle, square, and hexagon are the common simple cell shapes used in cellular automata modelling for wildfire (see Figure 3.3a). Among these three geometries, triangle cell have computational cost benefit, however, square cell are the most commonly used cell shape due to its higher accuracy. Despite this high accuracy, square cells suffer from spurious symmetry, as the shape of the burnt scar in the simulation tends to become rectangular (D'Ambrosio *et al.*, 2006). This problem can be

solved by using hexagonal cells, which are equidistant to all the neighbouring cells, however, the spread in hexagonal cells is limited to only six directions and this type of cell requires higher computational resources than square cells (D'Ambrosio *et al.*, 2006). The other type of cells used are irregular and Voronoi cells (see Figure 3.3b; Braun and Sambridge, 1995; Zhao, 2011). Irregular cells aim to resemble the fuel configuration in the landscape perfectly (Zhao, 2011). Meanwhile, the Voronoi cells use Voronoi tessellation to create a set of polygons that makes the boundary lines between each pair of black dots in Figure 3.3b, separate the two dots with equal distance, where each polygon represents a Voronoi cell (Braun and Sambridge, 1995). The black dots in Figure 3.3b are the representative points of each cell. These dots are irregularly distributed, depending on the locations that have largest difference one another (e.g., a pair of the middle of a lake and the middle of a crop field; Braun and Sambridge, 1995). This tessellation aims to improve the classification of fuel type in the landscape (Braun and Sambridge, 1995). Both irregular and Voronoi cells benefit from a better fuel classification in the landscape but suffer from higher computational cost than cells with simple geometry.

The most common neighbourhood for cells with simple shape are the surrounding cells in which the number of neighbours is order dependent (see Figure 3.3a). The higher order neighbourhoods benefit from higher accuracy, such as in model radiative heat transfer (Collin, Bernardin and Sero-Guillaume, 2011), but suffer from higher computational cost. The other neighbourhoods are elliptical, multi-range, extended, and minimal time (see Figure 3.3b). Elliptical neighbourhoods benefit from better elliptical shape obtained which is the expected shape of wildfire spread (Green, 1989). The elliptical neighbourhood shown in Figure 3.3b is the 1st neighbourhood, however, similar to Figure 3.3a, elliptical can also have more neighbours with higher order neighbourhood. Multi-range neighbourhood consist of short- and long-range neighbours (see Figure 3.3b). Short-range neighbourhoods adopt other neighbourhoods such as 1st order and elliptical (Porterie *et al.*, 2007). Meanwhile, long-range neighbourhoods are governed by a characteristic length L_c, where the cells at L_c are neighbours but the cells between L_c and the outermost part of the short range neighbours are not. This neighbourhood is the modification of high order neighbourhood (L_c^{th} order), which allows the modelling of firebrand without significant increase in computational cost (Porterie *et al.*, 2007). The minimal time neighbourhood covers the possible neighbouring cells with the shortest time to ignite that are not always the 1st order neighbours, whereas the extended neighbourhood increases the number of possible directions of spread in hexagon cells (L. H. Encinas *et al.*, 2007; Sousa, dos Reis and Pereira, 2012). While these neighbourhoods

increase the accuracy of the models and enable the modelling of more phenomena, they suffer from higher computational cost.

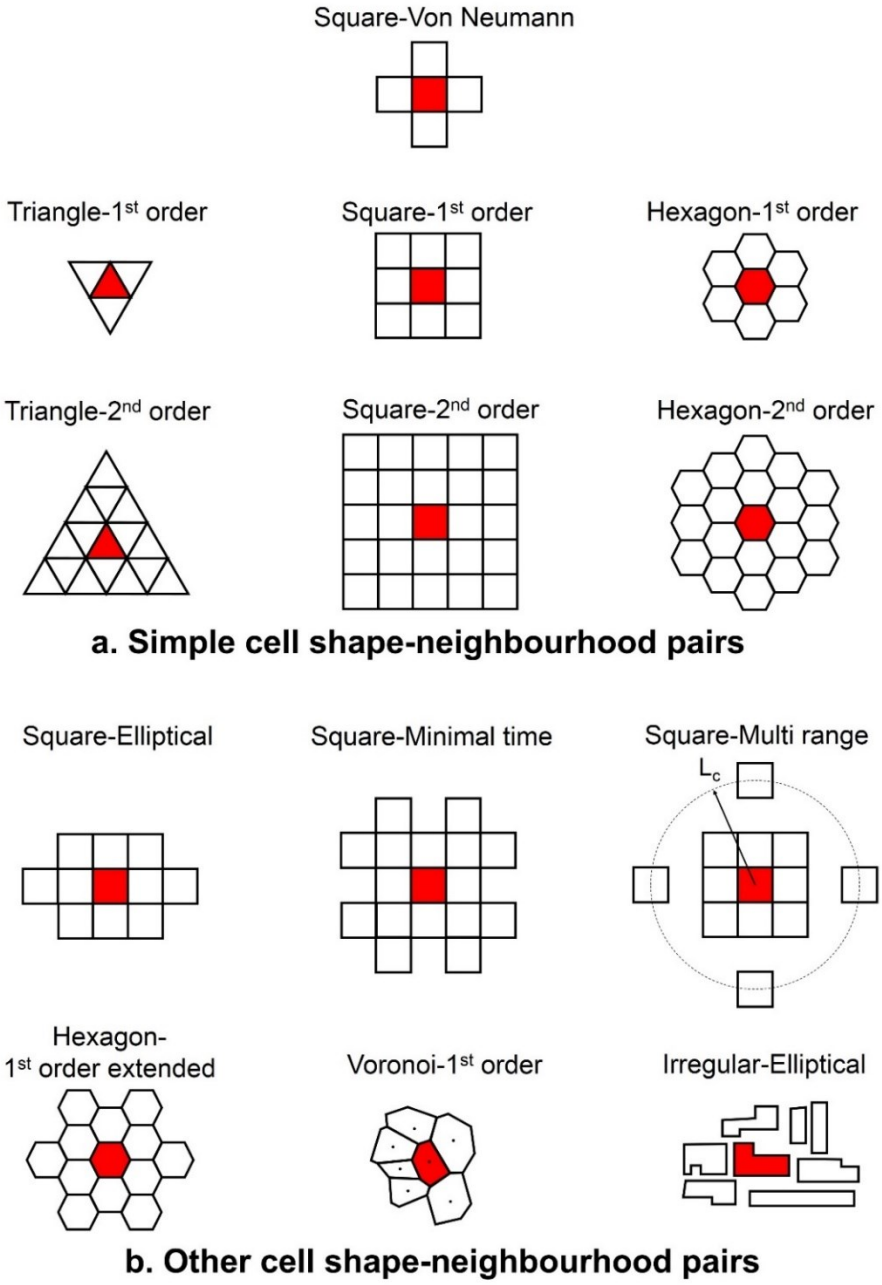

Figure 3.3. (a) Illustration of the simple cell shape and neighbourhood pairs used in cellular automata modelling for wildfires in order from simple to complex shapes and neighbourhoods from left to right and top to bottom respectively. (b) Illustration of the cell shapes and neighbourhood pairs which are more complex than in (a) used in cellular automata modelling for wildfires. These pairs are in order from simple to complex pairs, from left to right. The central cells (red) in (a) and (b) are the burning cells which are surrounded by neighbours (white). The multi-range neighbourhood in (b) consists of short-range neighbours such as the eight surrounding white cells and long-range neighbours which are located at L_c from the central cell. Cells located in between L_c and short-range neighbours are not considered as neighbours.

The rules on cellular automata for wildfire modelling can be categorized as deterministic or stochastic and the number of studies on each category are similar (see Figure 3.4). The main difference between deterministic and stochastic category is the results from deterministic models do not have uncertainty, whereas the results from stochastic models do. Although using stochastic is less computationally demanding than using deterministic, the inherent uncertainty needs to be considered. However, in large scale modelling, this uncertainty is needed to cope with the system variability (e.g., inhomogeneous fuel MC), therefore, trade-offs between desirable and undesirable uncertainty are also of importance. Each category has many different concepts, in which the pioneering work of each concept is shown by the authors in bold fonts in Figure 3.4, and will be discussed thoroughly in chapter 3.3 and 3.4. To simplify Figure 3.4, cyan groups four or more works within ten years which adopt the same model (connected by the blue lines).

Following the studies on wildfire modelling, cellular automata have also been used in several studies on building (within one building) and urban (across buildings) fires (see Figure 3.4). There are significantly fewer such studies than in wildfire modelling, however, the concepts that are used are similar. Therefore, cellular automata can be applied on various types of fire hazard modelling. There are four types of fire hazard that have used cellular automata models: flaming wildfires (white), smouldering wildfires (grey), urban fires (blue), and building fires (green). The authors at the intersection between two fire types represent the studies that consider both phenomena, for instance, Spyratos, Bourgeron and Ghil (2007) and Li, Cova and Dennison (2019) consider flaming wildfires and urban fires and Purnomo *et al.* (2021) considers flaming and smouldering wildfires. In this review, all the works in Table 3.1 and Figure 3.4 are grouped and addressed based on their similarities, thus, the discussion is based on the prominent features of the model (e.g., the consideration of crown fire that is addressed in several models), instead of the detail discussion of the model one by one.

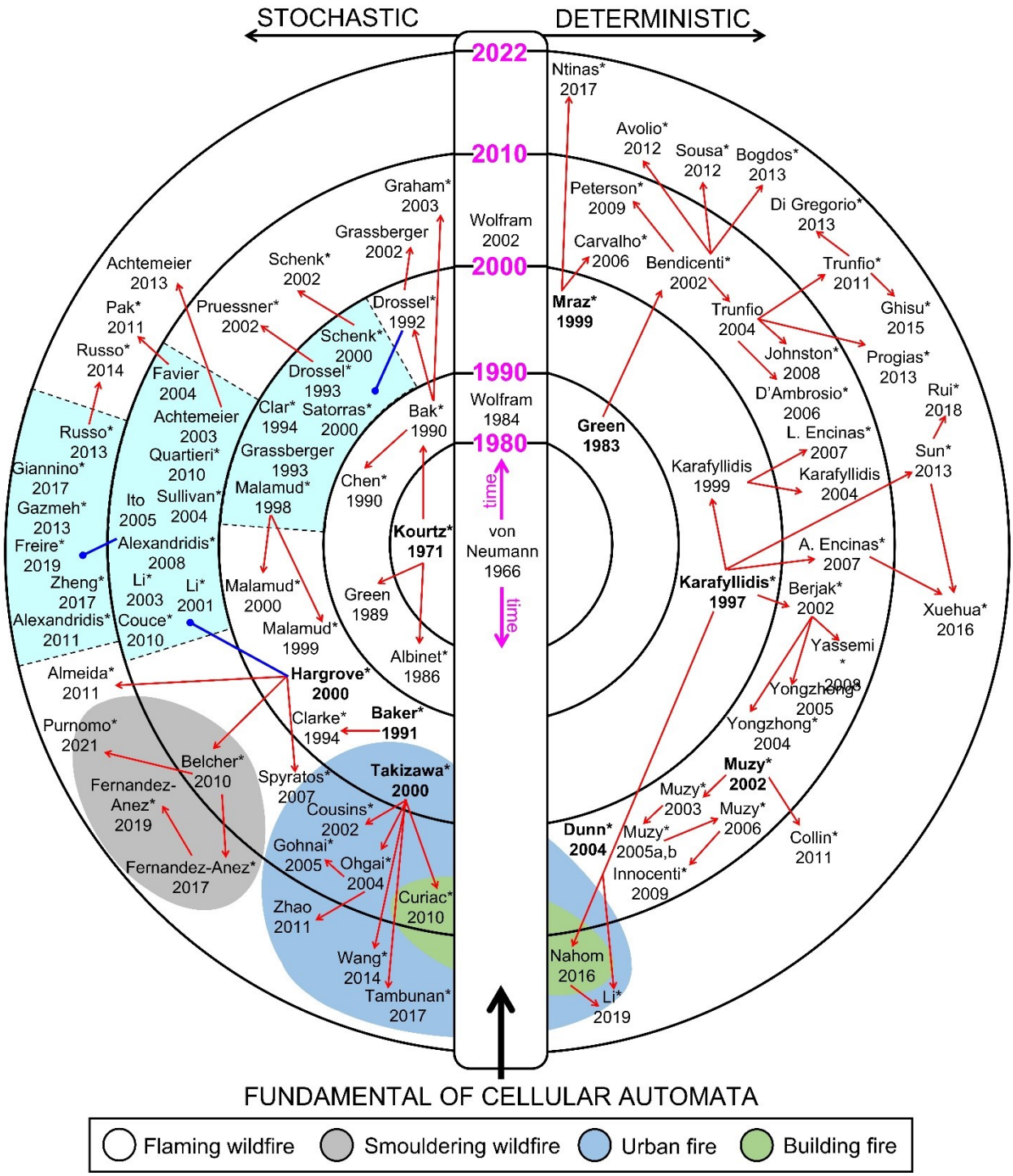

Figure 3.4. Diagram illustrating the development of cellular automata for modelling flaming wildfires (white), smouldering wildfires (grey), urban fires (blue), and building fires (green). Red arrows represent the modification of a previous model in more recent models. Cyan shaded areas are groups of more than three studies within the ten years which adopt the same model (connected by the blue lines). Bold fonts represent the pioneering work on each concept. The symbol (*) represents the work of more than one author. An author that is placed between two fire regimes considers these two fire regimes.

Table 3.1. Chronological table of details of previous studies on cellular automata for wildfires.

Authors	Principle and Case	Domain (cell size, neighbourhood, domain size)	Environmental parameters	Conclusions and notes
Kourtz and O'Regan (1971)	Site percolation‡ for single event wildfires	Square cell, von Neumann, 50 × 50 cells	Fuel type	Model shows expected results. Need environmental factors consideration
Green (1983)	Wave propagation† for single event wildfires	Square cell, vary, max 2401 × 2401 cells	Wind	Model shows different burnt scar of wildfires. Needs detail heat dynamic
Albinet, Searby and Stauffer (1986)	Site percolation‡ for multiple event wildfires	Square/triangle cell, 1-5th order, max 300 × 300 cells	Wind, slope, fuel type	Model shows the fractal fire front in many different domain.
Green (1989)	Site percolation‡ for multiple event wildfires	Square cell, elliptical, 50 × 50 cells	Wind, slope, fuel type, rain, soil effect	Wildfire is still needed to eliminate less competitive vegetation
Bak, Chen and Tang (1990)	Site percolation‡ for multiple event wildfires	Square cell, von Neumann, 256 × 256 cells	n/a	Model demonstrates criticality in a "turbulent" non-equilibrium system
Chen, Bak and Jensen (1990)	Site percolation‡ for multiple event wildfires	Square cell, von Neumann, 400 × 400 cells	n/a	Criticality of wildfires can be achieved with deterministic model
Baker, Egbert and Frazier (1991)	Diffusion limited aggregation‡ for multiple event wildfires	Square cell, 1st order, 200 × 200 cells	Slope, fuel type and age, weather	Model shows effect of global warming on wildfires over centuries
Drossel and Schwabl (1992)	Site percolation‡ for multiple event wildfires	Square cell, von Neumann, n/a	n/a	Model is critical in large range of parameter with lightning ignition
Drossel and Schwabl (1993)	Site & bond percolation‡ for multiple event wildfires	Square cell, von Neumann, n/a	n/a	Immune trees cause wildfires criticality become highly conditional
Grassberger (1993)	Site percolation‡ for multiple event wildfires	Square cell, von Neumann, 8192 × 8192 cells	n/a	Wildfires are still critical on large lattices
Clar, Drossel and Schwabl (1994)	Site percolation‡ for multiple event wildfires	Square cell, von Neumann, 16384 × 16384 cells	n/a	Critical exponents of criticality in 1 to 8 dimension are derived

† means deterministic, ‡ means stochastic, and 'n/a' means no consideration of environmental parameters

Table 3.1. (Continued)

Authors	Principle and Case	Domain (cell size, neighbourhood, domain size)	Environmental parameters	Conclusions and notes
Clarke, Brass and Riggan (1994)	Diffusion limited aggregation‡ for single event wildfires	Square cell, 1st order, (3335 ha)	Wind, slope, fuel type, weather	Model shows ability for risk assessment
Karafyllidis and Thanailakis (1997)	Heat accumulation† for single event wildfires	Square cell, 1st order, max 100 × 100 cells	Wind, slope, fuel heterogeneity	Model has expected results. Need comparison with real fires
Malamud, Morein and Turcotte (1998)	Site percolation‡ for multiple event wildfires	Square cell, von Neumann, n/a	n/a	Similar criticality between simulations and real fires
Karafyllidis (1999)	Heat accumulation† for single event wildfires	Square cell, 1st order, 260 × 260 cells	Wind, slope, fuel heterogeneity	Model significantly improves computational efficiency.
Mraz, Zimic and Virant (1999)	Fuzzy logic† for single event wildfires	Square cell, 1st order, n/a	Wind, fuel flammability scores	Model enables the use of descriptive uncertain knowledge
Malamud and Turcotte (1999)	Site percolation‡ for multiple event wildfires	Square cell, von Neumann, n/a	n/a	Criticality is found in earthquakes
Hargrove *et al.* (2000)	Bond percolation‡ for single event wildfires and fire risk	Square cell, 1st order, 500 × 500 cells (62500 ha)	Wind, fuel characteristic	High degree of variability found in wildfires
Pastor-Satorras and Vespignani (2000)	Site percolation‡ for multiple event wildfires	Square cell, von Neumann, 19000 × 19000 cells	n/a	Extended moment analysis improves model criticality
Schenk *et al.* (2000)	Site percolation‡ for multiple event wildfires	Square cell, von Neumann, max 2000 × 2000 cells	n/a	Finite-size effect significantly affects wildfire criticality
Malamud and Turcotte (2000)	Site percolation‡ for multiple event wildfires	Square cell, von Neumann, n/a	n/a	Criticality is found in landslides
Li and Magill (2001)	Bond percolation‡ for single event wildfires	Square cell, 1st order, max 512 × 512 cells	Wind, slope, fuel heterogeneity	Bush density has critical value to sustain wildfires

† means deterministic, ‡ means stochastic, and 'n/a' means no consideration of environmental parameters

Table 3.1. (Continued)

Authors	Principle and Case	Domain (cell size, neighbourhood, domain size)	Environmental parameters	Conclusions and notes
Berjak and Hearne (2002)	Heat accumulation† for single event wildfires	Square cell, 1st order, 50 × 50 cells (25 ha)	Wind, slope, fuel type, weather	Model satisfactorily simulated three independent wildfires
Muzy *et al.* (2002)	Discrete physical events† for single event wildfires	Square cell, von Neumann, (1 m^2)	n/a	The efficiency of a physical model is significantly improved with CA
Schenk, Drossel and Schwabl (2002)	Site percolation‡ for multiple event wildfires	Square cell, von Neumann, max 4096 × 4096 cells	n/a	The critical exponents change with the model length scale
Grassberger (2002)	Site percolation‡ for multiple event wildfires	Square cell, von Neumann, max 65536 × 65536 cells	n/a	Tree density in criticality is >50% higher than state of the art model
Pruessner and Jensen (2002)	Site percolation‡ for multiple event wildfires	Square cell, von Neumann, max 32000 × 32000 cells	n/a	Criticality in previous models depends on characteristic scales
Bendicenti *et al.* (2002)	Wave propagation† for single event wildfires	Square cell, 1st order, 168 × 131 cells (880 ha)	Wind, slope, fuel type, weather	Model agree with observation. Square cells cause spurious shape
Li and Magill (2003)	Bond percolation‡ for single event wildfires	Square cell, von Neumann, max 256 × 256 cells	Wind, slope, fuel type, weather	Critical tree density ranges from 50% to 70% based on environment
Graham and Matthai (2003)	Site percolation‡ for multiple event wildfires	Square cell, von Neumann, max 128 × 128 cells	n/a	Small-world network model can obtain scale-free criticality
Achtemeier (2003)	Bond percolation‡ for single event wildfires	Square cell, von Neumann, n/a	Wind, slope, fuel type, weather	Agent-based CA is a baseline prior to more complex models
Muzy *et al.* (2003)	Discrete physical events† for single event wildfires	Square cell, von Neumann, (1 m^2)	n/a	Active cell rule speeds up the DEVs-CA simulations
Dunn and Milne (2004)	Interacting automata† for single event wildfires	Square cell, 2nd order, n/a	Wind, slope, fuel type	Explicit communication rules enable the most efficient CA

† means deterministic, ‡ means stochastic, and 'n/a' means no consideration of environmental parameters

Table 3.1. (Continued)

Authors	Principle and Case	Domain (cell size, neighbourhood, domain size)	Environmental parameters	Conclusions and notes
Karafyllidis (2004)	Heat accumulation† for single event wildfires	Square cell, 1st order, 260 × 260 cells	Wind, slope, fuel heterogeneity	Specific purpose computer speeds up simulation 10^5 times
Yongzhong *et al.* (2004)	Heat accumulation† for single event wildfires	Hexagonal cell, 1st order, 60 × 60 cells (36 ha)	Wind, slope, fuel characteristic	Hexagonal cells reduce the spurious shape of burnt scar
Trunfio (2004)	Wave propagation† for single event wildfires	Hexagonal cell, 2nd order, 60 × 60 cells (36 ha)	Wind, slope, fuel type, weather	Model can be used for wildfire prevention and risk assessment
Sullivan and Knight (2004)	Bond percolation‡ for single event wildfires	Square cell, 1st order, max 160 × 160 cells (2.56 ha)	Wind, fuel type	Fire-wind rules improve the agreement with experiments
Favier (2004)	Bond percolation‡ for single event wildfires	Square cell, von Neumann, 400 × 400 cells	n/a	Model catches dynamic and static properties of wildfires
Yongzhong *et al.* (2005)	Heat accumulation† for single event wildfires	Square cell, 1st order, (45318 ha)	Wind, slope, fuel type	Wind reduction factor improves the accuracy of the model
Ito (2005)	Bond percolation‡ for multiple event wildfires	Square cell, 1st order, 200 × 200 cells (40000 ha)	Wind, fuel type, weather	Carbon-fire model estimated carbon budget in Siberia
Muzy *et al.* (2005a)	Discrete physical events† for single event wildfires	Square cell, von Neumann, (1 m^2)	n/a	Object-oriented framework improves the usability of CA
Muzy *et al.* (2005b)	Discrete physical events† for single event wildfires	Square cell, von Neumann, (1 m^2)	n/a	Trade-off between efficiency and accuracy is important
Muzy *et al.* (2006)	Discrete physical events† for single event wildfires	Square cell, von Neumann, (1 m^2)	n/a	Basic CA limitations are reduced in the improved model
Carvalho, Carola and Tomé (2006)	Fuzzy logic† for single event wildfires	Voronoi cell, 1st order (258 ha)	Wind, slope, fuel type, weather	Voronoi tessellation improves the accuracy of fuzzy based CA

† means deterministic, ‡ means stochastic, and 'n/a' means no consideration of environmental parameters

Table 3.1. (Continued)

Authors	Principle and Case	Domain (cell size, neighbourhood, domain size)	Environmental parameters	Conclusions and notes
D'Ambrosio *et al.* (2006)	Wave propagation† for single event wildfires	Hexagonal cell, 2nd order, 170 × 130 cells (884 ha)	Wind, slope, fuel type, weather, suppression	Hexagonal cells and suppression rules improve model accuracy
A. H. Encinas *et al.* (2007)	Heat accumulation† for single event wildfires	Square cell, 1st order, 1024 × 1024 cells	Wind, slope, fuel heterogeneity	New diagonal spread rules improve model accuracy
L. H. Encinas *et al.* (2007)	Heat accumulation† for single event wildfires	Hexagonal cell, 1st order extended, 100 × 100 cells	Wind, slope, fuel heterogeneity	Improved rules for hexagonal CA improve model accuracy
Porterie *et al.* (2007)	Heat accumulation† for single event wildfires	Square cell, multi range, 300 × 300 cells (1 m^2)	Wind, slope, fuel heterogeneity	Long-range neighbour enables deterministic firebrand model
Spyratos, Bourgeron and Ghil (2007)	Bond percolation‡ for single event WUI fires	Square cell, 1st order, 48 × 48 cells (576 ha)	Fuel type	WUI fire is affected by density and flammability of buildings
Yassemi, Dragićević and Schmidt (2008)	Heat accumulation† for single event wildfires	Square cell, 1st order, (24000 ha)	Wind, slope, fuel type, weather	The use of GIS improve the accuracy and usability of model
Johnston, Kelso and Milne (2008)	Wave propagation† for single event wildfires	Voronoi cell, 1st order (30 ha)	Wind, slope, fuel type, weather	Shape distortion of CA is solved with Voronoi tessellation
Alexandridis *et al.* (2008)	Bond percolation‡ for single event wildfires	Square cell, 1st order, (600 ha burnt area)	Wind, slope, spotting, fuel type & density	Simulation with simple rules agree with a real wildfire
Peterson *et al.* (2009)	Wave propagation† for single/multiple wildfires	Square cell, 1st order, (max 65871 ha)	Wind, slope, fuel type, weather	Model can simulate single and multiple fire events
Innocenti *et al.* (2009)	Discrete physical events† for single event wildfires	Square cell, von Neumann, (1 m^2)	n/a	Parallelization of algorithm speeds up the simulation
Couce and Knorr (2010)	Bond percolation‡ for single event wildfires	Square cell, 1st order, (2.88 × 10^8 ha)	Wind, slope, fuel type, weather	CA model is calibrated against 750,000 wildfires in Africa

† means deterministic, ‡ means stochastic, and 'n/a' means no consideration of environmental parameters. WUI and GIS stand for Wildland Urban Interface and Geographic Information System respectively

Table 3.1. (Continued)

Authors	Principle and Case	Domain (cell size, neighbourhood, domain size)	Environmental parameters	Conclusions and notes
Belcher *et al.* (2010)	Bond percolation‡ for single event wildfires	Square cell, 1st order, 50 × 50 cells (100cm^2)	Oxygen concentration	Oxygen variation determined fire activity in Earth's history
Quartieri *et al.* (2010)	Bond percolation‡ for single event wildfires	Square cell, 1st order, n/a	Wind, slope, fuel type	CA model agrees with other models and experimental data
Adou *et al.* (2010)	Heat accumulation† for single event wildfires	Square cell, elliptical, (2333 ha)	Wind, slope, fuel type	Detailed radiation and flame size and shape are introduced
Trunfio *et al.* (2011)	Wave propagation† for single event wildfires	Square cell, 1st/2nd, 382 × 266 cells (4064 ha)	Wind, slope, fuel type	Model agrees with FARSITE but runs faster
Collin, Bernardin and Sero-Guillaume (2011)	Discrete physical events† for single event wildfires	Square cell, high order, 201 × 201 cells (4 ha)	Fuel type, humidity	Advanced physics of wildfires are introduced to the CA model
Alexandridis *et al.* (2011)	Bond percolation‡ for single event wildfires	Square cell, 1st order, (30000 ha)	Wind, slope, fuel type, weather, suppression	Airborne firefighting strategy is optimised using improved CA
Almeida and Macau (2011)	Bond percolation‡ for single event wildfires	Square cell, 1st order, 201 × 201 cells	Fuel heterogeneity	Burning risk of a landscape is quantified using Monte Carlo
Pak and Hayakawa (2011)	Bond percolation‡ for single event wildfires	Square cell, von Neumann, 100 × 100 cells	n/a	Wildfires size are finite when using probability below critical
Sousa, dos Reis and Pereira (2012)	Wave propagation† for single event wildfires	Square cell, minimal time, 2048 × 2048 cells	Wind, slope, fuel type, weather	Using GPU is 200 times faster than using CPU
Avolio *et al.* (2012)	Wave propagation† for single event wildfires	Square cell, 2nd order, 450 × 450 cells (32400 ha)	Wind, slope, fuel type, weather	Local randomization rule enable deterministic CA to create BPM
Di Gregorio *et al.* (2013)	Wave propagation† for BPM of wildfires	Square cell, 2nd order, 461 × 445 cells (32823 ha)	Wind, slope, fuel type, weather	GPU showed potential to speed up the creation of BPM

† means deterministic, ‡ means stochastic, and 'n/a' means no consideration of environmental parameters. BPM, GPU, and CPU stand for Burning Probability Map, Graphic Processing Unit, and Central Processing Unit

Table 3.1. (Continued)

Authors	Principle and Case	Domain (cell size, neighbourhood, domain size)	Environmental parameters	Conclusions and notes
Progias and Sirakoulis (2013)	Wave propagation† for single event wildfires	Hexagonal cell, 1st order extended, 30 × 30 cells	Wind, slope	Specific purpose computer speeds up simulation 10^6 times
Sun *et al.* (2013)	Heat accumulation† for single event wildfires	Square cell, 1st order, (45 ha)	Wind, slope, fuel type, weather	Modified rules improve accuracy of CA for mountain fires
Bogdos and Manolakos (2013)	Wave propagation† for BPM of wildfires	Square cell, 1st order, 450 × 450 cells (4556 ha)	Wind, slope, fuel type, weather	BPM is created based on satellite and web-based CA
Gazmeh *et al.* (2013)	Bond percolation‡ for single event wildfires	Square cell, 1st order, (471 ha)	Wind, slope, fuel type, weather	The use of optimisation algorithm improves CA accuracy
Achtemeier (2013)	Bond percolation‡ for single event wildfires	Square cell, von Neumann, (63 ha)	Wind, slope, fuel type, weather	Agent-based CA agrees with a field-scale experiment
Russo, Vakalis and Siettos (2013)	Bond percolation‡ for single event wildfires	Square cell, 1st order, 13240 ha)	Wind, slope, fuel type, weather	Model agrees with real fire and can run real time simulations
Russo *et al.* (2014)	Bond percolation‡ for single event wildfires	Square cell, 1st order, 1400 × 1000 cells (3500 ha)	Wind, slope, fuel type, weather	Ignition points significantly affect burnt area.
Ghisu *et al.* (2015)	Wave propagation† for single event wildfires	Square cell, 1st order, 1200 × 1200 cells (14400 ha)	Wind, slope	Improved CA agrees with FARSITE but runs faster
Xuehua *et al.* (2016)	Heat accumulation† for single event wildfires	Square cell, 1st order, n/a	Wind, slope, fuel type, weather	Modified terrain factors improve accuracy of CA for mountain fire
Ntinas *et al.* (2017)	Fuzzy logic† for single event wildfires	Square cell, 1st order, 230 × 159 cells (1462 ha)	Wind, slope	Specific purpose computer speeds up simulation 10^4 times
Zheng *et al.* (2017)	Bond percolation‡ for single event wildfires	Square cell, 1st order, (max 10000 ha burnt area)	Wind, slope, fuel type, weather, rain	The use of machine learning algorithm improves CA accuracy

† means deterministic, ‡ means stochastic, and 'n/a' means no consideration of environmental parameters. BPM stands for Burning Probability Map

Table 3.1. (Continued)

Authors	Principle and Case	Domain (cell size, neighbourhood, domain size)	Environmental parameters	Conclusions and notes
Giannino *et al.* (2017)	Bond percolation‡ for single event wildfires	Square cell, 1st order, (max 123 ha)	Wind, slope, fuel type	Model accurately simulated 2 real wildfires in Italy
Fernandez-Anez, Christensen and Rein (2017)	Bond percolation‡ for single event wildfires	Square cell, von Neumann, 100 × 100 cells	n/a	Multi-layer rules introduce more physics to CA model for smouldering fires
Rui *et al.* (2018)	Heat accumulation† for single event wildfires	Square cell, 1st order, 230 × 159 cells (1462 ha)	Wind, slope, fuel type, weather	Fuel classification and correction factor improve model
Fernandez-Anez *et al.* (2019)	Bond percolation‡ for single event wildfires	Square cell, von Neumann, 100 × 100 cells	n/a	Simulated complex fingering phenomenon in smouldering
Freire and Dacamara (2019)	Bond percolation‡ for single event wildfires	Square cell, 1st order, (90000 ha)	Wind, slope, fuel type	Model satisfactorily simulated a severe Portugal fire
Purnomo *et al.* (2021)	Bond percolation‡ for single event wildfires	Square cell, 1st order, (573 ha)	Wind, fuel type, flaming & smouldering	Simulated smouldering initiated by flaming in Borneo peatland

† means deterministic, ‡ means stochastic, and 'n/a' means no consideration of environmental parameters

Table 3.2. The previous works on cellular automata for urban and building fire modelling.

Authors	Principle and Case	Domain (cell size, neighbourhood, domain size)	Environmental parameters	Conclusions and notes
Takizawa *et al.* (2000)	Bond percolation‡ for single event urban fires	Square cell, von Neumann, 50 × 50 cells (6.25 ha)	Fuel type	Model accurately simulated urban fire post-earthquake
Cousins, Heron and Mazzoni (2002)	Bond percolation‡ for single event urban fires	Square cell, 1st order, (8 ha)	Wind, spotting, fuel type	Wind and ignition location define the post-earthquake fire severity
Ohgai *et al.* (2004)	Bond percolation‡ for single event urban fires	Square cell, elliptical, 152 × 76 cells (10.4 ha)	Wind, fuel type	Model agrees with real fires and firefighting strategy is optimised
Gohnai *et al.* (2005)	Bond percolation‡ for single event urban fires	Square cell, elliptical, n/a	Wind, fuel type	Web-based mitigation planning support of urban fire is developed
Curiac *et al.* (2010)	Bond percolation‡ for single event building fires	Square cell, 1st order, n/a	Air flows, fuel type	Interconnected CA for fire/smoke in building is developed
Zhao (2011)	Bond percolation‡ for single event urban fires	Irregular cell, elliptical, n/a	Wind, fuel type	Model agrees with real fires, life and economic loss are estimated
Wang and Zhou (2014)	Bond percolation‡ for single event urban fires	Square cell, 1st order, n/a	Wind, fuel type	Model agrees with real fires and evacuation strategy is optimised
Nahom (2016)	Heat accumulation† for single event building fires	Square cell, 1st order, 32 × 26 cells (3276 m2)	Air flows	Model accurately estimates arrival time of fire and smoke
Tambunan, Salamah and Asriana (2017)	Bond percolation‡ for single event urban fires	Square cell, 1st order, (25 ha)	Wind, fuel type	Building material and open space are key factors
Li, Cova and Dennison (2019)	Heat accumulation† for single event urban fires	Square cell, 1st order, (18 km^2)	Wind, fuel type	Evacuation during WUI fire is optimised

† means deterministic, ‡ means stochastic, and 'n/a' means no consideration of environmental parameters

3.3. Deterministic Cellular Automata for Wildfires

There are four applied concepts in deterministic cellular automata for wildfire modelling: discrete physical event (Muzy *et al.*, 2002), wave propagation (Green, 1983), heat accumulation (Karafyllidis and Thanailakis, 1997), and linguistic (Mraz, Zimic and Virant, 1999; Dunn and Milne, 2004). These concepts are in order of decreasing physical and chemical compliance, which is inversely proportional to the computational efficiency. The first three concepts have been used more extensively than linguistic concept. Here, the fundamental rules and the development of these concepts are discussed.

3.3.1. Discrete physical events

Discrete physical event is a cellular automata model closest to physical model; however, the states involved are discretised and the computation is only performed on the neighbourhood of the burning cells (see Figure 3.5a). In this concept, physics and chemistry phenomena such as chemical reaction and heat transfer are considered (Collin, Bernardin and Sero-Guillaume, 2011). Despite considering the same phenomena as in the physical model, the number of phenomena considered in cells with different states is different. For example, discrete physical event CA consider reaction rate only in oxidizing cells, whereas in physical model the reaction rate (e.g., using Arrhenius law) is considered regardless the state of the cells.

Discrete physical event CA (DEVs-CA) uses 2-D reaction diffusion expression comprising conduction, convection, radiation and heat generation (Muzy *et al.*, 2002; Collin, Bernardin and Sero-Guillaume, 2011). The states in the model are discretized based on thresholds, e.g., evaporation and ignition temperatures (Collin, Bernardin and Sero-Guillaume, 2011). Once this threshold is reached, the cell's state changes, for instance, from unburned to burning. The physical variables and thresholds are translated to non-dimensional parameters and thresholds respectively, where the change of state corresponds to the value of the non-dimensional parameters that exceed non-dimensional thresholds. The values of these parameters change based on the average of the initial and final values. For example, within one state, the change in the non-dimensional parameters are only based on the initial and final temperature which are averaged over the time-steps, while the other physical variables such as density and heat generation are kept constant (in physical models the density and heat generation continuously change based on temperature and time). DEVs-CA have been validated against lab-scale experiments (Muzy *et al.*, 2002) and compared to other deterministic concepts, and Muzy *et al.* (2005b) reported that DEVs-CA performed more accurately and efficiently than other deterministic concepts.

The claim of higher accuracy is reasonable since DEVs-CA consider number of physical phenomena, whereas the claim of higher efficiency, despite involving sophisticated mathematical expressions of those in physical model, was achieved by implementing active cells principle (Muzy *et al.*, 2003). Active cell principle limits the number of cells undergoing computation based on the significance of the change (Muzy *et al.*, 2003). The cells considered in this category are the cells which have significant change on its non-dimensional parameters such as those changing states or those encounter other cells with different states (Muzy *et al.*, 2003). For instance, in Figure 3.5a, the computations are only executed on the red and orange cells. Therefore, the number of computations executed is significantly fewer when using the active cells principle. However, the claim of higher computational efficiency than other CA models is not strongly justified because there is no study that systematically compares CA models.

The traditional DEVs-CA models suffer from basic CA limitations, e.g., non-flexible rules and neighbourhood, static structure, and inability to accommodate external events (Muzy *et al.*, 2005a, 2006). Muzy *et al.* (2005a, 2006) introduced an object-oriented framework which successfully enables the model to avoid the basic limitations of CA. In conventional frameworks (procedural and functional programming), the attributes (e.g., vegetation type and density), rules, and neighbourhood of a cell are typically uniform. The non-uniformity of the cell attributes can be implemented by using additional matrix to store the information on the non-uniform attributes. For instance, if there are two non-uniform attributes, such as vegetation type and density, of the matrix of cells in the domain, three matrices of data are required, consisting matrix that store the cell state, cell's vegetation type, and cell's vegetation density. Therefore, although non-uniformity can be implemented in conventional frameworks, the additional computational cost needed is significant. Moreover, if the rules and neighbourhoods are non-uniform, then the additional matrix method is insufficient to implement non-uniformity and higher additional computational cost is required, causing an inefficient cellular automata model. In object oriented programming, each cell in the matrix of the domain is treated as an object (Muzy *et al.*, 2005a). This object contains information of attributes, rules, and neighbourhood. The domain is constructed from a matrix of objects which can have different attributes, rules, and neighbourhood. Therefore, the non-uniformity of attributes, rules, and neighbourhood can be implemented in the model without significant increase in computational cost.

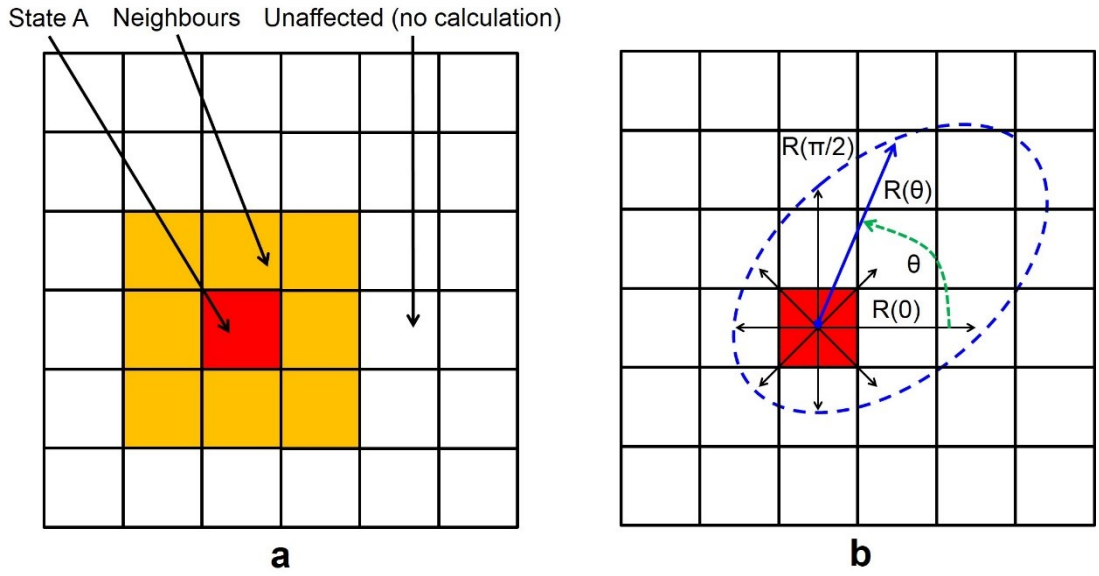

Figure 3.5. (a) Illustration of discrete physical event CA. The red (burning) and the orange (neighbourhood) cells are the active cells which undergo computation, whereas the white cells are the cells outside the neighbourhood where no computations are performed. (b) Illustration of wave propagation CA. The red cell is the ignited centre cell and the blue dashed ellipse is the velocity vector (Bendicenti et al., 2002). R(θ) is the spread rate along angle θ.

In earlier models of DEVs-CA (Muzy *et al.*, 2002, 2003, 2005a, 2005b, 2006; Innocenti *et al.*, 2009), ignition temperature was the only threshold, thus, the states are discretized between unburned and burning cells. Other phenomena have been introduced in the more recent models such as evaporation, radiative heat transfer, and pyrolysis degradation, by considering additional temperature thresholds to the model, i.e., evaporation and pyrolysis temperature thresholds (Collin, Bernardin and Sero-Guillaume, 2011). Consequently, high order neighbourhood was used to model the radiative heat transfer, since it is not limited to immediate neighbours of burning cell (Collin, Bernardin and Sero-Guillaume, 2011). Despite the increase of phenomena covered, which indirectly improve the accuracy, the computational efficiency of this improved model is to be concerned, especially when the model is implemented on a field-scale wildfire.

3.3.2. Wave propagation

A wave propagation concept executes change of states on cells which are bounded by a certain geometry, such as circle and ellipse (see Figure 3.5b). The shape and size of the geometry are determined based on maximum spread rate and spread rate in every direction from the centre cell which are calculated, for instance, by using the semiphysical approach of Rothermel (1972) and the Huygens principle respectively (Trunfio *et al.*, 2011). The spread rate in every direction defines the time-step required by fire to spread from

burning cell to its neighbours (see Figure 3.5b). The spread rate depends on the fuel characteristics (e.g., vegetation types, MC, density) and environmental conditions (e.g., topography and wind). Therefore, the spread rate distribution is anisotropic which then is visualised as ellipse by using the Huygens principle. The integration of the semiphysical spread rate formulation and the Huygens principle is argued to be the simplification of the reaction-diffusion model which is used in DEVs-CA model (Chapter 3.3.1; Séro-Guillaume *et al.*, 2008).

The wave propagation concept has been extensively used to simulate field-scale wildfires. Green first introduced this concept on CA for wildfire modelling and explored the shape of the fire front produced by the model with different mathematical expressions of time-step needed to spread the fire to neighbours (Green, 1983). He reported that the ellipse-shaped fire front produced by the "toy" model resembled historical wildfires. A more realistic approach was introduced to this model by implementing a semiphysical approach, which mostly used the mathematical model of Rothermel (1972), to determine the maximum spread rate of the fire (Bendicenti *et al.*, 2002). This improved model considered wind, slope, weather (e.g., ambient temperature and humidity), and fuel properties, and successfully simulated many real wildfires (Bendicenti *et al.*, 2002; D'Ambrosio *et al.*, 2006; Johnston, Kelso and Milne, 2008; Peterson *et al.*, 2009; Avolio *et al.*, 2012; Bogdos and Manolakos, 2013). D'Ambrosio *et al.* (2006) further improved the model by considering crown fire phenomena, which have different behaviours to surface fire and are very difficult to suppress (Pastor *et al.*, 2003). They used a specific fire intensity threshold which allows a transition from surface to crown fire following the work of van Wagner (1977, 1993). Once this threshold is exceeded, the spread rate to every direction are modified adopting the mathematical expressions in van Wagner (1977, 1993). Their model also implemented the effect of fire intervention, e.g., firefighting attempts (D'Ambrosio *et al.*, 2006).

The evolution of fire front at every time-step in wave propagation CA can be seen as a growing ellipse (which is referred to as global ellipse). The rules for this fire front evolution have been improved in an attempt to increase the accuracy of the model. The first improvement was by the creation of local ellipses on new ignited cells (see Figure 3.6a), which depends on the intersection between the global ellipse and the edge of the cell (Trunfio *et al.*, 2011; Di Gregorio *et al.*, 2013; Ghisu *et al.*, 2015). Once the global ellipse intersects the cell's edge and ignite the corresponding cell, this ignited cell creates a new local ellipse that grows over time-steps and affects the global ellipse shape (Trunfio

et al., 2011). This modification improved the accuracy of the model significantly with slight increase in computational time (Trunfio *et al.*, 2011).

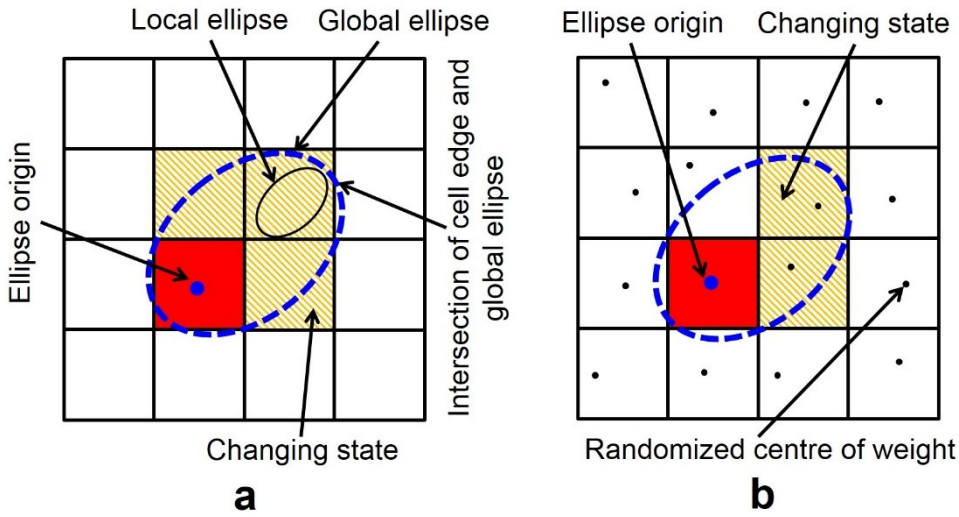

Figure 3.6. Illustrations of (a) the creation of local ellipse and (b) local randomization. The red cell is a burning cell, the white cells are unburned cells, and the patterned cells are the unburned cells that transition to burning cells. In (b), the centre of weight of a cell (black dot) in locally randomized domain slightly deviates from the centre of the cell.

The second improvement was made by introducing correction factors to the mathematical expressions in the model (Peterson *et al.*, 2009; Ghisu *et al.*, 2015). Although both Peterson *et al.* (2009) and Ghisu *et al.* (2015) implemented correction factors in the model, their correction factors were not used for the same mathematical expression. Peterson *et al.* (2009) applied the correction factor for the length to width ratio of the ellipse, which depends on wind, whereas Ghisu *et al.* (2015) applied the factor for the wildfire spread rate. These correction factors improved the accuracy of the model. The third improvement was by using adaptive time-step, i.e., time-step are not constant during simulation (Peterson *et al.*, 2009; Sousa, dos Reis and Pereira, 2012; Ghisu *et al.*, 2015). This adaptive time-step was implemented mainly to avoid the spread beyond the neighbourhood in one time-step (Peterson *et al.*, 2009; Ghisu *et al.*, 2015). On the other hand, Sousa, dos Reis and Pereira (2012) determined the time-step based on the minimum time needed to ignite unburned cell. To accommodate this rule, Sousa, dos Reis and Pereira (2012) employed minimal time neighbourhood (see Table 3.1) in which a neighbourhood that covers several cells in the second layer of the surrounding cells allow the fire to jump over the first layer of surrounding cells (see Figure 3.3b). This jump rule is executed if the time to ignition in a cell within the second layer is shorter than within the first layer. The last significant improvement was by introducing local randomization (see Table 3.1; Avolio *et al.*, 2012; Di Gregorio *et al.*, 2013). This local randomization

changes the centre weight of each cell in the grid to be slightly randomly deviate from the centre of cell (see Figure 3.6b). Therefore, the unburned cells transition to burning cells only after the ellipse reach the centre of weight of the cells, which are not at the centre of the cells (Avolio *et al.*, 2012). This additional rule provides preliminary consideration of heterogeneity within one cell in the landscape.

Square cell is the typical cell used for wave propagation CA, however, this cell suffer from an erroneous shape (polygon shape instead of ellipse) due to the square symmetry (Progias and Sirakoulis, 2013), which consequently lowers the model accuracy. Hexagonal cells have been proposed to address this problem (see Table 3.1; Trunfio, 2004; D'Ambrosio *et al.*, 2006; Progias and Sirakoulis, 2013). By using hexagonal cells, the burning cell has equidistant to its neighbours, unlike those of square cells which has diagonal neighbours, therefore, the erroneous shape of the square cells can be avoided. In wave propagation CA, the neighbourhood of this hexagonal cell is either 1st order (Progias and Sirakoulis, 2013) or 2nd order (Trunfio, 2004; D'Ambrosio *et al.*, 2006) neighbourhood (see Table 3.1). Both square and hexagonal cells, however, still face the problem of pre-fixed and limited number of spread direction (Johnston, Kelso and Milne, 2008). To avoid this limitation, Voronoi tessellation (see Chapter 3.2) was implemented, which made the spread more flexible and fire shape distortion was reduced (Johnston, Kelso and Milne, 2008). By using Voronoi tessellation, the number of spread directions depend on the shape of the polygon of each cell. Therefore, the number of spread directions can be as few as three (triangle cell shape) or as many as possible. The implementation of Voronoi tessellation, however, induced higher computational burden.

Bogdos and Manolakos (2013) extended the application of wave propagation CA by integrating satellite data to simulate wildfires across Europe. Their model also utilised random sampling on weather condition and Monte Carlo simulation to create burning probability map of the wildfires (see Table 3.1; Bogdos and Manolakos, 2013). Therefore, wildfire event and risk at arbitrary locations in Europe can be predicted based on the estimated weather conditions. The creation of a burning probability map was also studied by Di Gregorio *et al.* (2013); however, instead of using random sampling, Di Gregorio *et al.* (2013) implemented local randomization of Avolio *et al.* (2012) to provide uncertainty in the model. On the other hand, Progias and Sirakoulis (2013) successfully implemented wave propagation CA to a specific purpose computer, which led to a six order of magnitude faster simulation. By using a specific purpose computer, the number of hardware components are limited to only those required to run the model, therefore, dramatic increases on computational efficiency can be achieved.

3.3.3. Heat accumulation

In the CA model with heat accumulation concept, the transition of state depends on the intrinsic value of a cell which increases due to the difference of intrinsic values between cells within neighbourhood, resembling the accumulation of heat (Karafyllidis and Thanailakis, 1997). Once the intrinsic value (U) of a cell exceeds a certain threshold, the cell changes its state (see Figure 3.7a). The rate of change of intrinsic value in heat accumulation CA (ΔU) is mostly formulated based on spread rate, which generally varies at each direction from the centre cell and depends on fuel characteristics and environmental conditions (see Figure 3.7a). This concept is similar to DEVs-CA; however, while DEVs-CA use simplified physics and chemistry laws to determine the rate of change of the intrinsic value, heat accumulation utilises simpler approaches such as empirical and semiphysical approaches. Therefore, comparing DEVs-CA and heat accumulation CA is similar to comparing physical and semiphysical or empirical models.

Heat accumulation CA has been used to simulate many real historical wildfires (Berjak and Hearne, 2002; Yongzhong *et al.*, 2004, 2005; Yassemi, Dragićević and Schmidt, 2008; Sun *et al.*, 2013; Rui *et al.*, 2018) by also considering environmental and weather effects such as wind, topography, ambient temperature, and fuel properties (Sun *et al.*, 2013; Xuehua *et al.*, 2016; Rui *et al.*, 2018) which directly affect the spread rate of wildfires (see Table 3.1). The spread rate was firstly modelled based on empirical approach from (McRae, 1990), which then is used to determine the increment of intrinsic values. This increment is calculated by dividing the distance travelled at one time-step, given the spread rate, with the cell size (Karafyllidis and Thanailakis, 1997; Karafyllidis, 1999, 2004; A. H. Encinas *et al.*, 2007; L. H. Encinas *et al.*, 2007). Heat accumulation CA has also adopted the most commonly used spread rate calculator in wildfire modelling (Perry, 1998), a semiphysical approach of Rothermel (1972), into the model to improve the determination of the spread rate (Berjak and Hearne, 2002; Yongzhong *et al.*, 2004, 2005). However, Sun *et al.* (2013) argued that the model of Rothermel (1972) is less accurate in mountainous regions such as China due to the steep slopes on the landscape, and therefore, another empirical approach of Wang (1992) was implemented into heat accumulation CA (Sun *et al.*, 2013; Xuehua *et al.*, 2016; Rui *et al.*, 2018). Meanwhile, Rui *et al.* (2018) improved the spread rate in Sun *et al.* (2013) by multiplying the formulation of Wang (1992) with an additional adjustment factor which is calibrated against a real wildfire. This additional factor increased the accuracy of the model, however, the model accuracy cannot be generally validated because the model accuracy could plummet when the model simulates different wildfires due to an overfitting from the calibration process.

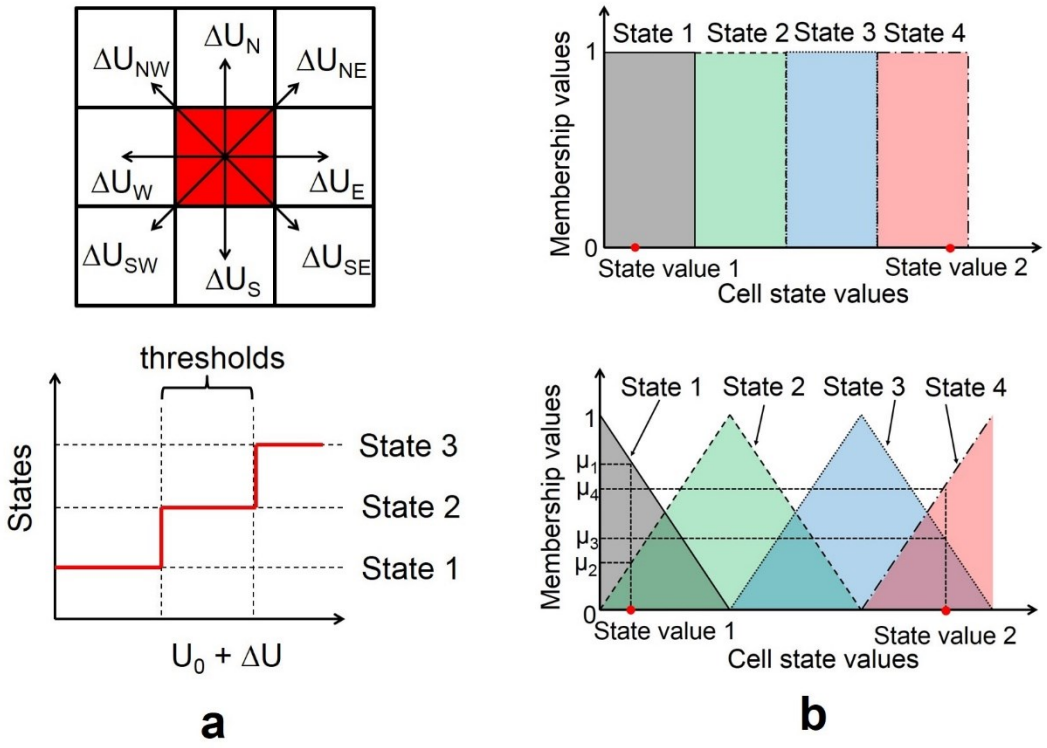

Figure 3.7. (a) Illustration of heat accumulation CA. The red cell is the burning cell. U is the intrinsic value and ΔU is the rate of change in intrinsic value which depends on the fire spread rate. The fire could spread, with different spread rates, to 8 neighbours i.e., N, S, W, E, NW, NE, SW, SE which represent North, South, West, East, North West, North East, South West, and South East. The state changes if the intrinsic value is higher than a threshold. (b) Illustration of membership values in fuzzy logic CA and comparison of state transition between CA without fuzzy logic (top) and CA with fuzzy logic (bottom). Membership values represent the fraction of cell belonging to a certain state. In CA without fuzzy logic (top) the membership value of a cell is either 0 or 1 which means the cell's intrinsic value corresponds to one state only. In CA with fuzzy logic (bottom) the membership value of a cell (μ) is ranging from 0 to 1 for each state, i.e., the cell's intrinsic value may correspond to more than one state.

Small world network concept, another form of heat accumulation CA has been proposed to simulate firebrand in deterministic CA (Porterie *et al.*, 2007). In small world network, the neighbourhood used in the model is multi-range (see Table 3.1), which consist of short-range (von Neumann or elliptical neighbourhood) to simulate fire propagation via heat transfer (predominated by radiation) and flame contact and long-range to simulate firebrand ignition (see Figure 3.3b). The transition of state in short-range neighbourhood follows the heat accumulation concept where a cell changes state when its intrinsic value exceed a certain threshold. However, the model of Porterie *et al.* (2007) reformed this rule into time-step delay. Therefore, the unburned cells within the

short-range neighbourhood of a burning cell, ignite after a certain time-step depending on their distances from the burning cell. This time-step delay is determined based on the energy balance and simplified radiative heat transfer principles. Meanwhile, the transition of state in long-range neighbourhoods is determined probabilistically, where the number of firebrands generated by a burning cell and their trajectories are probabilistically determined based on fuel characteristic and wind conditions (Porterie *et al.*, 2007). This small world network has been improved by Adou *et al.* (2010) to include more detail in the radiative heat transfer part, where the size and shape of the flame is considered. However, in this model, firebrand is not considered and high order elliptical neighbourhood is used instead of a multi-range neighbourhood. Both models have been validated against lab-scale experiment and the model of Adou *et al.* (2010) has been used to simulate a real historical wildfire.

To improve the accuracy of heat accumulation CA, similar attempts to wave propagation CA have been implemented. The first attempt is adaptive time-step; however, in heat accumulation CA, the time-step is limited to the minimum time required to burn one neighbouring cell instead of within a growing area such as the global ellipse area in wave propagation CA (see Table 3.1; L. H. Encinas *et al.*, 2007; Rui *et al.*, 2018). The second attempt is a correction factor, which in heat accumulation CA was implemented on wind effect (Yongzhong *et al.*, 2005). Wind effect was corrected because wind speed varies with altitude, whereas weather station records wind speed at only a single altitude (Yongzhong *et al.*, 2005). This correction factor was calibrated, based on real wildfires, to minimize the discrepancies between the model and real wildfires. The last non-trivial improvement, which has not been applied to wave propagation CA, is the rule for overlapping burnt areas (Yassemi, Dragićević and Schmidt, 2008). With this rule, the shape and location of burnt areas within one cell are considered. For instance, when the left and top neighbours of an unburned cell are burning, the top-left corner of the centre cell is burnt because of both the neighbours. The overlapping burnt area rule forbids the burnt contribution from more than one cell. Therefore, the increase of the intrinsic value of the centre cell is the summation of the intrinsic value transferred from the two neighbours but subtracted with the value that represent the overlapping burnt area. This rule aims to avoid the overestimation of burnt areas.

A spurious shape (polygon instead of ellipse) of fire front due to square cell symmetry was also found in heat accumulation CA (A. H. Encinas *et al.*, 2007; L. H. Encinas *et al.*, 2007). The first attempt to tackle this issue was by modifying the rule on diagonal spread (A. H. Encinas *et al.*, 2007; Xuehua *et al.*, 2016), which is the source of fire shape distortion.

The spread to diagonal cells, which was previously linear, was changed to be circular (A. H. Encinas *et al.*, 2007). Therefore, instead of creating a triangular slice of burning area, in the improved model the slice of burning area has a circular wedge shape (A. H. Encinas *et al.*, 2007). The second attempt, which is similar to those in wave propagation CA, was to use hexagonal cell (see Table 3.1; Yongzhong *et al.*, 2004; L. H. Encinas *et al.*, 2007). However, L. H. Encinas *et al.* (2007) introduced 6 additional distant neighbours (see Table 3.1), therefore, the fire can spread to 12 directions (see Figure 3.3b of hexagonal – 1st order extended), instead of a 6 directional spread of those using 1st order neighbourhood (Yongzhong *et al.*, 2004), and reduce erroneous shape.

The intrinsic values in heat accumulation CA is typically continuous (Karafyllidis and Thanailakis, 1997), e.g., from 0 to 1 which represent unburned and burning cell respectively; however, this continuous CA is computationally demanding. This continuous CA has been discretized (e.g., instead of 0 to 1, there are only three values: 0, 0.5, and 1) to increase computational efficiency (Karafyllidis, 1999, 2004; L. H. Encinas *et al.*, 2007). In the discretized model, the number of states are finite and selected based on the results from optimization of number of states and their values to obtain minimum number of finite values which still have sufficiently high accuracy (Karafyllidis, 1999). Therefore, while increasing the efficiency, the model does not significantly lose accuracy. To improve the efficiency even more, Karafyllidis (2004) implemented this discretised model into specific-purpose computers. This implementation accelerated the execution time of the model up to five orders of magnitude. On the other hand, Berjak and Hearne (2002) and Yassemi, Dragićević and Schmidt (2008) successfully integrated GIS to the heat accumulation CA which made the model more realistic and consequently improved its accuracy.

3.3.4. Linguistic

Cellular automata models that use linguistic rules govern the behaviour of the models using explicit rules, which are represented in the state diagram (Dunn and Milne, 2004). The state diagram define the transition of state of cells over certain triggers, for instance, "*at north wind condition, an unburned cell will become moderately burning if its south neighbour is a strongly burning cell*". This rule is implemented linguistically with *if-then* premise instead of mathematical expression. Each cell is connected to its neighbours and their state diagram are synchronized. Therefore, the discrepancies of the state transition between each cell do not exist. This model was used solely to maximise the computational efficiency of the wildfire model, which is the main benefit of using cellular automata. This

model has also been used to simulate real fires and produced reasonable results (Dunn and Milne, 2004).

Fuzzy logic has been applied in linguistic cellular automata to reduce the stiffness of the model due to the finite number of states of a cell (Mraz, Zimic and Virant, 1999). The state of a cell is no longer a discrete value, but a continuous intrinsic value, similar to heat accumulation CA, which is translated (fuzzification) to membership values of either one or more than one states (see Figure 3.7b). These membership values represent the fraction of cell which belong to a certain state. For example, as shown in Figure 3.7b (bottom), cell 1 has a fraction of μ_1 which belongs to state 1 and a fraction of μ_2 which belongs to state 2, whereas cell 2 has a fraction of μ_3 which belongs to state 3 and a fraction of μ_4 which belongs to state 4. Without fuzzy logic (as shown by Figure 3.7b, top), the cell only has one state regardless the intrinsic value. However, the intrinsic and membership values are only a representation of a state and the spread behaviour in fuzzy logic CA (i.e., the effect of intrinsic and membership values of neighbour cells) is still governed linguistically without arithmetical operation. For instance, with the same premise as linguistic CA in the previous discussion, a moderately burning cell corresponds to a certain membership value. The cell's intrinsic value was updated by translating this membership value (defuzzification) by a certain rule such as fuzzy mean method (Ntinas *et al.*, 2017). The updated intrinsic value then was used to determine the state of the cell.

The behaviour of the fuzzy logic CA is determined based on pre-defined linguistic rules similar to linguistic CA; however, the determination of intrinsic and membership values is calibrated based on real physical variable such as fire spread rate. This calibration can be done manually (Mraz, Zimic and Virant, 1999) or using an optimization algorithm that could increase the accuracy of the model (Ntinas *et al.*, 2017). Another attempt had been made to increase the accuracy of the model by implementing Voronoi tessellation to avoid fire shape distortion (see Table 3.1; Carvalho, Carola and Tomé, 2006). Moreover, GIS has been integrated to fuzzy logic CA (Carvalho, Carola and Tomé, 2006). Therefore, fuzzy logic CA bridges the linguistic CA with real phenomena of wildfires. Meanwhile, Ntinas *et al.* (2017) proved the feasibility of this concept to be implemented in specific-purpose computers. This implementation increased the computational efficiency of the model to be fourth order faster.

3.4. Stochastic Cellular Automata for Wildfires

There are two stochastic concepts that have been explored in cellular automata modelling for wildfires: diffusion limited aggregation (Baker, Egbert and Frazier, 1991) and percolation theory (bond and site percolations; Kourtz and O'Regan, 1971; Hargrove

et al., 2000). Differing from the concepts in deterministic cellular automata, these concepts have various applications for wildfires modelling, which capture different phenomena in wildfires. Here, the implementation and development of stochastic concepts for wildfires modelling with cellular automata are discussed.

3.4.1. Diffusion limited aggregation

In cellular automata with the diffusion limited aggregation (DLA) concept, the spread of fire is restricted to a specific number of directions at every time-step (see white arrow in Figure 3.8a). The directions in which the fire is allowed to spread depend on the weight and probability of movement to those directions (Clarke, Brass and Riggan, 1994). The weight is a function of the fuel characteristics and environment, which is used to update the probability value. The updated probability value determines the movement of the fire to the direction with the highest probability.

Baker, Egbert and Frazier (1991) used DLA concept to study the effect of global warming on wildfire within century timeframe. They used GIS to define the topography and used probabilistic approach based on climate regime to estimate the weather over centuries. Fuel characteristics, which affect the probability of each cell and consequently the direction of fire spread, depend solely on vegetation type in their model. Their model revealed fluctuations in landscape structure (e.g., vegetation configuration) despite a constant ignition with specific frequency.

On the other hand, Clarke, Brass and Riggan (1994) used DLA concept to simulate a field-scale test wildfire, which has an irregular shape of burnt area (not a simple geometry such as ellipse), and created a burning probability map using Monte Carlo simulation. Their model improved the model by Baker, Egbert and Frazier (1991) by introducing *firelet* rules and considering firebrand which is highly probabilistic (Sullivan, 2009a), thus cannot be modelled by using deterministic rules. The spotting phenomenon (firebrand) creates new hotspots that are relatively distant from the fire front and could trap firefighters between two fire fronts (Pastor *et al.*, 2003; Rein and Huang, 2021). In their model, they defined two different types of burning cells: fire source and *firelet*. The fire source is the type of burning cells that can facilitate the spread of the fire by producing *firelets*, whereas *firelets* are unable to directly produce another *firelets*, but do have the ability to become fire source. The transition of *firelets* to become fire source is determined probabilistically, therefore, not all *firelets* can become fire source. Once a *firelet* becomes a fire source, it can produce new *firelets* and spread the fire. Therefore, *firelets* are analogous to low intensity fires that cannot spread the fire to surroundings, whereas a fire source is analogous to a high intensity fire that can spread the fire to surroundings.

The low intensity fire can either become high intensity fire or extinct, in which in the model of Clarke, Brass and Riggan (1994) are probabilistically determined. They reported that the model provide high accuracy simulation when compared with the test fires.

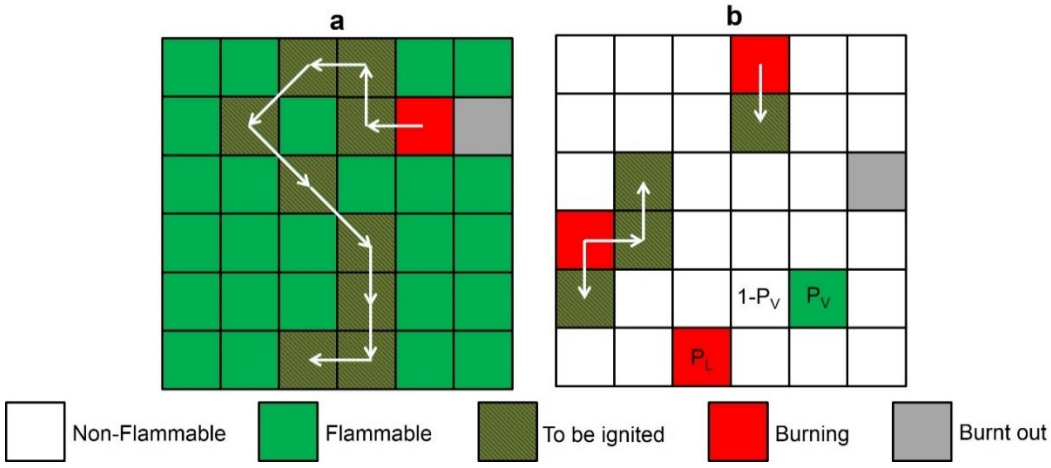

Figure 3.8. (a) Illustration of diffusion limited aggregation CA. The white arrows are the direction of fire spread, which only spreads in the direction with highest spread probability. The burning cells (red) become burnt out (grey) after several time-steps. (b) Illustration of site percolation CA. The cell type is probabilistically determined either become flammable (green) or non-flammable (white) with a probability of P_V and 1-P_V respectively. Each flammable cell could ignite at every time-step with a probability of P_L. Once ignited burning cells spread the fire to all flammable neighbouring cells deterministically (white arrow). The burning cells become burnt out (grey) after several time-steps and the burnt out cells reset to become flammable or non-flammable cells.

3.4.2. Bond percolation

Percolation is a transport phenomenon of fluid through porous media, which consequently leads to irregular movement of the fluid since the existence of connecting channels between pairs of entities in the medium are randomly distributed (Sullivan, 2009c). In cellular automata with bond percolation concept, fire spreads from the burning centre cell to its neighbours with a specific probability. This probability depend on fuel characteristics and environment conditions, and dictates the spread rate of the fire (Alexandridis *et al.*, 2008). The grid and the fuel configurations in the computational domain of bond percolation CA are predefined and constant. This concept is similar to DLA; however, the direction of the fire spread is not limited to a certain number of directions, thus, at the subsequent time-step the fire could spread to all direction of the neighbouring cells.

The spread probability in bond percolation CA is typically selected based on calibration either against spread rate models or historical fires (Hargrove *et al.*, 2000;

Alexandridis *et al.*, 2008; Freire and Dacamara, 2019). The calibration against spread rate models mostly employs mathematical models based on empirical approaches (Hargrove *et al.*, 2000; Achtemeier, 2013; Russo *et al.*, 2014), such as from Albini and Brown, (1996) and Andrews (2008). The calibration against historical wildfires involves many incidents, e.g., 750 thousands wildfires in Africa (Couce and Knorr, 2010), resulting in the ability of bond percolation CA to simulate real wildfires (Hargrove *et al.*, 2000; Alexandridis *et al.*, 2008; Couce and Knorr, 2010; Gazmeh *et al.*, 2013; Russo, Vakalis and Siettos, 2013; Giannino *et al.*, 2017; Zheng *et al.*, 2017). The calibration process can be done manually (Achtemeier, 2013), using optimization algorithms (Alexandridis *et al.*, 2008; Gazmeh *et al.*, 2013; Giannino *et al.*, 2017), and using machine learnings (Zheng *et al.*, 2017) (see Table 3.1). The calibration process ensures the CA models to accurately simulate wildfires, for instance, based on the comparison of burnt area between simulation and field observations. However, the high accuracy of the models due to calibration process means that they may be unreliable when used to simulate other wildfires that are not involved in the calibration process. This drawback becomes prominent when the calibration is performed against historical wildfires, because the overfitting between simulation and the calibration data can occur, especially when historical wildfires data are limited.

Bond percolation CA has considered many affecting factors in wildfires, including wind, weather (rain, ambient temperature, and humidity), topography, and fuel characteristics (see Table 3.1; Li and Magill, 2001, 2003; Alexandridis *et al.*, 2008; Couce and Knorr, 2010; Quartieri *et al.*, 2010; Almeida and Macau, 2011; Gazmeh *et al.*, 2013; Russo, Vakalis and Siettos, 2013; Zheng *et al.*, 2017; Giannino *et al.*, 2017; Freire and Dacamara, 2019). The information on these factors is obtained mostly from GIS that have been extensively integrated in bond percolation CA by storing information from GIS into the cells in the model (see Table 3.1; Alexandridis *et al.*, 2008; Quartieri *et al.*, 2010; Russo, Vakalis and Siettos, 2013; Giannino *et al.*, 2017; Freire and Dacamara, 2019). However, each of these factors were treated separately and provide distinct effects on the spread probability, unlike those in deterministic CA that mostly used semiphysical approach and integrated these factors into a single value, e.g., spread rate.

Gazmeh *et al.* (2013) considered fire suppression by nature (rain), whereas Alexandridis *et al.* (2011) considered fire suppression by human activity, i.e., firefighting attempts. The firefighting attempts in the model of Alexandridis *et al.* (2011) resembled airborne firefighting (water bombing) where the effectiveness of the firefighting activity

can be assessed based on the air tanker capacity and schedulling. This consideration provided insights into the management of firefighting activities for wildfires.

When fires reach and ignite the canopy of vegetation (crown fire), the hazard of wildfires increases significantly Bond percolation CA has modelled this phenomenon by introducing a probability threshold (Ito, 2005), which is similar to the approach in wave propagation CA. However, since the threshold is probabilistic, the occurrence of crown fire in this model has uncertainty unlike those in wave propagation CA.

The wind dynamic around the fire heavily depend on the fire dynamics (Sullivan and Knight, 2004; Achtemeier, 2013), which could lead to pressure anomalies, and should be treated differently from undisturbed wind (Sullivan, 2009a, 2009c; Achtemeier, 2013). One method used to simulate this fire-atmosphere interaction was the dynamic bubble concept (Sullivan and Knight, 2004). This dynamic bubble concept employs an imaginary bubble that absorbs part of the energy from the fire and moves depending on the energy absorbed, which then affect the local wind dynamics (Sullivan and Knight, 2004). Each cell in the domain has this bubble, which moves upward with certain rate, proportional to the fire intensity of the corresponding cell. The upward movement of the bubbles are coupled with the wind velocity to obtain the fire-affected wind vector, which then is used as the wind effect for the fire spread direction, instead of using the undisturbed wind (Achtemeier, 2013). Therefore, this bubble concept resembles the effect of buoyancy to the wind dynamics, which also have a feedbacks effect on fire dynamics.

The interaction between wildfires and other fire hazards has also been modelled with bond percolation CA. Spyratos, Bourgeron and Ghil (2007) and Li, Cova and Dennison (2019) used bond percolation CA to simulate wildland urban interface (WUI) fires, where the fire from wildland can initiate fire in urban areas. This modelling mainly aims to provide a risk-based assessment for the development of fire-safe WUI regions (although WUI fire models have not been validated with real WUI fires). WUI fires have been investigated by considering vegetation and houses as fuel, and also spotting phenomenon, where ember can fly to the rooftop and initiate urban fires. Spotting is also an important phenomenon in wildfires, as it can provide new sources of ignition at a relatively distant location from the fire front, causing firefighting attemps become more difficult and dangereous. Since the dynamics of the flying embers are unlikely to be deterministic, bond percolation CA is the most commonly used concept to simulate spotting (see Table 3.1; Alexandridis *et al.*, 2008; Couce and Knorr, 2010; Freire and Dacamara, 2019). However, the details of the spotting phenomena such as the trajectory and the distance travelled by the firebrand have not been sufficiently discussed.

Bond percolation CA have also been used to model smouldering fires (Belcher *et al.*, 2010; Fernandez-Anez, Christensen and Rein, 2017; Fernandez-Anez *et al.*, 2019), which is the dominant type of combustion in peatland wildfires, involving flaming wildfires igniting the peat underneath. All the CA models of smouldering fires are still at the small-scale (Belcher *et al.*, 2010; Fernandez-Anez, Christensen and Rein, 2017; Fernandez-Anez *et al.*, 2019), and its development mainly focuses on the introduction of more physical considerations. For instance, the pioneering work of Belcher *et al.* (2010) only considered ignition and extinction of smouldering, whereas Fernandez-Anez, Christensen and Rein (2017) and Fernandez-Anez *et al.* (2019) improved this model by considering drying, pyrolysis, oxidation, and extinction of smouldering.

There are many extended uses of bond percolation CA. Li and Magill (2001, 2003); Favier (2004); Almeida and Macau (2011) and Pak and Hayakawa (2011) explored the probability values in the models to find the critical probability values that facilitate the sustainability of the wildfires, whereas Ito (2005) used the model to simulate carbon budget in boreal forest, the results of which could reduce the uncertainties of global carbon cycle estimation. Due to the inherent uncertainty of bond percolation CA, Almeida and Macau (2011) used the model to create a burning probability map (BPM) for risk-assessment. Meanwhile, Achtemeier (2003, 2013) modified the bond percolation CA concept by implementing an agent based concept, which mimics rabbit behaviour to simulate wildfires. In this concept, fire and landscape are different entities. The fire is represented by the agent, i.e., the rabbit, and the cells represent the landscape which contains the information on wind, topography, fuel characteristics, and weather. Their model considered the fire behaviour: fire consumes fuel, fire jumps between adjacent fuel elements, fire spreads, and fire extinct, analogous to the way rabbits eat food, rabbits jump, rabbits reproduce, and rabbit dies, and these behaviours are affected by the environment, fuel properties, and weather (Achtemeier, 2003, 2013).

Since there are numerous methods and applications of bond percolation CA, the method that should be used depend on the case to be simulated. For instance, to simulate crown and surface fires, threshold rules can be implemented, and if fire-atmosphere interaction need to be considered, these threshold rules can be integrated with the bubble concept. Therefore, the additional phenomena considerations, means additional rules, and the rules to be used can be chosen from previous works presented here (developing new rules is also possible). This feature means that the modelling using bond percolation CA is modular, which increases the flexibility of the model.

3.4.3. Site percolation

Although also stems from the randomly distributed medium and its internal channels, site percolation CA has different approach to in bond percolation CA. In site percolation CA, the fuel configuration is probabilistic and changes over time (Malamud, Morein and Turcotte, 1998), and bond percolation makes this constant. On the other hand, in site percolation CA, the fire spread from a burning cell to adjacent flammable cells is executed deterministically (Kourtz and O'Regan, 1971; Green, 1989), and bond percolation executes this rule probabilistically. Therefore, in site percolation, once a burning cell encounters adjacent flammable cells, the fire always spreads to the flammable cells at the subsequent time-step. However, each cell in site percolation can either become flammable cell or inflammable cell with a specific probability (see Figure 3.8b). Each flammable cell has a probability of igniting, e.g., caused by lightning, at every time-step (see Figure 3.8b). The ignited cell spread the fire to its neighbours deterministically (see Figure 3.8b) and once the burning cell is burnt out, this cell can become either flammable or nonflammable cell probabilistically at the subsequent time-step. This reset of cell state corresponds to vegetation regrowth process after wildfires.

Site percolation CA was initially used to simulate the Euclidean shape (such as circle and ellipse) of wildfire spread and aid mitigation strategy, the same as in other CA models (Kourtz and O'Regan, 1971; Green, 1989). However, its function shifts to the simulation of the fractal shape of the forest ecosystem caused by wildfires and vegetation regrowth over many years (hundreds of years; Sullivan, 2009c). In most of the wildfire models, the fire spread is assumed to have Euclidean geometry (see Figure 3.9a); however, in the real event of wildfires, the burnt scar caused by the fire spread has fractal geometry (see Figure 3.9b as example of fractal geometry; Ball, 2001). Figure 3.9c shows an example of fractal geometry of forest ecosystem caused by wildfires and different regrowth phases of the vegetation in Borneo in 2018; region 1 is burnt, region 2 is early stage regrowth, region 3 is late stage regrowth, and region 4 is fully regrown and undisturbed vegetation.

Fractal geometry is irregular geometry which involve loop and *seed* for its construction; thus, while fractal geometry cannot be formulated the same way as in Euclidean geometry (e.g., parabola, hyperbola), with the help of computers fractal can be constructed with only limited number of instructions (Mandelbrot, 1974). For example, the fractal shape of a snowflake can be constructed from loop of *seed* of triangles (see Figure 3.10; Mandelbrot, 1974). The triangle seeds are shrunk, rotated, and repeatedly drawn at the apexes of the geometry on the previous loop. Fractal geometry is argued to be the geometry of nature, seen in non-spherical clouds, non-conical mountains, and non-straight path of lightning

strikes (Mandelbrot, 1974). In the spread pattern of a fire, Zik and Moses (1999) observed the fractal shape of a fingering phenomenon in smouldering fire of solid fuel due to the scarcity of oxygen. Figure 3.9b shows an example of fractal geometry of a fingering phenomenon in smouldering fire. This figure is the result from the model of Fernandez-Anez *et al.* (2019) who successfully simulated fingering phenomena in smouldering fire of Zik and Moses (1999) using bond percolation CA.

The fractal shape of the forest ecosystem caused by wildfires can be simulated when the system is in the critical state (Bak, Chen and Tang, 1990). The criticality theory generalizes the phenomena which experience criticality as the system that result in fractal (irregular) energy dissipation when given uniform energy input (Bak, Chen and Tang, 1990). An example of this system is found in fluid flow, where once a critical point such as critical Reynold number is reached, uniform inputs of energy (e.g., higher pump power than in laminar flow) result in turbulent flow which has high irregularities and consequently dissipate the energy irregularly (Mandelbrot, 1974). This fractal energy dissipation is not only found in turbulent fluid but also many other phenomena (Mandelbrot, 1974). Many studies attempted to prove the critical behaviour of nature, for instance, the criticality found in earthquakes and landslides (Malamud and Turcotte, 1999, 2000).

A critical system satisfies scaling law, where a physical variable scales another variable over a significant range (Clar, Drossel and Schwabl, 1994). This scaling law mostly use a power law relationship, $y = x^{\alpha}$, to correlate two variables (x and y) in a phenomenon (Bak, Chen and Tang, 1990). Therefore, when the fractal shape of the forest ecosystem is successfully simulated, there are pairs of variables in the system which can be correlated using the power law relationship with a corresponding critical exponent (α; Bak, Chen and Tang, 1990). These pairs of variables are important in translating the theoretical system for the mitigation of wildfires (Malamud, Morein and Turcotte, 1998). For example, Malamud, Morein and Turcotte (1998) used site percolation CA model to simulate the fractal geometry of forest ecosystem and found that the frequency and the size of wildfires have a power law relationship. This study has been used for the campaign of prescribed fires (Malamud, Morein and Turcotte, 1998; Waldrop and Goodrick, 2018).

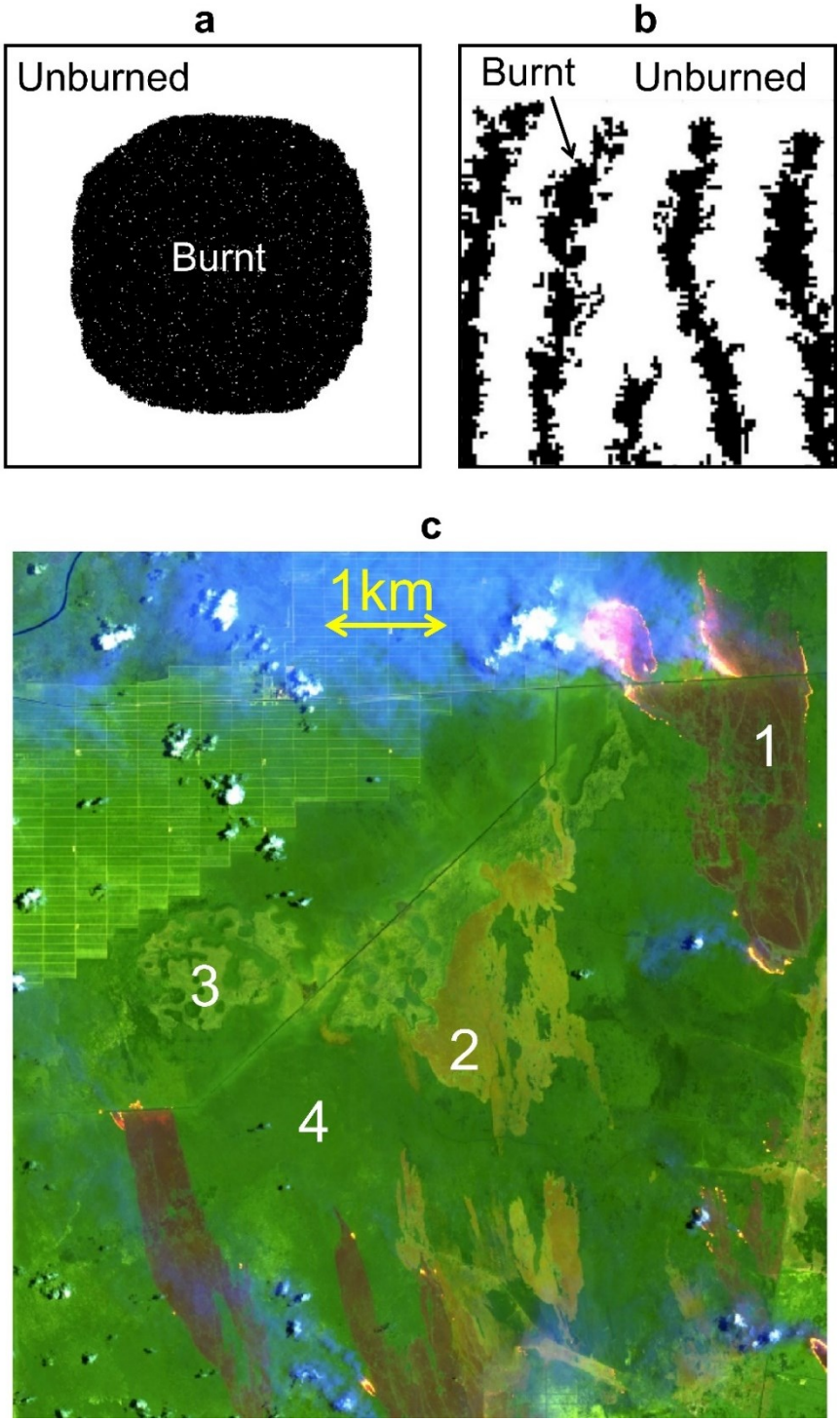

Figure 3.9. (a) Typical Euclidean burnt scar in modelling of wildfires (modified from Purnomo et al., 2021). (b) An example of a fractal burnt scar of fingering phenomenon in smouldering fire spread (modified from Fernandez-Anez et al., 2019). (c) Satellite image of fractal geometry of forest structure caused by wildfires and vegetation regrowth. Region 1 is burnt, region 2 is early stage regrowth, region 3 is late stage regrowth, and region 4 is fully regrown and undisturbed vegetation.

Studies on the criticality of wildfires aim to estimate the critical exponents that correlate pairs of variables in wildfires. These attempts are executed by using computational models where uniform inputs such as constant tree regrowth rate are introduced, and irregular outputs such as fractal shape of the burnt scar are expected (Bak, Chen and Tang, 1990). Although different studies find different critical exponents for different pairs of variables (not limited to a pair of frequency and size of wildfires), these behaviours are key in enabling the criticality of wildfires (Bak, Chen and Tang, 1990). The development and improvement in the CA models that study criticality of wildfires focus on implementing different rules to approximate real wildfires by introducing more realistic variables, but still satisfy the core behaviours of critical wildfires.

Albinet, Searby and Stauffer (1986) pioneered the study of criticality in wildfires using a *forest fire* model (implementing site percolation CA) which considered wind, slope, and fuel type and used both triangular and square cells domain (see Table 3.1). Although the *forest fire* model by Bak, Chen and Tang (1990) did not consider environmental and climatic factors, it is the base model for other works on criticality of wildfires instead of the pioneering model by Albinet, Searby and Stauffer (1986). Bak, Chen and Tang (1990) studied critical behaviour of nature by combining the *forest fire* model with Monte Carlo simulation, where the first ignition was at random location and the model was simulated repeatedly. The trees grew uniformly, with a specific probability (see Figure 3.8b), and if the trees are ignited then the fire spreads deterministically to the neighbouring cells (Bak, Chen and Tang, 1990). By using these simple rules, criticality was obtained (when the tree growth probability is very small) where the uniform input, i.e., uniformly growing trees results in fractal dissipation, i.e., irregular shape of burnt areas (Bak, Chen and Tang, 1990).

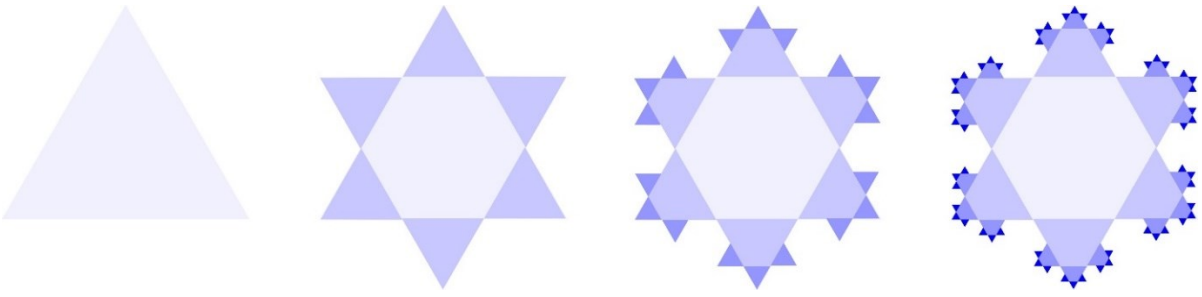

Figure 3.10. An example of the construction of the fractal geometry of a snowflake (Mandelbrot, 1974). The snowflake is constructed from the loop of seed of triangles (left to right) which are shrunk and rotated in every loop. The seed of triangles are placed at the apexes of the geometry obtained from the previous loop.

The *forest fire* model was slightly modified by Chen, Bak and Jensen (1990), by implementing deterministic and continuous ignition, instead of single ignition, which is combined with the Monte Carlo simulation, as in Bak, Chen and Tang (1990). Once the density of trees exceed a certain threshold, the fire starts and spreads following the same rules as in Bak, Chen and Tang (1990). This model successfully showed criticality of system when the tree density increment is adequately small (Chen, Bak and Jensen, 1990). This deterministic ignition approach was then replaced with the stochastic ignition approach by introducing "*lightning ignition*" with a specific frequency of occurrence (Drossel and Schwabl, 1992, 1993; Grassberger, 1993; Clar, Drossel and Schwabl, 1994), and this model become the new generation base model (see Figure 3.4). This model captured the criticality behaviour for a certain conditions of parameters (i.e., very small lightning frequency per tree growth probability). The *forest fire* model was generalised by introducing immune trees (Drossel and Schwabl, 1993; Pruessner and Jensen, 2002). These immune trees resemble the concept of bond percolation in which flammable cells do not burn deterministically when making contact with burning cells, and instead they burn with a specific probability. However, Pruessner and Jensen (2002) investigated the behaviour of the cluster size distribution in this generalised model and revealed that the model is not critical in the sense that there is no pair of variables in the system correlate with power law relationship. Therefore, the immune trees concept was not used extensively in criticality studies.

There have been many attempts to improve the *forest fire* model for finding more reasonable critical exponents. The first improvement was by simulating the *forest fire* model with high statistics of domain variation (e.g., grid size) and very close to the critical point (Grassberger, 1993, 2002). The critical exponents found were significantly different from the base models (Bak, Chen and Tang, 1990; Drossel and Schwabl, 1992), and the implementation of these new exponents improved the critical behaviour of the model (Grassberger, 1993, 2002). The second improvement involved simulating the *forest fire* model in square and triangular cell from one to eight dimension domain (see Table 3.1; Clar, Drossel and Schwabl, 1994). This model, which found different critical exponents, was reported to perform better than the base models (Bak, Chen and Tang, 1990; Drossel and Schwabl, 1992), near the critical points (Clar, Drossel and Schwabl, 1994). The third improvement involved introducing corrections factor to the critical exponents (Pastor-Satorras and Vespignani, 2000). These correction factors were derived based on the extended version of moment analysis technique (see detail in Pastor-Satorras and Vespignani, 2000). The last non-marginal improvement was by considering the finite size

effect on the criticality of the model (Schenk *et al.*, 2000; Schenk, Drossel and Schwabl, 2002). The finite size effect was implemented by reducing the grid size. From tree density and fire size distributions evaluation it was revealed that the critical exponents change when the grid size decreases, if the other input parameters are kept constant (Schenk *et al.*, 2000; Schenk, Drossel and Schwabl, 2002).

Although *forest fire* model is a "*toy*" model, this model has been compared with real historical wildfires (Malamud, Morein and Turcotte, 1998). This study found a good agreement between the correlation of fire size and frequency in the simulations with the same correlation obtained from the data in around 5000 wildfires in the United States and Alaska, thus, this study bridges the theoretical behaviour of criticality in wildfires with real historical wildfires. They used thousands of historical wildfires to compare with the *forest fire* model and found that the power law correlation between occurrence frequency and size of wildfires in the model has good agreement with real historical wildfires (Malamud, Morein and Turcotte, 1998).

The criticality in traditional *forest fire* model could be achieved when certain conditions are met, for example, very small lightning frequency per tree growth probability. However, Graham and Matthai (2003) argued that by using small world network, the criticality of *forest fire* model can be achieved without fine tuning of the parameters. This result was achieved by using multi-range neighbourhood (see Table 3.1), where the neighbourhood is not limited to immediate adjacent cells but randomly selected cells, which mostly are distant (see Figure 3.3b; Graham and Matthai, 2003).

3.5. Cellular Automata for Urban and Building Fires

When wildfires occur in wildland urban interface (WUI) regions, they can spread to urban areas and cause urban fires (Spyratos, Bourgeron and Ghil, 2007). Urban fires are fire hazards that occur in the populated areas, which spread from one building to another building and feed on flammable materials in the buildings and houses (e.g., furniture). This fire has different behaviour to wildfire because urban areas have different fuel configurations and structures from the vegetation in the forest.

Bond percolation was the main concept used to simulate urban fires, which has been validated using real historical fires (see Table 3.2; Takizawa *et al.*, 2000; Cousins, Heron and Mazzoni, 2002; Ohgai *et al.*, 2004; Gohnai *et al.*, 2005; Wang and Zhou, 2014). The spread probability in the CA model for simulating urban fires mainly depends on wind effect and fuel properties (see Table 3.2; Ohgai *et al.*, 2004; Gohnai *et al.*, 2005; Zhao, 2011; Wang and Zhou, 2014; Tambunan, Salamah and Asriana, 2017). The wind affects the probability through both wind speed and direction (Wang and Zhou, 2014), whereas

fuel properties accommodate the effect of building structure and materials into the probability (Tambunan, Salamah and Asriana, 2017). The factors that affect the spread probability were extended to cover stages of the fire (Ohgai *et al.*, 2004; Gohnai *et al.*, 2005; Wang and Zhou, 2014). The ability of fire to spread to the neighbours depends on the stage of fire, for instance, a cell which has just been ignited has lower ability to spread the fire than a cell which has been burning longer. The stage of fire was typically defined based on the burning time (Ohgai *et al.*, 2004; Gohnai *et al.*, 2005; Wang and Zhou, 2014).

The fact that fire in urban areas spreads in many ways have been addressed by distinguishing the mode of fire spread: direct spread, radiation spread, and spotting spread (Cousins, Heron and Mazzoni, 2002). Direct spread is a deterministic spread to unburned adjacent cells, radiation spread happened when the heat received by the building exceeds a certain threshold, and spotting spread was initiated if there are embers thrown off, probabilistically, from burning cells (Cousins, Heron and Mazzoni, 2002). Firefighting activity (Ohgai *et al.*, 2004; Gohnai *et al.*, 2005) and evacuation attempts (Wang and Zhou, 2014) have also been considered in the urban fire model (see Table 3.2). The model for firefighting activity and evacuation aims to provide planning support for fire mitigation (Ohgai *et al.*, 2004; Gohnai *et al.*, 2005; Wang and Zhou, 2014).

The accuracy improvement for the model of urban fire mainly focused on using different cell shape and neighbourhoods (see Table 3.2). Instead of using regular cell shapes, Zhao (2011) implemented irregular cells in which each cell perfectly matches with the shape of each building in the landscape, thus, there was no cell that combined both building and open spaces such as road. Because of the irregular structure of the grid while using these irregular cells, the neighbourhood of this model was represented by cells covered by an ellipse (Zhao, 2011). The size and shape of this ellipse, depend on the wind speed and direction, thus, the neighbourhood changed during simulation (Zhao, 2011). This wind-constrained neighbourhood was also used in the model of cells with simple geometry (Ohgai *et al.*, 2004; Gohnai *et al.*, 2005). However, the wind-constrained neighbourhood in cells with simple geometry did not have an elliptical shape, although the neighbourhood also did change during simulation according to wind speed and direction (Ohgai *et al.*, 2004; Gohnai *et al.*, 2005). Another improvement for the urban fire model was performed by integrating GIS (Gohnai *et al.*, 2005; Zhao, 2011; Wang and Zhou, 2014), which made the landscape of the urban landscape more realistic.

The main application of the urban fire model was to simulate real urban fire, however, there have been attempt to extend the application of this urban fire model. The first extended application was for loss assessment post urban fire (see Table 2; Cousins,

Heron and Mazzoni, 2002; Zhao, 2011). The assessments considered were economy and loss of life (Cousins, Heron and Mazzoni, 2002; Zhao, 2011). The second extended application was to provide fire risk assessment in urban regions where urban fires have not started (Gohnai *et al.*, 2005; Tambunan, Salamah and Asriana, 2017). This fire risk assessment aims to provide fire safety insights to developers and residents of urban areas (Gohnai *et al.*, 2005; Tambunan, Salamah and Asriana, 2017).

On the other hand, Curiac *et al.* (2010) adopted the urban fire model to simulate fire spread inside a building, while considering fire and smoke interaction. Their model also considered air flows, based on real measurement, in the building. Although aiming for the same goal, Nahom (2016) utilised heat accumulation CA to simulate the spread of fire and smoke inside a building. Both of these works on building fires have reasonable results compared to the real fires. These building fire models are extensions of the urban fire model, since the conventional models of urban fires do not consider the details of fire behaviour inside a building.

3.6. Qualitative Comparisons between Concepts

Each concept used in cellular automata modelling for wildfires has different prominent behaviours that can be visually observed and distinguished. Figure 3.11 presents a qualitative comparison of the expected burnt scar shape when using different concepts for the CA rules. This comparison is based on a simplified case of wildfire, where fuel is homogeneous, terrain is flat, and wind speed and direction are constant. This simplified case is used, rather than the actual case that consider more environmental factors and their spatial and temporal variations, to isolate the effect of using different concepts and minimise the effect of the selection of the parameters in the model. If more environmental factors and their variations are considered, the comparison would be biased, since the difference between the concepts are influenced more significantly by the parameters in the model.

When wind effect is considered, there are three main basic shapes created in deterministic CA, ellipse, ovoid, and deviated ovoid, which correspond to wave propagation, heat accumulation, and linguistic respectively. Wave propagation CA has a basic shape of ellipse because it forces the burnt scar in the simulation to become an ellipse by using a growing ellipse as the rule for state transition. The ellipse is calculated and updated every time-step where cells inside the ellipse change state, therefore, the shape of burnt scar is ellipsoid. Although heat accumulation CA involves ellipse calculation to determine the spread rate at every direction, the limited number of spread directions in this model (i.e., only to North, South, West, East, Northeast, Northwest,

Southeast, and Southwest neighbouring cells) causes the burnt scar in heat accumulation CA become ovoid. This ovoid shape complies with the rules implemented in heat accumulation CA where the downwind spread is the fastest, and upwind is the slowest similar to those of the ellipse shape. However, the 1st order neighbourhood of a square cell is insufficient to shape the burnt scar into an ellipse. Linguistic CA also have ovoid shape of burnt scar, however, this ovoid shape slightly deviates from the ovoid in heat accumulation CA. This deviation stems from the rule of a cell with multi-states which is the main idea of fuzzy logic that is used in linguistic CA. Without fuzzy logic, the burnt scar in linguistic CA will have lower deviation from ovoid, however, the shape becomes stiffer, for example, having many sharp corners. When the wind effect is not considered, all deterministic CA produce a circle shape of burnt scar (see discrete physical events in Figure 3.11 as an example). However, wind effect has never been considered in discrete physical events CA, therefore, a circle shape of burnt scar is the only shape has been produced by this concept in previous works.

The main difference between the results from deterministic and stochastic CA is the shape of the fire front. The fire front shape of a deterministic CA model is relatively smooth, whereas a stochastic CA model results in a non-smooth front (see Figure 3.11). The probabilities involved in stochastic CA models cause uncertainty of propagation of the fire which leads to this non-smoothness feature. Non-smoothness can be treated as either inaccuracy or nature variability consideration depending on the aims of the modelling. In stochastic CA, different concepts are used for different purposes, therefore, causing significantly different results. The results of bond percolation CA are the closest to the deterministic CA models. Although fractal geometry can be observed at the fire front (non-smooth fire front), the shape of the results from bond percolation CA resemble an Euclidean shape such as circle, ellipse, and ovoid, which are also found in deterministic CA. On the other hand, the fractal geometry in diffusion limited aggregation and site percolation CA become very dominant and the Euclidean shape in these concepts is untraceable (see Figure 3.11). This result stems from the limited movement in the models because of the spread direction restriction for diffusion limited aggregation, and the presence of randomly distributed non-flammable cells for site percolation. Therefore, while the non-smoothness also present in the fire front of these models, the shape of burnt scar in these models do not resemble an Euclidean shape. Meanwhile, compared to diffusion limited aggregation, site percolation also has fractal structure in addition to a fractal shape. The fractal structure corresponds to the multiple geometry present in the domain without a traceable pattern. This fractal structure stems from the multiple

ignition involved in site percolation CA, which are also executed at random locations and times. Therefore, the models in stochastic CA category can be divided based on the level of fractal involved: bond percolation with only fractal fire front but non-fractal shape and structure; diffusion limited aggregation with fractal fire front and shape but non-fractal structure; and site percolation with fractal fire front, shape, and structure. The stochastic part in Figure 3.11 is ordered based on this distinction.

Most of CA models for wildfires only consider two states: unburned and burnt out, which means the other states are neglected and the burning state is instantaneous (it changes to burnt state after one time-step). However, discrete physical events and linguistic CA models have considered more states. Discrete physical events CA consider more states to comply with physical phenomena, therefore, the additional states represent physical states such as drying, pyrolysis, and oxidation (burning). Each state has recursive behaviour where it remain in the same state for more than one time-step. Linguistic CA also considers this recursive behaviour of the states. However, in contrast to discrete physical events, linguistic CA considers additional states which represent the strength of the fire. Within burning states, the fire is categorised as either weak, moderate, or strong, which are determined using *if-then* premise.

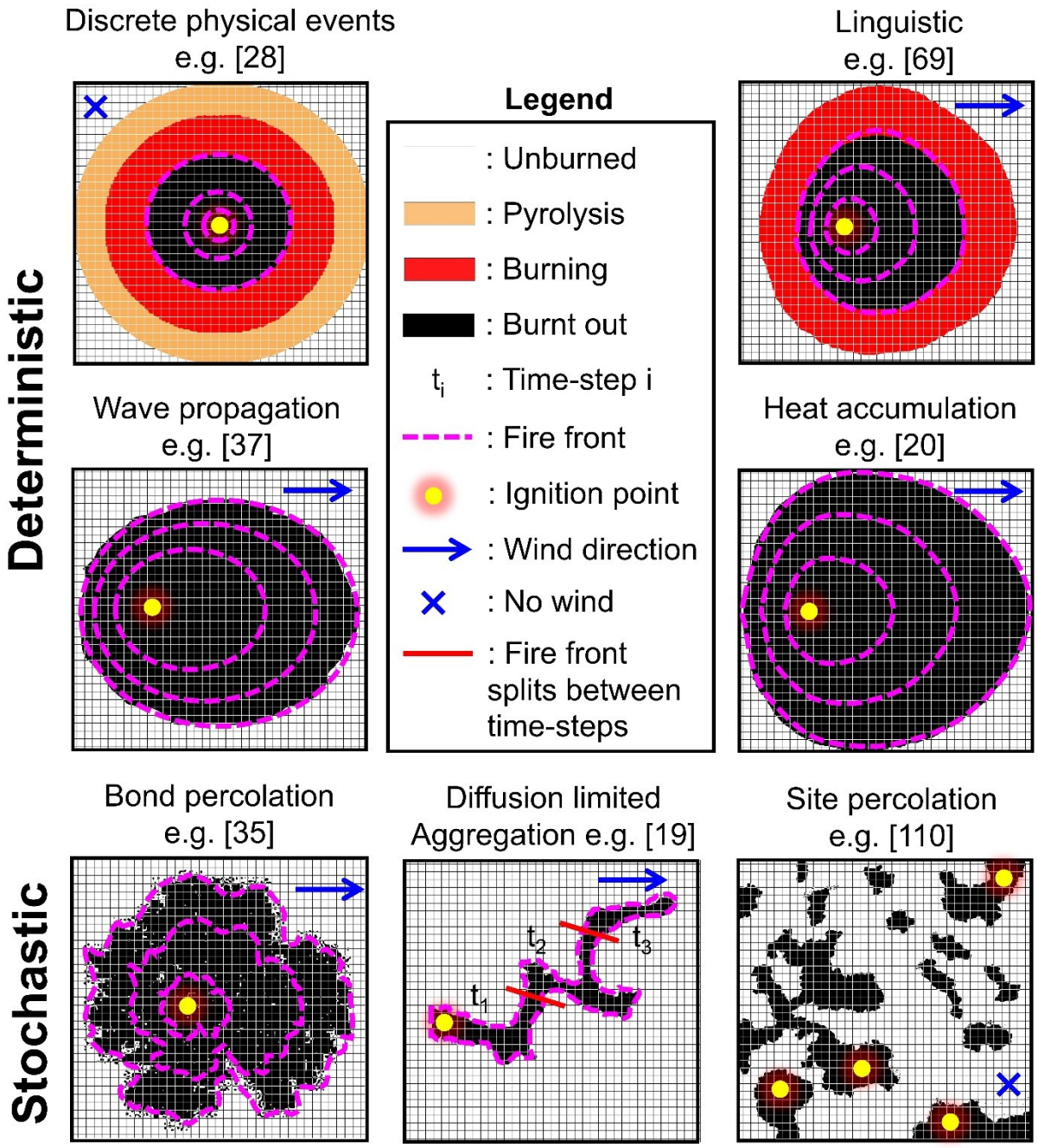

Figure 3.11. Examples of simulation results from cellular automata models with different concepts. The case simulated in this figure is the same between different concepts, a flat and homogenous landscape. Wind condition is considered in most concepts except discrete physical events and site percolation which have no previous works that consider wind. A single ignition is used in most concepts except site percolation which has simultaneous multiple ignitions to study criticality. The fire front at different time-steps in diffusion limited aggregation is distinguished with a fire front splitter to increase clarity of figure. In site percolation, fire front is not drawn due to the complexity of the pattern caused by the multiple ignitions. Different number of regions in different concepts follow regions declared in previous works.

3.7. Gaps in the Literatures

Cellular automata modelling for wildfire has had over 50 years of development, however, there is still incomplete understanding of the phenomena involved, and its development has become marginal in recent years. Three main areas remain insufficiently covered in state-of-the-art of cellular automata modelling for wildfires: emerging phenomena during wildfire, multi regime wildfires, and comparison between models for wildfires. A summary of gaps in these three areas is shown in Figure 3.12. This section discusses the most recent development of each area, the gaps exist, and the direction of future research.

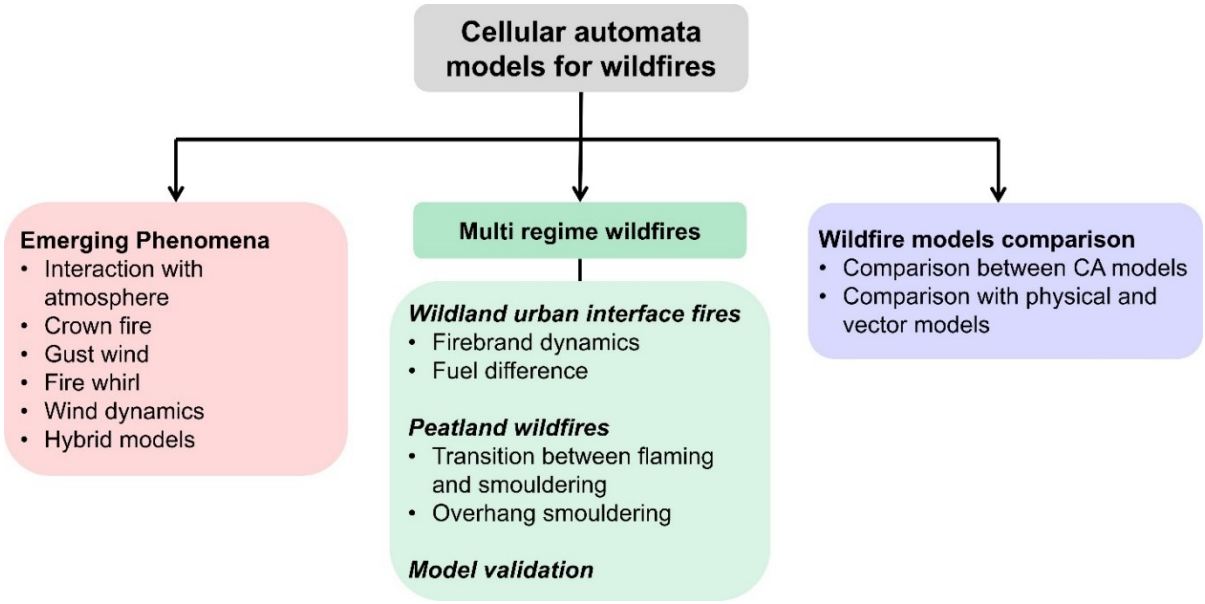

Figure 3.12. Schematic of gaps in cellular automata modelling for wildfires.

3.7.1. Modelling of emerging phenomena during wildfire

During wildfire, numerous physical phenomena can emerge and interact with each other. This interaction can happen across entities, for example, fire-atmosphere and smoke-fire interaction (Clarke, Brass and Riggan, 1994). Fire-atmosphere interaction represents the local wind field which is affected by the fire, and consequently, this local wind affects the fire, e.g., the vortices of the wind which are caused by fire dynamics (Alexandridis *et al.*, 2008; Sullivan, 2009a, 2009c) which then can lead to fire whirl of the fire. These vortices can also be caused by the topography of the landscape (Russo, Vakalis and Siettos, 2013). Meanwhile, smoke that contributes to preheating the fuel can also affect the fire dynamics during wildfires (Clarke, Brass and Riggan, 1994). Despite these important aspects, there is no cellular automata modelling for wildfires that address them.

Available models have indeed addressed many phenomena such as environmental effects (e.g., wind, topography, fuel characteristic), spotting, crown fire (Ito, 2005;

D'Ambrosio *et al.*, 2006; Alexandridis *et al.*, 2008), and fire-atmosphere interaction (Sullivan and Knight, 2004; Achtemeier, 2013). However, these consideration were insufficient, especially when interaction between phenomena are involved. This insufficiency lies in the variability, such as wind field variability and gusty wind (Alexandridis *et al.*, 2008), and insufficient knowledge, for example, of the crown fire behaviour which in Ito (2005) and D'Ambrosio *et al.* (2006) was modelled based on threshold, and therefore, was insufficiently understood (Perry, 1998). Complete understanding of these phenomena could improve the accuracy and ability of the model significantly.

Introducing more physical phenomena to the model needs to adopt physical approach even more. This issue could be tackled by integrating physical model to cellular automata, for instance to model the wind dynamics (Alexandridis *et al.*, 2008). However, implementing physical model to the CA introduces two issues: the selection of the values of additional physical parameters and the significant increase of the computational burden, which need further efficiency improvement such as using parallel computing (Russo, Vakalis and Siettos, 2013). For the parametrisation issue, to avoid the compensation effect, high accuracy achieved since the error of different criteria are cancelling each other, sufficient experiments are required for selecting the optimum values of few additional physical parameters. Once the values of these parameters are sufficiently analysed based on the experiments, the other additional parameters can be determined with a lower level of uncertainty. For the computational cost issue, discrete physical events can become alternative, however, the models using this concept have not advanced to that level of complexity (Muzy *et al.*, 2002, 2003, 2005a; Collin, Bernardin and Sero-Guillaume, 2011). Therefore, the remaining challenges are to consider more physical phenomena as well as their interaction in cellular automata modelling, while ensuring a reasonable uncertainty due to parametrisation and computational feasibility.

3.7.2. Modelling of multi regime wildfires

Wildfires cause other fire hazards when these fires emerge at certain regions: WUI fires and smouldering peatland wildfires. At the interface of wildland and urban areas (see Figure 3.1), the embers that are created by the wildfires (firebrand) could be sent into the urban areas and initiate urban fires (see Chapter 3.5). Urban fires could also be initiated when there is no firebreak between wildland and urban regions, and the flame from wildfires make a direct contact with houses and burn them. On the other hand, if wildfires occur in peatlands, the fire from surface vegetation can ignite organic soil (peat) and cause smouldering wildfires.

Only two CA models (Spyratos, Bourgeron and Ghil, 2007; Li, Cova and Dennison, 2019) have considered WUI fires and no CA model has considered peatland wildfires, other those developed in this thesis (see Chapter 1). The WUI fires are very complex phenomena since an understanding of fire behaviour in both wildland and residence are required (see Figure 3.1). While the environmental and weather factors are still present for wildfire modelling, additional considerations of fuel characteristics (e.g., houses) in urban areas and spread within urban areas where there are many fuel discontinuities (e.g., open spaces) significantly increase the modelling complexity. The initiation of urban fires from wildland fires either via firebrand or flame contact also leads to additional complexity. Firebrand dynamics, although discussed in some works, remains a scientific challenge to date (Rein and Huang, 2021). Spyratos, Bourgeron and Ghil (2007) developed a "toy" model to characterise the fire risk on WUI development, whereas Li, Cova and Dennison (2019) utilised GIS and considered the evacuation in a WUI fire event; however, neither compared these with real fires in either forest or urban sites. Independently, cellular automata models for both wildland fires, e.g., Alexandridis *et al.* (2008) and Freire and Dacamara (2019), and urban fires, e.g., Ohgai *et al.* (2004) and Zhao (2011), have considered a comparison with real historical fires, however, the integration of both validated models that represent fires in WUI regions have not been developed. Neither works considered the dynamics of the firebrand that initiate urban fires, and the fuel configuration and the involved phenomena were insufficiently considered. This gap is becoming more urgent as there have been increasing WUI incidents over the years, for example, WUI fire in California (Bump, 2018). Sufficient knowledge from filling this gap could improve land management an urban planning to make the WUI regions safer from fire.

3.7.3. Generalization of suitable case-dependent model

In cellular automata modelling for wildfires, seven concepts have been developed, however, apart from site percolation which is suitable for simulating criticality of wildfires (Malamud, Morein and Turcotte, 1998), there is no generalization of which concept should be used for a specific case. For example, a suitable concept to simulate lab-scale experiments might be different from a suitable concept to simulate field-scale wildfires. This suitability can be focused on the accuracy of simulation and the computational efficiency of the model (Pastor *et al.*, 2003). A concept which peaks in both accuracy and efficiency for a certain case should be selected instead of other concepts. By wisely selecting the concept, the model can accurately simulate fires with adequate level of details, however, this model will not suffer from a high computational cost. For instance,

when comparing DEVs-CA and wave propagation which are both deterministic, DEVs-CA is more suitable for simulating lab-scale experiment where more detailed phenomena can be captured with a high level of accuracy, whereas the more efficient wave propagation is more suitable for field-scale wildfires where marginal phenomena can be neglected.

Expanding the comparison of cellular automata model for wildfires, another comparison can also be performed to include physical models and vector techniques. The physical models which have the highest level of detail can lie in the other end of cellular automata where the DEVs-CA is the closest. Between DEVs-CA and physical models there are significant gaps that can be considered as gradual simplifications of physical models. Once the comparison include physical models, more choices of the model, thus the level of detail of phenomena can be captured, are available. On the other hand, including the vector techniques in the comparison expands the usage over discrete and continuous models. The selection then can be made between continuous vector-based models and discrete raster-based models, which currently are still competing over one another without systematic performance comparison and generalisation.

Of the gaps presented in this chapter, the modelling of WUI fires has the highest priority to be considered. As communities continue to expand into rural, fire-prone areas, wildfires are responsible for an increasing amount of damage and destruction to property and life. For instance, over the last decade, wildfires in California have been responsible for damaging or destroying thousands of structures and killing hundreds of people, and the frequency of such WUI fire is expected to increase (Bump, 2018). This exacerbates a growing housing crisis and continues to threaten the health and safety of residents. Study on crown fires are the second most important gap to consider, due to their significant hazards, such as their high power and spread rate (Ito, 2005). Other gaps to consider after these two gaps are peatland wildfire, which has significant negative effect on the climate change, the detail phenomena in the event of wildfires such as firebrand, fire-whirl, and gust wind, and the generalization of the models, in that order.

3.8. Conclusions

This chapter reviewed the development of cellular automata modelling for wildfires and elaborated on the seven different concepts used. The developments which are emphasized in this review focus on the phenomena covered in the model, methods to improve the accuracy, and the extended applications of the model. Each concept has different characteristics and inherent benefits and shortcomings which have been implemented in a range of applications and across scales. However, the use of each

concept has not been generalised to draw its optimum potential. This generalisation could specify the most suitable concept for a particular case, and create optimal results, for example, by balancing accuracy and computational efficiency. Emphasizing the role of cellular automata modelling among physical models and vector-based models is also of importance to fit cellular automata into the bigger picture of wildfire modelling.

Cellular automata have modelled many phenomena occurring in wildfires such as crown fire and rain. The consideration of environment, fuel, and weather conditions have also become common practices in the modelling. However, the number of phenomena that have been considered are limited compared to the number of phenomena emerging in real wildfires. This gap is due to the significant number of emerging phenomena during wildfires which needs to consider the interaction between entities, e.g., fire and atmosphere interaction, which then lead to a complex behaviour such as fire whirl. The fact that wildfires are not always isolated incidents means such fires becomes multi-regime wildfires (WUI fires and peatland wildfires). Therefore, the interactions between wildfire and other fire hazards are important fields to explore. Of these gaps, the models for WUI fires are of utmost importance, due to the casualties it causes and the increase in such fires over the years. These gaps lead to the requirement of greater computational resources. However, the computational efficiency of these models should be maintained because this benefit is one of the main benefit of using cellular automata. Therefore, the challenge of increasing the complexity of the model without significantly compensating with computational efficiency remains for future studies. The discussion and recommendation on the potential solutions for the existing gaps in cellular automata modelling for wildfires in this review, provide fundamental and practical knowledge and direction of research in cellular automata modelling for wildfires.

Chapter 4 – BARA: Cellular Automata Simulation of the Three Dimensional Spread of Smouldering Peat with Horizontally Heterogeneous Moisture

Summary[3]

In this chapter, a cellular automata model was developed (BARA) to simulate 3-D smouldering spread in peat with horizontally heterogeneous MC in both laboratory and large scale domains. BARA was developed based on heat accumulation and bond percolation approaches (see Chapter 3). In BARA, a novel method was implemented to introduce the third spread component, in-depth spread, in addition to the 2-D horizontal spread in previous works. BARA was calibrated (within 10% error), and blind predicted complex phenomena such as encirclement of wet peat and fire front merging in the laboratory scale simulation, due to the changes of fire front shape and spread direction that depend on the peat moisture profile. In the large scale simulation, BARA showed how smouldering burns the dry peat while avoids the wet one, creating unburnt patches. The model also showed that a horizontal layer of wet peat with sufficient width and moisture can discontinue the smouldering spread, minimising the burnt area. This chapter provides the knowledge on the smouldering behaviour in realistic conditions, knowledge that can be used to locate smouldering front and assess the vulnerability of peatlands based on its peat moisture distribution, to help mitigating peatland wildfires.

4.1. The Development of BARA

4.1.1. Introduction to BARA

In this chapter, a cellular automata model was developed to simulate 3-D smouldering spread in peat with horizontally heterogeneous MC for the first time. Although the model is not a 3-D model in its full essence, the model can capture the 3-D spread of smouldering peat: 2-D horizontal spread and 1-D in-depth spread. The

[3] This chapter is based on "Dwi M J Purnomo, Eirik G Christensen, Nieves Fernandez-Anez, Guillermo Rein, 2022. BARA: Three Dimensional Simulation of Smouldering Fire of Peat with Horizontally Heterogeneous Moisture. *International Journal of Wildland Fire*, (submitted)."

advancement of the model to be a true 3-D model is possible, however, its computational cost will increase significantly, especially at the field-scale, which is not the aim of this thesis. The model developed here integrates a heat accumulation approach to model heat transfer and a bond percolation approach to introduce the uncertainty (see Chapter 3), adapting Fernandez-Anez *et al.* (2019). The heat accumulation approach mimics heat transfer from burning fuel to unburned fuel, which governs the fire spread, whereas bond percolation introduces uncertainty in the model that is related to the variability of nature, for example, caused by landscape heterogeneity. In the model, the intrinsic values (see Chapter 3) of the cells are updated every time-step based on the intrinsic values of their neighbours, and the state of the cells are updated stochastically (with a probability less than one), when their intrinsic values exceed predetermined thresholds. The simplest neighbourhood for CA, a von Neumann neighbourhood, was used, which includes the four adjacent cells: North (N), South (S), West (W), and East (E); of the centre cell (see Figure 3.3a). From here on, the model in this chapter is referred as BARA, which originates from 'smouldering' in Indonesian language.

4.1.2. States and rules of BARA

BARA considers 3 states: *peat (P), smouldering (S), and burnt out (B)*. These states represent the simplified structure of smouldering fires. In physical terms, the *peat* state represents undisturbed peat that can transition to the *smouldering* state where the peat is burning. Once the full depth of the peat is consumed, the *smouldering* extinguishes and the cell transitions to *burnt out* state. Each cell in BARA has an intrinsic value, which in this work will be referred to as a heat value (U), analogous to temperature in physical terms. The information of states and heat values of cells are stored in two different computational layers: the fuel layer and the heat layer, adapting Fernandez-Anez *et al.*, (2019). This multi-layer approach enables BARA to replicate the physics of combustion. The fuel layer mimics the evolution of fuel during the combustion process (e.g., unburned fuel, oxidation), whereas the heat layer accommodates the heat dynamics of combustion processes that are commonly observed based on temperature distribution.

The transition from *peat* to *smouldering* state depends on the U of the cell: when the U of a *peat* cell exceeds a burning threshold (Θ), the *peat* cell transitions to *smouldering* with a probability of P_s (smouldering probability). The U of each cell is affected by the sum of U transferred (U_t) to or from its neighbouring cells (n). If U_t is greater than zero, then the heat is transferred to the neighbours, otherwise, the heat is transferred from the neighbours to the centre cell. The value of U_t depends on the difference of U between centre (i) and neighbouring cells, the number of cells separating

the two cells (l), and heat transfer coefficient (φ) as shown in Eq. 4.1 (see detail in Appendix Chapter 4B). l was used in the formulation of U_{t}, instead of the physical distance between two cells (in mm), since this refer to the discretized domain of BARA, where the smallest length quantity in BARA is one cell (i.e., l is integer). φ determines the fraction of ΔU transferred to or from neighbour cells that imitates the heat transfer coefficient in physical terms, however, its value was simplified and translated to BARA domain. These heat transfer dynamics depend on the neighbouring cells involved in the process, therefore, ΔU, l, and φ differ between neighbours. However, since the neighbourhood selected was von Neumann that only contains the four adjacent cells, $l_{\mathrm{i-n}}$ in the model is constant i.e., one cell.

$$U_{\mathrm{t}} = \varphi_{\mathrm{n}} \cdot \frac{\Delta U_{\mathrm{i-n}}}{l_{\mathrm{i-n}}} \tag{4.1}$$

Heat loss to the surroundings (top boundary condition) is also considered in BARA, which depends on the difference between the U of a cell with U of the ambient (U_{o}) and heat loss coefficient (μ). U_{o} is held constant at zero, for simplification purposes, as in nature, ambient condition varies daily and seasonally. At every time-step, some amount of heat value (μU) from each cell is lost to the surroundings, representing the heat loss due to convection and radiation. Although μ depends on many variables (e.g., convective and radiative heat transfer coefficient, peat temperature), μ is set to be constant for simplicity. Meanwhile, at the bottom of cell i, it is assumed to be without interaction, which is analogous to adiabatic in physical term. These heat dynamics rules are summarized in Figure 4.1a. BARA adapts the concepts used in Fernandez-Anez *et al.* (2019) with reduction of the number of states to increase the computational efficiency.

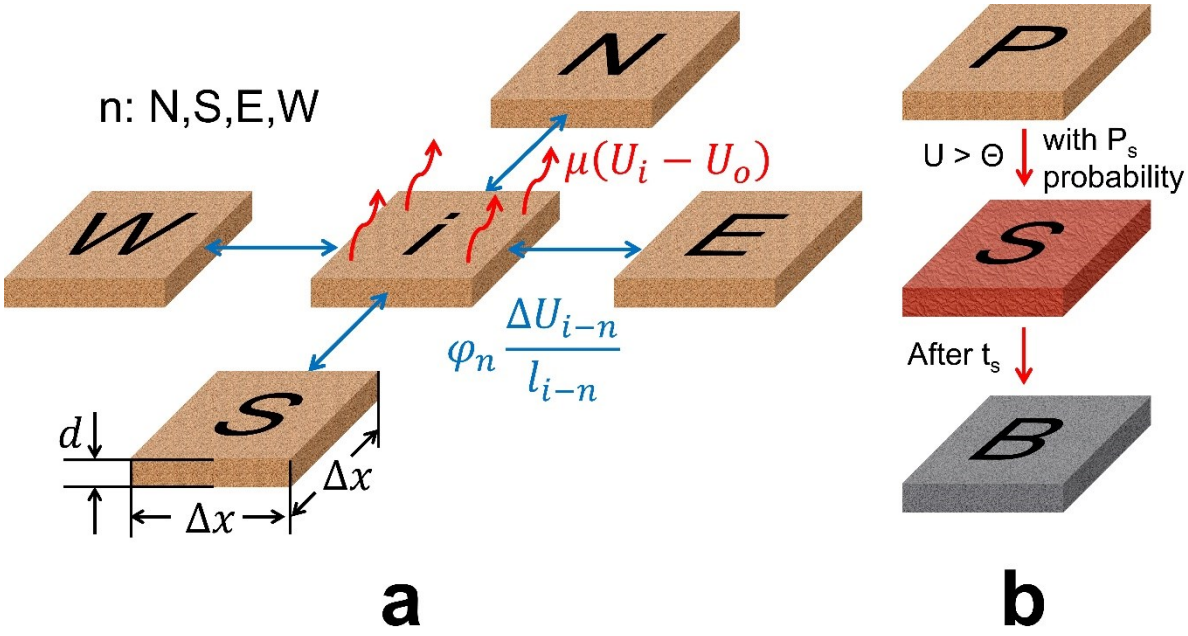

Figure 4.1. (a) The schematic of the rules in BARA. The subscripts (n) represent the neighbours position relative to the centre cell (i), i.e., North (N), South (S), East (E), and West (W). The double-edge arrows represent that the flow could be reciprocal. The red arrows represent the heat loss to surrounding. (b) The schematic of the state change in BARA from peat (P) to smouldering (S) to burnt out (B). The state change from peat to smouldering occur when U exceeds Θ with a probability of P_s. Smouldering cells remain in that state until t_s when they become burnt out.

In BARA, a novel method was implemented to introduce the in-depth spread, in addition to the 2-D horizontal spread in previous works (Fernandez-Anez *et al.*, 2019). In Figure 4.1a, the thickness of the peat (d) decreases with time during fire due to the in-depth spread that consumes the peat vertically. One cell of peat contains inorganic and organic matter, water, and air (see Figure 4.2). Every time-step, when a cell is smouldering, the organic fraction of the cell with a thickness of δ is consumed by the fire. The fire completely consumes one cell of peat when the total of δ is equal to d. This phenomenon is modelled by using a smouldering time variable (t_s). Once the *peat* cells become *smouldering*, the cells remain burning for a certain t_s (i.e., $d = \delta t_s$). This recursive behaviour of the *smouldering* state mimics the in-depth spread of smouldering peat where in the top view of the landscape the area is still smouldering although the leading edge (smouldering front) has become relatively distant from the trailing edge.

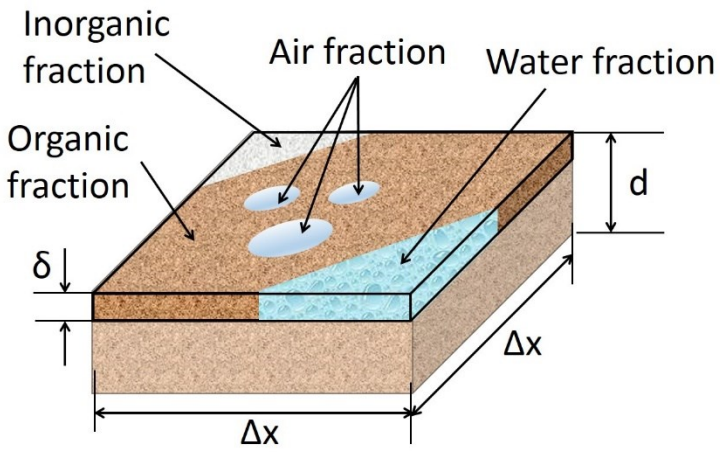

Figure 4.2. The details of the components present in one cell in BARA. Each cell in the model contains inorganic, organic, water, and air components. In every time-step in the smouldering cells, peat with a thickness of δ is consumed by the fire.

During t_s, the *smouldering* cells generate heat of Q_R (heat release rate) in every time-step, increasing their U, reproducing the heat generation phenomenon of a combustion process. In physical terms, heat generation depends on the time after ignition, which follows the Arrhenius law. However, for simplicity, Q_R is set to be constant at any time (i.e., constant from the ignition until t_s), only depending on peat properties (e.g., organic density). The *smouldering* cells become *burnt out* after t_s is reached. This *burnt-out* state represents that the peat is completely consumed by the fire (see Figure 4.1b). In the borders of the domain (edge regions), the cells are treated as non-flammable cells, thus, it can be considered as heat sinks, where the heat is transferred to the borders but the borders do not ignite

4.1.3. Sensitivity analysis

The variables used in BARA were selected based on calibration against experiments. However, prior to this calibration, sensitivity analysis was performed on BARA to determine the range of values of the model's variables. The sensitivity analysis was performed by exploring different combination of values of the variables in the model (P_s, φ, Q_R, t_s, Θ, and μ), which make BARA prediction concur with the experimental results. The results from the experiments of Christensen, Fernandez-Anez and Rein (2020) showed that the smouldering spread have circular ring pattern when the fire is ignited at the centre of a shallow reactor and spread radially, thus, the expected results from the sensitivity analysis are the predictions that have circular ring patterns. An exclusion is considered to the values of variables that make BARA predictions have significantly deviated shapes from circular ring, e.g., polygon as shown in Figure S4.1.

Therefore, from this exclusion, the range of values of variables in BARA are narrowed, leading to targeted and quicker calibration processes, and the calibration process becomes quicker since the search space becomes narrower.

Both the sensitivity analysis and calibration were undertaken in a 400 × 400 cells grid, where the cell size (Δx) is 1 mm and d is 1.6 cm (see Figure 4.1a). This domain follows the reactor size of the experiments used for calibration (40 cm × 40 cm × 1.6 cm; Christensen, Fernandez-Anez and Rein, 2020), whereas the cell size was selected because the results converged when the domain resolution is higher (see Figure 4.3). One time-step (Δt) in BARA resembles 20 s in real time, which is selected to satisfy the stability criteria given the spatial resolution (Δx). The stability criteria in this thesis follow Courant–Friedrichs–Lewy conditions, which limits the cell size and time-step to avoid the diffusion of an entity exceeding one cell at one time-step. By using this domain, BARA is tested to simulate smouldering experiments with ignition in the centre of the domain and the smouldering spreads radially.

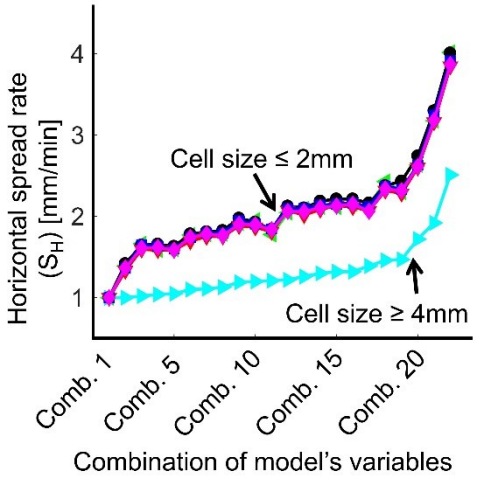

Figure 4.3. Results from the BARA sensitivity analysis at different cell sizes. The model with different cell sizes was run by using different combination of model's variables. Within one combination of model's variables, the variation of horizontal spread rate (S_H) is insignificant, once the cell size is less than 2 mm. From this analysis cell size (Δx) of 1 mm is used in BARA.

Since there are six variables in the model (P_s, φ, Q_R, t_s, Θ, and μ), the ideal sensitivity analysis can be conducted by using many different combinations of the six variables. However, to speed up the sensitivity analysis, the variables were split into four groups of combinations of three variables. Therefore, the sensitivity analysis was done only with the combination of only three variables (instead of six), setting the other three variables as constant, and this approach was performed four times (for the other three variables one by one). The variables were grouped as follows: group 1 (P_s, φ, and Θ); group

2 (Q_R, φ, and Θ); group 3 (t_s, φ, and Θ); and group 4 (μ, φ, and Θ); in which within each group, different combinations of values of the three variables were explored, while keeping the other three variables outside the group constant. The members of each group were selected based on initial sensitivity analysis where the combinations of the six variables in BARA (P_s, φ, Q_R, t_s, Θ, and μ) were explored, but with significantly rougher intervals. From this initial sensitivity analysis, P_s, Q_R, t_s, and μ have little dependency to one another, but these variables highly depend on φ and Θ. This dependency corresponds to the compliance of the simulation results with experiments, when the value of a variable changes. For instance, to maintain the spread rate accuracy of BARA against the experiment, when t_s changes, Q_R does not significantly change, but when φ or Θ changes, Q_R changes significantly.

From the sensitivity analysis of group 1 (see Figure S4.2), increasing P_s could make BARA fails to produce similar shape with the experiments, whereas decreasing P_s could make the smouldering fails to be self-sustained, thus, the range of which P_s is plausible, is narrow. P_s was then selected to be 0.1, and set to be a control variable, i.e., constant throughout this chapter.

From the sensitivity analysis of group 2 (see Figure 4.4), the range of φ that enables BARA to give expected results are from 0.05 to 0.2. With φ lower than this range caused the smouldering to be non self-sustained, whereas higher value of φ caused the shape to be inaccurate. This reasoning was also adopted to determine the range of Θ, which was found to be 0.01 to 0.2. With constant φ and Θ, the increase of Q_R increases the horizontal spread rate (S_H) without violating the 'expected result' criteria, thus, wide range of different values of horizontal spread rate can be simulated by BARA. This capability is required by the model to be able simulate all the horizontal spread rate in Christensen, Fernandez-Anez and Rein (2020) in the calibration process. As shown in Figure 4.4, to fully capture the range of horizontal spread rate in the experiments, Q_R was varied with the minimum value of one. Therefore, during calibration process, the minimum value of Q_R was set to be one while the upper limit of Q_R was not specified.

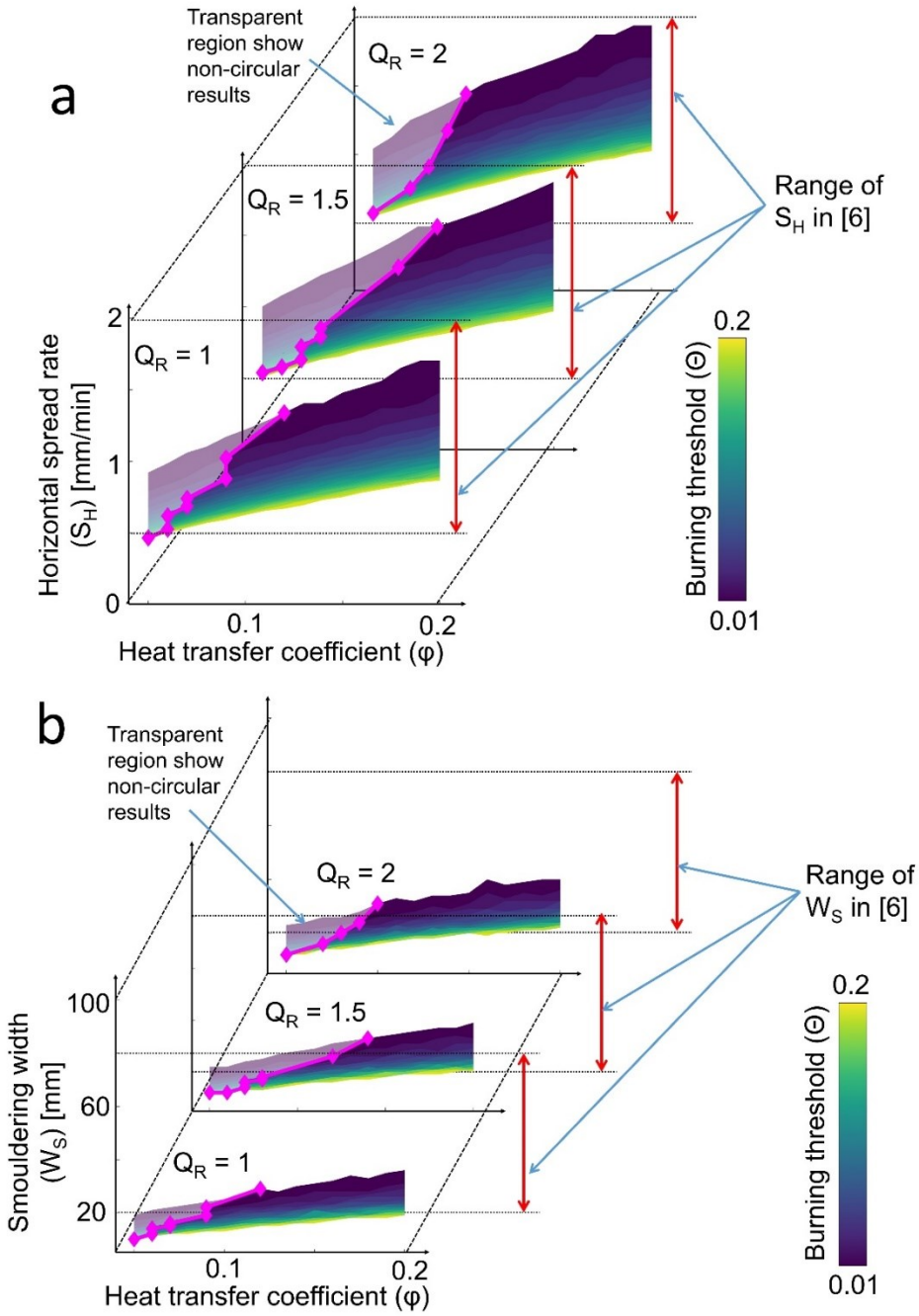

Figure 4.4. Sensitivity analysis of Q_R on different Θ and φ based on (a) horizontal spread rate and (b) smouldering width. The magenta lines represent the boundary between the circular (non-transparent) and non-circular (transparent) shapes from the simulation results.

However, none of the combinations of variables in group 2 successfully simulate all the smouldering width (W_S) in the experiments of Christensen, Fernandez-Anez and Rein, (2020). Only after t_s, which belong to group 3, was explored, could all the smouldering widths in the experiments be successfully simulated (see Figure 4.5). From these sensitivity analysis, BARA can be used to fit all the experiments conducted in Christensen, Fernandez-Anez and Rein (2020).

From the sensitivity analysis of group 4, μ does not affect the horizontal spread rate or the smouldering width significantly when other variables are constant (within 20% variations), but μ determines the sustainability of the smouldering spread. With a very high μ, the smouldering spread was not self-sustained. However, with $\mu = 0$, there was no significant change to the BARA predictions. Therefore, the range of μ was set to be 0.01 to 0.9. The upper limit of this range was selected based on the value at which the smouldering spread was not self-sustained with a minimum value of Θ and a maximum value of φ, whereas the lower limit was selected to be 0.01 since the distribution of U during simulation with lower μ did not significantly differ.

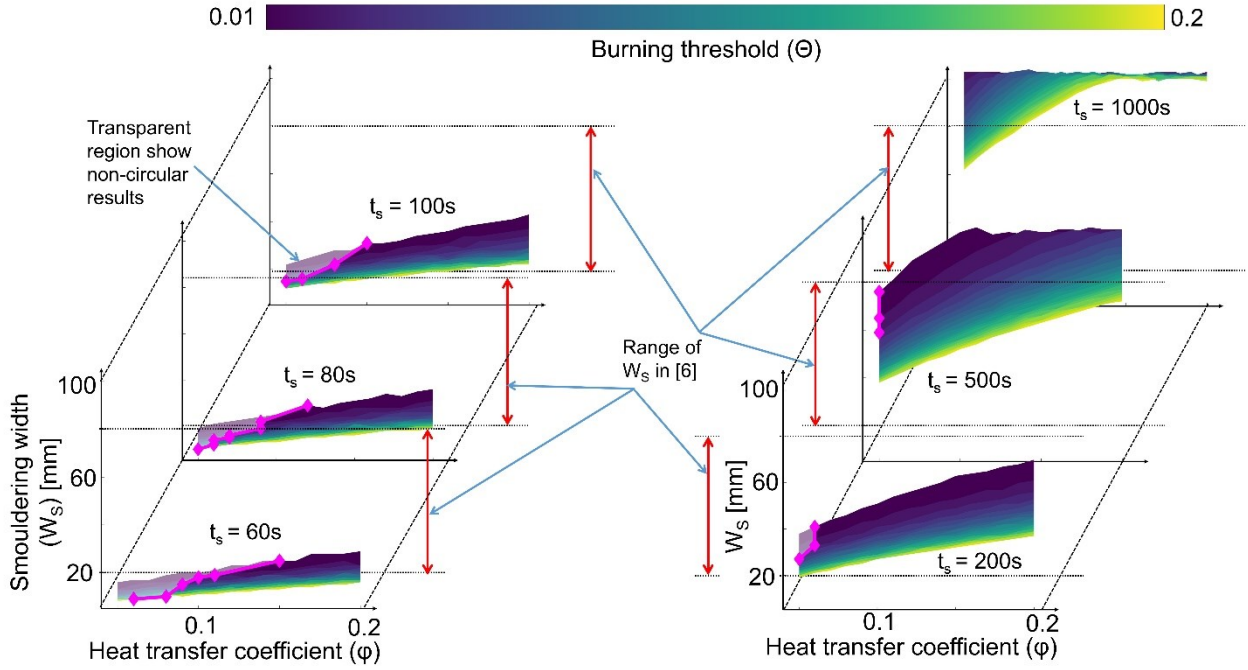

Figure 4.5. Sensitivity analysis of t_s on different Θ and φ based on smouldering width. The magenta lines represent the boundary between the circular (non-transparent) and non-circular (transparent) shapes from the simulation results.

The change of values of variables used in BARA (P_s, φ, Q_R, t_s, Θ, and μ) can be related with the change of physical parameters. In the simulation, with higher φ, the increase of U of cells become faster, which corresponds to the faster increase of temperature when thermal conductivity is higher in physical term. Meanwhile, with higher μ, the net change of U can become negative, thus, the value of U was decreasing instead of increasing, which corresponds to the decrease of temperature when the heat loss is very strong (imagine igniting a sample inside a fridge with initial condition of sample is at room temperature). A higher value of Q_R also causes the acceleration of the increase of U of cells. Although the effect of φ and Q_R is similar, from the rules of BARA

(see Chapter 4.1.2), Q_R corresponds to the heat of combustion in physical term, which also has an effect of accelerating the temperature increase when its value is higher. When Θ is higher, the U of cells cannot reach Θ and smouldering in the simulation does not ignite, thus, this variable corresponds to the temperature of ignition, in which if its value is too high, ignition never happen. A higher value of t_s simply makes the smouldering in the simulation sustain longer, thus, higher t_s means thicker sample. P_s is used to introduce uncertainty and it has no physical interpretation, but P_s is important to simulate the variability in nature.

The ranges of variable values found in this sensitivity analysis are not unique. Significantly different value of one variable can be compensated with different values of other variables to maintain the goodness of the simulation (e.g., maintain the circular ring shape). For instance, if the range of value of Θ or μ is few times higher, the model can prevail its goodness with φ or Q_R that has a range of values few times higher, since in BARA these variables are interconnected, and this has been tested in the initial sensitivity analysis with larger interval. However, once a variable is set, the other variables have certain ranges to maintain the goodness of the model. Therefore, the possibility of ranges of variable values that can be used in BARA become unique and the possibility of values outside these ranges to can be used when a variable has been set is very small.

4.1.4. Calibration of BARA

The variables used in BARA (P_s, φ, Q_R, t_s, Θ, and μ) were calibrated against lab-scale experiments (Frandsen, 1987, 1997; Christensen, Fernandez-Anez and Rein, 2020). Of these variables, P_s is a control variable ($P_s = 0.1$, see Chapter 4.1.3); φ, Q_R, and t_s are variables that depend on peat properties; and Θ and μ are independent variables. This categorization was performed to further simplify the calibration process, i.e., only independent variables are systematically explored within their usable ranges, to make BARA predictions concur with the experiments.

t_s is the time required by the fire, with in-depth spread rate of S_d, to consume the peat vertically in an area equal to the area of one cell, from the surface throughout its thickness (d). Therefore, t_s was formulated as shown in Eq. 4.3 in Table 4.1. In-depth spread rate (S_d) was formulated as shown in Eq. 4.2, based on the relationship established in Christensen (2021), which found a strong correlation between in-depth spread and the inverse of the organic density. Therefore, BARA only requires peat properties as its input variables. Since BARA only needs peat properties data: MC, inorganic content (IC), and bulk density (ρ_b); it can be used to simulate smouldering spread with any peat conditions

(any MC, IC, and ρ_b). In Eq. 4.2, ρ_o is organic density, whereas a_1 (-0.31 mm/min) and a_2 (110.7 kg.mm/m^3.min) are constants in which their values follow Christensen (2021).

$$S_d = a_1 + \frac{a_2}{\rho_o} \quad (4.2)$$

The formulation of Q_R was derived based on the heat generated from combustion of a consumed peat at one time-step with a constant heat generation per unit volume (see Appendix Chapter 4B). Q_R depended on ρ_o and S_d as shown in Eq. 4.4 in Table 4.1, however, Q_R was non-dimensionalized by using a constant (a_3) to translate a physical variable in BARA domain. a_3 was selected to be 0.39 m^{2}s/kg that make the minimum value of Q_R during calibration process is equal to one (see Chapter 4.1.3).

The formulation of φ was derived based on 1-D transient conduction heat transfer, which considers effective thermal conductivity (k_e) that includes the radiative heat transfer across pores, adapting Huang, Rein and Chen (2015) (see Appendix Chapter 4B). φ depended on ρ_b and effective specific heat of inorganic, moisture, and organic content (c) as shown in Eq. 4.5 in Table 4.1. The effective specific heat was formulated as the sum of individual specific heat multiplied by its mass fraction (e.g., for organic content its mass fraction is organic mass per total mass). φ was normalized within the range of 0.05 to 0.2 (see Chapter 4.1.3) by using constants ($a_4 = 0.05$ and $a_5 = 78{,}912$ K/m^{3}J).

Table 4.1. List of variables in BARA with their values and units.

Variable	Value	Unit
Smouldering time (t_s)	$t_s = d/S_d$ (4.3)	s
Heat release rate (Q_R)	$Q_R = a_3 \cdot \rho_o \cdot S_d$ (4.4)	Non-dimensional
Heat transfer coefficient (φ)	$\varphi = a_4 + {}^{a_5}/_{c\rho_b}$ (4.5)	Non-dimensional
Burning threshold (Θ)	0.01 – 0.2	Non-dimensional
Heat loss coefficient (μ)	0.01 – 0.9	Non-dimensional
Smouldering probability (P_s)	0.1	Non-dimensional

Θ was calibrated by systematically explore the value between 0.01 and 0.2 (see Chapter 4.1.3) that enables BARA to replicate the experiments (Christensen, Fernandez-Anez and Rein, 2020) in different conditions, i.e., different MC, IC, and ρ_b. The objective of the calibration of Θ is finding Θ that enables BARA to produce horizontal spread rate and smouldering width that agree with the experiments in Christensen, Fernandez-Anez and Rein (2020) given the dependent variables (φ, Q_R, and t_s).

μ was calibrated by exploring the value between 0.01 and 0.9 (see Chapter 4.1.3) that enables BARA to have critical conditions close to the experiments (Frandsen, 1987, 1997). These critical conditions are conditions (MC and IC) where a slight increase in MC

or IC could lead to non-self-sustained smouldering (Frandsen, 1987, 1997). The summary of the variables in BARA are listed in Table 4.1. Of these variables, only t_s that has dimension because BARA considered the spatial and temporal units, but not the energy unit (due to its complexity).

4.2. Results and Discussions

4.2.1. Calibration results

BARA accurately simulated the experiments of Christensen, Fernandez-Anez and Rein (2020) in all MC, IC, and ρ_b conditions (examples of the comparison are shown in Figure 4.6). Figure 4.7 summarizes the comparison between BARA predictions and experiments based on horizontal spread rate and smouldering width, in which in both results, BARA predictions have good fit against experiments with less than 10% difference. These predictions were obtained by varying the value of Θ, therefore, Figure 4.7 represents the deviation of the calibration of Θ from the experiments. During the calibration of Θ, the value of dependent variables, Q_R, φ, and t_s, were determined by adopting the physical variables, whereas μ was set to be constant, as explained in Chapter 4.1.4. In Figure 4.7, each blue circle represents the comparison of prediction and experiment at one peat condition, whereas the black line represents the predictions which would perfectly match with experiments. Therefore, if the horizontal spread rate or smouldering width from BARA predictions are equal to the values in experiments, the blue circles overlap with the black line. The error bars represent uncertainties in both experiments (x-axis error bar) and predictions (y-axis error bar). The uncertainty in the experiments were obtained by conducting two additional experiments with identical conditions for each condition (Christensen, Fernandez-Anez and Rein, 2020). The uncertainty in the predictions were obtained by repeating the identical simulations ten times, and this uncertainty was insignificant. In term of computational efficiency, BARA can finish one simulation in averagely 3 min for 1 h of smouldering peat simulation, a 20 times faster-than-real-time.

The main sources of errors that make BARA predictions deviated from experimental results are ignition regime, boundary conditions, and environment factors. The ignition protocol of experiment (ignition coil with a certain shape and provide a certain amount of power with a certain distribution along the coil length) could not be modelled in BARA perfectly (BARA used square region of ignition at the centre of reactor with a uniform power distribution), thus, the ignition regime became the largest source of error, especially due to the non-uniform power distribution. The boundary conditions in the experiment were also not perfectly modelled in BARA, for instance, at the four sides

BARA assumed the boundary to be non-flammable cells but these cells could receive heat value from the burning cells, thus, acting as heat sink, whereas at the bottom, BARA assumed that there is no interaction of heat value, thus, similar to adiabatic. These boundaries could not be considered as the actual boundary in the experiments, in fact these boundaries were the very simplified version of the real boundary conditions. Meanwhile, source of error from environment factors could be because of many external factors such as the effect of hot smoke of the combustion process and the effect of changing temperature and humidity near the reactor, which were not considered in the model.

Although BARA predictions have good fit with experiments, there are possibility that the error in each part of the model and variable are cancelling each other, instead of accumulating, which make the total error become relatively small, a compensation effect (Bal and Rein, 2013). This issue is an emerging issue in the physics-based model, such as the modelling of pyrolysis (Bal and Rein, 2013). The main idea to tackle this issue is by limiting the complexity of the model, which means limiting the number of variables that are used (Bal and Rein, 2013). BARA used small number of variables (only six) and each variable has its own role in the model. In term of the rules in the model itself, BARA considered the very basic physics without additional complexity, which have been widely known, such as heat transfer from one cell to another when their heat value (correspond to temperature) are different, heat loss to the surrounding when the heat value of a cell is higher than the surroundings, and heat value that is generated when combustion process is taking place.

Compensation effect might still happen, in fact in Chapter 4.1.3 it has been explained that the range of values of variables in BARA were not unique and different range of values could also maintain the goodness of the model, unless the value of a variable was set. However, the variables in BARA were non-dimensional variables, unlike the variables in physics-based models that have exact units and physical meaning, thus, how good the variables in BARA work together is more important than how accurate the value of each variable is. For instance, the value of Q_{R} that was equal 1 does not literally mean that the heat of combustion has a certain value that correspond to 1, although in the model, Q_{R} was the variable that represents heat of combustion in BARA. Therefore, with a certain value of heat of combustion, the Q_{R} could be of any value, but to limit the volatility of BARA variables, the value of a variable in BARA was set, which depends on the user.

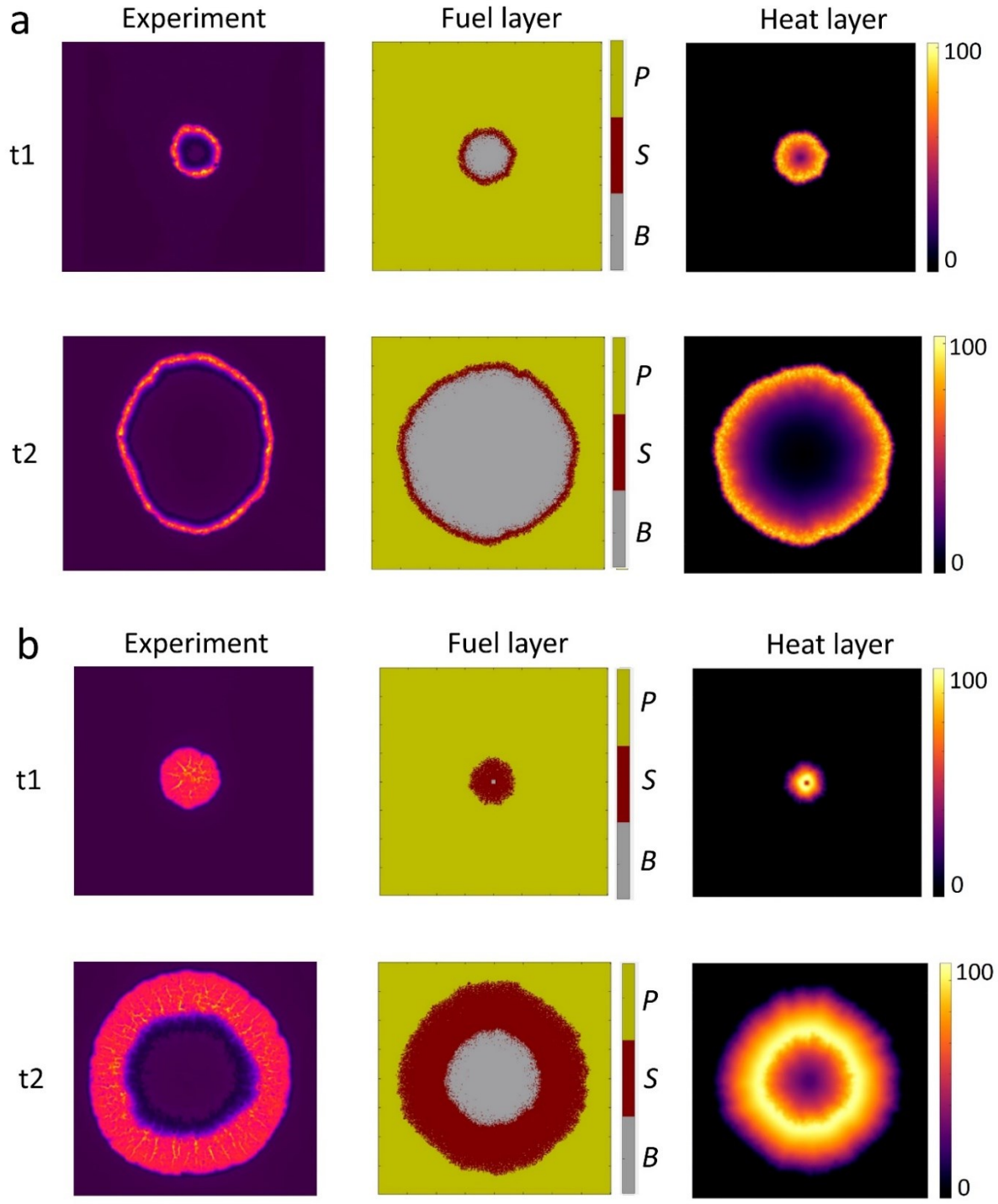

Figure 4.6. Comparison examples between BARA prediction and experiment of Christensen, Fernandez-Anez and Rein (2020) in the calibration process at two different conditions: (a) 2.5% IC and 110% MC; (b) 20% IC and 0% MC.

The calibration shows that Θ have strong linear correlation (R = 0.91) with thermal inertia (I_T) in log-log axes as shown in Figure 4.8. Therefore, Θ was formulated as shown in Eq. 4.6, where I_T is a function of k (thermal conductivity), ρ_b, and c as shown in Eq. 4.7. While thermal inertia represents the ability of a material to conduct and store heat, the

correlation of Θ with thermal inertia does not have a strong physical interpretation, in which higher thermal inertia does not mean lower ignition temperature (the physical variable that is represented by Θ). The correlation in Eq. 4.6 was the correlation in computational term to increase the usability of the model, in which by using this correlation, BARA can be used to simulate peat smouldering at any conditions apart from the ones of the experiments that were used for calibration, given the peat properties data are available.

$$\Theta = \exp(-1.1938\ln(I_T) - 16.599) \tag{4.6}$$

$$I_T = k\rho_b c \tag{4.7}$$

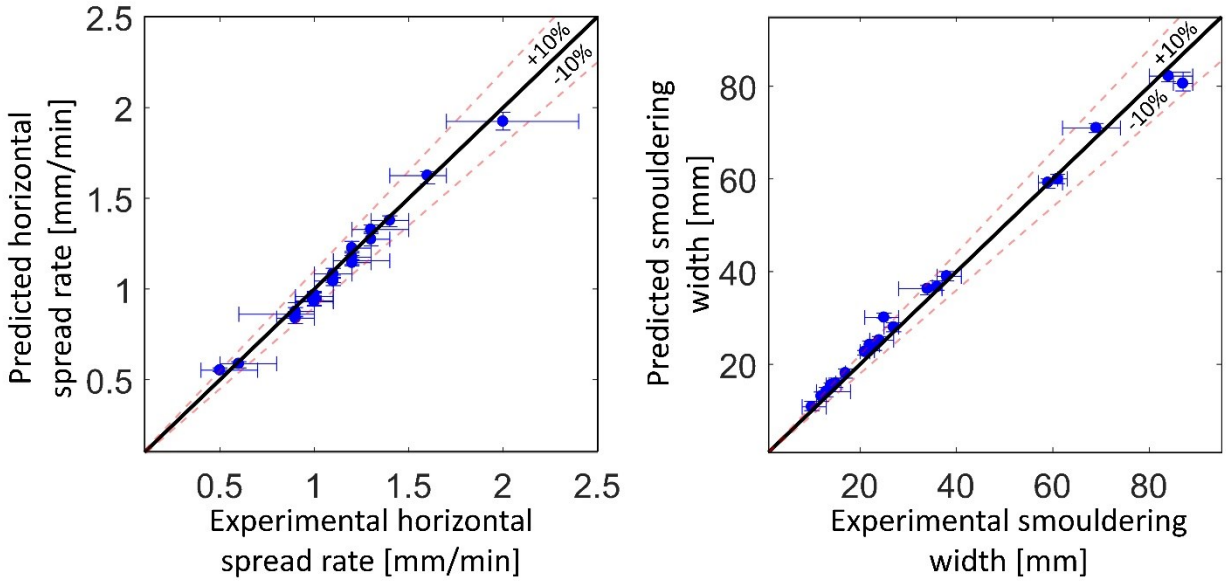

Figure 4.7. The calibration results of Θ in BARA against experiments (Christensen, Fernandez-Anez and Rein, 2020) on horizontal spread rate (left) and smouldering width (right). The solid black line represents the target, at which the prediction perfectly matches with the experiments. The blue circles are the simulation results from BARA with their uncertainty (10 repetitions).

μ was calibrated separately based on the experiment at critical conditions (critical MC and IC; Frandsen, 1987, 1997). Figure 4.9 shows the critical conditions of BARA for different μ compared with experiments. When using low μ, the critical conditions of BARA were significantly higher than the experiments, meaning the smouldering spread could be self-sustained in more adverse conditions. When using high μ, the critical conditions of BARA were significantly lower than the experiments. When $\mu = 0.1$, the critical conditions of BARA have good agreement with the experiments. From this calibration, $\mu = 0.1$ was selected and set constant. The calibration of μ has insignificant effect on the calibration of Θ (μ does not affect horizontal spread rate and smouldering width

significantly), thus, although they were calibrated separately, the results obtained are still valid.

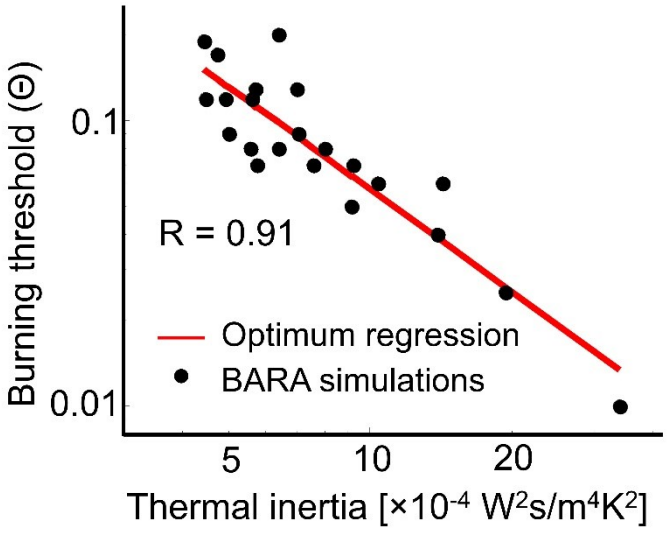

Figure 4.8. The correlation between Θ in BARA and thermal inertia. The black circles are the data point of Θ obtained from the calibration results at corresponding thermal inertia. The solid red line represents the optimum regression line of Θ that gives a low error from the calibration results.

Although with $\mu = 0.1$ BARA predictions have a reasonable fit against the experiments of (Frandsen, 1987, 1997), there are sources of errors that can be addressed in future work to improve the fit. The main sources of errors are ignition regime, boundary conditions, and the variability of peat properties. The line ignition (5 cm of ignition coil) in the experiments, became the largest source of error due to the non-uniformity of power distribution along the ignition coil, which could not be modelled in BARA, and due to the use of line ignition, the power distribution non-uniformity became stronger (since it is longer) than the non-uniformity of radial ignition in Christensen, Fernandez-Anez and Rein (2020). The difference of boundary conditions between BARA and experiments, such as at the four sides and at the bottom (as previously explained), could also become significant source of error. While the peat sample in Frandsen (1997) was pre-treated prior to the experiment, the peat sample in Frandsen (1987) was used without pre-treatment (natural sample), thus, the variability of peat properties in Frandsen (1987) was significant, although this properties variability also presented in Frandsen (1997) but weaker. This variability can be seen in Figure 4.9 where the critical MC and IC in Frandsen (1987) has strong deviation from a straight line, whereas in Frandsen (1997), the critical MC and IC almost fall into one straight line. The peat properties variability,

is therefore, also an important source of error in the model since this variability was not considered in BARA.

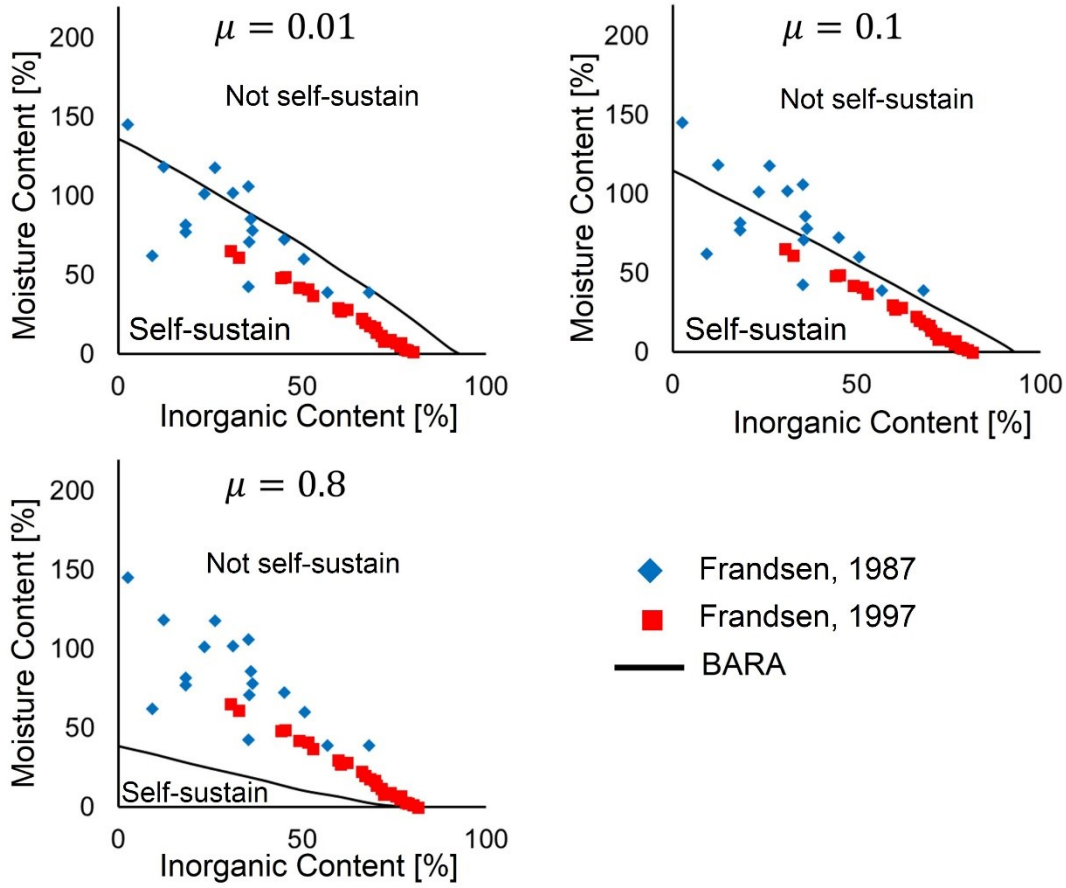

Figure 4.9. The calibration of μ in BARA against experiments (Frandsen, 1987, 1997) of critical conditions of self-sustained spread. The region at top-right of the figure is the region of non-self-sustained spread, whereas the bottom-left region is the region of self-sustained spread. The solid black lines represent the simulation results of BARA. The symbols show the experiment results on previous works (Frandsen, 1987, 1997).

4.2.2. Blind predictions of controlled experiments

Once calibrated, BARA was used to blind predict (without fitting of parameters) lab-scale experiments of smouldering fire in dry (0% MC) and wet (60% MC) peat variation. Three different peat MC configurations were studied: halftone, stripes, and checkerboard, as shown in Figure 4.10a, which are selected due to the availability of the experimental data for validation. The terminologies that are used to explain the results of these simulations are depicted in Figure 4.10b. In the halftone configuration, region 1 is wet and 2 is dry, whereas the edge region is the region in the proximity of the reactor sides. The edge region also has the same meaning for stripes and checkerboard configuration. In the stripes configuration, region 1 is wet, 2 is dry, and 3 is wet again (see Figure 4.10a).

In the checkerboard, the configuration is represented in column and row indexes, which are arranged according to Figure 4.10a. For instance, in column 2 and row 3, the peat is dry. Different regions in these three configurations are separated by MC boundary (magenta line). At this MC boundary, the region with high MC meets the region with low MC creating an abrupt change of MC.

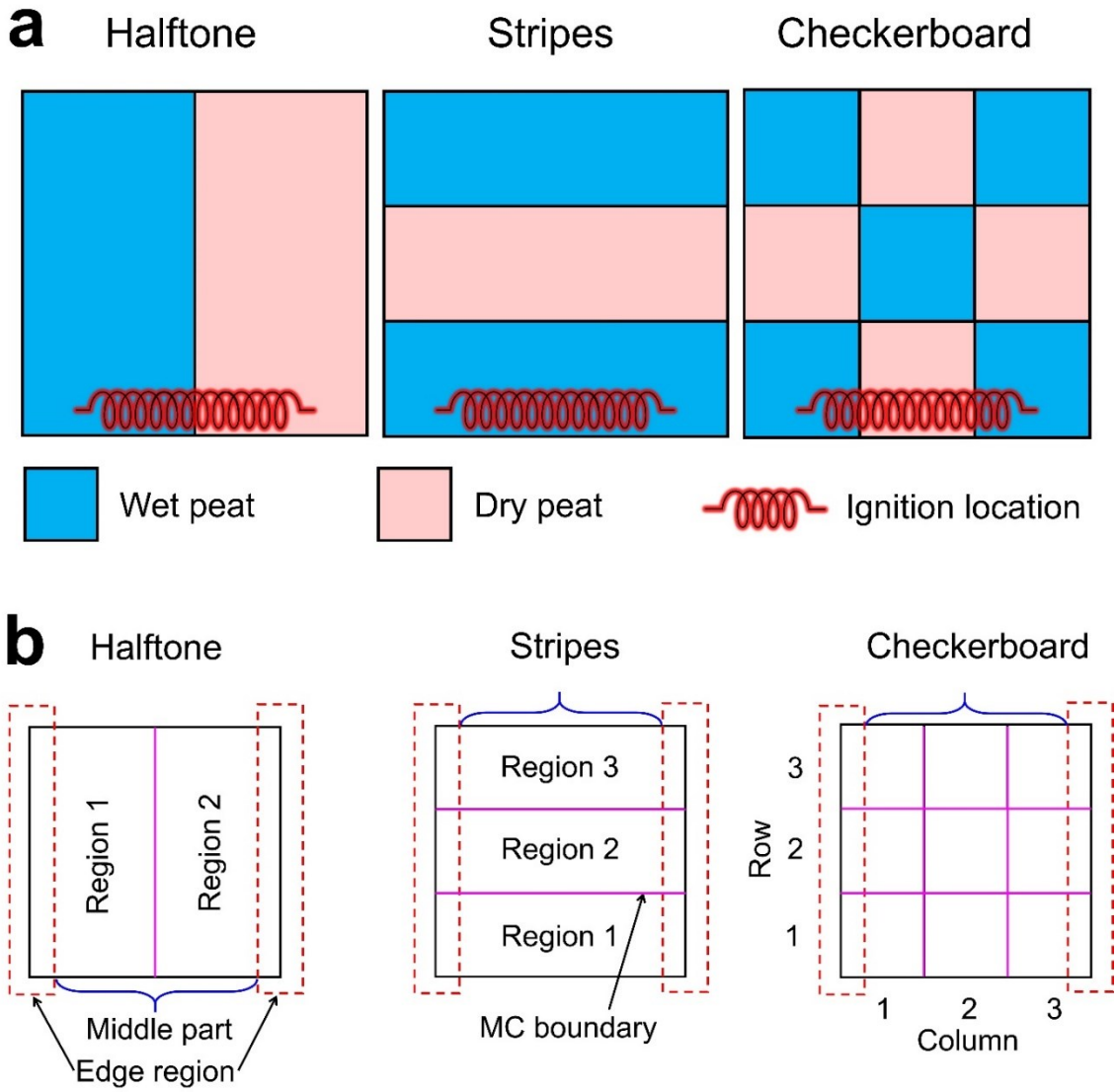

Figure 4.10. (a) The configuration of MC distribution of the lab-scale experiments. The wet peat is 60% MC, whereas the dry peat is 0% MC. The experiments were conducted in a 20cm × 20cm × 6cm reactor with line ignition at the bottom edge of the pictures. (b) Schematic of region terminologies for the simulation results of BARA in lab-scale experiments with halftone, stripes, and checkerboard configurations. In each configuration, there are edge regions, regions near the reactor sides; middle part, the regions relatively distant from the reactor sides; and MC boundary, the location at which peat with high MC and low MC meet.

Simulation results from BARA were qualitatively compared to the lab-scale experiments since the conditions and reactor dimension between the calibration data and the varied MC experiments are different. The reactor used in the calibration data was a shallow reactor (40cm × 40cm × 1.6cm) with a centre ignition that causes the fire to spread radially, whereas the varied MC experiments used 20cm × 20cm × 6cm reactor with a line ignition at one side on the reactor and the fire spreads linearly. The depth of the reactor influences the behaviour of the smouldering fire, for instance, the horizontal and in-depth spread rate at equal MC and IC are slightly different between two reactors with different depth (compare Christensen, Fernandez-Anez and Rein, 2020 with Huang and Rein, 2017). Due to this small difference, the goodness of the model is expected to prevail, although it has discrepancy, when the model is used to simulate experiments with a deeper reactor.

Figure S4.3 compares BARA against the experiment in halftone configuration, and shows that the smouldering front in BARA fuel layer has a good agreement with the experiment. The slower spread on the wetter part (region 1), followed by the inclined front at the MC boundary, which indicates a transition from wet to dry peat which has faster spread rate on region 2, can be observed in both the experiment and BARA. The arc shape on the edge region in BARA prediction matches with the arc shape in the experiment. This arc shape indicates the retardation of the spread on edge region since the ignition does not cover the whole width of the reactor (see Figure 4.10a).

The colour distribution in the heat layer of BARA also has a good agreement with the infrared footage of the experiment to some extent, which indicates that the heat radiation distribution in the model was comparable with the experiment. However, the smouldering width in BARA was significantly different from the experiment. This difference was caused by the difference on the reactor depth, where BARA assumed a shallow reactor (1.6cm depth), whereas the experiment used a reactor with a several times greater depth (6cm depth). Using a greater depth in BARA was avoided since the model has not been calibrated with depth due to the unavailability of data of experiments on smouldering with depth variation. The use of a deeper reactor in the simulation caused the trailing edge of the smouldering has sharp edges, which significantly deviate from the experiments (and unrealistic), although these sharp edges did not present in the simulation of smouldering peat with uniform MC at a deeper reactor. This discrepancy is one limitation of BARA that is directly related to the rule for t_s, thus, in future work, the improvement of the rule for t_s, and its validation with corresponding experiments, is expected to solve this issue. Once this issue is resolved, the results from BARA can be

used and compared with the experiments quantitatively. However, since the leading edge of the smouldering peat in the simulation has a good agreement with the experiment, BARA can give an estimation on the leading edge of smouldering peat with varied MC, the estimation that can be used to assist firefighting attempts, for example, for the consideration of firefighters deployment from its multiple faster (~20 times faster) than real time simulations.

Applied to a more complex stripes configuration, BARA accurately simulated the lab-scale experiment as shown in Figure S4.4. In region 1 (t1), the smouldering fire spreads slowly since this region has a higher MC. Arc shapes on the edge regions are also observed in this configuration in both the experiment and BARA prediction, indicating that the ignition protocol used is the same with the halftone configuration. The smouldering front then enters region 2 (drier peat), and the smouldering spread accelerates (t2). However, since there are arc shapes in edge region, the acceleration of the spread in the middle part precedes the acceleration in the edge region. This delay causes the gap between fire front at the middle part and the edge region to become larger, and the arc shapes are stretched to become linear. This linear shape is similar to the shape in the halftone configuration, which indicates that there is MC difference between middle part and edge region, meaning that the smouldering front in the middle part has reached region 2, whereas the smouldering front in the edge regions are still in region 1. In region 3, where the MC is high again, the smouldering spread in the middle part decelerates. This deceleration, in addition to the fire front mismatch between the middle part and the edge region due to the ignition protocol, causes the smouldering front in the edge region to overtake the smouldering front in the middle part. The smouldering front in the middle part enters region 3 before the smouldering front in the edge region, thus, the smouldering front in the middle part starts decelerating, whereas the smouldering front in the edge region is still spreading relatively quickly since the front is still in the low MC region (region 2). These phenomena cause the smouldering front to flatten as shown in Figure S4.4 (t3). From these results, BARA has been proven robust simulating a more complex MC configuration where sequence of complex phenomena are involved (arc shape, arc stretching, and flattening).

Finally, the comparison between BARA prediction and a lab-scale experiment in the checkerboard configuration is shown in Figure 4.11. In the checkerboard configuration, there are nine regions with alternate MC between dry and wet peat. The spread behaviour of this configuration changes depending on the position of the smouldering front. In row 1 (t1), the smouldering in column 2 precedes the spread of the smouldering in column 1

and 3 which are wetter. Arc shapes in the edge region are also observed since the ignition protocol is the same with the halftone and stripes configurations. Once the smouldering front reaches row 2 (t2), the spread in column 2 decelerates since the peat is wet in that quadrant. The smouldering front in columns 1 and 3 is still in row 1 where the MC is higher, thus, the smouldering still spreads slowly. However, at the boundary (MC boundary) between column 2 with columns 1 and 3 in row 2, the smouldering changes direction to spread diagonally towards the lower MC quadrant (column 1 and 3 in row 2). This diagonal spread causes the creation of ear shapes at the MC boundary as shown in Figure 4.11 in both the experiment and the simulation (t2). These ear shapes continue to spread diagonally until the peat is fully consumed in columns 1 and 3 in row 2. During the diagonal spread, the smouldering front in column 1 and 3 in row 1 overtakes the smouldering front in column 2 and merge with the ear shapes. This merging phenomenon causes the smouldering front in columns 1 and 3 to flatten. During this flattening phenomenon, the smouldering in columns 1 and 3 spreads faster (they spread in a low MC region) than in column 2, which make the smouldering front in columns 1 and 3 precedes the smouldering front in column 2. However, once the smouldering front reaches row 3, the smouldering in columns 1 and 3 decelerate since the MC at those two quadrants is high. The smouldering spread at the MC boundary (between column 2 with columns 1 and 3 in row 3) changes direction, again, to move diagonally towards column 2. This diagonal spread merges with the smouldering front in column 2 that has just entered row 3. Therefore, at the end of the simulation (and experiment), the smouldering front is flat in column 1 and 3 and has a step profile in column 2 as shown in Figure 4.11 (t3). These sequences of complex phenomena have been captured by the blind predictions of BARA. Although BARA was only compared qualitatively, BARA accurately simulated the complex progression of the smouldering front (leading edge) in checkerboard configuration. Therefore, BARA is a powerful tool to simulate smouldering peat at varied MC. The main limitation of BARA is the simulation of the trailing edge, which deviated significantly from the experiments of smouldering spread at varied MC, and subject for future works, apart from the ignition regime, boundary conditions, and environmental factors that could not be perfectly modelled in BARA, which are similar with the limitations explained in Chapter 4.2.1. The full comparison of BARA with the lab-scale experiments of peat smouldering at varied MC can be found in supplementary material.

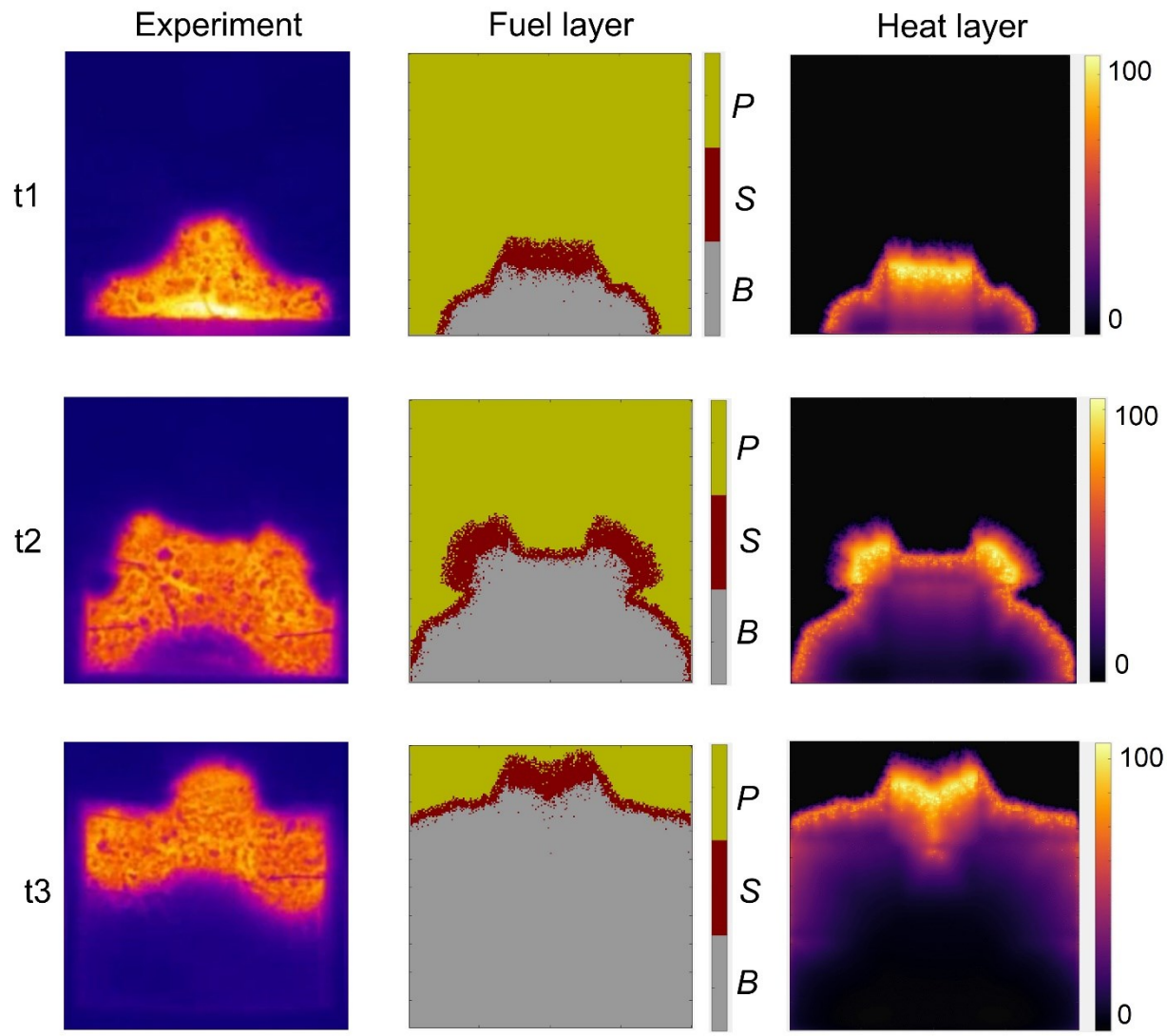

Figure 4.11. Comparison of smouldering profile between BARA simulations and the experiments of smouldering peat with heterogeneous MC in the checkerboard configuration. The comparison is focused on three different times after ignition that show significant differences. The full comparison can be found in supplementary material.

Complex progression of smouldering peat at varied MC indicates the difficulty of predicting the smouldering spread in peatland wildfires upon firefighting attempts. The failure of locating the smouldering front in firefighting attempts significantly reduces fire suppression effectiveness, since it means that the suppression water (or agent e.g., foam) is sprayed at a location distant from the smouldering front. This location mismatch means the suppression water must travel some distance before reaching the smouldering front. The water travels while also receives heat and disperses through the pores of the peat, meaning the suppression water significantly loss its heat-absorbing ability (due to the higher temperature and lesser amount of water) when reaching the smouldering front (Santoso *et al.*, 2021). By performing this smouldering front estimation, combined with

multiple faster-than-real-time simulations that can be performed to capture the uncertainty in nature (e.g., weather uncertainty), optimum firefighting strategy can be developed, for instance, for determining the number and deployment of firefighters, thus, the effectiveness of firefighting attempts could improve.

4.2.3. Predicting smouldering behaviour in a natural peatland

The use of BARA was extrapolated to predict (forecasting without fitting of parameters) how the smouldering would have behaved, given the MC variation provided in Prat-Guitart *et al.* (2017) (see Figure 1.3). The MC variation data of Prat-Guitart *et al.* (2017) were obtained from the measurement and modelling of the MC of peat in boreal peatland in Ireland within 150cm × 150cm area. Their model was calibrated against detailed measurement of MC in different combination of surface vegetation and micro-topography. The result of this larger scale simulation is shown in Figure 4.12 (left) and BARA required 2h of computational time (for simulating 43h of smouldering peat) to finish one simulation. The smouldering spreads following the contour of the MC profile and can spread at MC slightly higher than the critical condition (~120% MC) when the ignition sustains. However, the spread across critical condition only partially burns the peat (i.e., only few peat cells at critical conditions are consumed), which agrees with the lab-scale experiments (Prat-Guitart *et al.*, 2016a). This finding indicates that the heat has been accumulated prior to reaching the critical region, therefore, there is enough heat to partially burn the peat, even at critical condition. Once the accumulated heat is depleted for igniting the peat at critical conditions, the smouldering extinguishes. This depletion process is accelerated when the smouldering encounters region with a higher MC, leading to a smaller burnt area.

Since BARA was calibrated with many experimental data (22 independent experiments) and accurately blind predicted the leading edge of smouldering peat in other independent experiments that have more realistic condition (non-uniform MC), these results can give insight on how the smouldering spreads in a real peatland. The faster-than-real-time simulation of BARA can be used to assist the development of firefighting strategy, for instance, its multiple simulations to find the optimum allocation of resources. While in laboratory-controlled experiments there are sources of errors, the simulations of BARA in real peatland have even more sources of errors. Apart from ignition regime, boundary conditions, variability of peat properties, and environmental factors, the simulations in real peatland can also have sources of errors from the weather, temporal variation of peat properties, environmental factors, and weather, surface vegetation, and many others. Therefore, while BARA can give insights on the smouldering spread in real

peatland, it must be used with care and experts should be the one to make the final decision.

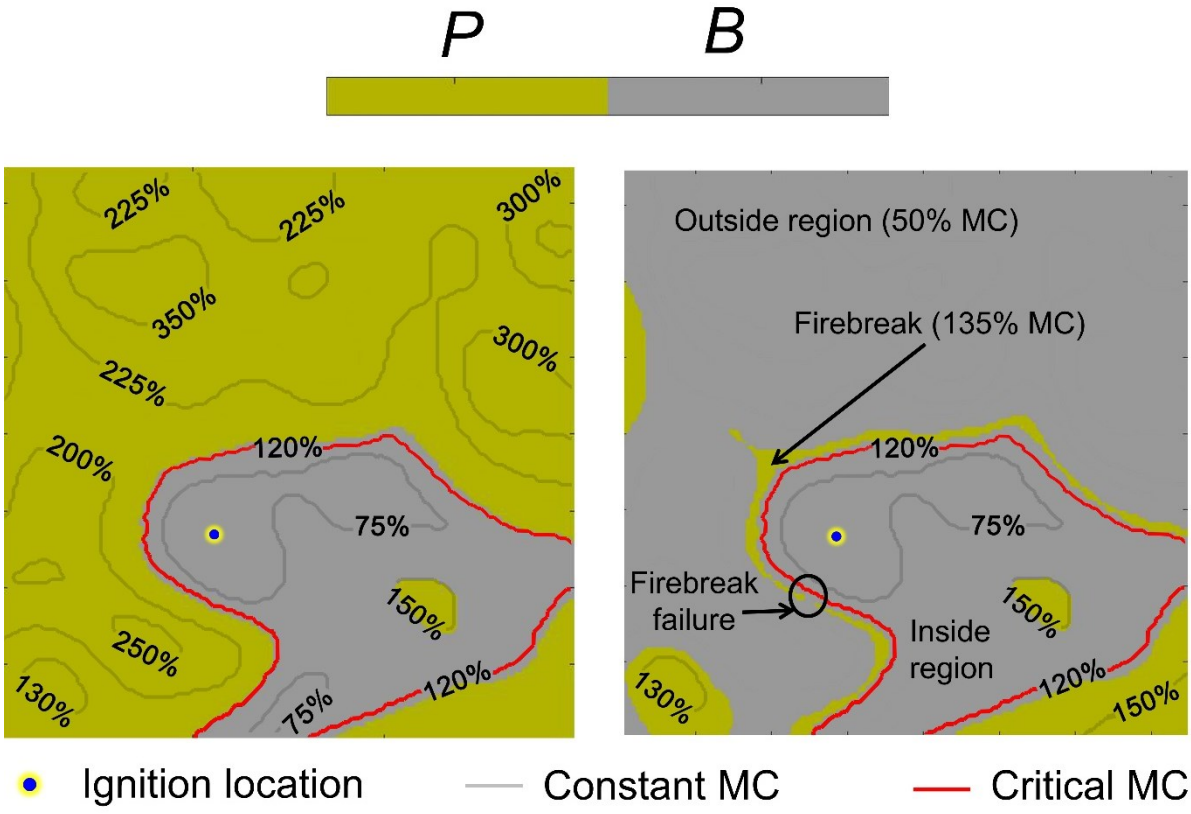

Figure 4.12. Simulation result of BARA in natural peatland with varied MC (left) and simulation result of BARA in hypothetical landscape (right). The ignition location is represented by yellow-glowing blue circle. The grey contour lines represent the constant MC and red lines represent the critical MC. The grey area represents burnt peat (B), whereas the green area represents undisturbed peat (P). Inside region is the region encircled by firebreak, whereas outside region is region across the firebreak.

BARA also captured the formation of patches of unburned peat during the smouldering spread. These patches are formed because the MC in the patches is significantly above the critical condition, but surrounded by peat with a lower MC. Therefore, while the surrounding area of the patches are burnt, the peat inside the patches remains intact, as shown in Figure 4.12 (left). The patches of unburned peat surrounded by burnt peat are commonly observed in real peatland wildfires (Prat-Guitart *et al.*, 2016a, 2017). BARA has successfully simulated this phenomenon which translates lab-scale experiments into the context of peatland wildfires.

The simulation result shown in Figure 4.12 (left) was ignited at the location with 50% MC, however, even if the ignitions were at different locations with different MC (50%, 75%, and 100%, where the ignition sustain), the burnt scars are not significantly different.

This finding implies that once the ignition sustains, the extinction of smouldering spread mainly depends on the contour of the MC profile. The smouldering consumes the peat that has MC lower than the critical MC, continues to spread following the contour of the peat with low MC, and stops spreading after reaching peat with critical MC or higher. The horizontal layers of peat with high MC, therefore, discontinue the smouldering spread, i.e., acting as smouldering firebreak, which can minimise the total burnt area caused by the fire. However, if the smouldering firebreak is thin or formed by layers with peat MC close to the critical condition, the smouldering can penetrate the firebreak, causing the fire to reach the other side of the firebreak (Huang and Rein, 2015; Lin, Liu and Huang, 2021). If the peat across the firebreak is dry, and the penetration of smouldering against the firebreak reaches the other side, the firebreak fails its purpose, and the burnt area caused by the fire becomes significantly larger. Therefore, sufficiently wide and moist firebreak, i.e., layers of wet peat, are required to discontinue the smouldering fire spread and minimise the burnt area caused by peatland wildfires.

These mechanisms were analysed by using BARA to simulate smouldering in a hypothetical landscape. In this hypothetical landscape, the peat MC profile in Figure 4.12 (left) was modified: the peat MC across the smouldering firebreak, the outside region (see Figure 4.12, right), was set to be 50%. The thickness and the MC of the firebreak were varied. The failure of smouldering firebreak (see Figure 4.12, right) highly depended on both firebreak width and MC. The smouldering could penetrate firebreak with MC of 160% if the firebreak width was less than 3mm, however, when the MC of firebreak was 135%, the smouldering fire could penetrate the firebreak even with width of 20mm (see details in Figure S4.5). These findings indicate the effectiveness of the wet peat layers acting as firebreak are affected by its MC and width, where the width has a higher influence than the MC (see Figure S4.5). These findings confirm with Huang and Rein (2015), however, with different critical width and MC. Part of the reason of these differences is due to the different reactor (domain) used in the model. While BARA used shallow reactor, Huang and Rein (2015) used vertical reactor, and unlike physical model, BARA require further calibration based on reactor depth to be able to simulate the smouldering spread in reactor with different depth (which cannot be done due to the unavailability of the experimental data). However, qualitatively, the findings in BARA regarding firebreak concur with the findings in Huang and Rein (2015) and BARA has more dimension (3-D spread compared to 1-D spread) and applied to a more realistic scenario. The firebreak failure causes the significant increase of total burnt area (compare Figure 4.12 left and right). This increase of burnt area could become more dramatic in real peatland wildfires, since in the

simulation the area of domain is limited, whereas the area in real peatlands are significantly larger, in order of thousands of hectares.

These model predictions indicate that the peat MC profile (which can be estimated, e.g., by using remote sensing) is highly related to the vulnerability and risk of smouldering peatland wildfires. BARA provides a tool to quantify the risk, e.g., based on burnt area, which make the mitigation efforts become more efficient. For instance, instead of maintaining peat with high MC in the entire peatland, such as by performing rewetting on the peatland, by using the prediction from BARA, this rewetting treatment can only be performed on the locations with high risk.

4.3. Conclusions

A cellular automata model was developed to simulate the three-dimensional (3-D) spread of smouldering fire in peat with heterogeneous MC profile. The model (BARA) was calibrated against lab-scale experiments in various conditions, with a relative absolute error of less than 10%. BARA was applied to blind predict lab-scale experiments of smouldering fire in peat with heterogeneous MC and accurately reproduced various phenomena observed in the experiments: tilting, flattening, and merging. Tilting is a phenomenon when the flat leading edges in dry peat (faster spread rate) and wet peat (slower spread rate) regions are connected by an inclined leading edge instead of a step (90^o angle). Flattening is a phenomenon when the dry and wet peat regions are reversed, causing the leading edges in both regions become relatively flat since the spread rates in the two regions are reversed. Merging is a phenomenon when the leading edges from different regions collide due to a diagonal propagation. These results prove the capability of BARA for simulating smouldering fire in peat with heterogeneous MC.

BARA was used to predict the smouldering spread at the large-scale on a boreal peatland in Ireland. BARA simulated the creation of patches of unburned peat, which is a common phenomenon observed in peatland wildfires. In this large-scale simulation, the model predicted that the smouldering could penetrate and partially burn wet peat, up to 135% MC, which confirm with the experiments (Prat-Guitart *et al.*, 2016a). This penetration phenomenon implies that horizontal layers of wet peat which discontinue smouldering spread, might fail if their width or MC are insufficient. These findings agree with physics-based model (Huang and Rein, 2015), qualitatively, however, BARA considers more spread direction (3-D spread compared to 1-D spread) and was applied to a more realistic scenario (heterogeneous MC). The peat MC profile significantly affects the vulnerability of peatlands to fire. With the prediction from the model, the vulnerability of peatlands can be quantified and better management strategies can be

performed, for instance, by performing multiple faster-than-real-time simulations to determine the optimum locations for the rewetting treatment of the dry peat. The findings and model provide knowledge on the behaviour of smouldering fire in peat with realistic conditions and a tool that can help, for instance, locating the smouldering front for suppression purposes and determining the optimum rewetting strategy, thus, can improve the effectiveness of peatland wildfires mitigation.

Chapter 5 – BARAPPY: Hybrid model of Cellular Automata and Physics-Based Equations to Simulate Three Dimensional Smouldering Fire

Summary[4]

In this chapter, a novel 3-D smouldering model (BARAPPY) was developed by combining cellular automata (CA) and physics-based models. A physics-based model was used to solve the in-depth smouldering profile, which the 3-D smouldering CA model (BARA) fail to accurately simulate due to the unavailability of the experimental data for the calibration (see Chapter 4). Both BARA and physics-based model were validated, independently, against experiments on peat with 12 combinations of moisture and inorganic contents, with average errors (relative absolute error) on spread rate of less than 20%, which is reasonable since this error is within the experimental uncertainty. Comparing the two models, the main benefits of physics-based model are the level of generality and detail that can be acquired such as temperature, species, and reaction profiles, whereas BARA benefits from two order of magnitude higher computational efficiency, which is of utmost important for field-scale modelling. BARAPPY accurately reproduced the 3-D spread of smouldering peat on non-uniform MC, a half wet-half dry configuration, and predicted the non-uniform DOB of smouldering peat. The selection of this simple peat MC configuration was based on two reasons: the availability of validation data and to avoid the additional complexity. BARAPPY also predicted the initiation of overhang formation when the moisture gradient is significant (greater than 20%), which was confirmed by physics-based models and experiments. This work provides fundamental knowledge of the 3-D smouldering which can help mitigating peatland wildfires and reducing their negative environmental impact.

[4] This chapter is based on "Dwi M J Purnomo, Han Yuan, Muhammad A Santoso, Guillermo Rein, 2022. BARAPPY: Hybrid model of Cellular Automata and Physics-Based Equations to Simulate Three Dimensional Smouldering Fire. (to be submitted)."

5.1. The Development of BARAPPY

5.1.1. Introduction to BARAPPY

In Chapter 4, the potential of cellular automata (CA) to simulate 3-D spread of smouldering is proved. However, the model in Chapter 4, BARA, suffers from the inaccuracy of the smouldering trailing edge simulation, which directly corresponds to in-depth spread. This inaccuracy stems from the unavailability of the experimental data for calibration (see Chapter 4). This in-depth spread governs the DOB, which can be used to estimate the amount of peat loss during wildfires (Rein *et al.*, 2008). Smouldering peat fire is often untraceable and can be detected only after the fire widely spread, due to the flameless nature and the tendency of smouldering to spread subsurface (Huang *et al.*, 2016). Therefore, the monitoring of the volume of peat that is burnt during wildfires (peat loss) can facilitate early detection, and this volume can be estimated based on burnt area and DOB. Beside early detection, the monitoring of this volume also enables estimation of the climate change impacts and the severity of peatland wildfires, such as the total carbon emission and microorganism loss, respectively (Rein *et al.*, 2008). Through a better understanding of 3-D smouldering behaviour, the DOB estimation will improve, thus, aiding the estimation of volume of burnt peat for the mitigation purposes.

This chapter aims to overcome the inaccuracy of the in-depth profile from BARA simulation by integrating a physics-based model to BARA. While BARA simulates the 2-D horizontal spread, the physics-based model simulates the in-depth spread. The development of the physics-based model is by simulating lab-scale experiments of smouldering peat with 12 different combinations of MC and IC (see Table 5.1), the same experiments that are used for calibrating BARA (Christensen, Fernandez-Anez and Rein, 2020), which were selected due to the availability of the experimental data. Although these peat conditions are mostly different from the peat conditions in nature (i.e., peat MC in nature is most likely above 60% even in drained peatland in a dry season; Nusantara, Hazriani and Suryadi, 2018), the results of the model can be considered as conservative since the model focuses on the extreme peat conditions (e.g., a very dry peat). However, while BARA consider the top view of the reactor, the physics-based model considers the side view of the reactor (see Figure 5.1a). For simplicity, the physics-based model will be referred to as GPyro (the solver). Once combined, the hybrid model will be referred to as BARAPPY which stems from BARA and GPyro and means “burning” in Indonesian.

Table 5.1. Pairs of MC and IC used for the validation of the models. These pairs are adopted from Christensen, Fernandez-Anez and Rein (2020).

MC [%]	0	0	0	0	0	20	40	60	80	20	40	60
IC [%]	0	20	40	60	70	0	0	0	0	40	40	40

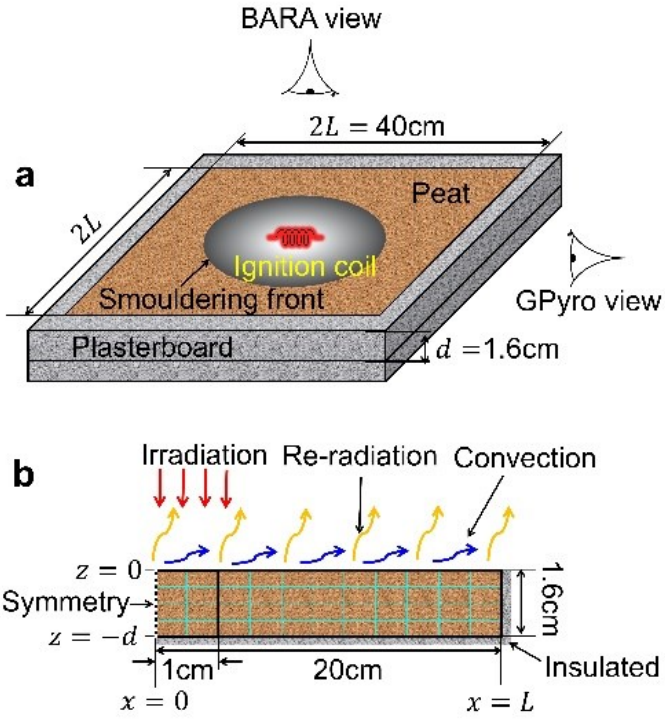

Figure 5.1. (a) Schematic of the experiments in Christensen, Fernandez-Anez and Rein (2020) used for validation of the cellular automata (BARA) and physics-based model (GPyro). (b) The computational domain used for GPyro. (c) The computational domain used for BARA.

5.1.2. Physics-based model

The domain of the physics-based model (GPyro) is shown in Figure 5.1b, which is half of the 2-D side view of the reactor (see Figure 5.1a). The side-view domain was selected since top-view domain in physics-based model requires the top and bottom boundaries to be equal (which is not the case). The experiments in Christensen, Fernandez-Anez and Rein (2020) resulted in uniform radial spread, thus, half 2-D computational domain was used to minimise computational cost, with symmetry boundary condition at the left side, as shown in Figure 5.1b, adapted from Yuan, Restuccia and Rein (2021).

The physics-based model is built on GPYRO (thus, named GPyro) which solves 2-D conservation equations for both solid and gas phases (Lautenberger and Fernandez-

Pello, 2009). The gas-phase temperature is assumed to be in thermal equilibrium with the condensed-phase temperature (Huang, Rein and Chen, 2015). The equations are shown in Eq. 5.1 to Eq. 5.6 (see details of formulation and assumption in Lautenberger and Fernandez-Pello, 2009) which are condensed-phase mass, condensed-phase species, condensed-phase energy, gas-phase mass, gas-phase species, and gas-phase momentum (Darcy's law), consecutively. These equations are solved implicitly by a using tri–diagonal matrix (Thomas) algorithm, which is discussed with more detail in Lautenberger and Fernandez-Pello (2009). Thomas algorithm was used because of its computational efficiency to solve recursive matrix operation (in the governing equations of GPYRO; Lautenberger and Fernandez-Pello, 2009).

In these equations, $\bar{\rho}$ is bulk density, t is time, $\dot{\omega}'''$ is volumetric reaction rate, Y is mass fraction, X is volume fraction, $\bar{h}$ is specific enthalpy, k is thermal conductivity, T is temperature, ΔH is change in enthalpy, $\bar{\psi}$ is porosity, $\dot{m}''$ is mass flux, D is diffusivity, κ is permeability, ν is viscosity, and p is pressure (see nomenclature for their units). Subscripts f is formation, d is destruction, g is gas, and eff is effective, whereas i and j refer to the condensed-phase species (water, peat, or sand) and gas-phase species (oxygen, nitrogen, or gaseous products), respectively. The physical variables in Eq. 5.1 to Eq. 5.6 are time and space dependent (their value differ at different position or time).

$$\frac{\partial \bar{\rho}}{\partial t} = -\dot{\omega}'''_{\mathrm{fg}} \tag{5.1}$$

$$\frac{\partial (\bar{\rho} Y_{\mathrm{i}})}{\partial t} = \dot{\omega}'''_{\mathrm{fi}} - \dot{\omega}'''_{\mathrm{di}} \tag{5.2}$$

$$\frac{\partial (\bar{\rho}\bar{h})}{\partial t} = k\frac{\partial}{\partial x}\left(\frac{\partial T}{\partial x}\right) + k\frac{\partial}{\partial z}\left(\frac{\partial T}{\partial z}\right) + \dot{\omega}'''_{\mathrm{di}}(-\Delta H_{\mathrm{i}}) \tag{5.3}$$

$$\frac{\partial}{\partial t}\left(\rho_{\mathrm{g}}\bar{\psi}\right) + \frac{\partial m''_{\mathrm{x}}}{\partial x} + \frac{\partial m''_{\mathrm{z}}}{\partial z} = \dot{\omega}'''_{\mathrm{fg}} \tag{5.4}$$

$$\frac{\partial}{\partial t}\left(\rho_{\mathrm{g}}\bar{\psi}Y_{\mathrm{j}}\right) + \frac{\partial}{\partial x}\left(m''_{\mathrm{x}}Y_{\mathrm{j}}\right) + \frac{\partial}{\partial z}\left(m''_{\mathrm{z}}Y_{\mathrm{j}}\right) = -\frac{\partial}{\partial x}\left(\bar{\psi}\rho_{\mathrm{g}}D_{\mathrm{eff}}\frac{\partial Y_{\mathrm{j}}}{\partial x}\right) - \frac{\partial}{\partial z}\left(\bar{\psi}\rho_{\mathrm{g}}D_{\mathrm{eff}}\frac{\partial Y_{\mathrm{j}}}{\partial z}\right) + \dot{\omega}'''_{\mathrm{fj}} - \dot{\omega}'''_{\mathrm{dj}} \tag{5.5}$$

$$\dot{m}'' = -\frac{\kappa}{\nu}\frac{\partial p}{\partial x} - \frac{\kappa}{\nu}\frac{\partial p}{\partial z} \qquad \left(\rho_g = \frac{p\bar{M}}{RT}\right) \tag{5.6}$$

The properties of the condensed-phase species (e.g., bulk density, specific heat, and porosity) are assumed to be constant, whereas all gaseous species have unit Schmidt number and equal diffusion coefficient and specific heat. The averaged properties in each cell are calculated by weighting with the appropriate mass or volume fractions (see Eq. 5.7).

$$\bar{c} = \sum Y_{\mathrm{i}}c_{\mathrm{i}}, \;\; \bar{k} = \sum X_{\mathrm{i}}k_{\mathrm{i}}, \;\; \bar{\rho} = \sum X_{\mathrm{i}}\rho_{\mathrm{i}} \tag{5.7}$$

At the top surface ($z = 0$), the convective, radiative, and mass transfer boundary conditions are considered (Eq. 5.8 and Eq. 5.9, with $h_{\mathrm{c}} = 10\,\frac{\mathrm{W}}{\mathrm{m}^2}\cdot\mathrm{K}$, $\varepsilon = 0.95$, and $h_{\mathrm{m}} = 0.02\ \mathrm{kg/m^2.s}$, Couette flow approximation), which were found empirically (Huang, Rein

and Chen, 2015; Yuan, Restuccia and Rein, 2021). The ambient pressure and temperature are assumed to be atmospheric and 300 K, respectively. At the symmetrical plane ($x = 0$), the thermal and diffusion boundary conditions are assumed to be adiabatic (Eq. 5.10) and impermeable (Eq. 5.11). At the right ($x = L$), the boundary conditions are thermally insulated with no re-radiation (Eq. 5.12, with h_c =3 W/m^2 · K) and impermeable (Eq. 5.11), following Huang, Rein and Chen (2015), who estimated the properties of the reactor used that was made of ceramic board. These boundary conditions are also implemented at the bottom ($z = -d$). During the first 30 min, a heat flux of 50 kW/m^2 is applied on $x = 0$ cm to $x = 1$ cm of the top surface ($z = 0$), to simulate the ignition protocol of the experiments, which was selected based on the size of the ignition coil, the power provided in the coil and the ignition duration (Christensen, Fernandez-Anez and Rein, 2020). Although the boundary conditions used here were not perfectly match with the experiments, the assumptions taken for these conditions resemble the experiments to great extent, for instance, the thermally insulated boundary conditions that are not adiabatic but with a reduced heat transfer coefficient. The simulations were sufficiently resolved with cell sizes of $\Delta x = 2$ mm and $\Delta z = 0.25$ mm, and an initial time step of 0.01 s. Reducing the cell sizes and initial time-step further do not significantly affect the results. On the other hand, increasing the size of cell or the time-step, which is of utmost importance for the field-scale modelling practicality, caused convergence problems, thus this coarsening stage needs additional treatment and is a subject to future works.

$$-k\left.\frac{\partial T}{\partial z}\right|_{z=0} = -h_c(T|_{z=0} - T_a) - \varepsilon\sigma(T^4|_{z=0} - T_a^4); \tag{5.8}$$

$$-\bar{\psi}\rho_g D_{eff}\left.\frac{\partial Y_j}{\partial z}\right|_{z=0} = h_m\left(Y_j^{\infty} - Y_j|_{z=0}\right); \tag{5.9}$$

$$-k\left.\frac{\partial T}{\partial x}\right|_{x=0} = 0 \tag{5.10}$$

$$-\bar{\psi}\rho_g D_{eff}\left.\frac{\partial Y_j}{\partial x}\right|_{x=0,L} = 0 \tag{5.11}$$

$$-k\left.\frac{\partial T}{\partial x}\right|_{x=L} = -h_c(T|_{x=L} - T_a) \tag{5.12}$$

For heterogeneous reaction, a mass basis is more commonly used than molar basis, which is written as in Eq. 5.13, where $\nu_{B,k} = 1 + (\rho_B/\rho_A - 1)\chi_k$, and χ_k quantifies the shrinkage or intumescence of the cell size. The destruction rate of condensed species A in reaction k satisfy Arrhenius law (see Eq. 5.14), and the formation rate of condensed species B and all gases from reaction k are the product of this destruction rate and the corresponding stoichiometry coefficient (ν). These processes affect the cumulative mass of each condensed species (see Eq. 5.15). The details of formulation, derivation, and

assumptions for these equations can be found in Lautenberger and Fernandez-Pello (2009).

$$A_{\mathrm{k}} + \sum_{\mathrm{j}=1}^{\mathrm{N}} \nu'_{\mathrm{j,k}} \mathrm{gas}\, j \rightarrow \nu_{\mathrm{B,k}} B_{\mathrm{k}} + \sum_{\mathrm{j}=1}^{\mathrm{N}} \nu''_{\mathrm{j,k}} \mathrm{gas}\, j \tag{5.13}$$

$$\dot{\omega}'''_{\mathrm{dA_k}} = \frac{(\bar{\rho} Y_{\mathrm{A}} \Delta \mathrm{z})_{\Sigma}}{\Delta \mathrm{z}} Z_{\mathrm{k}} \mathrm{e}^{-E_k/RT} \left[\frac{\bar{\rho} Y_{\mathrm{A}} \Delta \mathrm{z}}{(\bar{\rho} Y_{\mathrm{A}} \Delta \mathrm{z})_{\Sigma}}\right]^{\mathrm{n_k}} Y_{\mathrm{O}}^{\mathrm{n_{O_2,k}}} \tag{5.14}$$

$$(\bar{\rho} Y_{\mathrm{A}} \Delta \mathrm{z})_{\Sigma} = (\bar{\rho} Y_{\mathrm{A}} \Delta \mathrm{z})|_{\mathrm{t}=0} + \int_0^{\mathrm{t}} \dot{\omega}'''_{\mathrm{fi}} \Delta \mathrm{z}(\tau) d\tau \tag{5.15}$$

A five-step reaction scheme (see Eq. 5.16 to Eq. 5.20) was considered, which has been reported to be the best scheme to simulate smouldering peat, due to its accuracy when compared with the experiments (Huang, Rein and Chen, 2015). This scheme includes five condensed-phase species (H_2O, peat, α-char ß-char, and ash) and two gas-phase species (O_2 and Gas), and considers drying (dr), peat pyrolysis (pp), peat oxidation (po), α-char oxidation (αo) and β-char oxidation (ßo).

$$\mathrm{Peat} \cdot \nu_{\mathrm{w,dr}} H_2O \rightarrow \mathrm{Peat} + \nu_{\mathrm{w,dr}} H_2O \ (\mathrm{dr}) \tag{5.16}$$

$$\mathrm{Peat} \rightarrow \nu_{\alpha,\mathrm{pp}} \alpha\text{-char} + \nu_{\mathrm{g,pp}} \mathrm{Gas} \ (\mathrm{pp}) \tag{5.17}$$

$$\mathrm{Peat} + \nu_{\mathrm{O_2,po}} O_2 \rightarrow \nu_{\beta,\mathrm{po}} \beta\text{-char} + \nu_{\mathrm{g,po}} \mathrm{Gas} \ (\mathrm{po}) \tag{5.18}$$

$$\alpha\text{-char} + \nu_{\mathrm{O_2},\alpha\mathrm{o}} O_2 \rightarrow \nu_{\mathrm{a},\alpha\mathrm{o}} \mathrm{Ash} + \nu_{\mathrm{g},\alpha\mathrm{o}} \mathrm{Gas} \ (\alpha\mathrm{o}) \tag{5.19}$$

$$\beta\text{-char} + \nu_{\mathrm{O_2},\beta\mathrm{o}} O_2 \rightarrow \nu_{\mathrm{a},\beta\mathrm{o}} \mathrm{Ash} + \nu_{\mathrm{g},\beta\mathrm{o}} \mathrm{Gas} \ (\beta\mathrm{o}) \tag{5.20}$$

5.1.3. Thermo-physical properties and kinetics parameters

The thermo-physical properties of the condensed-phase species used in GPyro, taken from Huang, Rein and Chen (2015); Yuan, Restuccia and Rein (2021), which have optimised these values based on the accuracy of the models against experiments (see Table 5.2). The effective thermal conductivity is estimated by considering radiation heat transfer across pores (see Eq. 5.21), following Huang, Rein and Chen (2015), with $\gamma = 10^{-4}$~10^{-3} m depending on the pore size ($\gamma \sim d_{\mathrm{p}} = 1/S_{\rho}$) with the soil particle surface area S_{ρ}~0.05 m²/g (de Jonge and Mittelmeijer-Hazeleger, 1996). The permeability in GPyro ($\kappa \sim d_{\mathrm{p}}^2$) varies from 10^{-12} to 10^{-9} m². The α-char and β-char are assumed to have the same physical properties, and the ash is a homogenous mixture of natural minerals and sand. GPyro also considers tortuosity (τ), which is a ratio of actual average length (L_{a}) of the channel of fluid flow to straight-line length (L_{s}) across the medium in the porous material, which significantly influences the mass diffusion of gas species (Yuan, Restuccia and Rein, 2021). The effective diffusivity (D_{eff}), for instance, in Eq. (5.5), is the product of the diffusivity (D_{f}) of gas species in the free space and $1/\tau^2$.

$$k_{\mathrm{i}} = k_{\mathrm{s,i}}(1 - \psi_{\mathrm{i}}) + \gamma \sigma T^3 \tag{5.21}$$

Table 5.2. Physics-based properties of the condensed-phase species for the physics-based model. The values here follow Huang, Rein and Chen (2015; Yuan, Restuccia and Rein (2021).

Species (i)	ρ_i (kg/m^3)	ψ_i (–)	$k_{s,i}$ (W/m·K)	c_i (J/kg·K)	τ_i (-)
Water	1000	–	0.6	4186	n/a
Peat	110	0.927	1.0	1840	3.3
α-char	135	0.896	0.26	1260	n/a
β-char	135	0.896	0.26	1260	n/a
Ash	19.5	0.992	0.8	880	3.3
Sand	1477	0.2	0.4	920	100

The kinetics and stoichiometric parameters are taken from Huang, Rein and Chen (2015) (see Table 5.3), which have been optimised against thermogravimetric analysis of Scotland peat sample that is a similar type of boreal peat used in BARA (Christensen, Fernandez-Anez and Rein, 2020). This Scotland peat sample contains 60% *sphagnum magellanicum*, 25% *oxycoccus palustris*, 10% *scheuchzeria palustris*, 5% *sphagnum rubellum*, and trace of *carex rostara* and pine and birch woods (Cancellieri *et al.*, 2012). This peat was also expected to be non-homogeneous, for instance, in term of particle and pore sizes, since even for the commercial peat used in Christensen, Fernandez-Anez and Rein (2020), the peat sample was considerably non-homogeneous (Mooney *et al.*, 2001), thus, the natural peat sample in Huang, Rein and Chen (2015) most likely has greater degree of heterogeneity. This heterogeneity, also causes the values of parameters listed in Table 5.2 have uncertainty. Its direct influence can be seen from the heterogeneity of particle and pore sizes that control the particle density and porosity, and consequently determine the bulk density. For example, the bulk density in natural peatland can range from 10 kg/m^3 to 261 kg/m^3 (Boelter, 1968), thus, the value selected here (110 kg/m^3) can be considered the average value, which is a reasonable representative peat bulk density.

The heat of oxidation was calculated as $\Delta H_k = C_k(1 - \nu_k)$, a function of the fraction of oxidized organic matter. The oxygen consumption was related to the heat of oxidation by assuming a constant heat of combustion per unit of oxygen consumption as $\nu_{O_2,k} = \Delta H_k/(13.1\text{MJ/kg-}O_2)$ (Huggett, 1980).

Table 5.3. Kinetic and stoichiometric parameters of 5-step reactions for the physics-based model. The values here follow Huang, Rein and Chen (2015).

Parameter	dr	pp	po	αo	βo
lg Z_k (lg(s-1))	8.12	5.92	6.51	1.65	7.04
E_k (kJ/mol)	67.8	93.3	89.8	54.4	112
n_k (–)	2.37	1.01	1.03	0.54	1.85
$\nu_{B,k}$ (kg/kg)	0	0.75	0.65	0.03	0.02
ΔH_k (MJ/kg)	2.26	0.5	−3.54	−19.5	−19.5
$\nu_{O_2,k}$ (kg/kg)	0	0	0.27	1.48	1.49

5.1.4. The hybrid model (BARAPPY)

BARAPPY was developed based on a smouldering peat with heterogeneous MC experiment, a halftone configuration (see Figure 4.10a) in a deeper fuel bed (20 cm × 20 cm × 6 cm). The schematic of the BARAPPY is shown in Figure 5.2 where the leading edge in BARA is integrated with the in-depth profile of the peat decomposition from GPyro. While BARA is powerful to simulate top view of the smouldering fire, this model cannot adequately simulate the in-depth profile of the peat decomposition since there is no experiment which adequately shows this profile for the calibration (see Chapter 4). GPyro is unable to simulate the top view of the experiment unless the model use a 3-D domain that would exponentially increase the computational cost. By combining the two models, the benefits from each model can be retained and the drawbacks can be compensated.

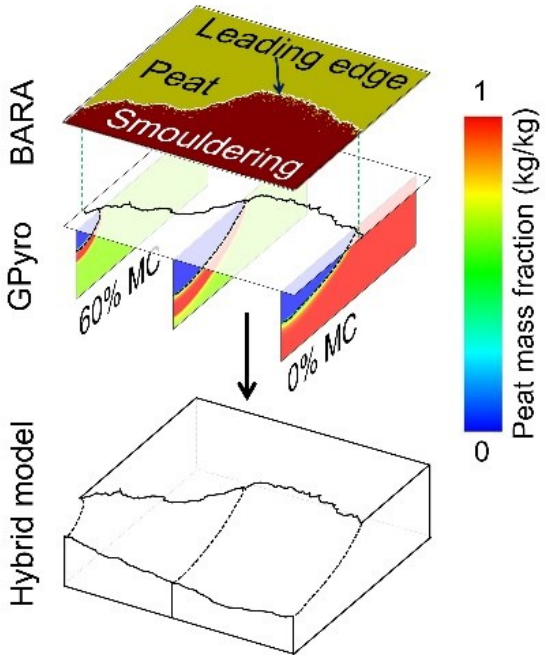

Figure 5.2. The combination of BARA and GPyro for 3-D smouldering model. The leading edge in BARA is combined with the surface of the peat from Gpyro which is represented as the interface between regions with zero fraction of peat and non-zero fraction of peat.

While the leading edge from BARA is directly obtained from the interface line between smouldering and peat states (see Figure 5.2), the in-depth profile of the peat decomposition from GPyro is obtained with several steps. To determine the in-depth profile from GPyro, the simulation results of peat mass fraction were used, which show the percentage of peat (among the other components: sand, water, gas) at certain locations. The region with 0% peat mass fraction (blue region in Figure 5.2) is assumed to be entirely filled with gas phase species since the experiments of smouldering peat with heterogeneous MC use peat with a very low IC (2.5%). The leading edge on the in-depth profile is selected as the interface line between regions with zero fraction of peat and non-zero fraction of peat (black dashed line). The region with non-zero fraction of peat correspond to the region that still has solid component, whereas the region with zero fraction of peat corresponds to the region without solid component, thus, their intersection is the surface of the peat during smouldering. This line is attached to the leading edge from BARA (black solid line) based on peat MC and the distance of the leading edge (see Figure 5.2). The in-depth profile of the peat decomposition is attached to each unit length of the leading edge, creating a surface which shows the DOB from the smouldering fire (see Figure 5.2). Since BARA and GPyro use different platform and governing rules, the hybrid model is initiated by solving GPyro, independently, and its results on the in-depth profile of the peat decomposition are stored. Once the in-depth profile data are available,

BARA is run to obtain the leading edge data. The leading edge results of BARA are combined with the corresponding in-depth profile of GPyro to create the 3-D profile of peat decomposition. While the results from GPyro are pre-stored, the results of BARAPPY are generated in real-time, matching with BARA simulation time.

5.2. Results and Discussions

5.2.1. Validation and comparison between the models

The models were validated based on the horizontal spread rate and smouldering width, which is the distance between the leading and trailing edges of the smouldering. Figure 5.3 shows the comparison between the CA (BARA), the physics-based model (GPyro), and the experiments with dry basis MC (IC) of 20% (0%) and 40% (40%). Since the GPyro used symmetry, the results shown in Figure 5.3 are the results of GPyro after being mirrored on the symmetrical plane. The smouldering region in GPyro is determined based on the region with temperature exceeding 600^{o}C (Huang, Rein and Chen, 2015). The results of BARA show the top view of the experiments, where the smouldering region is represented as the maroon colour. Figure 5.3 shows that BARA and GPyro accurately simulate the smouldering peat experiments at different MC and IC combinations. Both the models have good agreement with experiments in term of horizontal spread rate and smouldering width.

Figure 5.4 compares the predictions of GPyro and BARA to the experiments in term of horizontal spread rate and smouldering width. The black dashed line in Figure 5.4 represents the average of the experimental results, if the predictions of GPyro or BARA overlap with this line, then they have 0% error. For horizontal spread rate, all of the BARA predictions are within the experimental uncertainty (grey shade), while one-thirds of the GPyro predictions are outside the experimental uncertainty. For smouldering width, while all BARA predictions are within the experimental uncertainty, only one-quarters of the GPyro predictions are within the experimental uncertainty. However, for both horizontal spread rate and smouldering width, the predictions of GPyro are within 30% deviation from the experiments; and its average errors are within experimental uncertainty. Therefore, both BARA and GPyro provide powerful tools to simulate smouldering fire with a reasonable accuracy.

The higher accuracy of BARA compared to GPyro stems from the different level of generality between the two models. While GPyro includes kinetics parameters which are the results of optimisation against thermogravimetric experiments, the rest of the predictions (heat and mass transports) are the solutions of conservation equations (Eq. 5.1 to Eq. 5.6). On the other hand, BARA is optimised to a particularly detailed level to

the experiments in Christensen, Fernandez-Anez and Rein (2020), up to the level of heat transport and smouldering dynamics. GPyro would have the same level of accuracy (higher than 70%) when it is used to simulate different smouldering experiments. Meanwhile, BARA would have lower accuracy than 90%, possibly even lower than GPyro, when it is simulating different smouldering experiments (blind predictions), if no optimisation or calibration process is involved.

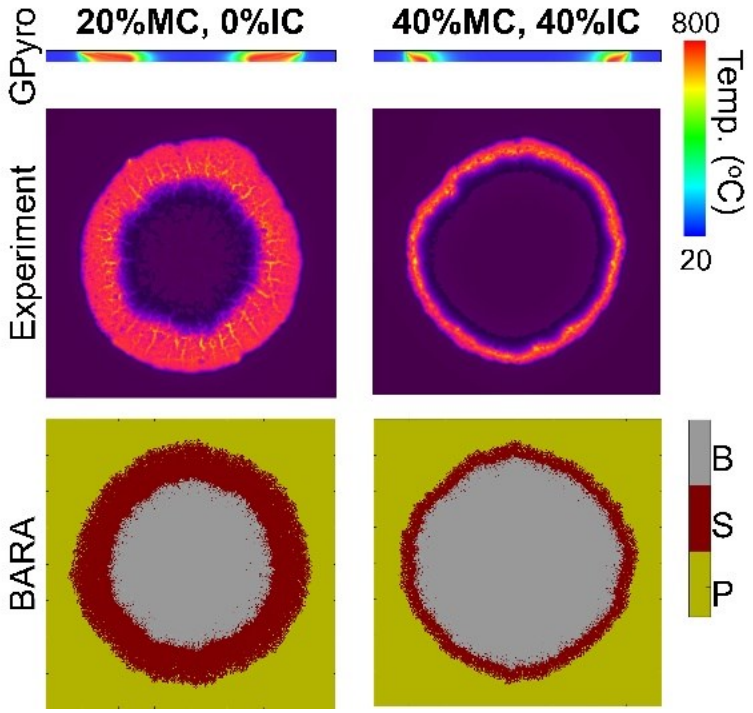

Figure 5.3. The validation and comparison of BARA (top view) with GPyro (side view). Two peat conditions, 20% MC – 0% IC and 40% MC – 40% IC are shown here, with both models accurately simulate 10 other conditions. P, S, and B are Peat*,* Smouldering*, and* Burnt *respectively.*

Another benefit of GPyro is the level of detail that can be obtained from the model results. While BARA only provides the smouldering region, GPyro provides results such as the distribution of temperature and distribution of species in the condensed-phase fuel bed. Therefore, by using GPyro, many phenomena can be studied, for instance, the region of dry peat, pyrolysis, and oxidation. However, BARA is significantly more computationally efficient than GPyro. BARA completed the calculation of one simulation, such as the ones shown in Figure 5.3, within 1h, whereas GPyro completed the calculation of the same experiment in 237h on the same computer. Therefore, physics-based models benefit from the accuracy of blind prediction and the level of detail of the phenomena to be captured, whereas cellular automata benefit from higher computational efficiency which is of utmost importance for large computational domain applications, such as field-scale. Since both BARA and GPyro are validated and both have good agreement with the

experiments in Christensen, Fernandez-Anez and Rein (2020), the hybrid of the two models (BARAPPY) are expected to have reasonable accuracy.

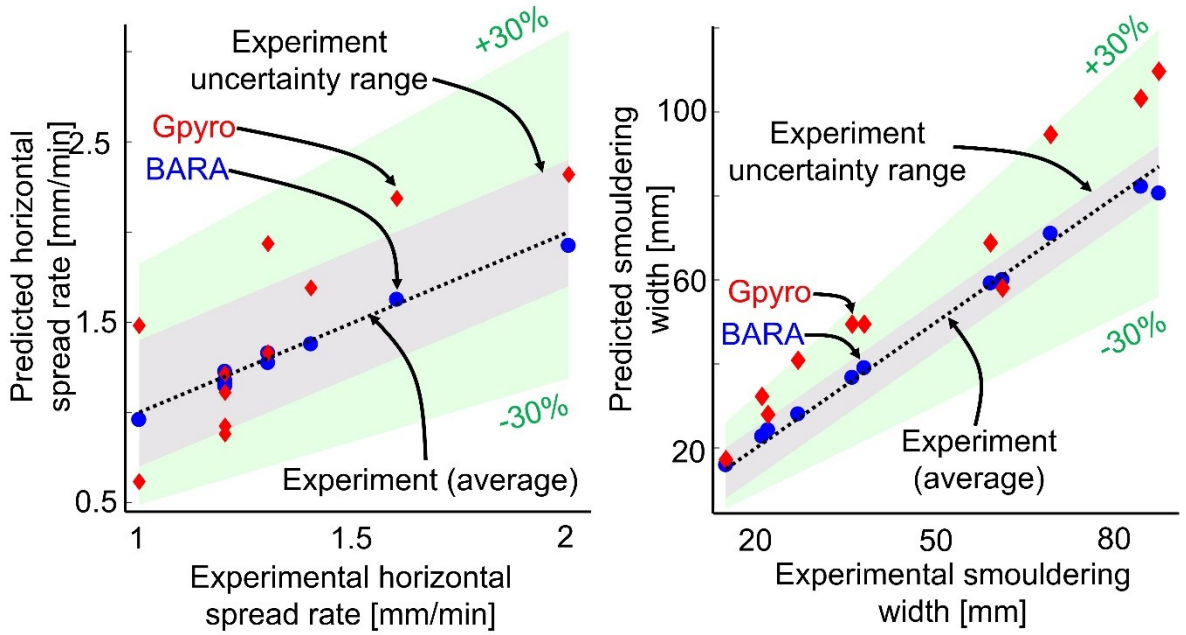

Figure 5.4. The prediction comparison between BARA (blue circle) and GPyro (red diamond) on horizontal spread rate (top) *and smouldering width* (bottom)*. The black dashed line is the average results of experiment, the grey shade is the experiment uncertainty, and the green shade is the region within 30% error from experiments and their uncertainty.*

5.2.2. 3-D Simulation of smouldering depth of burn

BARAPPY was used to simulate an experiment of smouldering peat with 60% MC (wet) on the left side and 0% MC (dry) on the right side (see Figure 5.5). Since BARAPPY is a 3-D model, apart from the smouldering region, the model also shows the structure of the smouldering peat caused by DOB. Figure 5.5 shows the simulation result of BARAPPY and its comparison with the experiment at two different times (t1 and t2). BARAPPY accurately simulated the experiment of smouldering peat with heterogeneous MC at both times. In the top view of the simulation, wet and dry peat have different distance of leading edge which is connected by an inclined line. This inclined line is part of the wet peat, where its tip is connected to the dry peat that has a relatively flat edge.

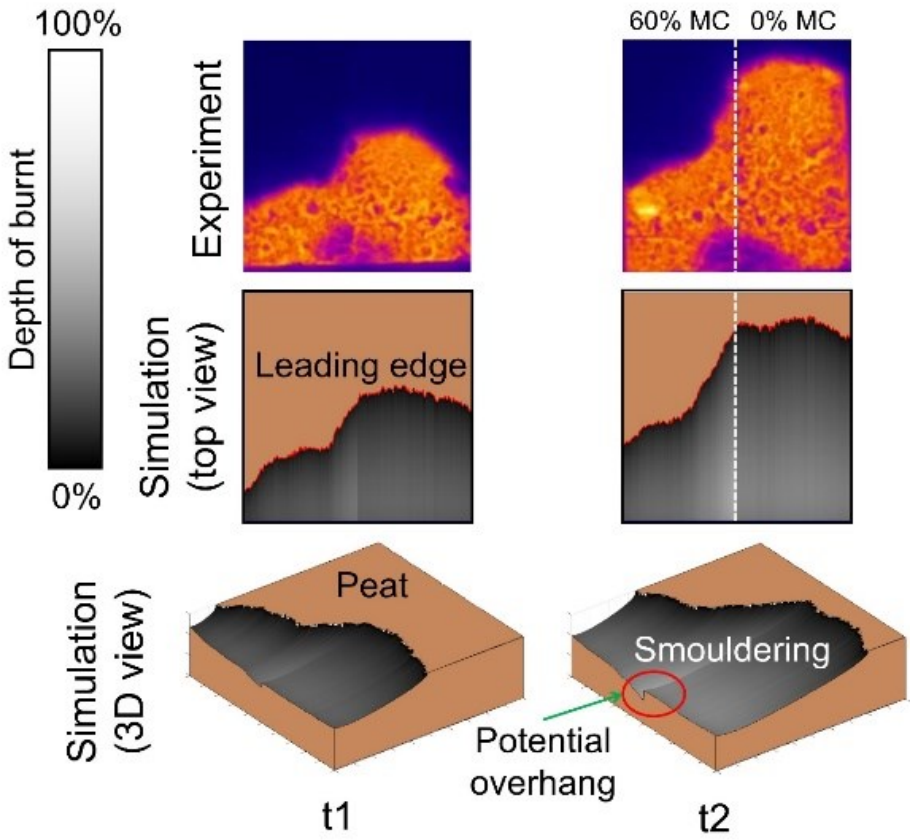

Figure 5.5. The results of the hybrid model (BARAPPY) and its validation against experiment at two different time-steps. The white dashed lines separate wet and dry peat. The smouldering region is quantified based on depth of burn, where black represent 0% burnt, white represents 100% of the reactor thickness has burnt, and grey represent the DOB between 0% to 100% of the reactor thickness. From the 3-D view overhang (red ellipses) are observed.

In Figure 5.5, the DOB of BARAPPY is represented as percentage of the reactor thickness, thus, 100% DOB corresponds to the smouldering having reached the bottom of the reactor. The DOB in the experiment is predicted to be non-uniform, especially in the wet peat. This finding stems from the leading edge in the wet peat which is stretched to create the inclined edge connected to the leading edge in the dry peat. Thus, inclined edge means that near the wet and dry peat interface, the wet peat has been smouldering approximately as long as the dry peat. Since the parts with the shorter leading edge in the wet peat are smouldering for a shorter time, the DOB near the wet-dry peat interface is greater than the other part. This pattern remains similar over time, which leads to the non-linear increment of the volume of soil loss. By using BARAPPY, therefore, the effect of smouldering on the degradation of peat can be estimated.

BARAPPY simulates an overhang phenomenon, a commonly observed phenomenon in peatland wildfire (Huang *et al.*, 2016), where smouldering creates a burrow when spreading, instead of spreading at the surface (see Figure 5.5). This

phenomenon is a very important phenomenon, especially for the detection of smouldering wildfire. The overhang can be caused by the non-uniformity of DOB which in BARAPPY is significant in the wet peat. The non-uniformity of DOB is caused by the inclined line that connects the leading edge of wet and dry peat. Therefore, overhang can be found near the interface between wet and dry peat, where the wet peat has been smouldering similarly long as the dry peat. This finding conforms to Christensen, Fernandez-Anez and Rein (2020), where smouldering spreads faster vertically in wetter peat, which can be explained by a decrease in organic density with MC. While horizontal spread rate is governed by the rate of drying and pyrolysis during the smouldering, in-depth spread rate is also affected by the amount of peat to burn, which is controlled by the organic density (Christensen, Fernandez-Anez and Rein, 2020). The limiting factor that control in-depth spread rate are the slower rate between the consumption of organic component in peat and drying and pyrolysis rate, thus, if the rate of consumption of organic component is slower than drying and pyrolysis rate, in-depth spread rate is a function of this consumption rate, i.e., organic density (Christensen, Fernandez-Anez and Rein, 2020). However, the consumption rate of the organic component should be slower than the drying and pyrolysis rate, otherwise, all the organic component would have burnt (e.g., in a very high MC) but the drying or pyrolysis process has not finished, thus, there is no longer energy provided to facilitate the drying and pyrolysis and the smouldering does not sustain (Christensen, Fernandez-Anez and Rein, 2020).

Overhang is formed when the convective cooling at the surface is significantly stronger than the heat generation of smouldering at the surface (Huang *et al.*, 2016). Therefore, overhang tends to occur in wet peat which generates relatively low net heat due to the required process of moisture evaporation, causing the effect of heat loss at the surface (aided with convective cooling) to be prevalent. This is also reported in Amin, Hu and Rein (2020) that the overhang phenomenon only happens in wet peat sample (50% MC or wetter).

BARAPPY successfully visualises the role of wet peat in the overhang formation in a more detailed manner than previously reported in literatures. Overhang is initiated with the non-uniformity of DOB, which is supported by the direction of the smouldering spread. From BARAPPY simulation, it is argued that the step of DOB is required to initiate overhang, which agrees with Huang *et al.* (2016). With this step profile, the airflow near the step is almost stagnant, thus, the convective cooling is significantly weaker. Due to this weaker cooling, the smouldering favour the spread near the step (see Figure 5.6a), forming overhang. Without a step of DOB, the convective cooling and oxygen

supply in the entire fuel bed is not significantly different. An example of this condition was observed in experiments by Huang and Rein (2017) on smouldering peat in a column reactor which spread downward. Although ranges of peat MC were considered, overhang phenomenon was not reported, meaning that in a column reactor, the downward spread across the cross section is relatively uniform which does not accommodate the step of DOB.

The height of the step of DOB increase linearly with the increase of MC difference (see Figure 5.7). By using 5% threshold of the ratio of step height and reactor thickness, the critical MC difference at which overhang can be potentially initiated is 20%. This finding indicates that BARAPPY, with the help of peat MC data which are readily available, can help finding the location at which subsurface smouldering could happen in natural peatland, which have spatially non-uniform peat MC (Bechtold *et al.*, 2018).

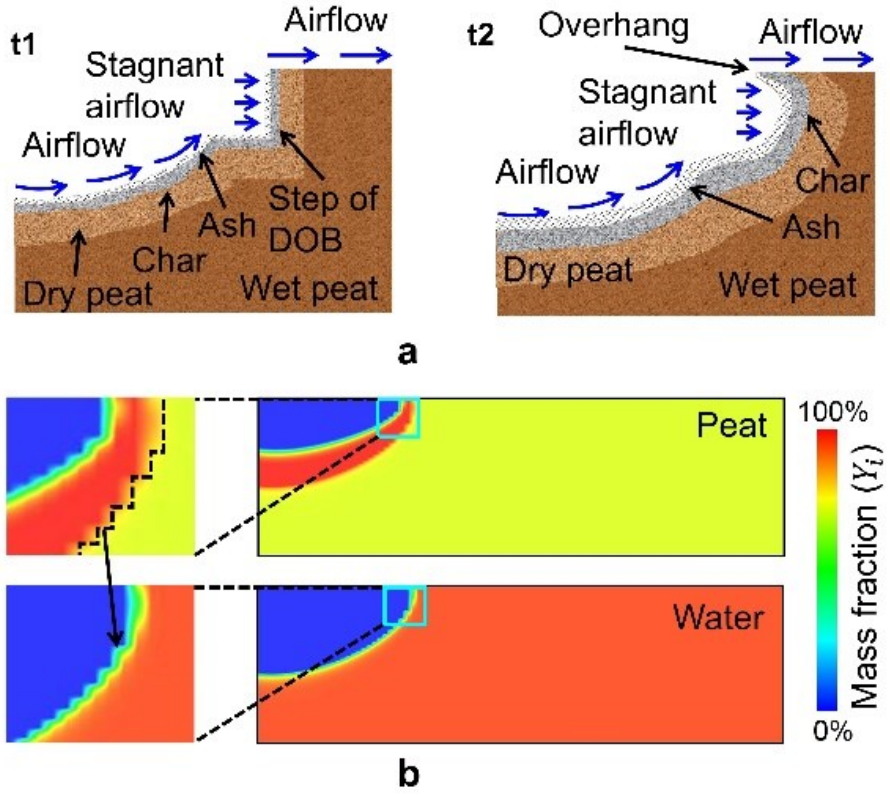

Figure 5.6. (a) Schematic of the formation of overhang which is initiated by step of DOB. (b) Steps of DOB of peat (top) *in the GPyro simulation (on peat with 60% MC) which correspond to steps of the peat MC distribution* (bottom)*.*

While in BARAPPY the step of DOB is formed clearly because of the MC difference between wet and dry peat, in Amin, Hu and Rein (2020) which used peat with uniform MC, the step is potentially formed because of the MC profile post drying process. GPyro simulation on smouldering peat with uniform MC in a deeper reactor shows that there

are steps of DOB formed near the leading edge, the location at which overhang is reported in Amin, Hu and Rein (2020) (Figure 5.6b *top*), which correspond to the step profile of MC (Figure 5.6b *bottom*). By using GPyro on wetter and drier peat, the steps of DOB and MC profile were found to be more significant in wetter peat. This finding confirm with the report of Amin, Hu and Rein (2020) on the formation of overhang. Therefore, this chapter improves the understanding of overhang phenomenon, in which overhang is initiated by step of DOB which is formed due to MC gradient either from the non-uniformity of peat condition (the real situation in natural peatland) or from the hydrological process inside the peat during smouldering (moisture diffusion and drying process).

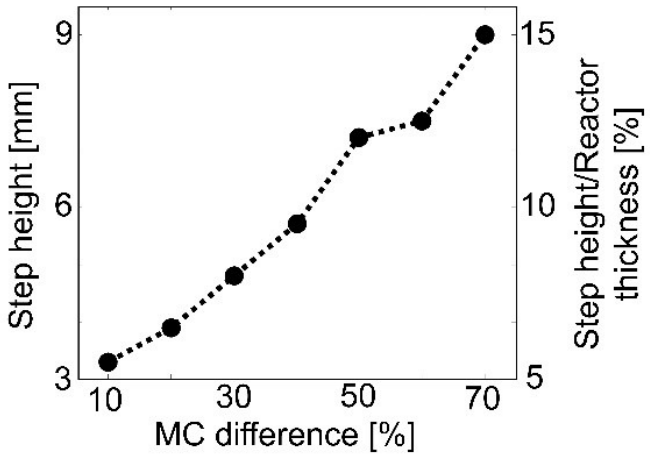

Figure 5.7. Height of the step of DOB with respect to the MC difference between wet and dry peat.

5.3. Conclusions

In this chapter, a hybrid computational tool of cellular automata (BARA) and physics-based model (GPyro) is developed, for the first time, to investigate smouldering combustion in a 3-D domain. BARA and GPyro were independently validated against laboratory-controlled experiments and was found to have accuracy on spread rate and smouldering width to be higher than 90% for BARA and higher than 70% for GPyro; the average error of both the models are within experimental uncertainty. The main benefit of BARA is its computational efficiency, which is 240 times higher than GPyro. The main benefit of GPyro is the level of generality and detail that can be acquired such as temperature, species, and reaction profiles. The hybrid model (BARAPPY) of BARA and GPyro was used to simulate an experiment of smouldering peat with non-uniform MC, a half wet-half dry MC configuration. The predictions from BARAPPY have good agreement with the experiment (the profiles of leading and trailing edges and spread rate) and the 3-D structure of the smouldering peat surface are obtained and investigated.

In wet peat, the depth of burn (DOB) is non-uniform, caused by the step profile of the leading edge. This profile also formed a step of DOB at the interface between wet and dry peat, and enabled BARAPPY to simulate overhang phenomenon. The DOB step height increases linearly with the MC gradient between wet and dry peat, and overhang is initiated when the MC gradient is higher than 20%. The initiation of overhang by the step of DOB conforms to Huang *et al.* (2016), thus, this chapter provides analysis on the creation of the step of DOB, improving the understanding of overhang in Huang *et al.* (2016); Amin, Hu and Rein (2020). The findings and model contribute to the better understanding on the depth of burn of smouldering peat and provide the tool to estimate it, thus, can help estimate the peat loss due to smouldering wildfires, an estimation that can be used to strategize the restoration and management of peatlands.

Chapter 6 – KAPAS: Cellular Automata Model to Simulate Field-Scale Flaming and Smouldering Wildfires in Tropical Peatlands

Summary[5]

This chapter investigated both flaming and smouldering in peatland wildfires at the field-scale by using a 2-D cellular automata model (KAPAS). KAPAS was calibrated against existing experiments in the literatures and used to predict the effect of peat MC on the behaviour of peatland wildfires. The model simulated how flaming initiates smouldering hotspots and how these hotspots merge – flaming spreads rapidly, consuming surface vegetation, leaving behind hotspots of smouldering peat which consumes most of the peat. KAPAS was then applied to study a prescribed fire that was performed in a 573 ha of peatland in Borneo in 2015, observed by drone footage. KAPAS was validated based on the number of smouldering hotspots against drone footage (flaming burned the entire plot in both field observation and simulation), with ~80% accuracy, and predicted that 2.9 ha of peatland burnt after 3 months with 70% peat MC (dry-based). By performing faster-than-real-time simulations, the model showed that the smouldering burnt area has an inverse exponential correlation with the peat MC, thus, the 2.9 ha burnt area could have been reduced to 0.02 ha if the peat MC had been above 100%, for instance, by performing prescribed fire in wet seasons or performing rewetting treatment to the peatland. This chapter improves the fundamental understanding of how peatland wildfires spread at the field-scale which has received little attention until now, and provide a tool to perform faster-than-real-time simulations, which can help with mitigating peatland wildfires.

6.1. The Development of KAPAS

6.1.1. Introduction to KAPAS

This chapter aims to create the simplest 2-D CA model that could still adequately capture the behaviour seen in peatland wildfires involving flaming and smouldering

[5] This chapter is based on "Dwi M J Purnomo, Matthew Bonner, Samaneh Moafi, Guillermo Rein, 2021. Using cellular automata to simulate field-scale flaming and smouldering wildfires in tropical peatlands. *Proceeding of Combustion Institute*, 38(3), pp. 5119–5127."

combustion. Inspired by previous CA studies (see Chapter 3), bond percolation approach was selected, for both flaming and smouldering. Bond percolation can be applied to wildfires, where the connections in bond percolation represent the flammability of the surrounding fuels when they are consumed by the fire (see details in Chapter 3).

BARA (see Chapter 4) was not used in this early stage of field-scale peatland wildfires modelling, because of two reasons: BARA is significantly more complex than bond percolation, and BARA has not considered field-scale domain, thus, the upscale of BARA is required prior to the integration with the flaming model. Since BARA is more complex than bond percolation, although BARA provide more detail results such as the 3D spread of smouldering, the computational cost of the model could increase significantly (see Chapter 8), especially when it is applied for field-scale modelling and consider an integration with flaming model. This chapter offers option for the users to decide which model is suitable for the emerging cases, for instance, the detail results from upscale version of BARA might not be necessary when the aim is to develop optimum strategy to mitigate peatland wildfires such as the allocation of resources based on faster-than-real-time simulations. Instead, faster simulation is more important, thus, more scenario can be tested and better strategy can be developed. For comparison, BARA simulates with 20 times faster-than-real-time speed (see Chapter 4), and from the comparative study in Chapter 8, bond percolation is 10 times faster than BARA, thus, by using bond percolation instead of BARA, 10 times more scenario can be tested when developing mitigation strategy.

In the model, an unburned cell will update itself to a burning cell with a probability P if there are other burning cells in its neighbourhood. The most used neighbourhood in the literature was chosen, known as a Moore neighbourhood – the eight cells directly surrounding the considered cell in a 3 × 3 square grid (see details in Chapter 3). From here on, the model in this chapter will be referred to as KAPAS, which stems from the abbreviation of "Cellular Automata for Flaming and Smouldering" and "cotton" in Indonesian language, a material that can facilitate both flaming and smouldering.

6.1.2. States and rules of KAPAS

KAPAS considers 5 possible states for each cell: *surface vegetation (SV), flaming vegetation (FV), exposed peat (EP), smouldering peat (SP),* and *burned peat (BP)* (see Figure 6.1). *EP* represents a cell which has lost its surface vegetation, due to flaming, but the peat underneath it remains intact since the smouldering has not started. These states represent the smallest number of states that can still capture the interaction between flaming and smouldering of two fuel types in peatlands. For simplicity, KAPAS did not

consider the possibility of flaming peat, because it happens rarely (Huang and Rein, 2015). KAPAS is initiated at $t = 0$ by igniting particular cells (i.e., changing from *SV* to *FV*). These *FV* cells will update their states after each time-step to either *EP* or *SP*, based on the probability of transition between flaming and smouldering P_t. Surface vegetation is limited compared to peat deposits and burn much faster with flaming (Huang and Rein, 2015), thus, *FV* has a 100% chance to transition to *EP* or *SP*. *SV* cells nearby any *FV* cell may become *FV* cells with probability P_f. *EP* cells nearby any *SP* cell may become *SP* cells with probability P_s. Finally, *SP* cells have a probability of extinguishing to become *BP* cells, with probability P_e.

KAPAS considers the surface vegetation and soil as 2 separate layers of cellular automata (multi-domain approach, see Chapter 1), meaning that smouldering can spread to nearby peat even if there is still surface vegetation above (see Figure 6.1). This multi-layer approach was inspired by Fernandez-Anez, Christensen and Rein (2017); Fernandez-Anez *et al.* (2019), which firstly (and most likely the only ones, based on the literature review of CA for wildfire modelling) introduced the concept of multi-layer approach in CA for fire modelling. Without using separate layers, the smouldering spread which reach unburned surface vegetation or firebreaks cannot be simulated, since it means that intact surface vegetation or firebreaks have to change to become smouldering peat. The change from surface vegetation directly to smouldering peat is not considered in the model since this transition involve significant additional phenomena such as transition from smouldering to flaming (Santoso *et al.*, 2019). The change from firebreaks to smouldering peat is also not possible since firebreaks are non-flammable cells. However, smouldering can spread underneath both intact surface vegetation and firebreaks. By using two separate layers, the intact surface vegetation and firebreaks do not change state in the surface layer, however, the cells in the soil layer change to smouldering peat.

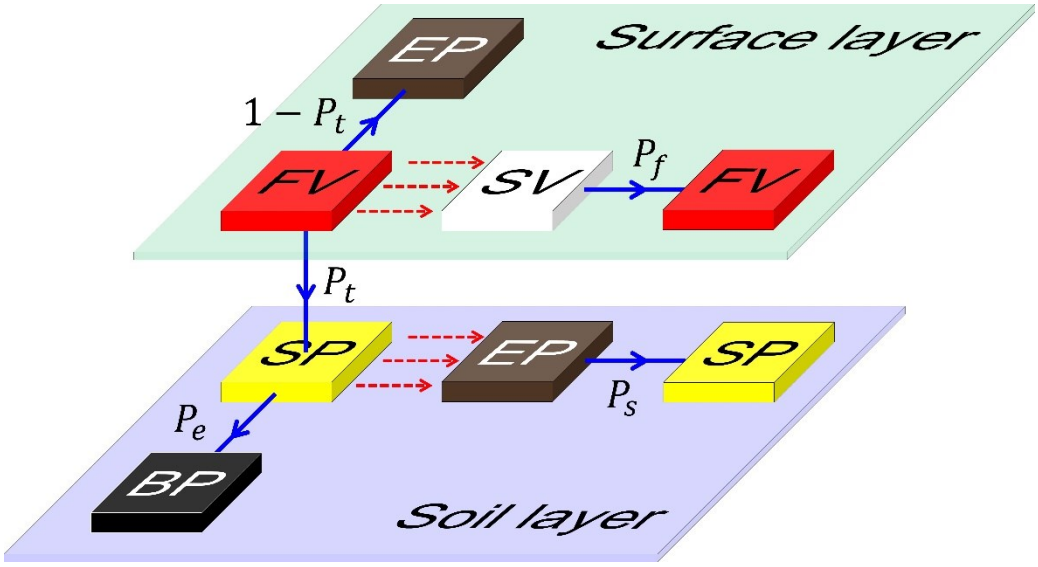

Figure 6.1. The states and rules of the model. SV is surface vegetation, FV is flaming vegetation, EP is exposed peat, SP is smouldering peat, BP is burned peat, and P_x are probabilities of state change. Solid arrows represent state change, whereas dotted arrows represent the influence from neighbouring cells.

The ability of KAPAS to represent coupling between flaming and smouldering combustion in peatlands is dependent on the choice of the four parameters P_f, P_t, P_s, and P_e. Such parameters are often found by fitting to a particular fire, however, in KAPAS, they were chosen based on many different sources and experimental studies, allowing the model to be more general in principle.

6.1.3. Selecting parameter values

The flame spread probability P_f was chosen by finding a base probability P_R of flaming spread rate based on the Rothermel model for surface fire spread (Rothermel, 1972), augmented by a parameter representing the effect of wind α_w. The spread rate (R) was estimated by using Rothermel semi-physical model (Rothermel, 1972), with a 0 m/s wind speed. P_R depends on both the cell size and time-step duration, as it is found by optimising a probability that enable KAPAS to produce R as its spread rate when applied to a cell of Δx m in size and time-step Δt seconds over many time-steps. In this chapter, with a cell size of 4.5m and a time-step of 300s, $P_R = 0.03$. These cell size and time-step were selected based on the highest resolution can be run with the available computing power.

P_R is then augmented by a wind parameter (α_w), following on from Alexandridis *et al.* (2008), which depends on the wind speed V, at around 6 m height above ground (weather station), and the angle between the fire propagation and the wind direction θ as shown in Eq. 6.1, where $c_1 = 0.045$ and $c_2 = 0.131$, following the work of Alexandridis *et*

al. (2008). The final probability of flame spread is then shown in Eq. 6.2, which means that each cell in the neighbourhood will have a different P_f depending on their relationship to the wind direction.

$$\alpha_w = \exp\left(U\left(c_1 - c_2(1 - \cos\theta)\right)\right) \tag{6.1}$$

$$P_f = P_R \cdot \alpha_w \tag{6.2}$$

Standard Rothermel model account for the wind effect, however, implementing this directly into KAPAS would significantly increase its computational cost, since P_R would need to be re-optimised every time the wind condition changed. For this reason, this method has never been used for *bond percolation* CA. By decoupling the wind effect as a separate parameter (P_f depends on P_R and α_w), KAPAS can simulate fires with different wind conditions in a computationally efficient way.

The probability of transition from flaming to smouldering P_t was found by adapting the work in Frandsen (1997), which investigated the smouldering ignition probability of peat based on its MC, inorganic content (IC), and bulk density (ρ). For simplicity, only MC was varied in this chapter, as this is the most important property of peat for fire (Rein, 2013). IC and ρ were set to 3.7% and 222 kg/m^3 respectively (Frandsen, 1997; Nusantara, Hazriani and Suryadi, 2018). This left P_t with a sigmoid relationship with respect to MC, shown in Figure 6.2a. The sigmoid relationship between P_t and MC has been observed in laboratory-controlled experiments (Frandsen, 1997), but there is no work that is found to confirm this relationship in a natural peatland. However, since the work of Frandsen, (1997) considers the three most important factors that control smouldering behaviour: MC, IC, and bulk density (Rein, 2016; Christensen, Fernandez-Anez and Rein, 2020); the sigmoid relationship between P_t and MC is expected to prevail in natural peatlands.

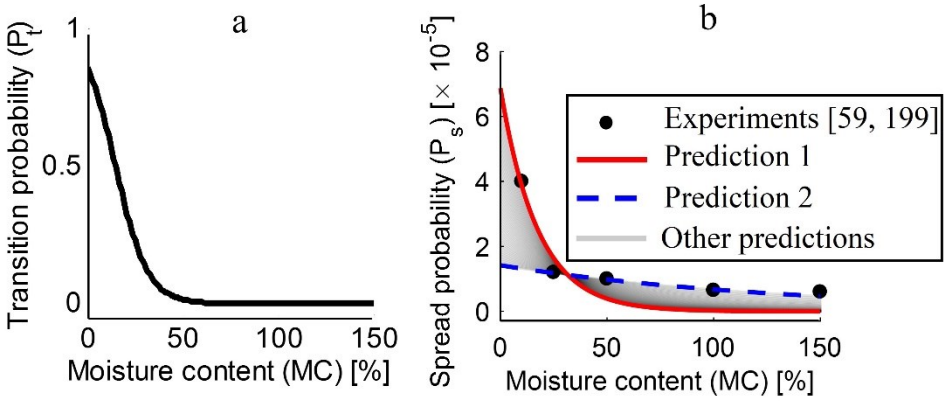

Figure 6.2. Dependency on moisture content for (a) P_t and (b) P_s. The shape of these relationships are extracted from literature (Frandsen, 1997; Huang *et al.*, 2016; Prat-Guitart *et al.*, 2016b). *Prediction 1 uses c_3 = 9.58 and c_4 = 0.057, whereas prediction 2 uses c_3 = 11.2 and c_4 = 0.006.*

The smouldering spread probability P_s was found by comparing smouldering spread rates taken from experiments on peat at different MC (Huang *et al.*, 2016; Prat-Guitart *et al.*, 2016b). These spread rates are also given in cm/min, therefore, P_s is dependent on cell size and time-step duration, similar to P_R. These experiments used boreal peat, as studies on tropical peat are limited (Usup *et al.*, 2004). When MC, IC, and ρ have been considered, the resulting probabilities are expected to vary relatively little between tropical and boreal peats. Assuming P_s also has a sigmoid relationship (Eq. 6.3) with respect to MC (similar to P_t) a variety of different curves could be fitted to the experiments considered, by changing c_3 and c_4, as shown in Figure 6.2b. The grey lines in Figure 6.2b represent predictions which have good agreement with experiments. These plausible predictions are bounded by two polar opposite predictions, prediction 1 and 2. Prediction 1 has high accuracy for lower MC and low accuracy for higher MC, whereas prediction 2 is the opposite. Among the plausible predictions, prediction 1 ($c_3 = 9.58$ and $c_4 = 0.057$) was selected to determine P_s on a specific MC for KAPAS, because this prediction has the highest accuracy for peat with lower MC, which poses a greater hazard in fire.

$$P_s = \frac{1}{1+\exp(c_3+c_4\mathrm{MC})} \tag{6.3}$$

The smouldering extinction probability P_e was chosen based on the persistency of smouldering fire, i.e., once ignited, smouldering fires are very difficult to extinguish and will continue to burn for a long time (Rein, 2013). These fires extinguish when they encounter a ground water table (GWT) or mineral layer. In Indonesian peatlands, the peat layer is deep and the GWT is low in dry season (Hayasaka, Usup and Naito, 2020). These typical conditions were considered (deep peat layer and low GWT) in the model. Therefore, to make the smouldering fire remain active for a long time in KAPAS, P_e is set to be much lower than P_s. Setting P_e to be much lower than P_s means the smouldering fire remain active after the smouldering fire front has propagated relatively distant, which shows that the fire also has in-depth spread. Unfortunately, no previous work was found that could be used to derive P_e directly. Therefore, in KAPAS, the value was chosen to be 5×10^{-7} to represent this persistency, three order of magnitude lower than the minimum value of P_s.

6.2. Results and Discussions

6.2.1. Effect of moisture content in uniform fuel grid

KAPAS was used to investigate the effect of MC on both smouldering spread and the transition from flaming to smouldering. This investigation began by considering a

uniform fuel grid (simplest case), completely filled with surface vegetation, and ignited in the centre (see Figure 6.3a). The flaming spread and ignite the peat underneath (see Figure 6.3b), which then grow bigger over time (see Figure 6.3c). In the model, MC was varied from 0 to 150% in increments of 10%. KAPAS was run for a total duration of 10,000 time-steps (35 days in real time) in this first case. This total duration is selected since smouldering wildfires spread slowly and sustain for weeks (Rein, 2013). The wind effect was ignored ($\alpha_w = 1$) in this first case, to isolate the effect from varying MC.

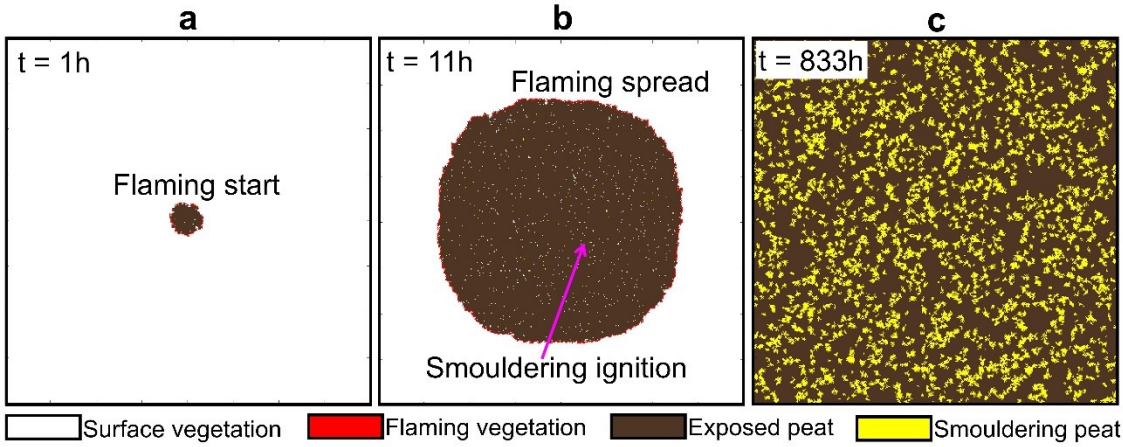

Figure 6.3. The visualization of the model for one specified moisture content (50%) which shows: (a) the ignition of flaming, (b) flaming spread and smouldering ignition, and (c) smouldering spread. The surface flaming is initiated at the centre of the domain which then ignite the soil.

A grid of 400 x 400 cells (representing 324 ha) was used in this uniform fuel grid. This large grid size was used to avoid the finite size effect and minimize the uncertainty. Based on a sensitivity analysis, shown in Figure 6.4, the burnt ratio (φ_b) and their standard deviation (from 10 simulation repetitions) do not differ significantly once the grid size is larger than 400 x 400 cells. φ_b is calculated as the sum of *smouldering peat* (*SP)* and *burned peat* (*BP)* cells in the peat layer, divided by the total number of cells in the grid (i.e., area of the grid burned / total area of the grid). A sensitivity analysis was also performed on P_f as shown in Figure 6.5. This analysis shows that P_f does not significantly affect φ_b and their uncertainty.

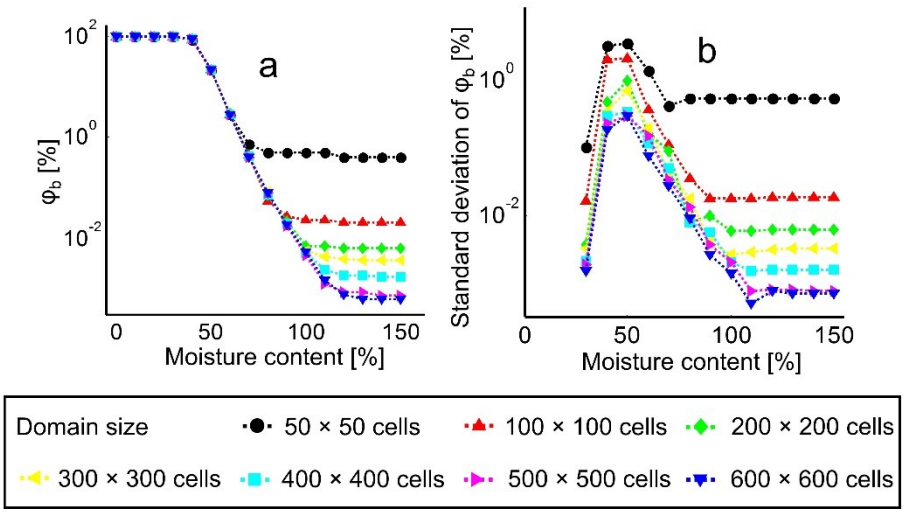

Figure 6.4. Sensitivity analysis of the simplified grid model based on different domain size. The analysis focus on: (a) φ_b, and (b) their standard deviation of 10 repetition. Smaller domain size has higher uncertainty and result in higher φ_b. Higher domain size converge both φ_b and their standard deviation.

Figure 6.6 shows φ_b at every 3.5 day (1,000 time-steps) after flaming ignition with increasing peat MC for IC of 3.7%. The line fitted through the blue circles represents φ_b immediately after all surface vegetation has been consumed, which only considers cells ignited from the transition from flaming to smouldering (P_t), which is referred to as the *transition ratio*. The line fitted through the red diamonds represents the final φ_b after 35 days. This is the *final burnt ratio*. The error bar in both transition and final burnt ratio represent the uncertainties of the simulation which are repeated 50 times for each MC.

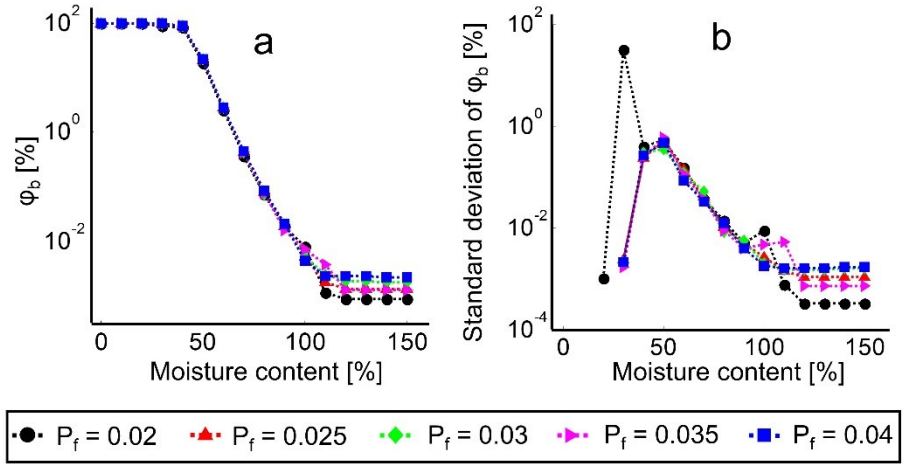

Figure 6.5. Sensitivity analysis of the uniform fuel grid model based on different flame spread probability (P_f). The analysis focus on: (a) φ_b, and (b) their standard deviation of 10 repetition. Different P_f does not significantly affect φ_b and their uncertainty.

The transition ratio follows a sigmoid relationship with MC, as would be expected from its dependence on P_t. This curve deviates from the ignition probability in Frandsen (1997) on average by 5.3%. KAPAS, therefore, demonstrates a novel way to augment the findings for ignition of smouldering of Frandsen (1997) (igniting peat with a metal coil) in the context of real wildfires. The final burnt ratio also follows a sigmoid relationship with respect to MC, which might be expected from the relationship of P_s. However, the shape of this sigmoid is significantly different from the sigmoid of the relationship between P_s and MC (see Figure 6.2b). Therefore, there are important interactions between the smouldering and flaming layers of the model, demonstrating the value of considering both layers.

At high MC, the uncertainty of final burnt ratio become significantly higher. This finding implies that near the critical MC, KAPAS becomes a volatile model. A plausible explanation for this behaviour is due to the nucleation of smouldering hotspots that have high uncertainty near the critical MC. When the peat MC is near critical and identical simulations were run repeatedly, there are cases where no smouldering hotspots were nucleated and there are cases where several smouldering hotspots were nucleated. At critical MC, it is expected that no smouldering hotspots are nucleated, thus, when due to the probabilistic approach after numbers of identical simulations smouldering hotspots are nucleated, it causes significant increase on the final burnt ratio. Referring to Figure 6.6, although the upper limit of the final burnt ratio is relatively high, the average final burnt ratio is close to zero. Therefore, although sometimes smouldering hotspots are nucleated at critical MC, most of the times these hotspots are not nucleated, which is the expected results.

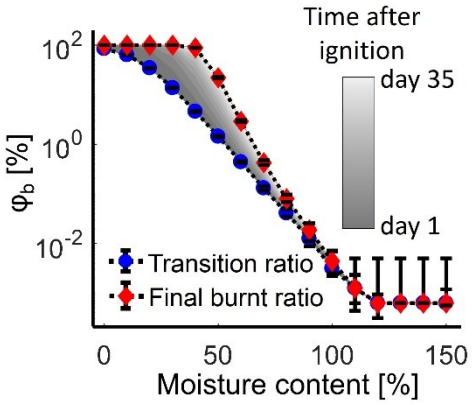

Figure 6.6. Predicted φ_b for different moisture contents. The colour gradation represents φ_b every 3.5 days (1000 time steps). Each simulation is repeated 50 times to report uncertainty (error bars) and the averages are shown (symbols and colour bar).

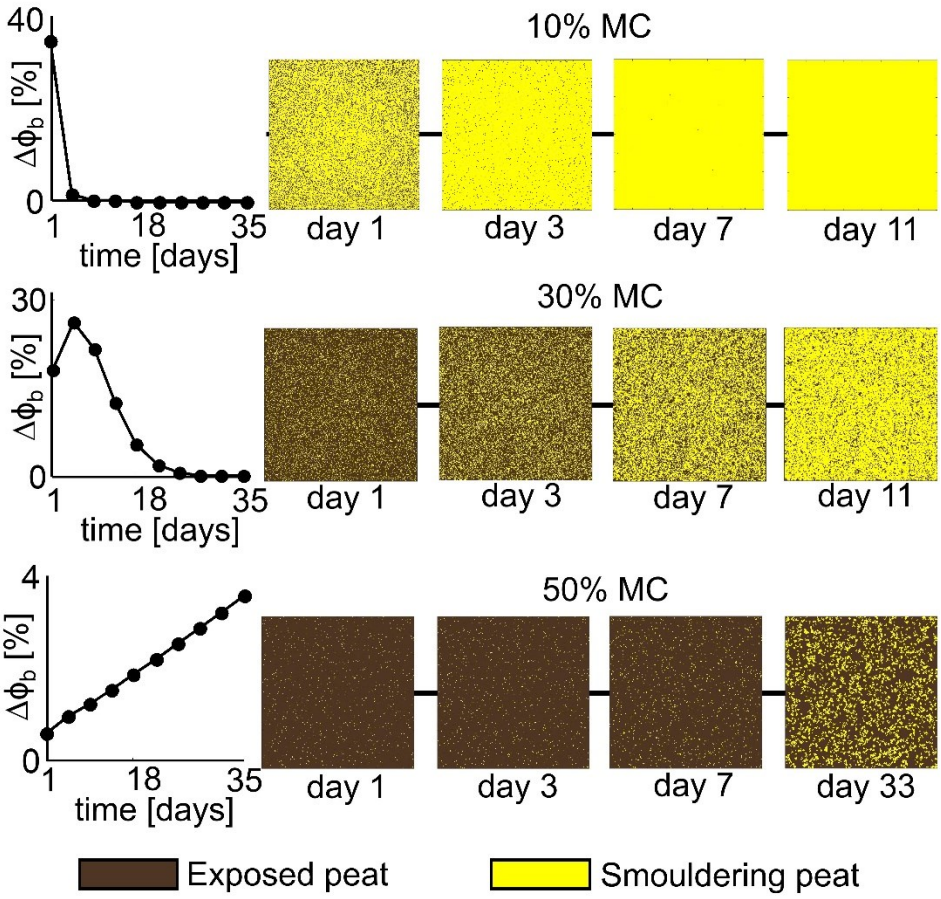

Figure 6.7. Predicted $\Delta\varphi_b$ with time and snapshots of the domain (400 x 400 cells) at different times and MC. $\Delta\varphi_b$ is relative to the previous 3.5 day.

Figure 6.7 shows the evolution of burnt ratio with time for 3 different MC values. The burnt ratio change ($\Delta\varphi_b$) is equal to the current value of φ_b minus the value of φ_b 3.5 day earlier. If the peat was ignited at the centre and allowed to spread with no interaction with the flaming vegetation, then $\Delta\varphi_b$ would increase linearly with time as the smouldering fire grew simply from one single hotspot. However, Figure 6.7 demonstrates that in the multi-layer model this linear growth only happens at high MC. At lower MC, $\Delta\varphi_b$ decreases with time after an initial increase. This decrease is caused by separate areas of smouldering peat (hotspots) merging. If the simulation at 10% and 30% MC was allowed to run indefinitely in an infinite grid, then eventually $\Delta\varphi_b$ would again start to increase linearly once all the hotspots had merged. In a real wildfire, this merging behaviour represents the point at which the fire is much harder to fight, as this phenomenon disables the safe routes for firefighting, whereas water bombing effectiveness against smouldering peat is questionable. Figure 6.8 shows an example of a merging phenomenon in real peatland wildfires in Sumatra, Indonesia in 2019.

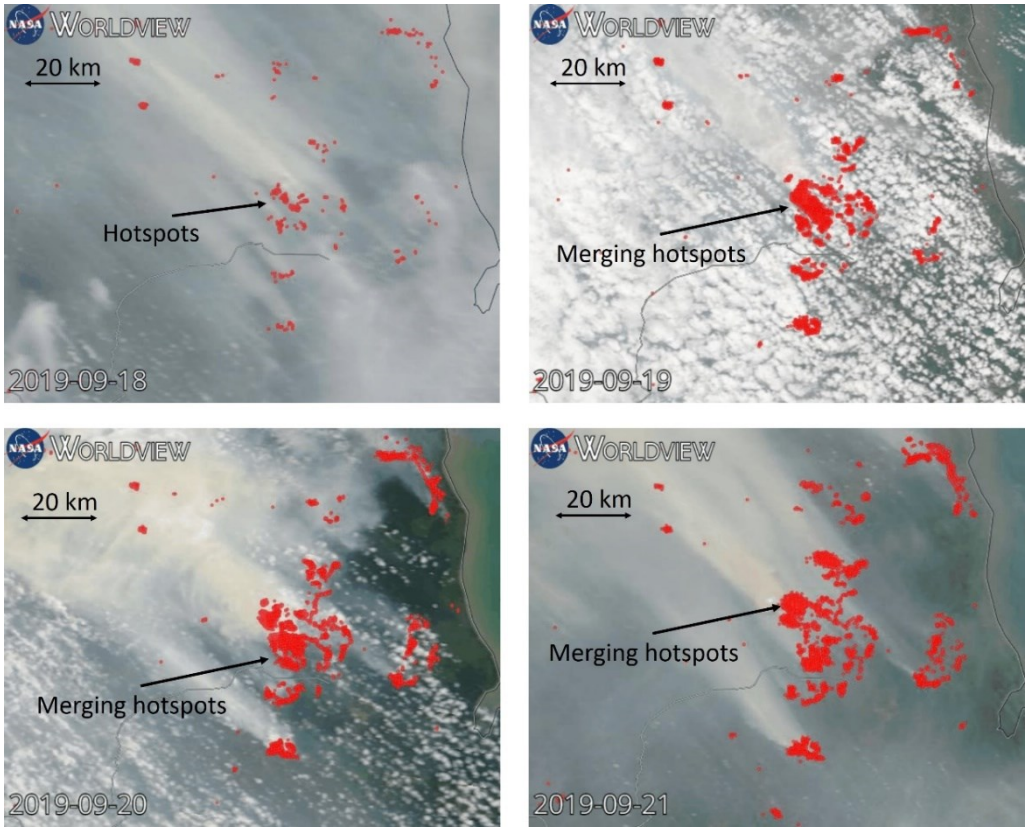

Figure 6.8. Satellite imageries of a peatland wildfire in Sumatra (Latitude: 1.301S, Longitude: 104.611E) in September, 2019. Hotspots (red circles) were separated on 18th September 2019 and began to merge on 19th September 2019 and eventually spread as larger hotspots afterwards. These imageries are obtained from satellite imaging of NASA Earth Observing System Data and Information System (EOSDIS).

KAPAS shows that a wildfire on peatlands with MC above 120% has transition and final burnt ratio converge to zero. Therefore, this peatland condition would be relatively safe for performing prescribed fires. KAPAS also demonstrates hotspots initiation by flaming vegetation and how complex behaviour (hotspots merging) can emerge from a simple rule-based model.

The MC threshold for a safe prescribed fire according to the model conforms to the experiments in Frandsen (1997) and Huang and Rein (2015). In these experiments, the critical MC to sustain smouldering was 110% for IC of 3.7%, which is only 10% lower than the threshold in the model. Therefore, the model also successfully captures observed trends.

6.2.2. Simulating field-scale wildfire in Borneo

KAPAS was also used to study a real prescribed wildfire that took place on peatlands in Borneo, Indonesia in 2015. This fire was chosen because a fuel map and airborne footage of the fire from Eyal *et al.* (2017) was obtained (see Figure 6.9). The field

where the fire took place was 573 ha in size, which was represented by a 416 x 620 cell grid in KAPAS, using the same cell size and time-step as mentioned in Chapter 6.2.3.

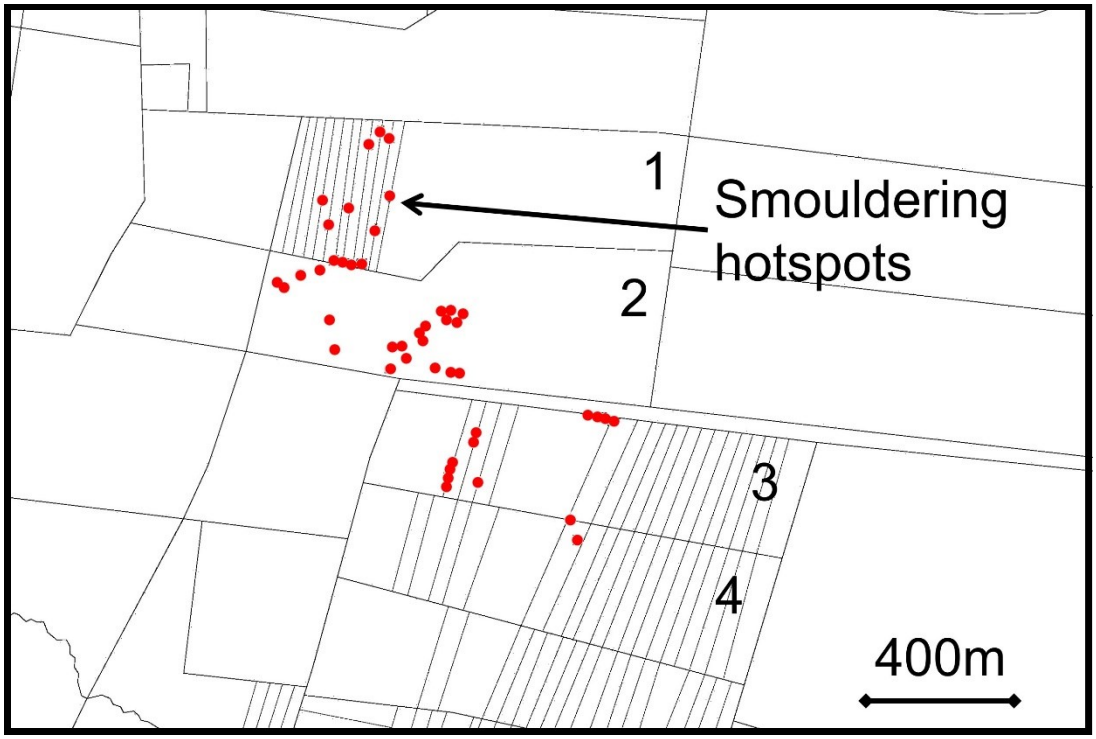

Figure 6.9. The map for the model and the location of the smouldering hotspots (red circles). This map illustrates the landscape of real prescribed fire in Borneo adopted from Forensic Architecture airborne footage which cover 573 ha of peatland. Flaming are initiated at region 1 to 4.

To simulate the Borneo wildfire, it was necessary to add 2 additional states to the model, representing 2 additional surface fuel types. These states were *dead surface vegetation (DV)* and *firebreak (FB)*. These were both similar to the regular *SV* state, but modified the base flame spread probability P_R. For the case of *DV* cells, P_R was multiplied by 1.12 following Rothermel (1972) for dead fuel, which increases the spread rate, and for the case of *FB* cells, P_R was multiplied by 0 because firebreak are created to stop the spread of flaming wildfire by removing all surface vegetation on its area. These firebreak were only on the surface, therefore, smouldering fires could still spread.

The wind was taken from local measurements during the wildfire. The data was only available for the first day, therefore, the wind speed and direction was assumed to repeat the first day data over the following days. MC was varied from 0-150% in increments of 10%, which is representative of the change in MC between dry and rainy seasons in Indonesia and demonstrates a range of possible conditions during the fire. However, it is assumed that a typical value of MC in Indonesian peatlands is around 70% (Nusantara, Hazriani and Suryadi, 2018). KAPAS was run for a total of 30,000 time-steps

in this second case, which corresponds to a duration of 105 days in real time. This total duration is selected based on typical smouldering peatland wildfire duration in Indonesia which is around 2-3 months (Hayasaka, Usup and Naito, 2020).

Figure 6.10 shows snapshots from the model with 70% MC at 4 different times for IC of 3.7%. The wind strength and direction are labelled in each snapshot, and the time presented in the figure is the real time since ignition. In Figure 6.10a, the surface vegetation has just been ignited (day 0). In Figure 6.10b, at day 1 since ignition, the flaming front is halfway sweeping the surface layer and hotspots have formed. However, hotspots are not visible because they are too small for the figure resolution. In Figure 6.10c, at 73 days since ignition, all of the peat has been exposed and hotspots are visible. There were a total of 57 smouldering hotspots initiated in the simulation, which has a good agreement with the footage (21% error). This comparison is without adjustment of parameters in KAPAS, thus, it can be considered as blind prediction. In Figure 6.10d, at 105 days since ignition, the hotspots are merging. By the end of the simulation, 2.9 ha of peat has burnt. The model captures the qualitative behaviour seen during the wildfire of multiple hotspots igniting and then merging over time. The merging behaviour from KAPAS simulation is similar to the merging in the real peatland wildfire shown in Figure 6.8. This result demonstrates the potential of cellular automata for modelling field-scale peatland wildfires.

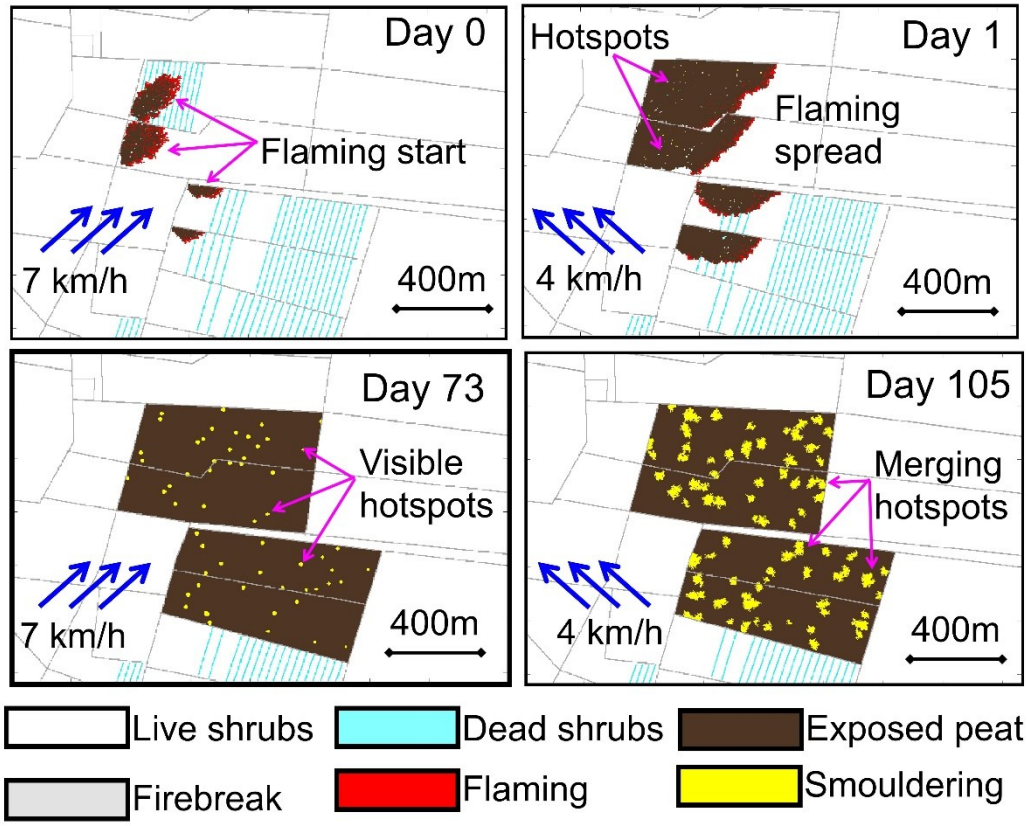

Figure 6.10. Snapshots of a simulation of the prescribed fire in 573 ha (416 x 620 cells) of peatland in Borneo taken at different times. (a) The start of the surface flaming, (b) the spread of surface flaming and the formation of smouldering hotspots, (c) the growth of smouldering, and (d) the merging of the smouldering hotspots.

In the simulation at 70% MC, the flaming spread rapidly and reached the firebreak within less than 48h. The peat that was ignited from this flaming took much longer to spread, and hotspots only became visible after 20 days. The hotspots continued to grow, spreading across firebreak, until 3 months when they began to merge. At this point, the burnt area became so large that suppressing the fire would be very difficult. Peatland wildfires which remain active for months are disaster of an unsafe prescribed fire on peatlands.

Figure 6.11 shows predicted burnt area (A_b) at different time after flaming ignition with increasing peat MC for IC of 3.7%. The line fitted through the blue circles represents A_b immediately after all surface vegetation has been consumed, which is referred to as the *transition area*. The line fitted through the red diamonds represents the final A_b after 105 days. This is the *final burnt area*.

Figure 6.11 shows that the prescribed fire would have resulted in a smaller wildfire at higher MC, with less than 200 m^2 of peatland being burnt after 3 months if peat were

above 100% MC. These results agree that prescribed fires should only take place when the MC of the peat is sufficiently high, in order to minimize the risk of smouldering.

Cellular automata predictions stem from the selection of the transition probability of each state, therefore, calibration against further experiments could improve the model significantly. The stochastic nature of the model makes the experiments of Frandsen (1997) suitable to calibrate the probabilities. Therefore, KAPAS could be improved when experiments similar to Frandsen (1997) are available for other phenomena in peatland wildfires (e.g., extinction probability instead of ignition probability of those in; Frandsen, 1997).

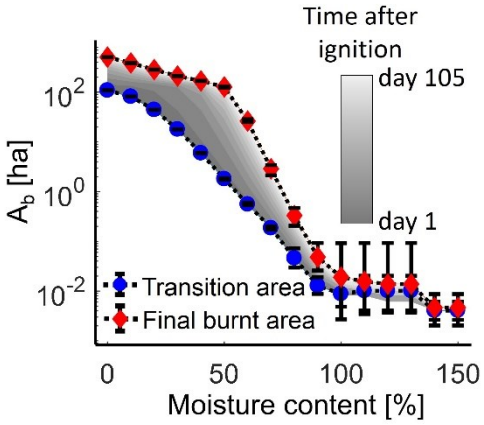

Figure 6.11. Predicted A_b of the Borneo prescribed fire for different moisture content. The colour gradation represents change of A_b every 10 days. Each simulation is repeated 10 times to report uncertainty.

6.3. Conclusions

Cellular automata was used for the first time to model field-scale peatland wildfires where both smouldering and flaming combustion are present. Considering simpler domains, the model, KAPAS, showed complex emergent behaviour that influenced the fire behaviour. In wildfires with multiple smouldering ignition points, smouldering hotspots merged over time, meaning the evolution of burnt area was non-linear. Both the transition ratio and final burnt ratio of smouldering peat followed a sigmoid relationship with MC, demonstrating the ability of the model to translate experimental data into the context of field-scale peatland wildfires by only using the simple rules of the cellular automata.

The model was also applied to a real peatland wildfire that took place in Borneo in 2015, and managed to capture qualitative behaviour. At a realistic MC of 70%, 2.9 ha of peatland was burnt after 3 months. This burnt area could be reduced to a 150 times smaller area (0.02 ha) by increasing the MC above 100%, suggesting that prescribed fires

should take place in conditions with high MC, such as during the wet season. The limitation of this quantitative results is the unavailability of the field-scale data to validate the effect of changing peat MC on smouldering burnt area, however, the exponential decrease of smouldering burnt area if the peat MC were wetter is expected to prevail (although there are variation and uncertainty of the exact values) since this correlation follows the results of laboratory-controlled experiments that consider the key factors that control smouldering behaviour. These findings and model can be used to assist and improve peatland wildfire mitigation, by performing faster-than-real-time simulations to find the optimum firefighting strategy, and to improve the procedure of prescribed fires on peatlands, which is one way to help prevent the widespread occurrence of peatland wildfires.

Chapter 7 – KAPAS II: Simulation of Peatland Wildfires with Temporally Varying Peat Moisture Contents

Summary[6]

This chapter aims improve the model in Chapter 6 (KAPAS), by considering the temporal peat MC variations. The 2-D cellular automata model in this chapter, KAPAS II, also improves KAPAS by enabling the simulation at any spatial and temporal resolution. KAPAS II was used to simulate 90 days of a peatland wildfire in Borneo (3.087°S, 113.991°E) in 2018. The input parameters of KAPAS II were derived from remote sensing data of vegetation type and density, and the temporal variation in peat MC was estimated using a peat-specific land surface model. KAPAS II reflects good agreement with satellite observations on flaming burnt scars (79% accuracy) and in the number of smouldering hotspots (85% accuracy). The model revealed that 0.55 km^2 of peat smouldered when considering temporally varying peat MC, but only 0.12 km^2 smouldered under constant moisture conditions with the same flaming burnt scar (111.43 km^2), emphasising the importance of considering MC variations. Simulations conducted in the same location in different months and years between 2000 and 2019, corresponding to contrasting Oceanic Niño Indices (El Niño), predicted smouldering areas ranging from 0 km^2 to 0.93 km^2. Seasonal variations in peat moisture, which are strongly influenced by climate, determine the severity of smouldering wildfires. This chapter provide knowledge and faster-than-real-time simulation tool that improve our understanding of wildfire spread in peatlands and can contribute to the mitigation of carbon emissions and haze from peatland wildfires.

[6] This chapter is based on "Dwi M J Purnomo, Sebastian Apers, Michel Bechtold, Parwati Sofan, and Guillermo Rein, 2022. Integrating Cellular Automata and Remote Sensing to Model Field-Scale Peatland Wildfires with Temporally Vary Peat Moisture Content. *International Journal of Wildland Fire*, (to be submitted)."

7.1. The Development of KAPAS II

7.1.1. Introduction to KAPAS II

In this chapter, KAPAS (see Chapter 6) was improved by integrating temporally varying peat MC, which is the more realistic conditions in natural peatlands (see Chapter 1), and allowing simulations at any spatial or temporal resolution. This improvement increases the applicability of the model, in which the improved model can be used in any computational domain without significant additional recalibration processes. The states and rules of the model in this chapter are the same as KAPAS, for instance, it uses bond percolation approach and considers 5 different states (see Chapter 6). Since the model in this chapter is the direct improvement of KAPAS, which uses the same approach and is used for the same purposes (modelling of flaming and smouldering in peatland wildfires), for simplicity, it is named KAPAS II. The differences between KAPAS and KAPAS II are in the formulation and calibration of the model's variables ($P_f, P_t, P_s,$ and P_e), where in KAPAS II, the effect of spatial and temporal resolution were embedded, and the method to obtain input parameters, where in KAPAS II, it was derived from GIS and remote sensing data.

7.1.2. Input parameters and validation datasets

KAPAS II was used to simulate a peatland wildfire in Borneo (3.087°S, 113.991°E) that started on 21 September 2018 and was fully extinguished on 10 October 2018. Figure 7.1a shows the progression of the flaming wildfire captured by the Sentinel-2 satellite (Copernicus, 2022). These satellite images were obtained by using false-colour urban composites that clearly distinguish among surface vegetation, burnt scars, and active fires (the colour depends on the fire intensity; Stavrakoudis *et al.*, 2020). The brown colour in Figure 7.1a represents the burnt area, whereas yellow and red areas represent regions of active fire. The brown colour at the bottom left of Figure 7.1a also represents a burnt area; however, this burnt area resulted from previous wildfires that were not considered in this chapter.

The data obtained from Sentinel-2 were used to estimate the flaming burnt scar in the validation process. In the model, the shape formed by *EP* cells corresponded to the flaming burnt scar. The seed-fill algorithm (Khayal *et al.*, 2011) was used to detect the burnt scar pixels (brown colour) from the satellite images shown in Figure 7.1a. Figure 7.1b shows the flaming burnt scar obtained by implementing the seed-fill algorithm with the satellite images shown in Figure 7.1a. The flaming burnt scar also shows the locations of firebreaks, which serve to stop flames from spreading. Firebreaks are indicated by the abrupt stop of a flaming wildfire, thus causing the burnt scar to exhibit smooth edges (see

day 20 in Figure 7.1a). Figure 7.2a shows the landscape distribution, including the estimated locations of firebreaks. The landscape in Figure 7.2a, however, reflects a satellite image taken of the location before the flames began (on 8 September 2018).

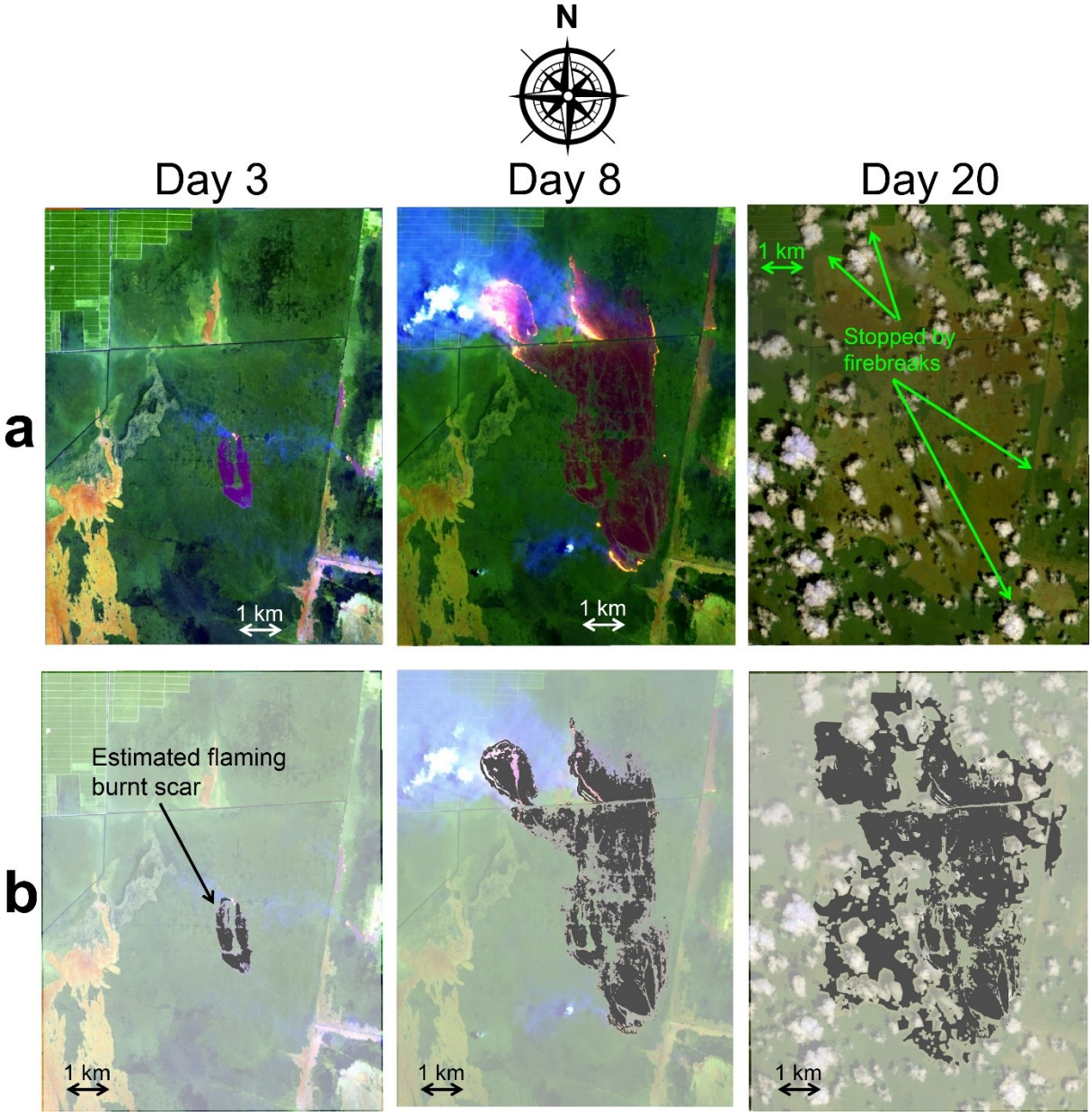

Figure 7.1. Satellite image of a landscape in Borneo (3.087°S, 113.991°E) in September 2018 obtained from Sentinel-2 (Copernicus, 2022). (a) The progression of a flaming wildfire in the Borneo landscape detected by Sentinel-2 (Copernicus, 2022). (b) Estimated flaming burnt scar in the Borneo landscape.

KAPAS II considers three different surface vegetation types, dry shrubs, wet shrubs, and trees (shown in Figure 7.2b); following Ferraz *et al.* (2019), who used field sampling and satellite observations to estimate vegetation types. KAPAS II also considers the rain and wind conditions to simulate flaming wildfires. Meteorogical data derived

from the observations of a local weather station (BMKG, 2018) were used to obtain daily precipitation, wind speed and wind direction data.

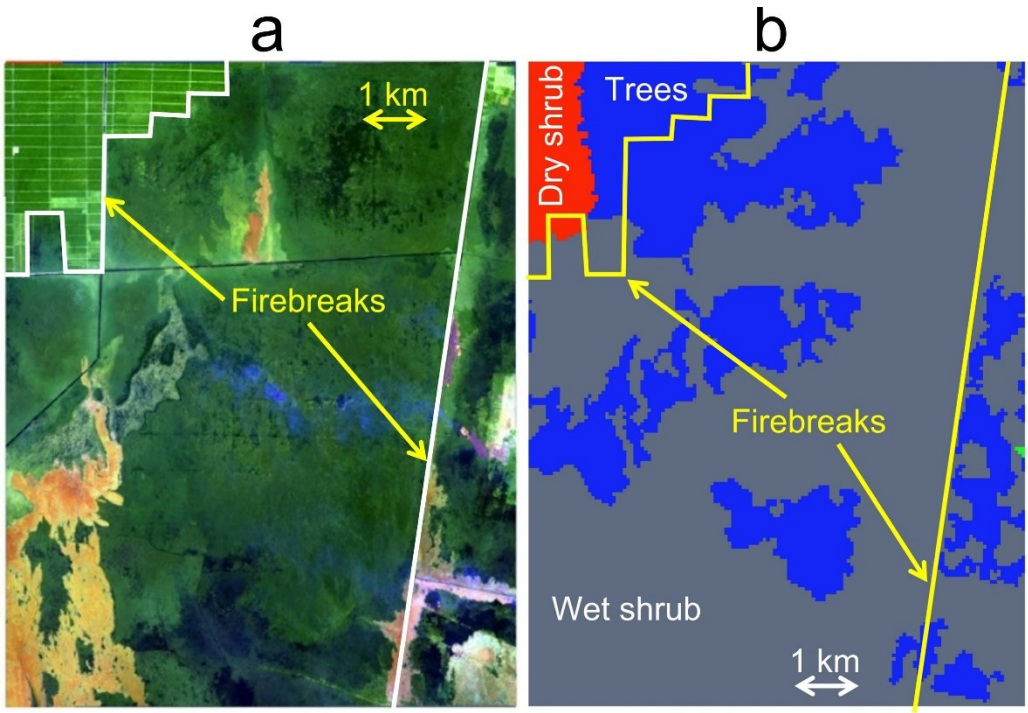

Figure 7.2. (a) Satellite image of a landscape in Borneo (3.087°S, 113.991°E) in September 2018 before the flames began; this image was obtained from Sentinel-2 (Copernicus, 2022). The white lines highlight firebreaks. (b) Remote sensing-based vegetation types identified in the peatlands in the Borneo landscape (3.087°S, 113.991°E), as obtained from Ferraz et al. (2019). Three vegetation types were considered: dry shrubs (red), wet shrubs (grey), and trees (blue). The yellow lines show the firebreaks, corresponding to the white lines in panel (a).

The vegetation density in KAPAS II was classified based on Normalised Difference Vegetation Index data (NDVI, a surface vegetation greenness index), which are commonly used to estimate vegetation density (Camps-Valls *et al.*, 2021), obtained from Sentinel-2 (Copernicus, 2022), as shown in Figure 7.3a. However, only three categories of vegetation density were considered, recently burnt, regrown, or intact vegetation, corresponding to the methods of Alexandridis *et al.* (2008). Therefore, the values shown in Figure 7.3a were reclassified into three classes: values ranging from 0 to 0.2 corresponded to recently burnt vegetation, 0.2 to 0.4 indicated regrown vegetation, and 0.4 to 0.65 indicated intact vegetation (as shown in Figure 7.3b). Recently burnt vegetation corresponds to vegetation that was burnt in recent previous wildfires; regrown vegetation corresponds to previously burnt vegetation that has started to regrow; and intact vegetation refers to vegetation that has not been affected by recent wildfires (see Figure 7.2a, in which the green colour in the landscape is not uniform; in Figure 7.2b the landscape is fully covered with

vegetation). Figure 7.3c shows the final vegetation density classification data used in the model. The black region in Figure 7.3c was not considered in the model, as this region and the study area were separated by firebreak (see Figure 7.2a); therefore, the flames could not spread to the black region. The data of NDVI were selected at the start of wildfire (on 21 September 2018), therefore, the data represented the actual ground conditions.

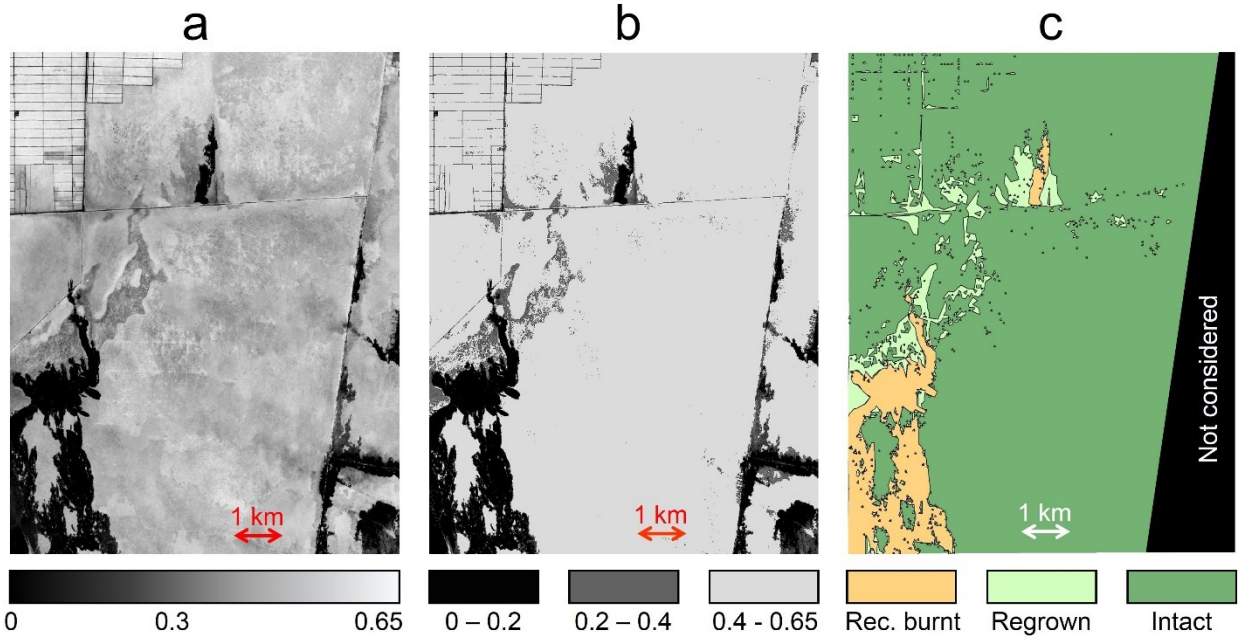

Figure 7.3. (a) The NDVI data of a landscape in Borneo (3.087°S, 113.991°E) on 21 September 2018; these data were used to estimate the vegetation density and were obtained from Sentinel-2 (Copernicus, 2022). (b) Reclassified NDVI data in the Borneo landscape (3.087°S, 113.991°E) on 21 September 2018; these data were used to simplify the vegetation density classification scheme and were adapted from Alexandridis et al. (2008). (c) The vegetation density data characterizing the Borneo landscape (3.087°S, 113.991°E) on 21 September 2018 used in the model; these data were based on the NDVI data and classified as recently burnt (rec. burnt), regrown, or intact. The black region was not considered because it was separated by a firebreak.

The peat MC data were obtained from simulations conducted with a peat-specific land surface model in Apers *et al.* (2020), using the tropical version of the peat-specific land surface model developed by Bechtold *et al.* (2019); this model was specifically developed and extensively evaluated for tropical lowland peatland conditions and was shown to perform best over Southeast Asia peatlands. This model is based on the Catchment Land Surface Model (CLSM) of the NASA GEOS Earth System Modelling framework and has two modules, one for drained tropical peatlands ($PEATCLSM_{Trop,Drain}$) and one for natural tropical peatlands ($PEATCLSM_{Trop,Nat}$); these different peatland types have distinct hydrological conditions and thus have different peat MC characteristics

(Apers *et al.*, 2020). Because canal projects had been underway in Central Kalimantan since the 1990s (Ritzema *et al.*, 2014), and from the canal map produced by (Dadap, 2020), number of canals in the study area were found, the peatland under the study area was assumed to be drained. The soil surface MC data were used in this chapter, as the ignition of smouldering wildfire occurs most of the times at the surface.

The MC information obtained from $PEATCLSM_{Trop,Drain}$ was volumetric, whereas that used in KAPAS II is gravimetric. Thus, to obtain gravimetric MC data, the volumetric MC from $PEATCLSM_{Trop,Drain}$ was divided by the peat bulk density (in g/cm^3). Peat bulk density is a function of the peat solid density and the peat porosity. In this chapter, the peat solid density was assumed to be 1.5 g/cm^3, adopting the value reporting by Huang and Rein (2017). The porosity of peat in natural peatlands varies significantly with depth; at the surface, the porosity can exceed 0.8, while at deeper points (~50 cm), it can be less than 0.5 (Rezanezhad *et al.*, 2016). Although the peat porosity described in Rezanezhad *et al.* (2016) corresponds to nontropical peatlands, a study of peat in Indonesian tropical peatlands revealed that the peat porosity at a 50-cm depth was estimated to be 0.41 (Islami *et al.*, 2018), thus confirming the values obtained by Rezanezhad *et al.* (2016). In this chapter, the average of surface (0.80) and deep (0.41) peat porosity values was selected; thus, a porosity of 0.61 was used for modelling with KAPAS II. This value was lower than the porosity values commonly used in smouldering models (higher than 0.9), as the values used in previous models were assumed to reflect the porosity of surface peat. However, the peat porosity used in KAPAS II was similar to that used in $PEATCLSM_{Trop,Drain}$ (0.68). From these selected values, the representative peat bulk density in KAPAS II was 0.585 g/cm^3; thus, the volumetric MC derived from $PEATCLSM_{Trop,Drain}$ was divided by 0.585 prior to being input to the model.

While flaming burnt scar data were used to validate the flaming component in the KAPAS II model, the smouldering model component was validated by using the data of smouldering hotspots, detected by a remote sensing algorithm developed by Sofan *et al.* (2020), called TOPECAL. TOPECAL performs arithmetic and logic operations on SWIR data from Sentinel-2 to detect the smouldering wildfires that are separated from flaming wildfires. Figure 7.4 shows the smouldering hotspots that were detected using TOPECAL and used to validate the smouldering component of the KAPAS II model. However, only the number of the smouldering hotspots were considered, rather than the shape of the smouldering burnt scar (which is the output of TOPECAL), when validating the smouldering component of the model. This consideration indicates that the validation was based only on the ignition of smouldering wildfires without considering wildfire spread.

The smouldering spread was not validated because the smouldering wildfires in natural peatlands can spread in the subsurface, thus invalidating detection results via remote sensing (see Chapter 2).

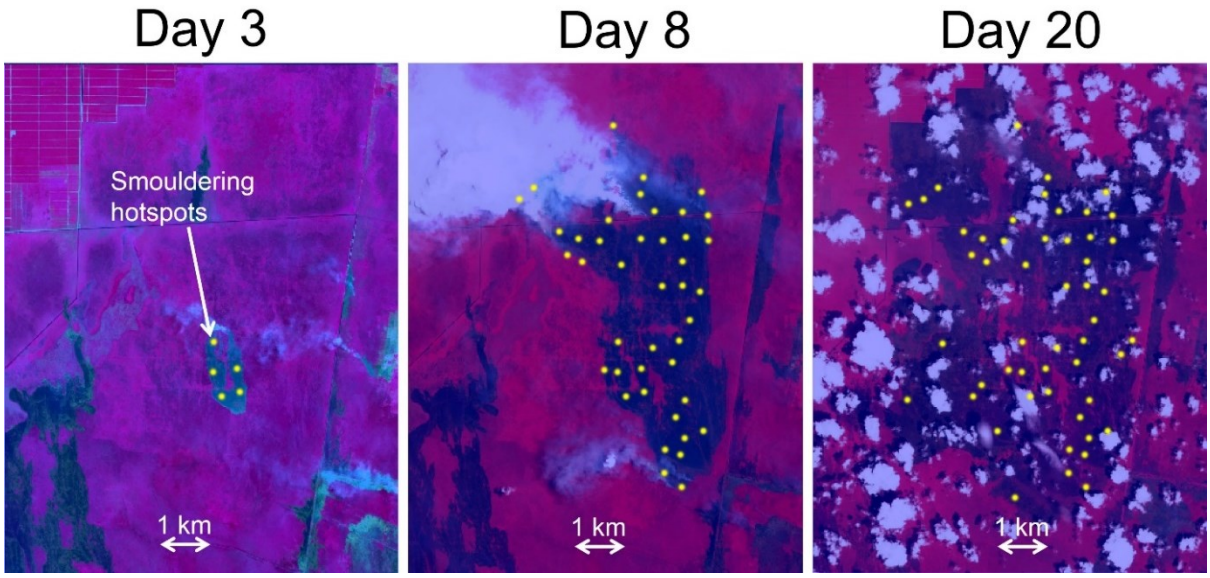

Figure 7.4. The smouldering hotspots (yellow circles) in a landscape in Borneo (3.087°S, 113.991°E) in 2018, detected by the algorithm developed by Sofan et al. (2020) and implemented in the remote sensing data of Sentinel-2 (Copernicus, 2022). The increases in the number of hotspots correspond to the progression of the flaming wildfire (see Figure 7.1a).

7.1.3. Calibration of KAPAS II

KAPAS II predictions are dependent on the values of the main probabilities (P_f, P_t, P_s, and P_e). In the model, P_f (Eq. 7.1) is a function of the flaming spread rate (R), spatiotemporal resolution (λ), vegetation density factor (α_d) and wind factor (α_w). The λ term contains the information of the cell size (Δx) and time-step (Δt) and is formulated as $\frac{\Delta x}{\Delta t}$. R is formulated based on the Rothermel model for surface-spreading fires (Rothermel, 1972) under 0-m/s wind conditions. R is translated into a probability value, depending on λ, which then becomes the base value of P_f (i.e., if α_d and α_w are equal to 1). Figure 7.5a clearly shows that R and the base P_f value have a linear relationship in the log-log axis with slopes independent of λ. With this method, any cell size and time step can be used in the model, thus significantly improving KAPAS (see Chapter 6).

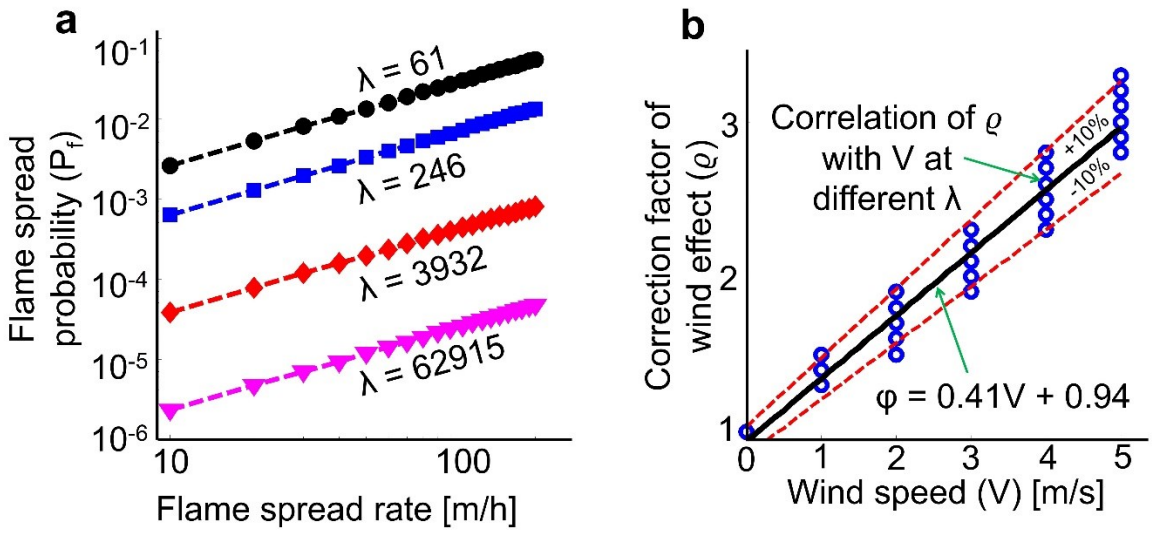

Figure 7.5. The calibration of variables in KAPAS II at different spatiotemporal resolutions (cell size per time step) of the computational domain (λ). (a) The translation of the flame spread rate, based on the Rothermel model calculation, into a probability value, P_f, at different λ values. (b) The correlation between the wind speed (V) and the correction factor of the wind effect (ϱ) at different λ values.

KAPAS II considers the effect of wind (α_w) as formulated in Eq. 7.2 The α_w value is based on the wind factor formulation in the Rothermel model (for maximum downwind spread rate) and on the wave propagation behaviour (regarding the two-dimensional velocity gain distribution; Rothermel, 1972; Alexander, 1985; Finney, 1998). The α_w term is a function of the wind coefficient (Φ_w), the direction of fire spread relative to the wind direction (θ), the ellipse parameters (semiminor axis (a), semimajor axis (b), and linear eccentricity (c)), and the correction factor (ϱ). Φ_w is determined based on the Rothermel model, whereas the ellipse parameters are formulated using Eq. 7.3 to Eq. 7.5 and depend on the wind speed (V), following the methods described by Finney (1998). These formulation methods represent and improved version of the wind effect formulation process in KAPAS (Chapter 6), as the wind effect formulation in KAPAS did not maintain an elliptical shape under high speed winds.

The correction factor of wind effect (ϱ) is required to maintain agreement in the downwind fire spread rate between the simulations and the Rothermel model calculations. Without this correction factor, the fire spread rate in the downwind direction differs significantly from that calculated using the Rothermel model (up to 90%). From the calibration, ϱ was found to be linearly correlated with V, as shown in Eq. 7.6, and the variations that arise due to different λ values remain within 10% (see Figure 7.5b).

$$P_{\mathrm{f}} = 0.016\alpha_{\mathrm{w}}\alpha_{\mathrm{d}}\left(\frac{R}{\lambda}\right)^{1.02} \tag{7.1}$$

$$\alpha_{\mathrm{w}} = \varrho\left(\frac{a^2}{b - c\cos\theta}\right)\Phi_{\mathrm{w}} \tag{7.2}$$

$$a = \left(\frac{r_{\mathrm{H}}+1}{2r_{\mathrm{L}}r_{\mathrm{H}}}\right);\ b = \left(\frac{r_{\mathrm{H}}+1}{2r_{\mathrm{H}}}\right);\ c = \left(b - \frac{1}{r_{\mathrm{H}}}\right) \tag{7.3}$$

$$r_{\mathrm{L}} = 0.936\exp(0.2566V) + 0.461\exp(-0.1548V) - 0.397 \tag{7.4}$$

$$r_{\mathrm{H}} = \frac{r_{\mathrm{L}} + \left({r_{\mathrm{L}}}^2 - 1\right)^{0.5}}{r_{\mathrm{L}} - \left({r_{\mathrm{L}}}^2 - 1\right)^{0.5}} \tag{7.5}$$

$$\varrho = 0.41V + 0.94 \tag{7.6}$$

The effect of vegetation density (α_{d}), which was not considered in KAPAS (Chapter 6), is determined herein by calibrating the model against satellite-derived flaming burnt scar data. Because KAPAS II considers only three different density classes, the intact, regrown, and recently burnt classes only the α_d value for regrown vegetation was calibrated herein. The α_{d} value for intact vegetation was set to 0, and that for recently burnt vegetation was set to 1 to ensure the simplicity of the model. From the calibration, at an α_{d} value of 0.01, the simulations exhibit good agreement with the satellite-derived flaming burnt scar data (21% error).

The cells with *FV* states, transition to become either *EP* or *SP* after several time-steps. If the transition undergoes after a too few time-steps, the spread of the flaming wildfire does not sustain, whereas if the transition undergoes after too many time-steps, the flaming wildfires sustain for too long which violates the observed phenomena. By using a probability of *FV* cells to change its state between $5P_{\mathrm{f}}$ and $25P_{\mathrm{f}}$, the flaming wildfires sustain but without sustaining for too long. The long sustaining flaming wildfires is indicated by the wide flaming vegetation front, which in this chapter, this width was determined to be less than 10 cells. This value was selected based on the width that facilitate continuous flaming vegetation layer. With less than 10 cells flaming vegetation width, the perimeter of the flaming vegetation is disconnected at several locations, which correspond to the unburned vegetation. Therefore, once the width of flaming vegetation layer exceeds 10 cells, the flaming wildfire can be considered has sustained for too long. Between $5P_{\mathrm{f}}$ and $25P_{\mathrm{f}}$, the value of ϱ to maintain the accuracy of the model against Rothermel model calculation does not significantly change. Therefore, the middle value was selected, in which the *FV* cells transition to either *EP* or *SP* at the subsequent time-step with a probability of $15P_{\mathrm{f}}$. However, this value changes to become $15P_{\mathrm{f}}\exp(0.2\sigma)$ when there are rains, where σ is precipitation, adapting from Alexandridis *et al.* (2011).

The P_t and P_e values applied in KAPAS II were formulated following the methods described in Chapter 6, in which P_t is a function of peat MC, as shown in Eq. 7.7, utilizing the ignition probability derived by Frandsen, (1997); P_e is selected to be 5×10^{-10}, thus sustaining a smouldering fire in the simulation for approximately three months (the typical duration of the wildfire season in Indonesia; Huijnen *et al.* 2016). P_e should be dependent on GWT; however, KAPAS II did not consider this variable. The formulation of P_s in KAPAS II was also adapted from KAPAS (see Chapter 6), however, different λ values were input to KAPAS II to enable modelling at any spatial and temporal resolution in the computational domain (thus improving the KAPAS model). P_s was found to be linearly correlated along the log-log axis with MC ($R^2 = 0.89$) and has a slope independent of λ (see Figure 7.6); P_s can be formulated as shown in Eq. 7.8. The MC values used in Eq. 7.7 and Eq. 7.8 change daily (date-based) based on the $\text{PEATCLSM}_{\text{Trop,Drain}}$ estimation; thus, P_t and P_s also change daily. The effects of the burning cells (i.e., *FV* and *SP*) in the soil layer are based on P_t and P_s at the corresponding time. Although KAPAS II considers temporal variation in peat MC, the MC on each day was assumed to be uniform across the entire landscape.

$$P_t = \frac{1}{1+\exp(-1.78+0.12MC)} \tag{7.7}$$

$$P_s = 0.01\text{MC}^{-0.71}\lambda^{-1.02} \tag{7.8}$$

In this chapter, a domain with a 45-m cell size and a 1200-s time-step (λ = 135 m/h) were used. This cell size selection stemmed from the resolution of the utilized remote sensing data, whereas the time step was determined based on the stability criteria (Courant–Friedrichs–Lewy conditions), given the derived cell size. However, any other domain configuration could be used in the model, given that stability criteria are met.

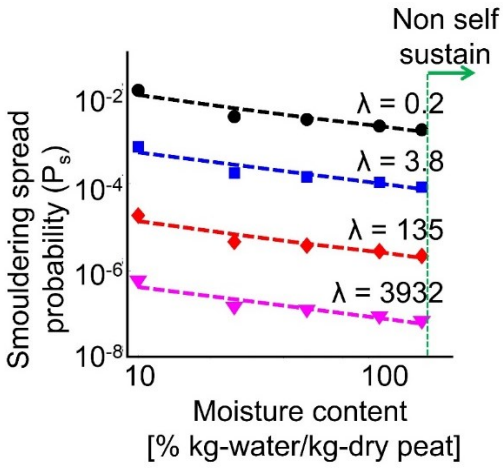

Figure 7.6. The relationship between smouldering spread probability (P_s) and the peat MC at different spatiotemporal resolution (λ), calibrated against experimental data (Huang et al., 2016; Prat-Guitart et al., 2016b).

7.2. Results and Discussions

Figure 7.7 shows snapshots of the KAPAS II simulations obtained at four different times from day 3 to day 90. Figure 7.7a – Figure 7.7c correspond to the spread of flames, whereas Figure 7.7d corresponds to the spread of smouldering. On day 3 after the start of the wildfire (Figure 7.7a), flames had burnt a relatively small area of surface vegetation, and the shape of the burnt scar was relatively circular, with nonsmoothness at the perimeter caused by the probabilistic approach of the KAPAS II model. The south-eastern wind, which had a speed of 7 km/h, had only a slight effect on the flaming burnt scar. The wind direction was considered to be the direction of the origin of the wind (azimuth); thus, for instance, south-eastern wind describes wind coming from the southeast and moving northwest. On day 8 (Figure 7.7b), the effects of the western wind conditions and vegetation density (see Figure 7.3) caused the westward spread of the flames to be minimised. The vegetation density effect also caused the formation of an unburned patch in the northern region of the flaming burnt scar. Smouldering hotspots (yellow colour) began to form at this stage; however, these hotspots were still not visible due to the domain resolution. On day 20 (Figure 7.7c), the flames had been fully extinguished, and the nucleation of smouldering hotspots had stopped. In the simulation, the flames were extinguish on day 15 following the start of the wildfire; however, Figure 7.7c shows a snapshot of day 20, a day for which a satellite image was also available (on other days, satellite images were either unavailable or significantly cloud-covered), for comparison purposes. The extinction of the flaming wildfire corresponded to the precipitation on day 15 (14.7 mm of water); this precipitation event continued for three days. Therefore, it is argued that the flaming wildfire and smouldering hotspot nucleation lasted for 16 days. From day 20, smouldering hotspots start to spread and grow larger, and at the end of the simulation (day 90), the hotspots had significantly enlarged, and some of them had merged (Figure 7.7d).

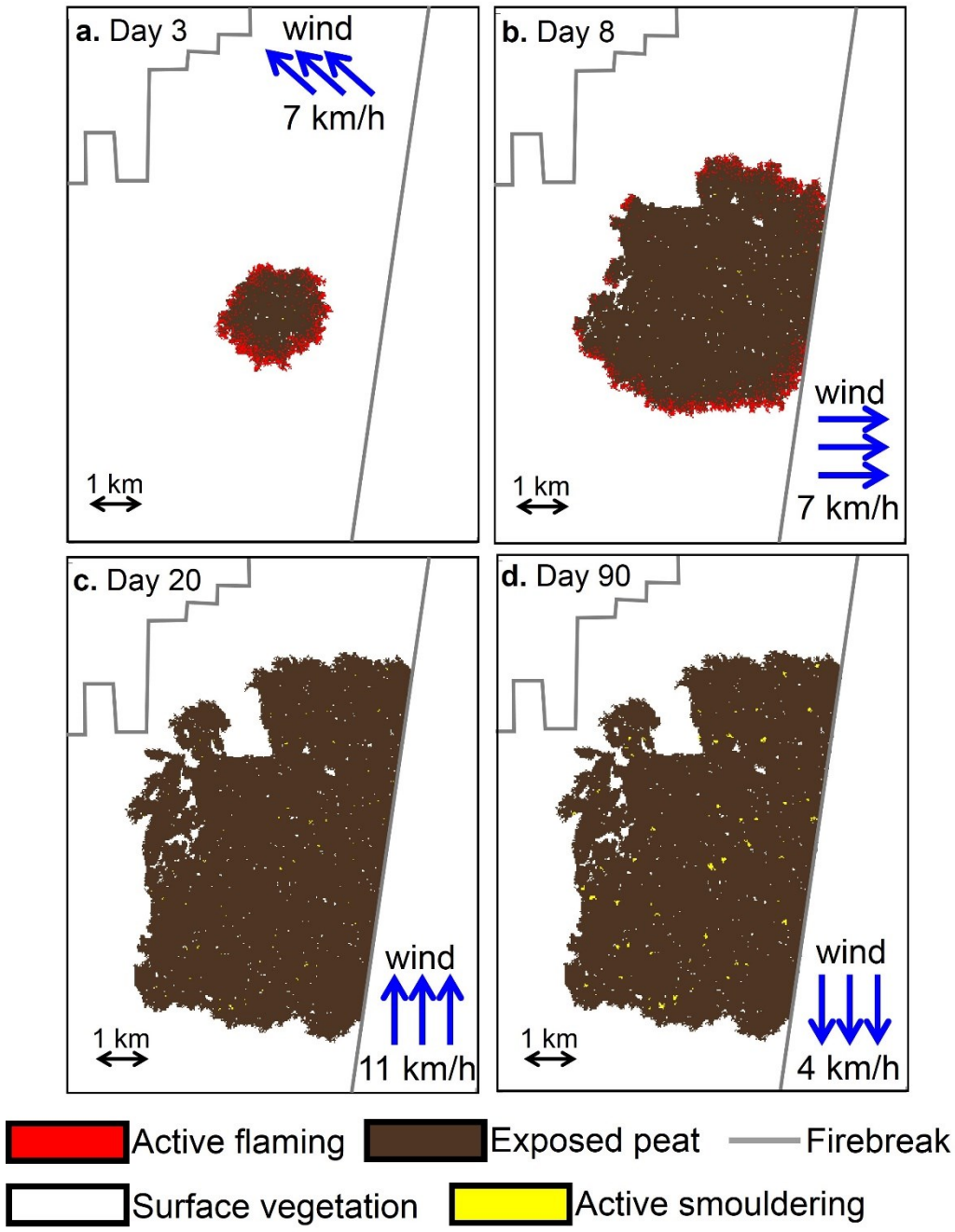

Figure 7.7. Snapshots of the peatland wildfire simulation in the Borneo landscape (3.087°S, 113.991°E) in 2018 at different stages: (a) the early stage of surface flames on day 3; (b) the spread of surface flames and the nucleation of smouldering hotspots on day 8; (c) the extinction of surface flames and the cessation of smouldering hotspot nucleation on day 20; and (d) the end of the simulation on day 90, at which time the smouldering hotspots had spread and enlarged. The surface vegetation (white) corresponds to the three different vegetation types shown in Figure 7.2b. The blue arrows show the wind speed and direction. Firebreaks (grey) stopped the spread of flames but could not stop the spread of smouldering.

Figure 7.8 shows the comparison between the satellite-detected flaming burnt scars (Figure 7.1b) and those predicted using the KAPAS II model (Figure 7.7a – Figure

7.7c) at three different times (on day 3, day 8, and day 20). In the figure, the red lines represent the perimeter of the actual flaming burnt scar detected by the satellite. The true positive and true negative terms represent accurate predictions in which the burnt scars identified from the satellite images and predictions both indicated burnt or unburnt conditions, respectively. False positives correspond to an area that was the predicted to be burnt but was not burnt in the satellite image, and false negatives indicate regions that were not predicted to be burnt but were observed to be burnt in the satellite image; both of these conditions were considered inaccurate predictions. In the analysed wildfire, the flames burned approximately 87.34 km^2 of surface vegetation among the 257-km^2 study area (based on the satellite observations). KAPAS II simulated this flaming wildfire with a 29.8% share of true positives, 49.2% true negatives, 16.9% false positives, and 4.1% false negatives compared to the observed flaming burnt scar detected by the satellite at the end of the flaming wildfire (on day 20). Therefore, a Cohen's kappa value of 0.57 was achieved, corresponding to reasonable agreement between the KAPAS II predictions and the observed flaming burnt scar. The main reason of these deviation is the effect of the wind. This finding can clearly be seen in Figure 7.8 on day 3 and day 8, at which times the flaming burnt scars identified from the satellite observations were elongated, whereas in the simulations, the elongation characteristics of the burnt scars were weaker. This discrepancy was potentially resulted from KAPAS II considering the daily average wind speed and direction, whereas in reality, both the wind speed and direction vary over the course of a day, especially when gusty winds (sudden increase in wind speed, at times accompanied by changes in direction) occur.

KAPAS II predictions overestimated the flaming burnt area (the area of the flaming burnt scar); in the model, 111.43 km^2 of surface vegetation was burnt by flames (see Figure 7.9a), but the predictions were reasonably accurate (above 70% accuracy). After 16 days, the burnt area by flames did not change, and no change is shown in Figure 7.9a. During the 16 days over which flames spread, the smouldering hotspots nucleated, as shown in Figure 7.9b. The smouldering component of KAPAS II was validated by comparing the number of smouldering hotspots simulated at different times against the hotspots observed by the satellite (see Figure 7.4). The number of smouldering hotspots predicted (0.51 hotspots per km^2 of landscape) agreed well with the observations (0.44 hotspots per km^2 of landscape), with an error of 15%. These validation results show the robustness of the KAPAS II model when simulating peatland wildfires.

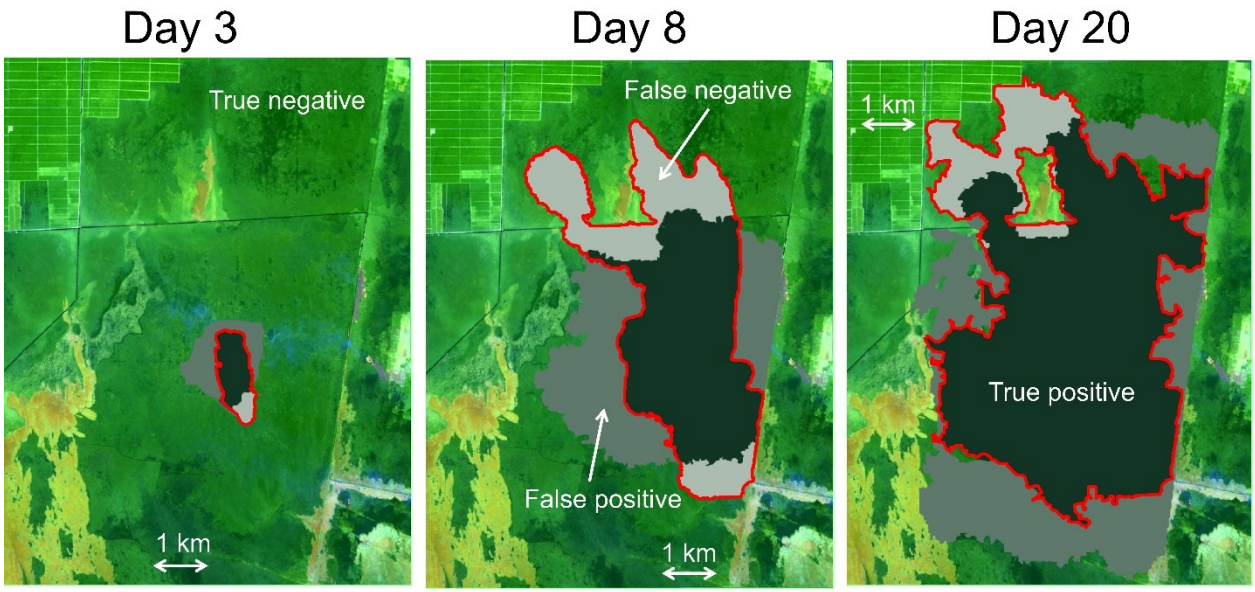

Figure 7.8. Comparisons between the flaming burnt scars (exposed peat) derived from the satellite detection (Figure 7.1b) and from the KAPAS II predictions at three different times (Figure 7.7a – Figure 7.7c) in the Borneo landscape (3.087°S, 113.991°E) in 2018. The red lines represent the perimeter of the actual satellite-detected burnt scar. True negatives and true positives denote accurate predictions, indicating that the predicted and satellite-detected results both suggested not burned or burned regions, respectively. A false positive corresponds to a predicted burn region that was not burn in the satellite detection results, whereas a false negative indicate that an area was predicted to be a nonburn region but was found to be burn in the satellite detection results.

The discrepancies in the location of smouldering hotspots between the predictions and observations may have stemmed from the spatial nonuniformity of peat MC in reality, as this feature was not considered in KAPAS II. This claim is supported by the number of smouldering hotspots observed on day 8 (0.35 hotspots per km^2), which dropped significantly on day 16 (0.09 hotspots per km^2), as shown in Figure 7.4, although the area burnt by flames was similar, indicating that the region covered by the flaming burnt scar on day 8 had potentially relatively dry compared to the other region within the burnt scar on day 16. Moreover, KAPAS II predicted that the numbers of smouldering hotspots nucleated on day 8 (0.23 hotspots per km^2) and day 16 (0.29 hotspots per km^2) were similar. While the flaming burnt area stopped growing after 16 days, smouldering continued to spread, and the hotspots became larger (indicating smouldering growth) and merged.

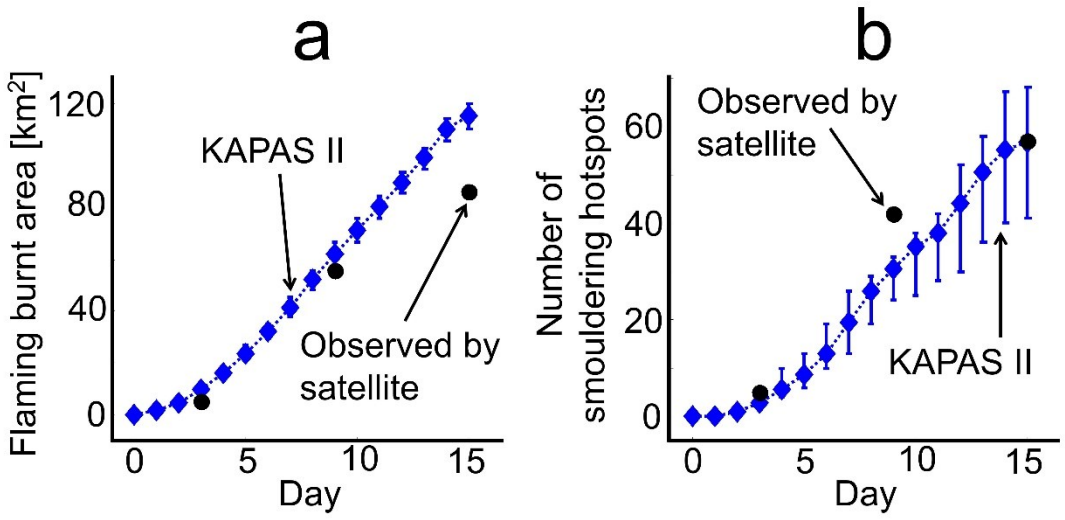

Figure 7.9. (a) Comparisons between the flaming burnt areas (area of the exposed peat) derived from the satellite observations (based on Sentinel-2; Copernicus, 2022) and from the KAPAS II predictions at different times. (b) Comparisons between the numbers of smouldering hotspots derived from the satellite observation (based on Sentinel-2; Copernicus, 2022) and from the KAPAS II predictions at different times. The error bars represent the uncertainty of KAPAS II results after 10 repetitions.

Figure 7.10a shows the evolution of the smouldering burnt area; in the figure, the magenta shade indicates the area under the smouldering nucleation regime (during the flame-spreading process), whereas the cyan shade indicates the area under the smouldering growth regime (after the flames were extinguished). Under both the nucleation and growth regimes, the smouldering burnt area increased exponentially with time, but this increase occur at a slower rate under the growth regime than under the nucleation regime. Smouldering had burnt a total of 0.55 km^2 of peat 90 days after the start of the wildfire.

This pattern prevailed in both the actual case in which temporal peat MC variations were implemented (transient MC) and in the simplified scenario in which the peat MC was assumed to be constant (constant MC) at 83% kg-water/kg-dry peat (the average peat MC calculated over 90 days; see Figure 7.10b). However, the total smouldering area (the sum of the smouldering burnt areas identified under the nucleation and growth regimes) was significantly smaller in the constant MC scenario (0.12 km^2) than under the transient MC scenario. This finding emphasised the importance of implementing temporal peat MC variations in the model. The omission of these variations could significantly underestimate the resulting total smouldering area predictions, which

could in turn cause ineffective mitigation strategies for peatland wildfires, such as those resulting from the incorrect allocation of resources.

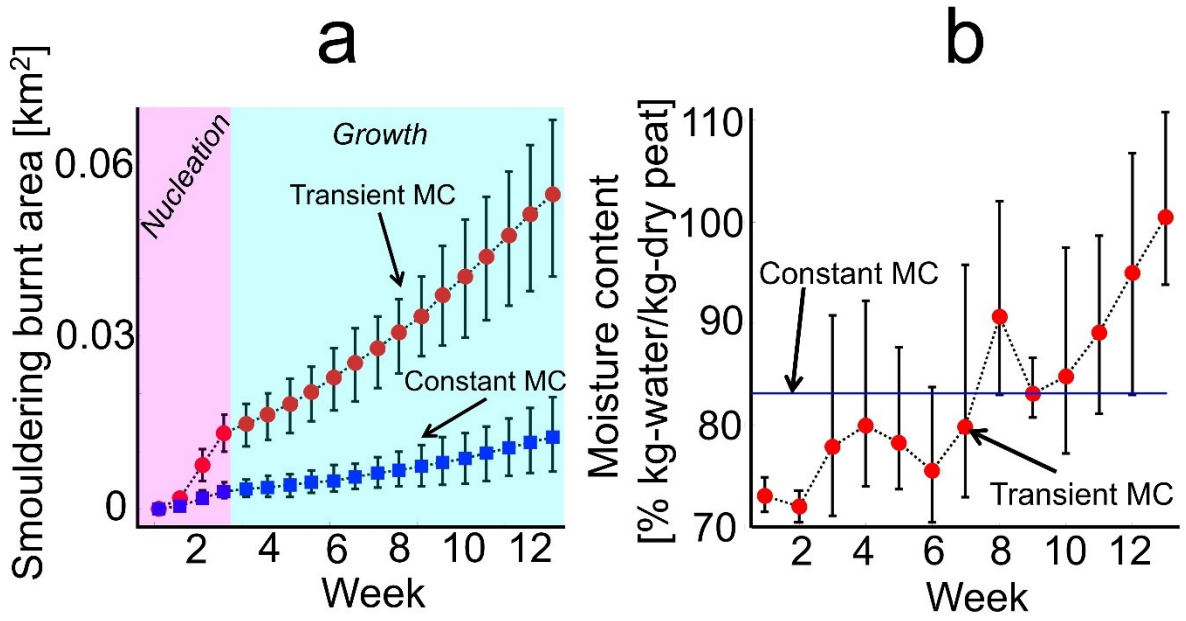

Figure 7.10. (a) The predicted evolution of the smouldering burnt area in the Borneo landscape (3.087°S, 113.991°E) over 90 days under the assumption of a constant peat MC (constant MC scenario, blue square) or temporally varying peat MC (transient MC scenario, red circle). Under the nucleation regime (magenta) smouldering hotspot nucleation was found to be dominant over growth, whereas in the growth regime (cyan), smouldering spread (growth) was dominant. The error bars represent the uncertainty of the model results after 10 repetitions. (b) The MC under the transient MC scenario averaged over one week and its range (error bars). The blue line denotes the MC averaged over 90 days, as used in the constant MC scenario.

KAPAS II (specifically, the transient MC scenario) was further used to predict the smouldering burnt area at the onset times of flames in different months and years between 2000 and 2019; each individual case lasted for 90 days. A total of 240 independent cases were considered; the first case began in January 2000 and ended in March 2000, whereas the last case began in December 2019 and ended in February 2020. Each of the cases reflect different temporal peat MC variations, and these variations were obtained by using the Apers *et al.* (2020) model (see Figure S7.2 for examples).

Figure 7.11a shows that the smouldering burnt area identified under the growth regime was linearly proportional to the smouldering burnt area obtained under the nucleation regime (R^2 = 0.98). This finding indicates that the smouldering burnt area derived under the growth regime was more significantly affected by the nucleation-regime peat MC (which controls the smouldering burnt area under the nucleation regime) than

by the growth-regime peat MC. Figure 7.11b proves this claim; the smouldering burnt area identified under the growth regime exhibited a strong inverse exponential correlation with the monthly average peat MC (averaged over one month) under the nucleation regime ($R^2 = 0.93$) but a weak correlation with the monthly averaged peat MC under the growth regime ($R^2 = 0.05$). Therefore, the peat MC under the nucleation regime is the crucial factor determining the total smouldering area, and its effects are more significant than those of the peat MC under the growth regime. When fewer smouldering hotspots are nucleated, the spread of these hotspots is less likely to overtake smouldering burnt area in cases in which more smouldering hotspots are nucleated, even when these hotspots spread more slowly. However, the peat MC differences identified between the nucleation and growth regimes shown in Figure 7.11a and Figure 7.11b are less than 20% in all cases; thus, these findings might not prevail when extreme peat MC differences occur between the nucleation and growth regimes. For instance, if the peat MC under the growth regime is extremely dry and the smouldering burnt area is affected by the spread of smouldering more significantly than by nucleation or if the peat MC under the growth regime is extremely wet and smouldering cannot be sustained under the growth regime, the smouldering burnt area under the growth regime will be zero regardless of the peat MC under the nucleation regime.

Figure 7.11c shows the temporal evolution patterns of the total smouldering areas obtained in different months and years; the smouldering area varied significantly and ranged from 0 to 0.93 km^2. The total smouldering area was minimal if the flames began during the wet season (i.e., resulting in wet peat); in Indonesia, the wet season typically spans between November and May. The total smouldering area the rose significantly in the dry season (i.e., with dry peat). In the wet season, due to the relatively high peat MC, smouldering hotspots were less likely to be nucleated; thus, some cases exhibited a total smouldering area of 0 km^2, whereas in the dry season, the peat became drier and more vulnerable to facilitating the nucleation of smouldering hotspots. This temporal pattern was mainly controlled by the peat MC, thus indicating the importance of temporal MC variations in affected peatland wildfires.

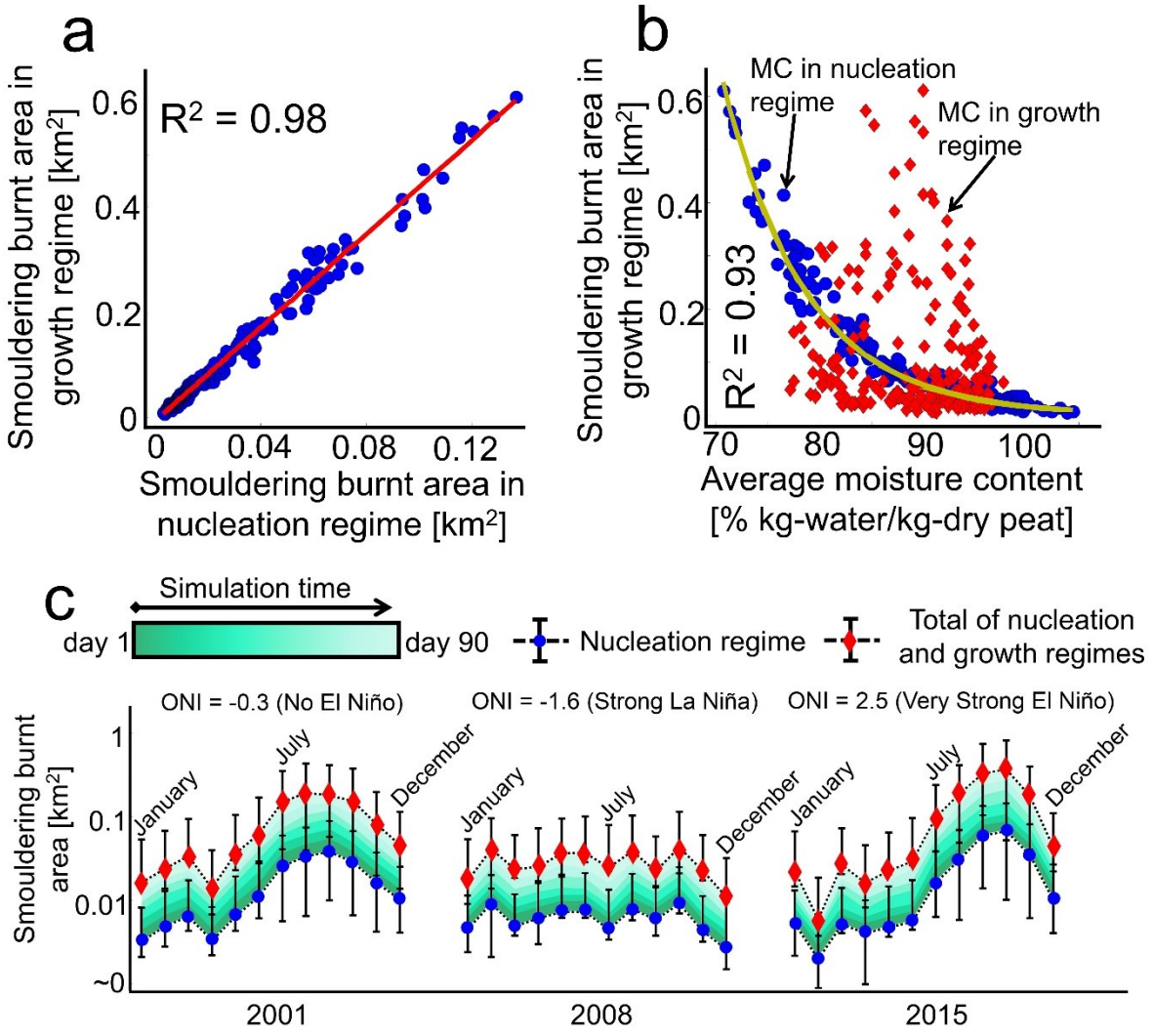

Figure 7.11. Predicted smouldering burnt areas in Borneo landscape (3.087°S, 113.991°E), when flames began in different months and years between 2000 and 2019 under continuous simulation runs (even after the flames were extinguished) lasting 90 days (time in the simulation). (a) The correlation between the smouldering burnt areas identified under the nucleation and growth regimes. (b) The correlation of the smouldering burnt area in the growth regime with the monthly average MC under the nucleation (blue circles) and growth (red diamonds) regimes. (c) The evolution patterns of the smouldering burnt areas in different months and years. The total smouldering burnt areas (red diamonds) represent the sum of the smouldering burnt area under the nucleation (blue circles) and growth (green gradient) regimes. The Oceanic Niño Index (ONI) determines the occurrence of El Niño and its counterpart La Niña (Null, 2021).

When a strong La Niña event occurred, the total smouldering area was found to be relatively constant throughout the year, i.e., less than 0.10 km² were found to be smouldering (see 2008 in Figure 7.11c), whereas when an El Niño event occurred, the total smouldering area significantly increased during the dry season, although the smouldering areas were similar during the wet seasons in these years, as El Niño mainly

affects the dry season (see 2015 in Figure 7.11c). The maximum total smouldering area identified during the dry season in a strong El Niño year (2015) was 0.93 km^2, whereas in a year without El Niño (2001), the maximum total smouldering area was 0.49 km^2 (see Figure 7.11c). These unique findings show that seasonal peat MC variations, which are strongly influenced by climate conditions, determine the severity of smouldering wildfires in peatlands. KAPAS II provides a tool for predicting the wildfire spread in peatlands, allows faster-than-real-time simulations, enables the improvement of peatland management, and thus can contribute to the mitigation of carbon emissions and haze-related adversities resulting from peatland wildfires.

7.3. Conclusions

In this chapter, KAPAS (see Chapter 6) was improved by considering the temporal variation of peat MC. The improved model in this chapter, KAPAS II, was validated against satellite observation based on flaming burnt scar (79% accuracy) and number of smouldering hotspots (85% accuracy). KAPAS II was used to simulate a peatland wildfire that occurred in Borneo in September 2018, and it was found that within 90 days, 0.55 km^2 of peat was affected by combustion losses due to smouldering. When considering a constant peat MC (KAPAS), the smouldering burnt area was significantly underestimated (with a 0.12-km^2 smouldering burnt area), with the same flaming burnt scar (111.43 km^2). This finding emphasises the importance of considering temporal peat MC variations.

The peat MC in the period of the formation of smouldering hotspots (nucleation regime) is the crucial factor that determine the overall severity of smouldering wildfire, and its influence is more significant than the peat MC in the growth regime, the period after flaming wildfire extinguish and the smouldering hotspots begin to spread. Wet peat condition within the nucleation regime could prevent the formation of smouldering hotspots, and minimise the smouldering burnt area of peat. This finding was supported when KAPAS II was extended to predict smouldering burnt area when flames began in different months and years between 2000 and 2019 (240 cases); each case lasted for 90 days. The smouldering burnt area in growth regime was found to have a strong correlation ($R^2 = 0.93$) with peat MC under the nucleation regime, but a weak correlation ($R^2 = 0.05$) with the MC under the growth regime. Therefore, the smouldering burnt area under both the nucleation and growth regimes are determined by the peat MC in nucleation regime.

The extended predictions also show that the smouldering burnt area varied significantly and ranged from 0 to 0.93 km^2; the area was below 0.1 km^2 if the flames began during the wet season and above 0.4 km^2 if the flames began during the dry season, except in La Niña years, when the burnt area remained steady throughout the year. In

strong El Niño years, while the wet-season smouldering burnt area was similar to other years, the dry-season smouldering burnt area could be doubled compared to years without El Niño; for instance, in 2015 (a strong El Niño year), the smouldering burnt area was 0.93 km^2, whereas in 2001 (a year in which no El Niño event occurred), the smouldering burnt area only 0.49 km^2. These findings show that seasonal peat MC variations, which are strongly affected by climate conditions, determine the extent of smouldering wildfires. The findings and model provide knowledge and a tool to improve the management of peatland, through faster-than-real-time simulations that can be used to predict the wildfire spread in peatlands in different scenarios, thus, can contribute to efforts in minimising the negative impact of peatland wildfires on people and the environment.

Chapter 8 – The Relevant Rules and Complexity in Cellular Automata for Smouldering Fire Modelling

Summary[7]

This chapter aims to investigate the rules that have been used in CA for smouldering fire modelling and assess the benefits and drawbacks of each rule. The goodness of the rules are compared based on accuracy, uncertainty, complexity, and capacity (the range of conditions that can be simulated by the models). From the comparison, the models with recursive burning rules, the burning state which remain burning for some time, either deterministic or stochastic, have better accuracy (15% - 20% higher), uncertainty (500% smaller), and capacity (300% - 500% larger) than other models. The deterministic recursive burning rule, however, outperforms the stochastic rule in term of accuracy (5% higher accuracy) and capacity (100% larger capacity). The models that attempt to mimic the physics of smouldering combustion have slightly higher accuracy than the models that use probabilistic approach, but with the consequence of increasing the complexity by 1000%, quantified by computational time,. However, the models that mimic the physics of smouldering benefit from its ability to be directly related with physical variables and phenomena. Therefore, the best model investigated in this chapter is the model which uses deterministic recursive burning rule and mimic the physics of smouldering fire, such as BARA (see Chapter 4). These findings can guide the selection of rules and provide direction for further development of cellular automata for smouldering fire modelling.

8.1. Methods

8.1.1. The CA models studied

This chapter aims to investigate the existing CA models for smouldering fire. Five CA models that have different set of rules, as shown in Figure 8.1, were compared, starting from the simplest model (M1) to the most complex model (M5). The simplest

[7] This chapter is based on "Dwi M J Purnomo and Guillermo Rein, 2022. The Relevant Rules and Complexity in Cellular Automata for Smouldering Fire Modelling. (to be submitted)."

model for modelling smouldering fire, adapting the model for flaming fire, is one order bond percolation (M1; Hargrove *et al.*, 2000). This model is the simplest form of bond percolation where the behaviour of the fire spread is governed by only one variable, i.e., probability of ignition, and becomes the basic for developing more complex CA model for smouldering fire. Belcher *et al.* (2010) introduced recursive behaviour of the smouldering fire to M1, aiming to simulate the persistent smouldering fire, by implementing second variable, i.e., extinction probability (M2), therefore, the burning cell extinguish in the subsequent time step with a probability less than one. This approach is referred to as two order bond percolation. Heat accumulation concept (see Chapter 3.3.1) is augmented to the bond percolation concept of M1 with threshold as the criterion to change the state (M3) as an attempt to mimic the physics of smouldering fire spread (Fernandez-Anez, Christensen and Rein, 2017; Fernandez-Anez *et al.*, 2019). M3 is further developed in two directions: (i) implementing recursive behaviour to capture three dimensional spread (M4), where the burning cells remain active until a specified time-step (burning time), such as in BARA (see Chapter 4), (ii) increasing the number of physics behaviour incorporated, i.e., adding more discrete states (M5; Fernandez-Anez *et al.*, 2019).

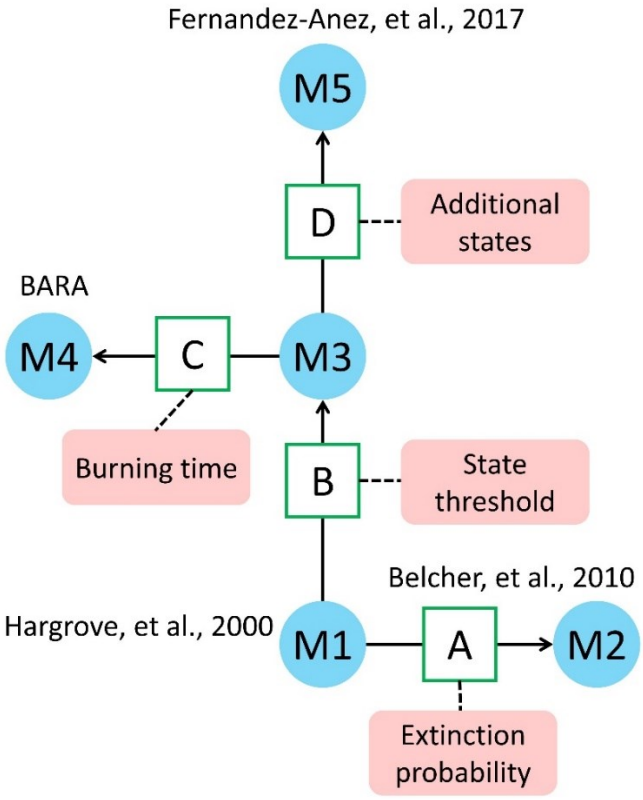

Figure 8.1. Scheme of the models (blue circle) considered in this work ranging from simplest model (M1) to the most complex model (M5). Arrows represent the connection between base model (origin of the arrow) and modified model (tip of the arrow). The modification is obtained by implementing concepts, which are shown in the green square (A to D), to the base model.

8.1.2. Rules of the models

The CA models for smouldering fire have several overlapping set of rules, thus, the set of rules for all the models can be put together as shown in Figure 8.2. For simplicity, the nomenclature of the states for all the models are generalised, which might be different from the nomenclature in the works that develop the models. For M1 to M4, the models only have three states, *peat* (P), *smouldering* (S), and *burnt out* (B), whereas for M5, two more states, *dry peat* (D) and *char* (C), are added. The neighbourhood in this chapter was selected to be von Neumann neighbourhood (North, South, East, and West neighbours), which is the simplest neighbourhood, for all the models. In Figure 8.2, the set of rules to update the states of cells for the models are represented by the different paths (black arrows) which connect *peat* to *burnt out* states. Each model has different path, in which the path for each model is indicated by the coloured circle. Each circle with unique colour defines the path to update the states of cells from *peat* to *burnt out*.

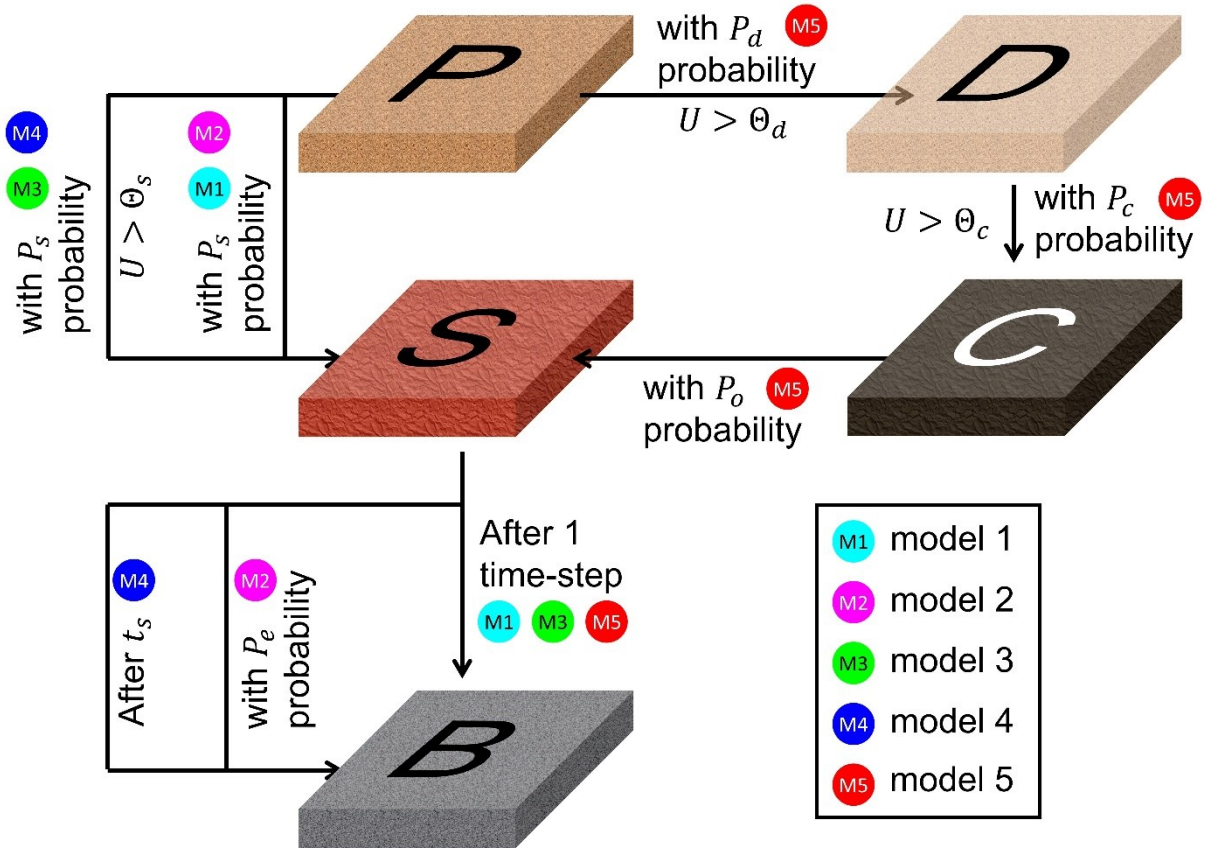

Figure 8.2. Scheme of the state change in model 1 to 5 from peat (P) to burnt out (B). Each model has different set of rules, which are distinguished using different coloured circles (M1 to M5). The coloured circles connect peat with burnt out via different paths that represent different rules to change the state. Model 1 to 4 have three states: peat (P), smouldering (S), and burnt out (B), whereas model 5 employs two additional states: dry peat (D) and char (C).

The *peat* cells in M1 (cyan circle) transition to *smouldering* when the peat cells encounter *smouldering* cells in their neighbourhood with a probability of P_s (smouldering probability; Hargrove *et al.*, 2000). The *smouldering* cells become *burnt out* at the subsequent time-step. The rule to transition from *peat* to *smouldering* in M1 is adopted in M2 (magenta circle), however, the transition from *smouldering* to *burnt out* in M2 at the subsequent time-step happen with a probability of P_e (extinction probability; Belcher *et al.*, 2010). M3 (green circle) and M4 (blue circle) add a criterion for the transition from *peat* to *smouldering*; i.e., the state of a cell changes if the cell's intrinsic value (U) exceeds smouldering threshold (Θ_s) with a probability of P_s. This intrinsic value is the representation of the heat accumulation concept (see Chapter 3), thus, it is referred to as heat value to give context in the physics of combustion process. M3 and M4 differs in the rule for transition from *smouldering* to *burnt out*. While M3 follows M1 where *smouldering* cells become *burnt out* at the subsequent time-step, M4 follows the concept of recursive behaviour in M2. However, the recursive behaviour in M4 is deterministic, in which the smouldering cells become *burnt out* after a specified time-step (t_s), which is referred to as burning time (see BARA in Chapter 4). The transition from *peat* to *smouldering* in M5 (red circle) follows a diversion path. Prior to the transition to *smouldering*, *peat* cells transition to *dry peat* when their U exceed drying threshold (Θ_d) with a probability of P_d (drying probability). The *dry peat* cells further transition to *char* when their U exceed charring threshold (Θ_c) with a probability of P_c (charring probability), after which the *char* cells transition to *smouldering* with a probability of P_o (oxidation probability; Fernandez-Anez, Christensen and Rein, 2017; Fernandez-Anez *et al.*, 2019). The *smouldering* cells in M5 then become *burnt out* at the subsequent time-step, following the rule in M1. These sequence of rules follow the process in smouldering combustion, i.e., drying – charring – oxidation – burnt out (Huang, Rein and Chen, 2015).

In M3 to M5, the states of cells change depend on the U of the cells. The U information are stored in heat layer, a different computational layer from the state layer which stores the information of states of cells, therefore, M3 to M5 employ multi-layer approach (Fernandez-Anez *et al.*, 2019). The rules which change the U of cells in M3, M4, and M5 are depicted in Figure 4.1a (see Chapter 4.1.2). The U of cells (i) are affected by the U transferred from or to the neighborhood (North, South, East, and West neighbors) and U transferred to the surrounding. The U transferred from or to the neighborhood depend on the difference in U between cell i and its each neighbour (ΔU). Fraction of ΔU will be transferred from or to the neighbours, which is quantified by heat transfer coefficient (φ). Fraction of U of cell i is also transferred to the surrounding (loss to

surrounding), which is quantified by heat loss coefficient (μ). The details of these rules can be found in Chapter 4.

8.1.3. Comparison criteria

The performance of the models (M1 to M5) were compared based on four criteria: accuracy, uncertainty, complexity, and capacity. The accuracy comparison represents the agreement between the models with real phenomena of smouldering fire. The uncertainty comparison represents the robustness of the models to produce same results when the simulation is repeated. The complexity represents the computational resource required by the models to run the simulations. The capacity represents the range of different conditions at which the smouldering fire occur can be simulated by the models. Therefore, the best model can be defined as the model which has the highest accuracy and capacity but has smallest uncertainty and complexity.

For accuracy and uncertainty, the models were compared against smouldering fire spread experiments of Christensen, Fernandez-Anez and Rein (2020). In their work, the smouldering fire experiments are conducted on different conditions of MC and IC, resulting in the smouldering fire with different horizontal spread rate and smouldering width. The experiments were conducted on 40cm × 40cm × 1.6cm reactor framed by insulated wall and ignited at the centre of the reactor, causing the smouldering fire to spread radially (see Figure 5.1a). This experiment setup is used as the domain for the models where the size of each cell in the models represent the resolution of the simulations. Higher resolution simulations have smaller cell size, resulting in greater number of cells in the domain to maintain the domain size to be equal the reactor size (40cm × 40cm). This domain is used for all the comparison criteria in this chapter. The accuracies of the models are determined based on the difference between the prediction of the models and the results from the experiments at various conditions. Three variables were compared, horizontal spread rate, smouldering width and burnt area, to investigate and compare the behaviour of the three direction of smouldering spread from the predictions. Horizontal spread rate represents the two dimensional lateral spread, whereas the smouldering width represents in-depth spread, which is the third direction of the smouldering spread. The comparison of burnt area was considered to investigate the pattern resulted from the predictions. The values of variables in the models (P_s, P_e, Θ_s, t_s, Θ_d, P_d, Θ_c, P_c, P_o, φ, μ) were explored, which make the predictions of the models have good agreement with the experiments. The simulation at one unique condition of experiment was repeated ten times, and the standard deviation of the results were calculated, to compare the uncertainties of the models.

The complexity of the models were quantified by using computational time required by the models to simulate the smouldering fire at the same condition. The resolution of the domain were varied, by changing the cell size and consequently the number of cells in the domain, to avoid resolution-dependent comparison results. For capacity, the variables of the models (P_s, P_e, Θ_s, t_s, Θ_d, P_d, Θ_c, P_c, P_o, φ, μ) were explored further to find all possible horizontal spread rate and smouldering width that can be simulated by the models. This capacity comparison is important to investigate the ability of the models to simulate many different cases and scales in addition to the experiments that are used in this chapter.

8.2. Results and Discussions

Figure 8.3 shows that only model 4 (BARA) that accurately simulated both leading edge and trailing edge in the experiments of Christensen, Fernandez-Anez and Rein (2020). The other models accurately simulated the leading edge of the experiments, however, they failed to simulate the trailing edge. Model 2 could simulate both leading and trailing edges only if the distance between them, i.e., smouldering width, is short, resulting in thin smouldering width. Otherwise, the simulation of model 2 resulted in randomly distributed smouldering cells as shown in Figure 8.3. The leading edge is the fire front at the surface of the sample that consume the peat at the surface layer, whereas the trailing edge is the fire front that consume the peat at the bottom of the reactor. The smouldering fire consumes the peat at different depth, from the surface to the bottom of the reactor, which is visualized by the burning region between the two edges. If the thickness of this region (smouldering width) is small, then the rate of in-depth spread is high, relative to the horizontal spread rate. Therefore, the leading edge represents the two dimensional horizontal spread of the smouldering fire, whereas the trailing edge represents in-depth spread of the fire.

These qualitative comparisons are confirmed with accuracy comparisons on the average horizontal spread rate and average smouldering width as shown in Figure 8.4. The horizontal spread rates are obtained by dividing the half of reactor size with the time required by the leading edge to reach the edge of the reactor. The smouldering widths are measured from the experiments and simulations, i.e., the distance between leading and trailing edges. Figure 8.4 shows that all the models have good agreement with experiments in term of horizontal spread rate, with error around 10% in various MC and IC conditions. However, model 1, 3, and 5 have significant error (more than 50%) in term of smouldering width. Model 2 has good agreement with experiments in term of smouldering width (within 10% error) when the smouldering width is less than 60mm.

This value is the largest value of smouldering width can be simulated by using model 2, larger value causes the randomly distributed smouldering cells as shown in Figure 8.3, thus, the error of smouldering width for values higher than 60mm are high in model 2. From these results, model 4 is the best model in term of the accuracy of horizontal spread rate and smouldering width, with error less than 10% for both the variables.

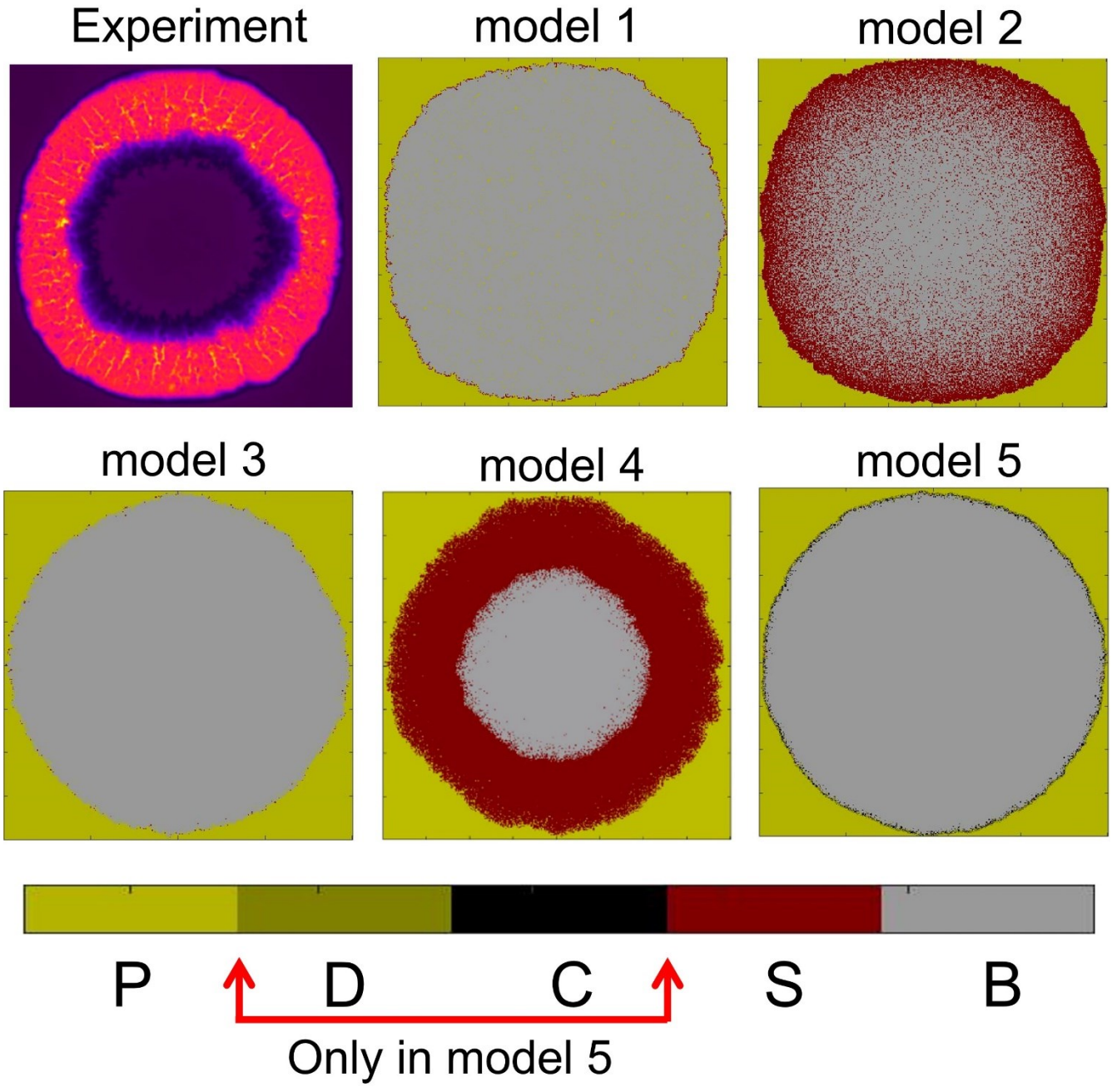

Figure 8.3. The comparison of experiment and predictions of model 1 to 5. Model 1 to 4 only have three states: peat (P), smouldering (S), and burnt out (B), whereas model 5 has two additional states, dry peat (D) and char (C).

Figure 8.5 shows that the burnt area at different times of the simulations from all the models have good agreement with experiments. This finding indicates that the shape of the simulation results are similar to those in experiments at different times after ignition. Model 1 has the largest deviation compared to other models since in model 1, there are patches of unburned peat that make the burnt area are under predicted. These accurate results for all the models despite large error on smouldering width, except for model 4, indicate that the burnt area is only affected by the horizontal spread. Therefore, since the errors on horizontal spread rate are low for all the models, low error on burnt area confirm the accuracy of the models in term of the shape produced by the models, which negates the possibility of compensation effect (Bal and Rein, 2013).

The errors of burnt area at different times after ignition for each model varies (see Figure 8.6a and Figure 8.6c), however, the time-averaged error for the models are similar (10-15%) and only model 1 which has considerably larger error (~25%) due to the patches of unburned peat. This finding infers that both recursive behaviour and heat accumulation concept increase the accuracy of the model by avoiding the creation of patches of unburned peat. These patches are commonly observed in real peatland wildfire, however, these patches are created due to the variability of conditions in natural peatland, for instance, non-uniform MC (see Figure 1.3). Therefore, for simulating smouldering fire in uniform condition, the patches of unburned peat are considered as inaccuracy.

The set of rules implemented in the models also affect the uncertainty of the models when the simulation is run repeatedly (see Figure 8.6b and Figure 8.6d). The standard deviation of the burnt area are different between models, however, the standard deviation of model 2, 4, and 5 are similar and both model 1 and 3 have significantly larger standard deviation than other models. The models were categorised in only two groups: a precise group (model 2, 4, and 5) that has small standard deviation and an imprecise group (model 1 and 3) that has large standard deviation.

There are two rules present in the precise group while absent in the imprecise group: recursive behaviour and additional states. The models in precise group either have the rules for recursive behaviour (model 2 and 4) or consider more states (model 5). Therefore, these two rules improve the precision of the models, i.e., lower the uncertainty.

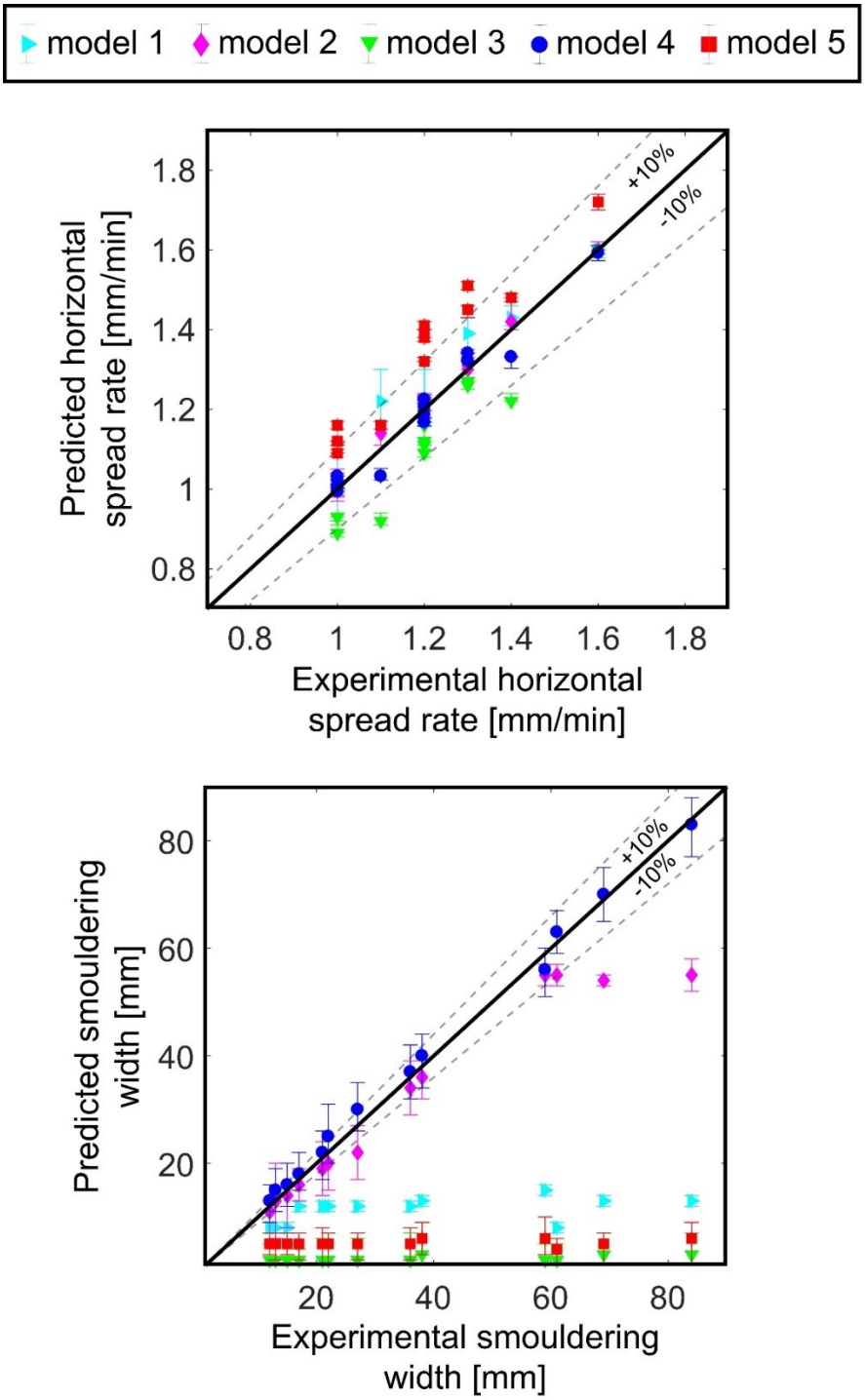

Figure 8.4. The comparison of predictions of model 1 to 5 against experiments on horizontal spread rate (top) and smouldering width (bottom). The solid black line represent the target at which the prediction perfectly match with the experiments. The symbols are the predictions from models with their uncertainties (10 repetitions).

Of the five models compared in this chapter, model 4 is the best in term of both accuracy and uncertainty, however, these good performances are accompanied with high complexity. Model 4 has error less than 10% for horizontal spread rate, smouldering width,

and burnt area and also has a relatively low standard deviation. However, the computational time required by model 4 to finish the simulation is the longest compared to other models (see Figure 8.7), and these computational times increase in quadratic manner when the resolution of the domain increases (meaning the increase of the number of cells). Although the difference in computational time between model 4 and model 3 and 5 are within 10%, the computational time required by model 4 to simulate the same scenario is more than 10 times longer than the time required by model 1 and 2. Therefore, heat accumulation concept significantly increases the complexity of the models, whereas additional rules to the heat accumulation concept, such as burning time and additional states, slightly increase the complexity. These findings indicate that model 2 provides alternative to model 4. For comparison, model 1 lacks both accuracy and uncertainty, whereas model 3 and 5 require similar computational time with model 4 despite having lower accuracy.

From the previous discussion, the only disadvantage of using model 2 instead of model 4 is the range of conditions can be simulated. This criterion is quantified by using capacity, the range of valid results. The valid results are defined as the simulations of self-sustained smouldering that have pattern similar to the shape found in the experiments of Christensen, Fernandez-Anez and Rein (2020), a circular ring pattern. With particular combination of variables in the models, the pattern resulted from the simulation could deviate from the circular pattern, for instance, a polygon as shown in Figure S4.1. The variables in the models were explored, all the variables that make the models do not give valid results were excluded, and the range of possible horizontal spread rate and smouldering width can be simulated by the models were compared. Both horizontal spread rate and smouldering width were normalised to avoid size effect of the domain. The normalised horizontal spread rate (R_S) is the ratio between horizontal spread rate and minimum horizontal spread rate that can be simulated by the models, whereas normalised smouldering width (R_W) is the ratio between smouldering width and half the size of the reactor (20cm).

From the comparisons, only model 1 which has a finite range of valid results in term of R_S (see Figure 8.8). Model 1 could only simulate with maximum R_S of 1.6, whereas the other models could simulate infinite range of R_S, therefore, more number of variables in the models increase the range of R_S can be simulated by the models. This finding indicates that the range of conditions of which model 1 can be used are very limited, especially when the phenomena involve both flaming and smouldering, where flaming could spread two orders of magnitude faster than smouldering (Rein, 2013). Model 1 also

has the narrowest range for Rw, however, this range is similar in model 3 and 5 in term of Rw.

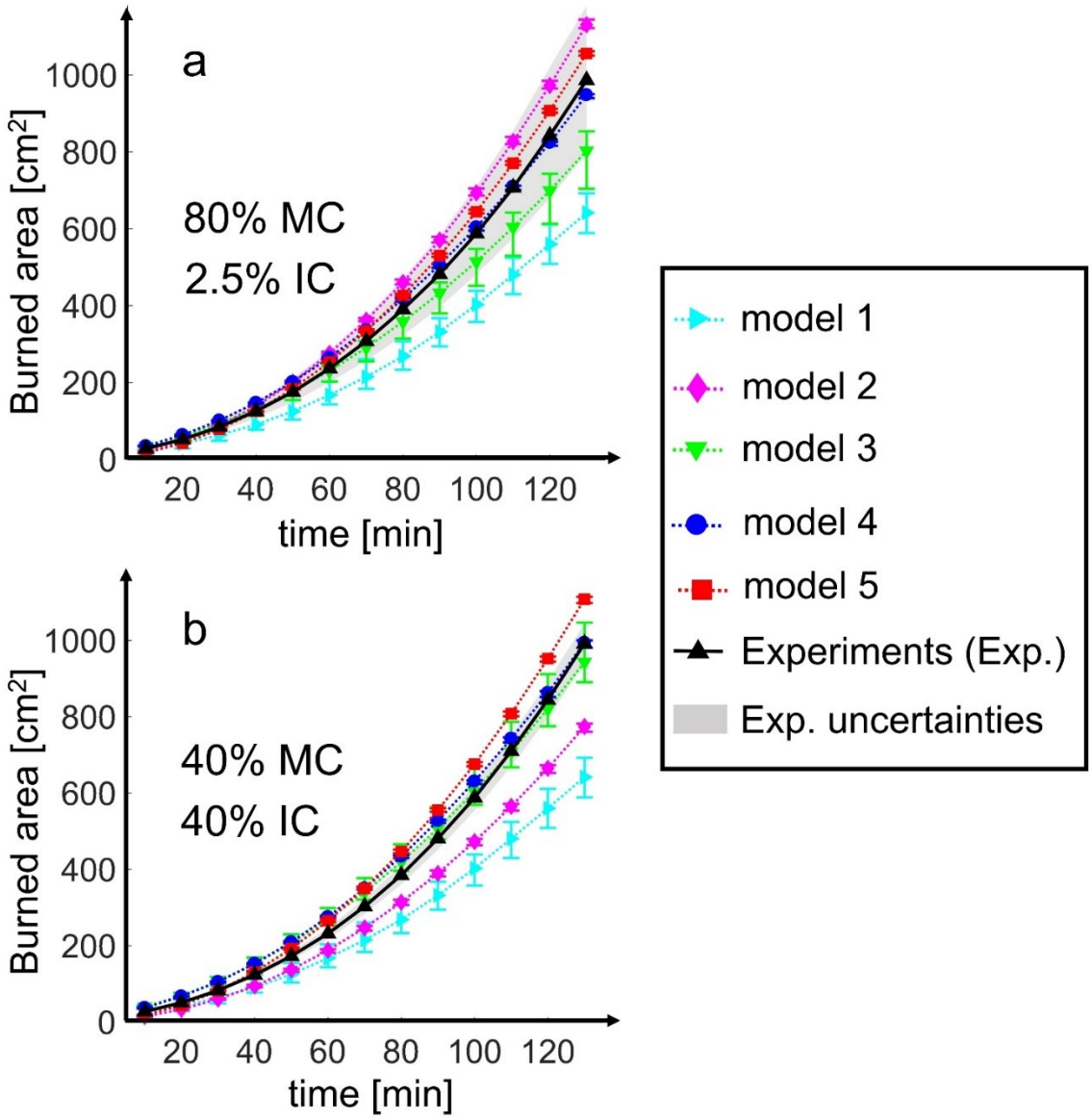

Figure 8.5. The comparison of predictions of model 1 to 5 against experiments on burnt area at two different conditions (MC and IC). The solid black line with triangle symbol represents the burnt area of experiments, with their uncertainties are indicated as grey shade. The dotted lines with symbols are the predictions from models with their uncertainties (10 repetitions).

Model 4 has the widest range of Rw among the other models. Model 4 could simulate smouldering fire with any smouldering width, which is five times wider range than model 1, 3, and 5 and more than twice the range of model 2. These findings indicate that recursive behaviour increase the range of Rw can be simulated by the models and the burning time rule, a deterministic recursive behaviour, is better than stochastic recursive behaviour, e.g., extinction probability. Therefore, model 4 is the best option to simulate

smouldering fire despite its complexity since model 4 has high accuracy, low uncertainty, and large capacity.

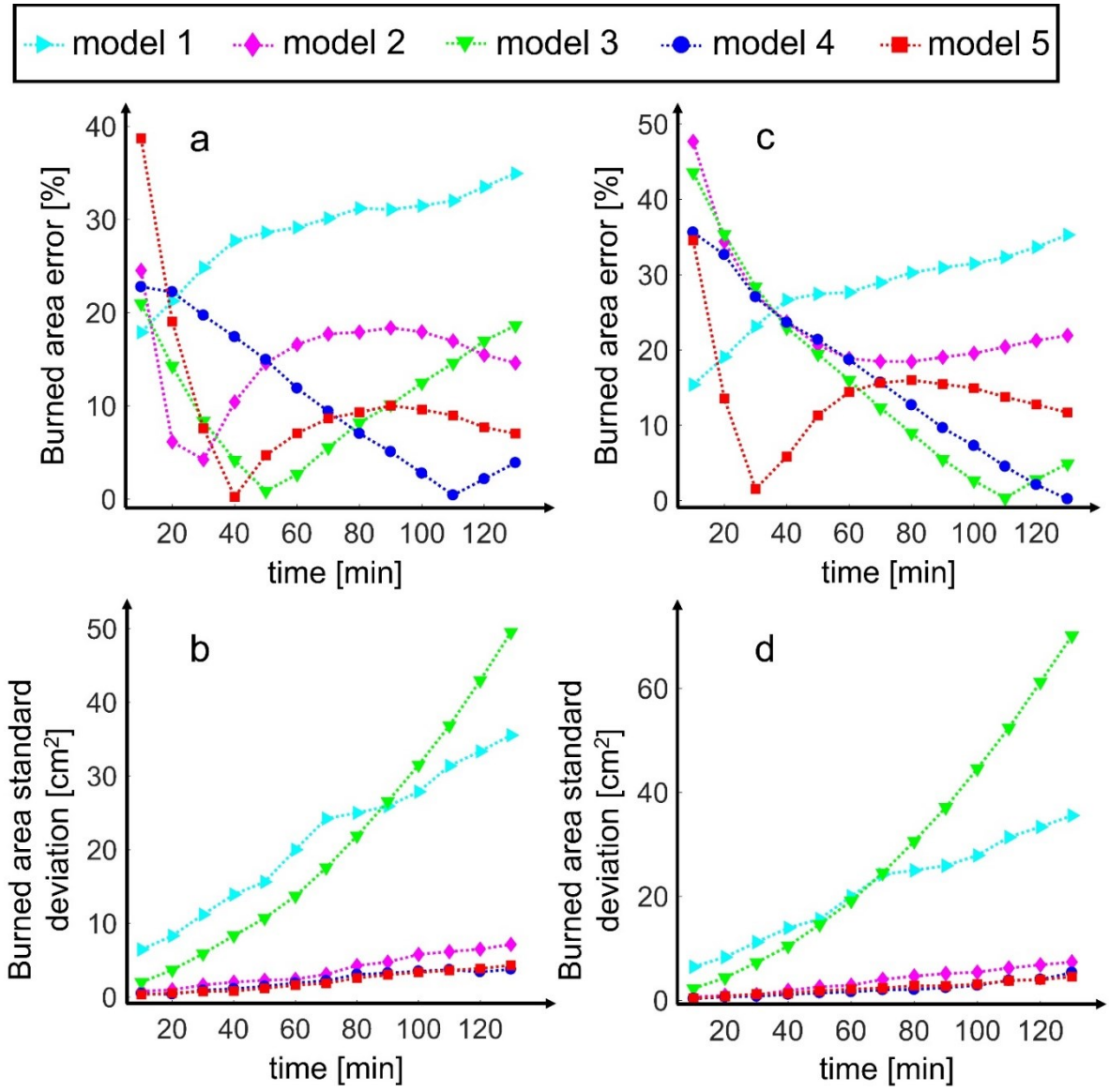

Figure 8.6. The error and standard deviation of model 1 to 5 compared to experiments at two different conditions. a and b are the results from smouldering peat with 80% MC and 2.5% IC, whereas c and d are the results from smouldering peat with 40% MC and 40% IC.

These results imply that each rule has different effect on the accuracy and uncertainty of the simulation results. The heat accumulation concept improves the accuracy, the additional states improve the uncertainty, and the recursive behaviour improves accuracy, uncertainty, and capacity. Although both deterministic and stochastic recursive behaviours enlarge the capacity of the models, the deterministic rule, such as burning time, increases the capacity larger than the stochastic rule.

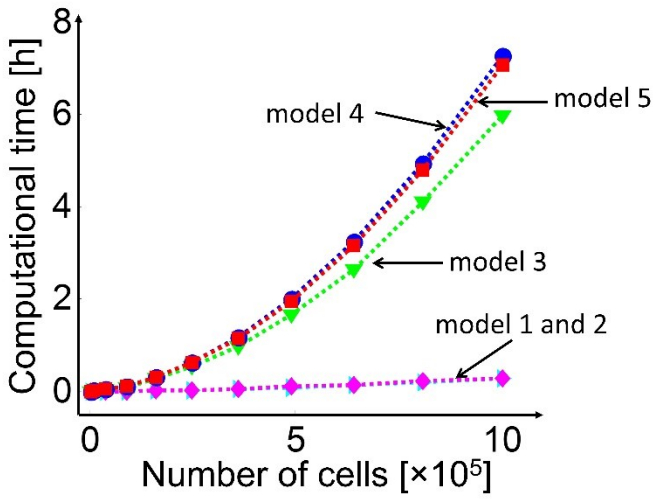

Figure 8.7. Required computational time of the models at different resolution (i.e., different number of cells for same reactor size). Despite having different computational time, the relationship between number of cells and required computational time of the models are the same, i.e., quadratic.

In term of the combination of the rules, the replacement of extinction probability rule in model 2 with burning time rule could become the best possible model since this hypothetical model could have similar accuracy, uncertainty, and capacity as model 4 but with significantly lower complexity. However, this hypothetical model is less compliant when compared with physical term. In the calibration of model 4, the variables in the model can be related to the variables in physical term, whereas the hypothetical model that only has two variables cannot be related with physical term. Therefore, the hypothetical model will be lack in the ability to forecast new phenomena.

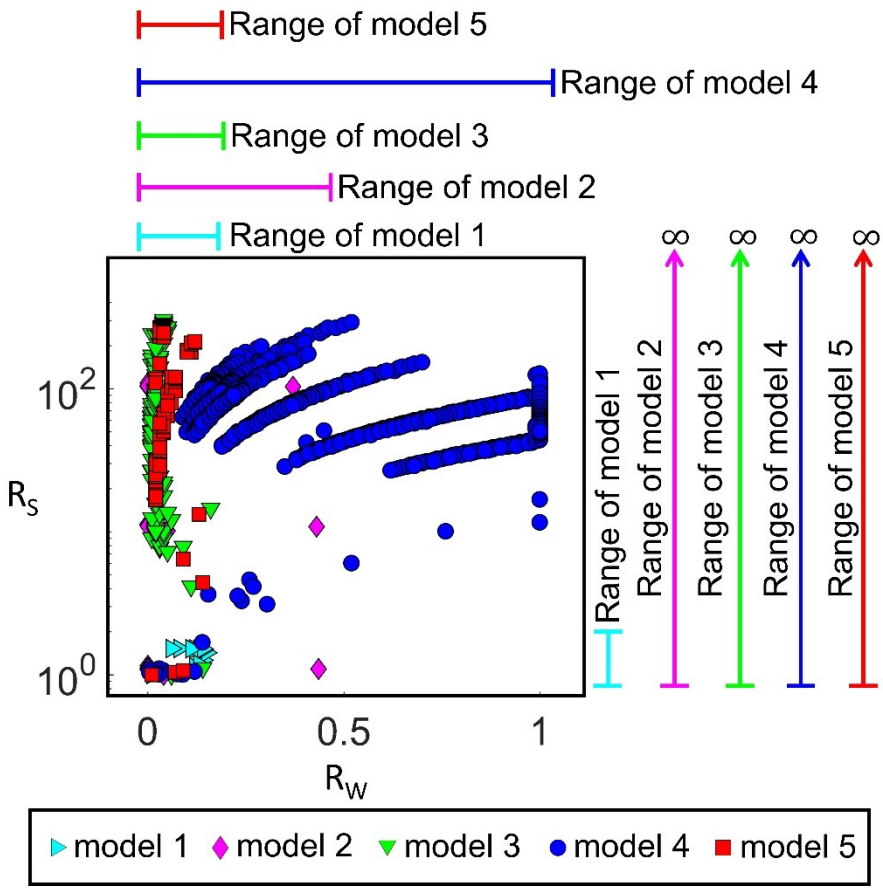

Figure 8.8. Range of normalized horizontal spread rate (R_S) and normalized smouldering width (R_W) of which the models have valid results (circular ring pattern). R_S is formulated as horizontal spread rate divided by the minimum horizontal spread rate obtained by the model, whereas R_W is formulated as smouldering width divided by the reactor width. The symbols represent the simulation results of each model, whereas the coloured lines represent the range of R_S and R_W which can be simulated using each model. The infinity symbols (∞) in the range of R_S indicate that the model could simulate smouldering fire with any horizontal spread rate.

8.3. Conclusions

In this chapter, the set of rules in cellular automata for smouldering fire modelling were investigated. Five different cellular automata models that have been developed in the literatures were compared based on their accuracy, uncertainty, complexity, and capacity and the rules which become the determining rule for the performance on each comparison criterion were analysed. From the comparison, BARA (see Chapter 4) is the best performer compared with other models in the literatures (Hargrove *et al.*, 2000; Belcher *et al.*, 2010; Fernandez-Anez *et al.*, 2019). BARA has high accuracy (within 10% error) and low uncertainty when compared to experiments (Christensen, Fernandez-Anez and Rein, 2020). This model also has the largest capacity, possible scenario can be

simulated by the model, compared to other models although the model requires longest computational to finish the simulation. BARA has two prominent rules, heat accumulation concept and deterministic recursive behaviour, which make this model performs the best. The recursive behaviour, both deterministic and probabilistic (developed by Belcher *et al.*, 2010), improve accuracy, uncertainty and capacity of the models. However, the capacity improved by using deterministic recursive behaviour is significantly greater than by using probabilistic recursive behaviour. Compared to bond percolation (e.g., in KAPAS and KAPAS II, see Chapter 6 and Chapter 7), heat accumulation concept has higher accuracy. Although the complexity of heat accumulation concept is significantly higher than bond percolation, heat accumulation concept can be related to the physical terms more easily, which is beneficial, for example, in the calibration process. Therefore, the combination of heat accumulation and deterministic recursive behaviour rules are the best for simulating smouldering fire. These findings can guide the selection of appropriate rules in cellular automata for modelling smouldering fire and provide direction on the further development of the model.

Chapter 9 – SUBALI: Three-Dimensional Cellular Automata Model to Estimate Burnt Area and Carbon Emission of Field-Scale Peatland Wildfires

Summary[8]

This chapter aims to upscale the 3-D CA model for smouldering in Chapter 4 (BARA) and integrate it with the model in Chapter 7 (KAPAS II), to develop the first 3-D model for field-scale peatland wildfires, SUBALI. SUBALI was used to estimate the smouldering burnt area based on peat MC and GWT that vary daily, derived from a peat-specific land surface model. The GWT was also used to estimate the depth of burn of smouldering wildfires. The predictions of SUBALI show that the peat MC within the lifespan of flaming wildfires has an inverse exponential correlation with the ratio between smouldering and flaming burnt area. From this correlation, GWT data, and flaming burnt area data, 0.33 Gt-C was estimated to be released to the atmosphere due to smouldering wildfires in Indonesia in 2015. The importance of peat conditions and GWT for the estimation of carbon emissions was revealed, in addition to the smouldering burnt area. The further estimation of carbon emission of peatland wildfires in Indonesia from 2016 to 2019 shows that the emissions from smouldering wildfires significantly predominates the emissions from flaming wildfires (only) in El Niño years. In 2019, a moderately strong El Niño year, the carbon emissions from smouldering wildfires were approximately 0.11 Gt-C. Although this value was only one-third of emissions in 2015, in the dry season, the carbon release rate from smouldering wildfires was 1.67 Mt-C/day, which is a similar rate to fossil fuel emissions in the European Union (2.42 Mt-C/day). The findings and models improve the understanding of smouldering wildfires and carbon emission estimation and provide a faster-than real-time simulation tool, which can be used to optimise the

[8] This chapter is based on "Dwi M J Purnomo, Sebastian Apers, Michel Bechtold, Parwati Sofan, Guillermo Rein, 2022. Estimation of Burnt Area and Carbon Emission of Indonesian Smouldering Wildfires from 2015 to 2019. (to be submitted)."

strategies for peatland management through multi-scenario simulations, thus can contribute to climate change mitigation.

9.1. The Development of SUBALI

9.1.1. Introduction to SUBALI

From the analysis in Chapter 8, BARA (Chapter 4) was found to be the optimum CA model to simulate the 3-D spread of smouldering. Although BARAPPY (Chapter 5) has a higher accuracy for in-depth smouldering, its two order of magnitude higher computational cost causes this model to be unsuitable for field-scale modelling. This chapter aims to upscale BARA (Chapter 4) and integrate it with KAPAS II (Chapter 7), to enable a CA model for field-scale peatland wildfires that consider 3-D spread of the smouldering component. Therefore, the model in this chapter uses bond percolation concept for the flaming component, and heat accumulation concept for the smouldering component (see Chapter 3). From here on, the model in this chapter will be referred to as SUBALI, originated from a warrior in Indonesian legend that can rise from the death, similar to peatland wildfires that are commonly known as 'zombie fires'.

SUBALI was used to correlate the smouldering burnt area with flaming burnt area, given the peat MC and GWT, which are derived from a peat-specific land surface model. From this correlation, the smouldering burnt area can be estimated from the flaming burnt area data, which are more readily available. The level of carbon emissions was estimated based on these burnt areas and the DOB that is derived from the GWT data. This approach was used to estimate the carbon emissions from Indonesian peatland wildfires from 2015 to 2019. The first part of this chapter discusses the estimation of smouldering burnt area based on the flaming burnt area and peat conditions, which is followed by a discussion on the estimation of carbon emissions from Indonesian peatland wildfires within five years period.

9.1.2. States and rules of SUBALI

SUBALI considers 5 possible states for each cell: *surface vegetation (SV), flaming vegetation (FV), exposed peat (EP), smouldering peat (SP), and burned peat (BP)*, as in KAPAS (Chapter 6) and KAPAS II (Chapter 7), as shown in Figure 9.1. To enable the simulation to involve both flaming and smouldering wildfires, SUBALI employs a multi-layer approach, following KAPAS (Chapter 6) and KAPAS II (Chapter 7), in which there are two interconnected layers: surface and soil (see Figure 9.1a). The soil layer only accommodates smouldering wildfires, whereas the surface layer mainly accommodates flaming wildfires, since the smouldering spread in the soil layer is also projected onto the

surface layer to provide better visual representation in the simulation, unless the surface vegetation in the surface layer has not become exposed peat (smouldering peat underneath intact surface vegetation). The surface layer considers a 2-D spread, whereas the soil layer considers a 3-D spread. This distinction aims to provide sufficient complexity in the soil layer where the vertical spread of smouldering peat is important, while simplifying the surface layer since the vertical spread of flaming vegetation is two order of magnitude faster than in smouldering peat.

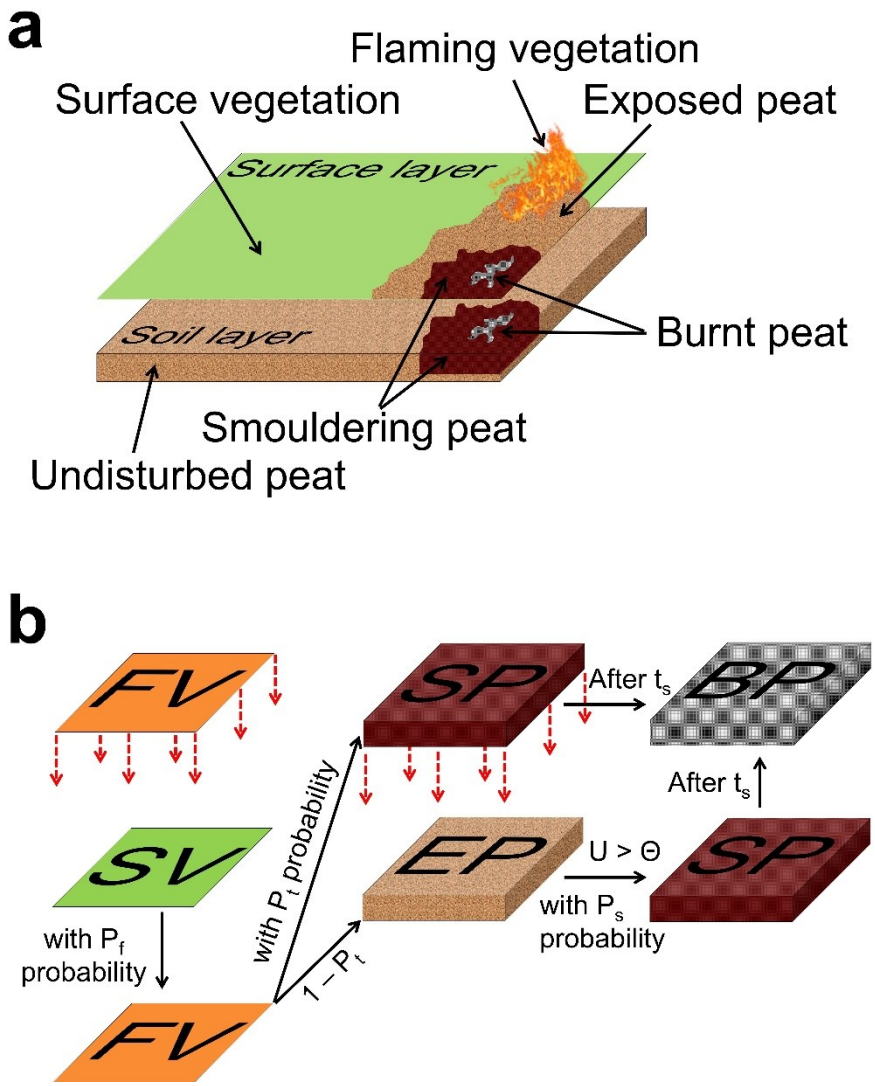

Figure 9.1. (a) Schematic of the multi-layer approach of SUBALI. (b) The states and rules of SUBALI. SV is surface vegetation, FV is flaming vegetation, EP is exposed peat, SP is smouldering peat, BP is burnt peat, P_f is the probability of the flames spreading, P_t is the probability of transition from flaming to smouldering occurring, and P_s is the probability of smouldering spreading. Solid arrows represent possible state changes, whereas dotted arrows

represent potential influences from neighbouring cells. U is intrinsic value, Θ is smouldering threshold, and t_s is smouldering time.

The rules used in SUBALI for flaming spread and smouldering hotspot nucleation in the surface layer are the same as the rules used in KAPAS II (Chapter 7). The flaming vegetation cells spread its fire to the neighbouring surface vegetation cells with a probability of P_f, and the flaming vegetation cells can ignite the peat underneath, creating smouldering hotspots, with a probability of P_t (see Figure 9.1b). The smouldering peat cells that are ignited by the flaming vegetation in the surface layer are projected onto the corresponding locations in the soil layer.

In the soil layer, the rules that are used follow the rules in BARA (Chapter 4). Each cell in the soil layer has an intrinsic value (U), which determines the change of states in the soil layer. The undisturbed peat cells (exposed peat and peat in soil layer underneath surface vegetation) change their state to become smouldering peat cells, when their U exceeds a smouldering threshold (Θ) due to the U transfer, with a probability of P_s (see Figure 9.1b). This U transfer happens when there is a difference in U value regardless of the state of the cells, and the fraction of the U that is transferred from cells with higher U to the cells with lower U is formulated as $\varphi\Delta U$, where φ denotes the heat transfer coefficient. The heat loss to the surroundings is also considered, and quantified as μU; μ denotes the heat loss coefficient.

All the smouldering peat cells generate value of Q_R, which is added to its U value, every time-step while they remain smouldering. The smouldering peat cells then become burnt peat after a certain time-step, t_s, and stop the generation of Q_R. The time delay (t_s) before smouldering peat becomes burnt peat represents the vertical spread, and its value depends on the in-depth spread rate.

9.1.3. Datasets for input parameters and validation

SUBALI was validated against two peatland wildfires that happened in Indonesia: in Central Kalimantan (3.087°S, 113.991°E) and in Jambi (1.305°S, 103.945°E). The wildfire in Central Kalimantan started on 21 September 2018 and was fully extinguished on 10 October 2018, and the one in Jambi started on 21 August 2019 and was fully extinguished on 30 September 2019 (see Figure 7.1a and Figure 9.2a). These wildfires were selected because of the availability of the data, the location of the sites on different islands (Central Kalimantan is on Borneo and Jambi on Sumatera), and because they happened in different years, to ensure the generality of the model. Figure 7.1a (for Central Kalimantan) and Figure 9.2a (for Jambi) show the progression of the flaming wildfires,

which can be detected by remote sensing via Sentinel-2 (Copernicus, 2022), by using false-colour urban composites that emphasize fires and burnt scars from other objects (Stavrakoudis *et al.*, 2020). The brown colour in these figures represents the flaming burnt scar, whereas yellow and red represent the fire. The white, green, and blue represent cloud, surface vegetation, and water bodies respectively.

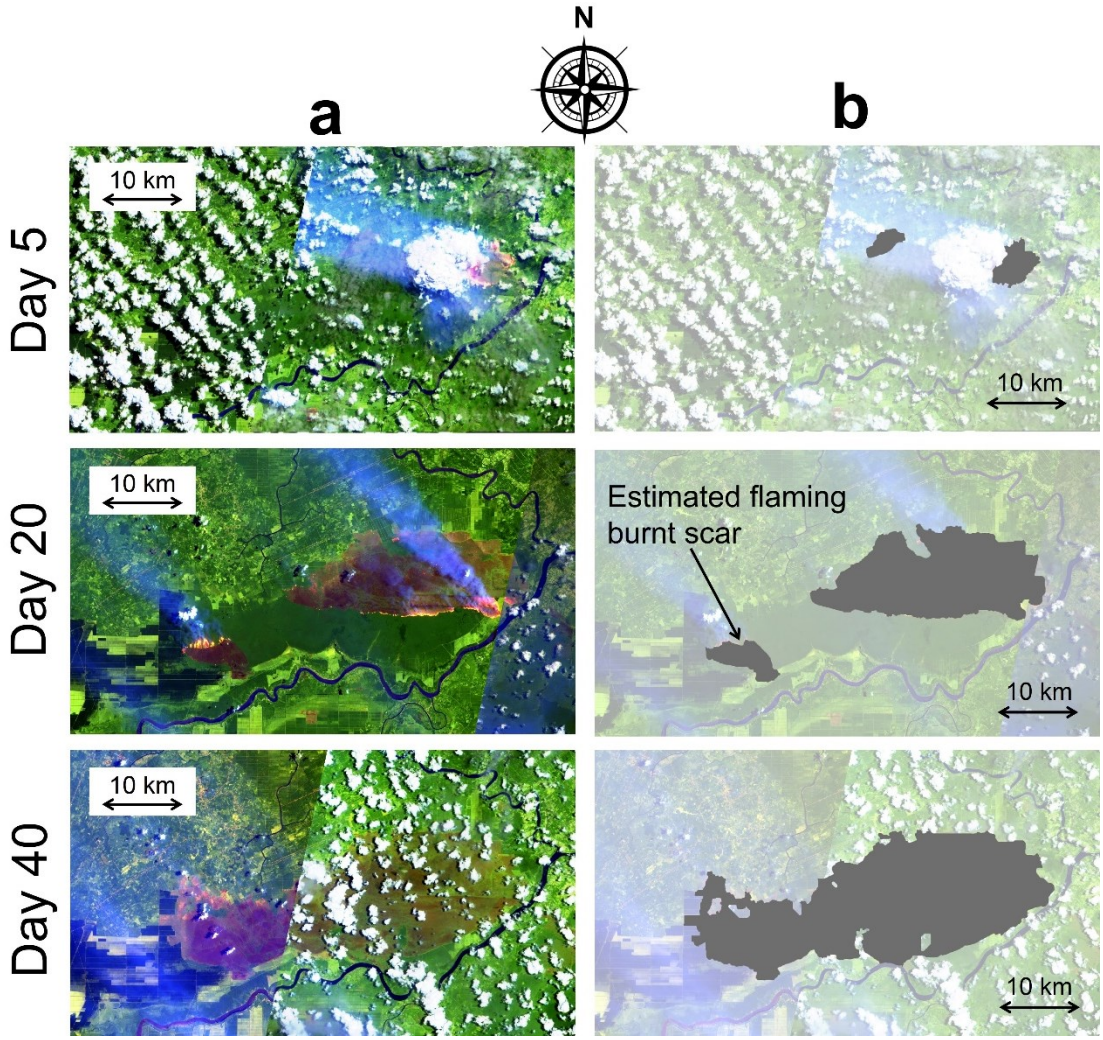

Figure 9.2. Satellite image of a landscape in Jambi (1.305°S, 103.945°E) in August 2019 obtained from Sentinel-2 (Copernicus, 2022) (a) The progression of a flaming wildfire in the Jambi landscape detected by Sentinel-2 (Copernicus, 2022). (b) Estimated flaming burnt scar in the Jambi landscape.

The burnt scar caused by flaming wildfire was estimated by using a seed-fill algorithm (Khayal *et al.*, 2011) that detects the burnt scar pixels (brown colour) from the false-colour urban composite images (Figure 7.1b and Figure 9.2b). These data were used to validate the flaming component of SUBALI. The firebreaks that stop the flames from

spreading were considered by observing the progression of burnt scar. Firebreaks were indicated by the abrupt stop of the flames, causing the burnt scar to have a relatively smooth edge (see day 20 in Figure 7.1a). The water bodies were also considered as firebreaks since they stop the spread of flames; however, their determination were significantly simpler. Figure 7.2a and Figure 9.3a show the landscape, including estimated firebreaks for Central Kalimantan and Jambi, respectively. The images in these figures were obtained from the data when the wildfires have not started to avoid misclassification.

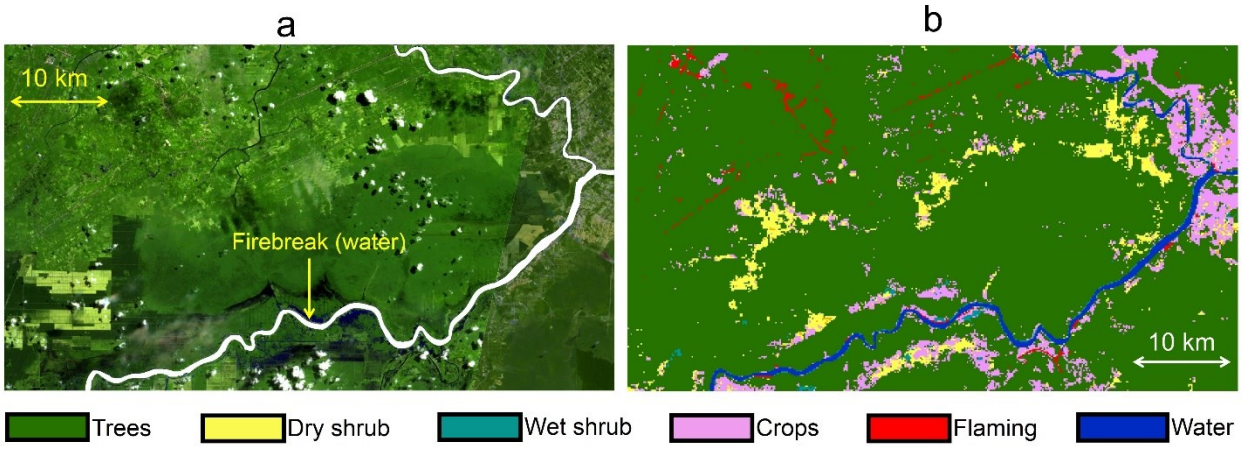

Figure 9.3. (a) Satellite image of a landscape in Jambi (1.305°S, 103.945°E) in August 2019 before the flames began; this image was obtained from Sentinel-2 (Copernicus, 2022). The white lines highlight firebreaks. (b) Remote sensing-based vegetation types identified in the peatlands in the Jambi landscape (1.305°S, 103.945°E), as obtained from Buchhorn et al. (2020). Four vegetation types were considered: dry shrubs (yellow), wet shrubs (cyan), crops (purple) and trees (green).

SUBALI considered three types of flammable surface vegetation for the Central Kalimantan wildfire: dry shrub, wet shrub, and trees; and four types of flammable vegetation for the Jambi wildfire: dry shrub, wet shrub, crop, and trees (see Figure 7.2b and Figure 9.3b), following Ferraz *et al.* (2019); Buchhorn *et al.* (2020). Rain and wind condition were also considered in SUBALI, using daily data from a local weather station (BMKG, 2018) on precipitation, wind speed and wind direction.

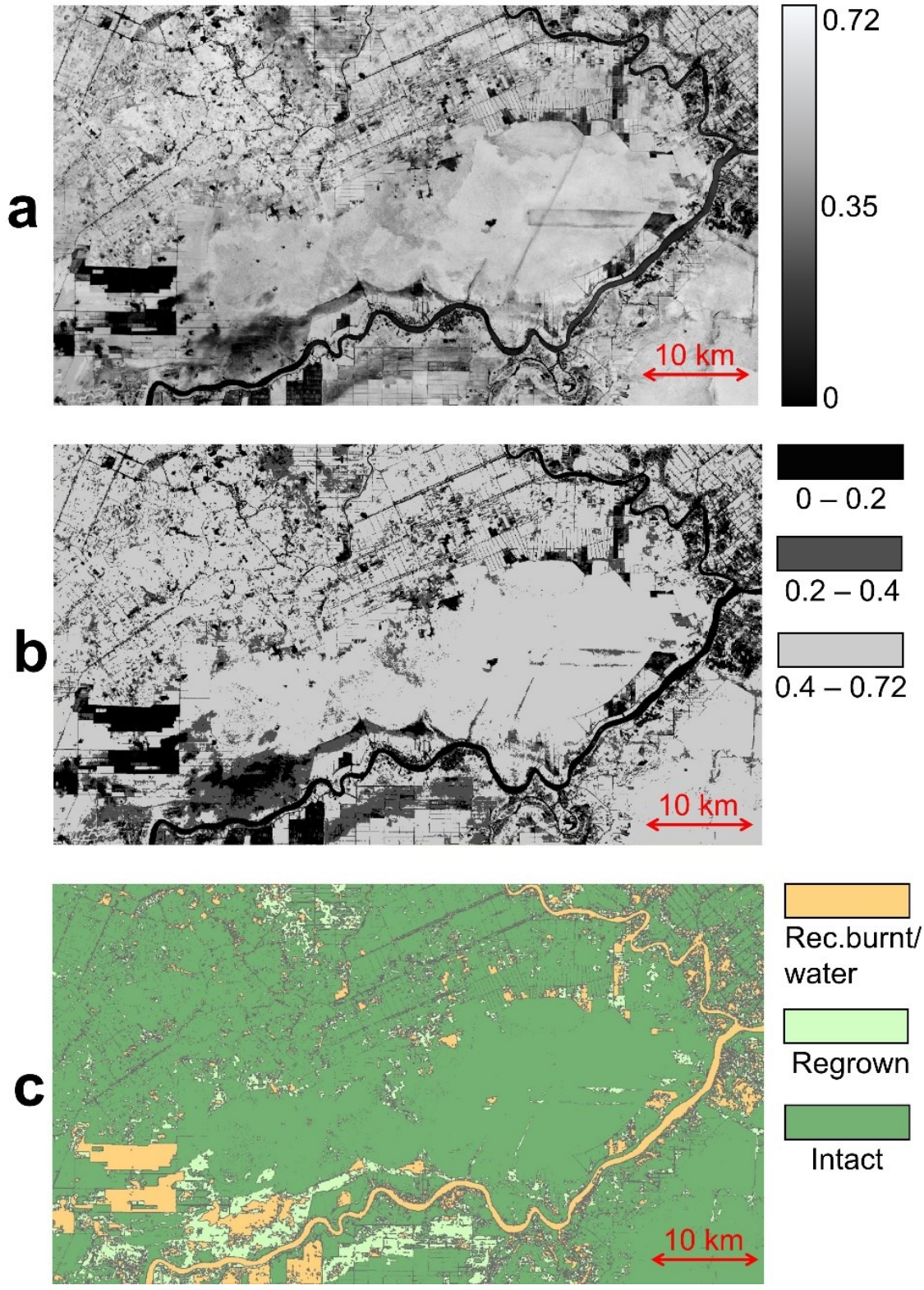

Figure 9.4. (a) The NDVI data of a landscape in Jambi (1.305°S, 103.945°E) on 6 August 2019; these data were used to estimate the vegetation density and were obtained from Sentinel-2 (Copernicus, 2022). (b) Reclassified NDVI data in the Jambi landscape (1.305°S, 103.945°E) on 6 August 2019; these data were used to simplify the vegetation density classification scheme

and were adapted from Alexandridis et al., (2008) (c) The vegetation density data characterizing the Jambi landscape (1.305°S, 103.945°E) on 6 August 2019 used in the model; these data were based on the NDVI data and classified as recently burnt and water (rec. burnt/water), regrown, or intact.

SUBALI considered the vegetation density, which is classified based on the Normalised Difference Vegetation Index (NDVI) data, the most commonly used data to estimate vegetation density (Camps-Valls *et al.*, 2021), obtained from Sentinel-2. Figure 7.3a and Figure 9.4a show the NDVI of the Central Kalimantan and Jambi sites, respectively. However, only three categories of vegetation density were considered: recently burnt and water, regrown, or intact (adapted from Alexandridis *et al.,* 2008); thus, the NDVI were reclassified into three classes: 0 – 0.2, 0.2 – 0.4, and above 0.4, respectively (see Figure 7.3b and Figure 9.4b). Recently burnt vegetation corresponds to vegetation that is burnt by previous wildfires, regrown vegetation corresponds to the previously burnt vegetation that has started to regrow, and intact vegetation is vegetation that is not affected by previous wildfires. Figure 7.3c and Figure 9.4c show the final data of the vegetation density classification for SUBALI. The NDVI data that were used were those from few days before the start of wildfires, thus, the data were actual.

SUBALI considered peat MC and GWT data that were derived from $PEATCLSM_{Trop,Drain}$ (Apers *et al.*, 2020), with the assumption of drained type and MC is at the surface, following KAPAS II (see Chapter 7). The gravimetric MC data required by SUBALI were derived from the division of volumetric MC of $PEATCLSM_{Trop,Drain}$ by 0.585, i.e., peat bulk density (in g/cm^3), which also follow KAPAS II (see Chapter 7). The data on smouldering hotspots were used to validate the smouldering component of SUBALI. These data were obtained from the remote sensing detection by using TOPECAL (Sofan *et al.*, 2020; see details in Chapter 7). Figure 7.4 and Figure 9.5 show the smouldering hotspots that were detected by using TOPECAL, for Central Kalimantan and Jambi sites, respectively.

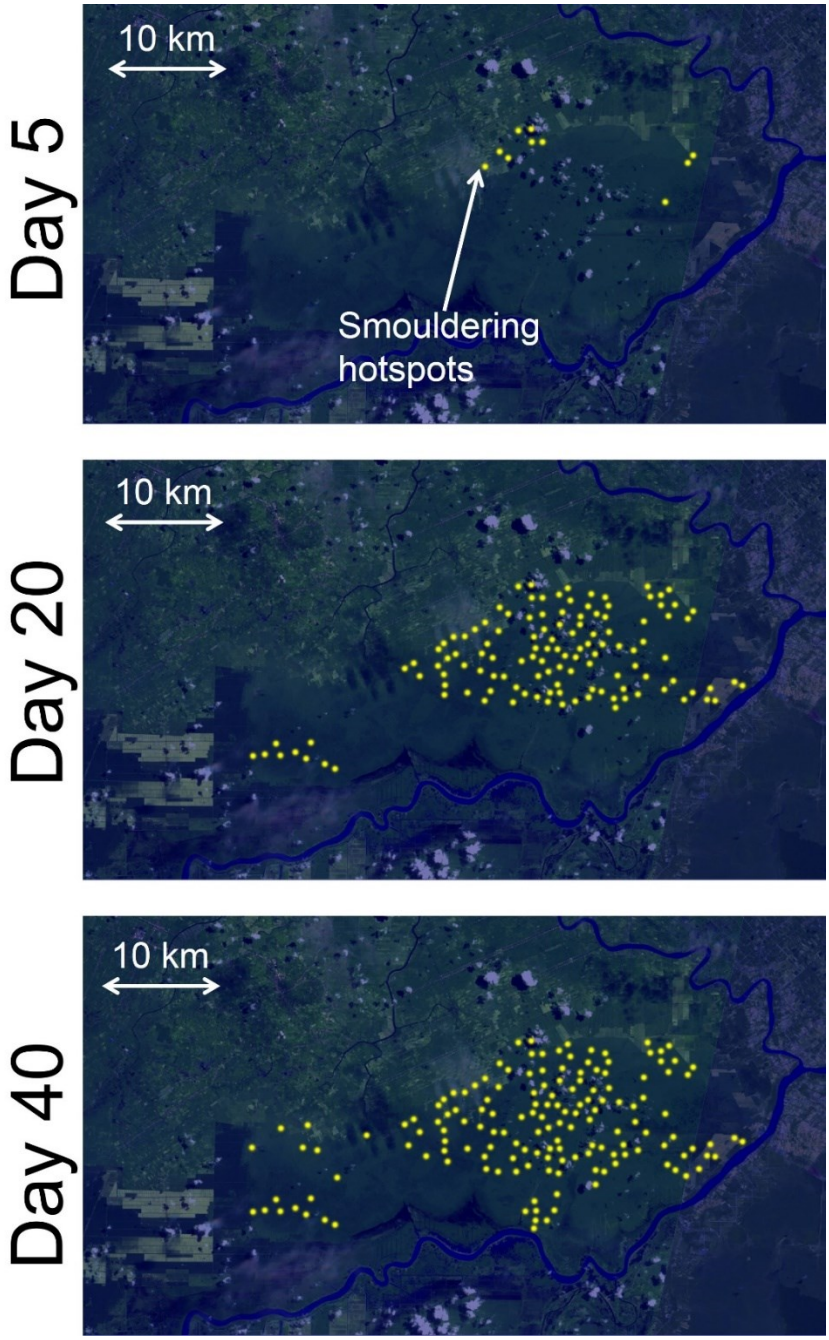

Figure 9.5. The smouldering hotspots (yellow circles) in a landscape in Borneo (1.305°S, 103.945°E) in 2019, detected by the algorithm developed by Sofan et al. (2020) and implemented in the remote sensing data of Sentinel-2 (Copernicus, 2022). The increases in the number of hotspots correspond to the progression of the flaming wildfire (see Figure 9.2a).

9.1.4. Calibration of SUBALI

The behaviour of SUBALI depends on the value of its variables both in surface layer (P_f and P_t) and in the soil layer (Θ, P_s, φ, Q_R, μ, and t_s). The values of P_f and P_t

follow KAPAS II (see Chapter 7), which were formulated in Eq. 7.1 – Eq. 7.7. The values of Θ, φ, and Q_R were formulated in Eq. 4.2 – Eq. 4.7, whereas μ was set constant to be 0.1, following BARA (Chapter 4). To enable the domain independent model in the soil layer, the value of P_s was re-calibrated with different λ, following the method in Chapter 7. In BARA (Chapter 4), P_s was set constant to 0.1 because if P_s was too large, the shape of the smouldering fire front became spurious (polygon instead of circular), whereas when P_s was too small, the smouldering was not self-sustained. In SUBALI, P_s was defined as 0.1η, where η is the smouldering probability correction factor that depends on the λ. Figure 9.6a shows the calibration results of η, where the value of η was explored to make the spread rate in the simulation at different λ (different spatial and temporal resolution) concur with the spread rate in the experiments of Christensen, Fernandez-Anez and Rein (2020). The correlation of η and λ can be formulated as $\eta = 0.16\lambda^{-1.03}$ with $R = 0.98$. Therefore, in SUBALI, $P_s = 0.016\lambda^{-1.03}$, which makes SUBALI a domain independent model. Figure 9.6b shows the comparison of spread rate from the experiments with the spread rate from simulations with the new formulation of P_s with a cell size of 45 m and a time-step of 1200 s. Without adjusting the formulation of other variables, the usage of the new formulation of P_s could simulate all the experiments in Christensen, Fernandez-Anez and Rein (2020) in a large scale case reasonably accurately.

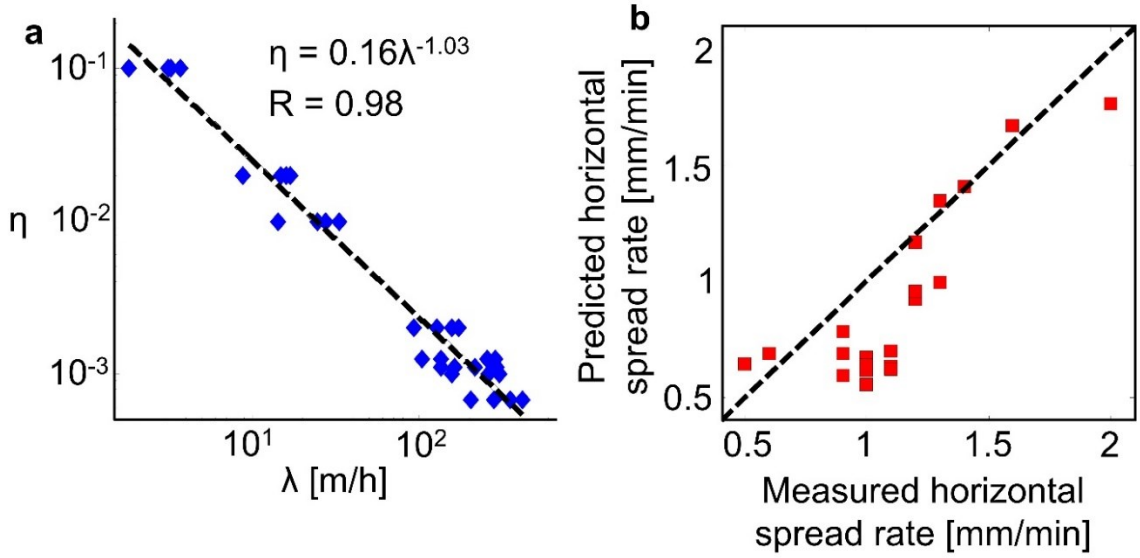

Figure 9.6. (a) Relationship between smouldering probability correction factor (η) and spatiotemporal factor (λ). (b) Comparison between the spread rate from experiments of Christensen, Fernandez-Anez and Rein (2020) and large scale simulations.

The restriction of a non-self-sustained smouldering when P_s is too low still prevail. In SUBALI, the formulation of t_s in BARA (Eq. 4.3) was modified to compensate the

restriction as shown in Eq. 9.1. BARA only uses the second term in Eq. 9.1, where t_s (in number of time-step) is a function of the peat thickness (d), in-depth spread rate (S_d), and time-step (Δt). This term represents the time required to consume the peat from the surface until the total depth of the peat. In BARA, it is assumed that once a cell is smouldering, the entire area ($\Delta x \times \Delta x$) of the cell is uniformly smouldering. This assumption is acceptable when Δx is relatively small (e.g., BARA uses $\Delta x = 1$ mm); however, when the cell size is in m order, the assumption is not justified. When the cell size is relatively large, apart from the in-depth spread within one cell, there is a horizontal spread inside a cell. Therefore, although the smouldering has consumed the entire thickness of the peat, the smouldering in one cell remains active due to the internal horizontal spread. However, since one cell is the smallest entity in the model, the internal horizontal spread cannot be modelled. To overcome these limitations, a new variable, β, was introduced, which provides additional time delay to transition from smouldering peat to burnt peat. This new variable represents the time delay that is caused by the internal horizontal spread without significant additional complexity. Therefore, in Eq. 9.1, the first term on the right hand side of the equation represent the time delay caused by the internal horizontal spread, and the second term represent the time delay caused by in-depth spread within one cell. Smouldering wildfires stop its vertical spread upon reaching mineral soil or peat with MC higher than critical. In SUBALI, the d in the second term of Eq. 9.1 is assumed to be equal to GWT, which has the highest MC vertically, as a conservative approach (smouldering can stop before reaching GWT), since the organic soil layer in Indonesian peatland is considerably thick (Rein, 2013; Turetsky *et al.*, 2015).

$$t_s = \beta + d/(\Delta t . S_d) \tag{9.1}$$

$$\beta = \lambda / S_H \tag{9.2}$$

$$S_H = (2.478 \times 10^9 / \Delta H_s - 3.601)/100 \tag{9.3}$$

$$\Delta H_s = \rho_w(c_w \Delta T_d + L_w) + \rho_o(c_o \Delta T_h + \Delta H_P) + \rho_i c_i \Delta T_h \tag{9.4}$$

The value of β is formulated in Eq. 9.2 where S_H is horizontal spread rate, which is based on the time required by smouldering to spread horizontally from one edge to the other edge of a cell (Δx), but in a time-step unit. S_H is formulated in Eq. 9.3, following the correlation of horizontal spread rate with heat sink density (ΔH_s) in Christensen (2021). ΔH_s (Eq. 9.4) is a function of density of water (ρ_w), peat (ρ_o), and inorganic matter (ρ_i), specific heat of water (c_w), peat (c_o), and inorganic matter (c_i), latent heat of water vaporisation (L_w), temperature increase to 100°C (water drying, ΔT_d), temperature

increase to peak value in smouldering (ΔT_h), and heat of pyrolysis (ΔH_P). The units of variables and parameters in Eq. 9.1 to Eq. 9.4 can be found in the nomenclature. By introducing these modifications, SUBALI, for the first time, provide a tool for the modelling of field-scale peatland wildfires that simulate the 3-D spread of smouldering and can be used in any domain configuration.

9.2. Results and Discussions

9.2.1. Estimation of smouldering burnt area

Figure 9.7 and Figure S9.1 show snapshots of the SUBALI simulations at four different times, and the corresponding number of pixels of different states (*EP*, *FV*, *SP*, and *BP*), on Jambi and Central Kalimantan sites, respectively. The selection of the first three times of snapshots, which correspond to the spread of flames, were based on the availability of remote sensing data; in Jambi it is day 5 (Figure 9.7a), day 20 (Figure 9.7b), and day 40 (Figure 9.7c), following (Figure 9.2), whereas in Central Kalimantan it is day 3 (Figure S9.1a), day 8 (Figure S9.1b), and day 20 (Figure S9.1c), following Figure 7.1. Figure 9.7d and Figure S9.1d show snapshots of the prediction at the end of simulation, which is defined as six months, since smouldering can sustain for a long time and across seasons (Scholten *et al.*, 2021). The start of the simulation is considered as day 0 (21 August 2019 for Jambi and 21 September 2018 for Central Kalimantan), and the six-month period of simulation time is calendar-based (20 February 2020 for Jambi and 20 March 2019 for Central Kalimantan).

The progression of peatland wildfires in Jambi and Central Kalimantan was found to be similar. These wildfires started with flames that burned a relatively small area of the surface vegetation at an early stage (Figure 9.7a and Figure S9.1a), followed by the spread of flames (Figure 9.7b and Figure S9.1b) that burned a larger area and initiated the nucleation of smouldering hotspots. The flaming wildfires were extinguished relatively quickly (Figure 9.7c and Figure S9.1c), which also stopped the nucleation of smouldering hotspots; however, the smouldering hotspots remained active and started growing. The stops of flaming wildfires in both sites corresponded to the relatively high precipitation, in which it was 11.3 mm (on 29th September 2019) for Jambi and 14.7 mm (on 6th October 2018) for Central Kalimantan. At the end of the simulation (Figure 9.7d and Figure S9.1d), the smouldering hotspots that were not visible in previous days due to the resolution of the domain, became visible since their size grew significantly.

At the end of the simulation, there are two distinctive phenomena that were simulated by SUBALI: smouldering that spreads beyond the flaming burn scar perimeter

and the extinction of smouldering upon reaching the GWT. In the top-left of Figure 9.7d, a region that covers the smouldering that spread beyond the flaming burn scar perimeter is zoomed. Although in the nucleation period of the smouldering hotspots the smouldering cells are all within the flaming perimeter, due to its growth, the smouldering can exceed the perimeter. Therefore, when the smouldering lifespan is sufficiently long, its burnt area can exceed the flaming burnt area. In the bottom-right of Figure 9.7d, a region that contains burnt peat cells is zoomed. In this region, a few of SP cells have reached the GWT, thus, it was extinguished, and SUBALI is able to simulate it for the first time.

The main difference between the SUBALI simulations on Jambi and Central Kalimantan sites are the multiple flaming ignitions in Jambi. While in Central Kalimantan there was only one flaming ignition at the beginning of the wildfire, in Jambi, there were three independent ignitions at different times: day 0, day 3, and day 10, which are estimated from the satellite images (see Figure 9.7a and Figure 9.7b). This multiple ignition caused the phenomenon of merging, when two or more flaming wildfires coalesce and form a larger wildfire that is more difficult and dangerous to mitigate. Another difference in the SUBALI simulations on the two sites is the spatial and temporal resolutions; the Jambi site has a 111-m × 111-m cell size and a 3600-s time-step, whereas Central Kalimantan has a 44-m × 44-m cell size and a 1200-s time-step. These cell sizes were selected to make the number of cells in the domain were less than 500,000, given the landscape size, for computational efficiency purposes; the time-steps were selected based on the coarsest temporal resolution that still satisfy the stability criteria (Courant–Friedrichs–Lewy condition), given the cell size.

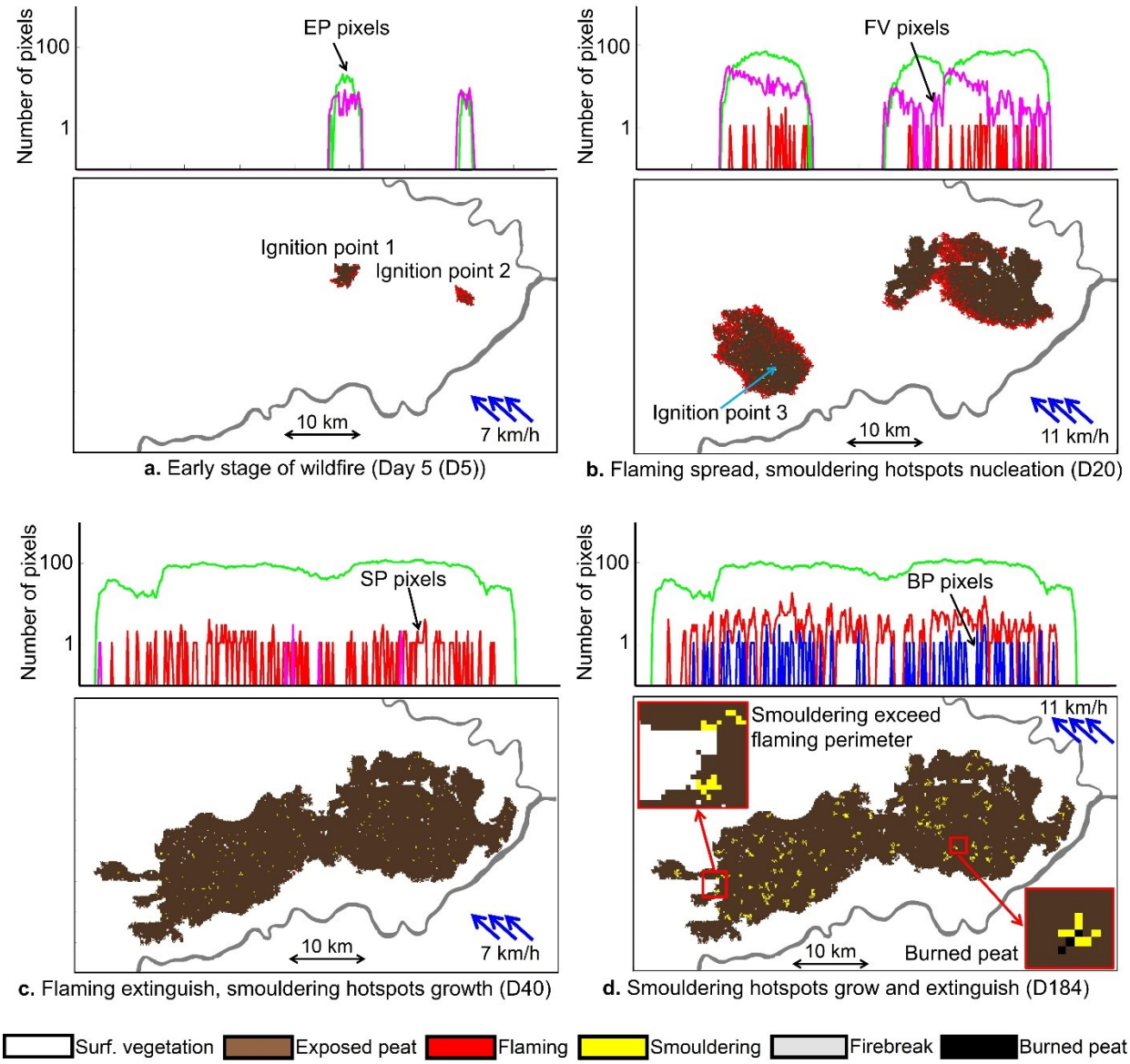

Figure 9.7. Snapshots of the peatland wildfire simulation in the Jambi landscape (1.305°S, 103.945°E) in 2019 at different stages and the corresponding number of pixels of different states (EP, FV, SP, and BP). ((a) the early stage of surface flames on day 5; (b) the spread of surface flames and the nucleation of smouldering hotspots on day 20; (c) the extinction of surface flames and the cessation of smouldering hotspot nucleation on day 40; and (d) the end of the simulation on day 184, at which time the smouldering hotspots had spread, enlarged, merged, and few were extinguished. The surface vegetation (white) corresponds to the four different vegetation types shown in Figure 9.3b. The blue arrows show the wind speed and direction. Firebreaks (shown in grey) stopped the spread of flames but could not stop the spread of smouldering. In (d), the top-left zoomed region represents the smouldering that grows beyond flaming perimeter, and bottom-right zoomed region represents the smouldering hotspots that reach GWT and were extinguished.

SUBALI accurately predicted the flaming burnt scar (see Figure 9.8 and Figure S9.2), with 86% (a Cohen's kappa value of 0.63) and 79% (a Cohen's kappa value of 0.57) accuracy for Jambi and Central Kalimantan, respectively. The accuracy in this validation was represented by the true predictions, both true negative and true positive, which means that the satellite detection and the prediction are both burnt or both unburned. Meanwhile, the false positive corresponds to the predicted burnt region which is unburned in the satellite detection, and false negative is the predicted unburned region which is burnt in the satellite detection, which are considered as the inaccurate predictions. The main reason of the deviation is the effect of the wind dynamic that cannot be fully simulated in the model, for instance, due to gusty wind and the difference between wind speed and direction at the weather station versus the actual location of the wildfire.

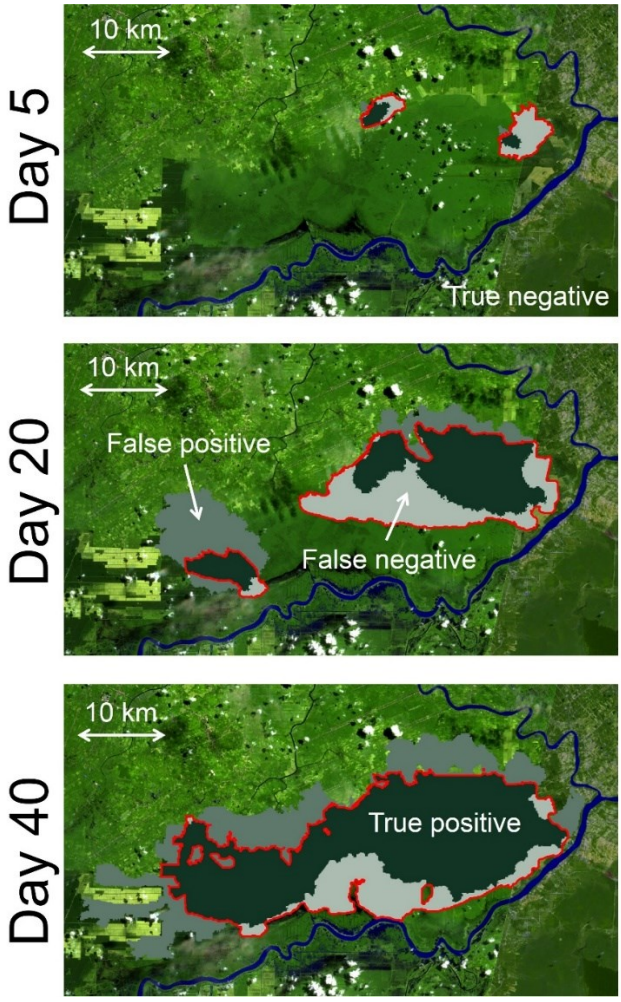

Figure 9.8. Comparisons between the flaming burn scars (exposed peat) derived from the satellite detection (Figure 9.2b) and from the SUBALI predictions at three different times (Figure 9.7a – Figure 9.7c) in the Jambi landscape (1.305°S, 103.945°E) in 2019. The red lines represent the perimeter of the actual satellite-detected burn scar. True negatives and true positives denote accurate predictions, indicating that the predicted and satellite-detected results both suggested

not burned or burned regions, respectively. A false positive corresponds to a predicted burn region that was not burned in the satellite detection results, whereas a false negative indicates that an area was predicted to be a nonburn region but was found to be burned in the satellite detection results.

SUBALI predicted that 111.43 km^2 and 350.88 km^2 of surface vegetation would be burnt by flames in Central Kalimantan and Jambi, respectively (see Figure 9.9a and Figure 9.9b). These predictions overestimated the actual burnt area, which were 89.86 km^2 and 290.64 km^2 in Central Kalimantan and Jambi, respectively. Although there is deviation between the actual burnt areas with the predicted burnt area, the predictions were reasonably accurate (higher than 70% accuracy). The number of the smouldering hotspots nucleated during these flaming wildfires was also validated. The model predicted that 0.51 and 0.36 smouldering hotspots would be nucleated per km^2 of landscape in the Central Kalimantan and Jambi wildfires, respectively (see Figure 9.9c and Figure 9.9d). These values have good agreement with the detection from the satellite (Figure 7.4 and Figure 9.5), in which there were 0.44 and 0.45 smouldering hotspots nucleated per km^2 of landscape in the Central Kalimantan and Jambi wildfires, respectively. The discrepancies in these numbers stem from the spatial non-uniformity of peat MC, which was not considered in SUBALI due to the lack of the data. From the validation on both flaming and smouldering components and the ability of the model to be used with significantly different domain spatial and temporal resolution, SUBALI was proved to be robust to simulate field-scale peatland wildfires at any domain.

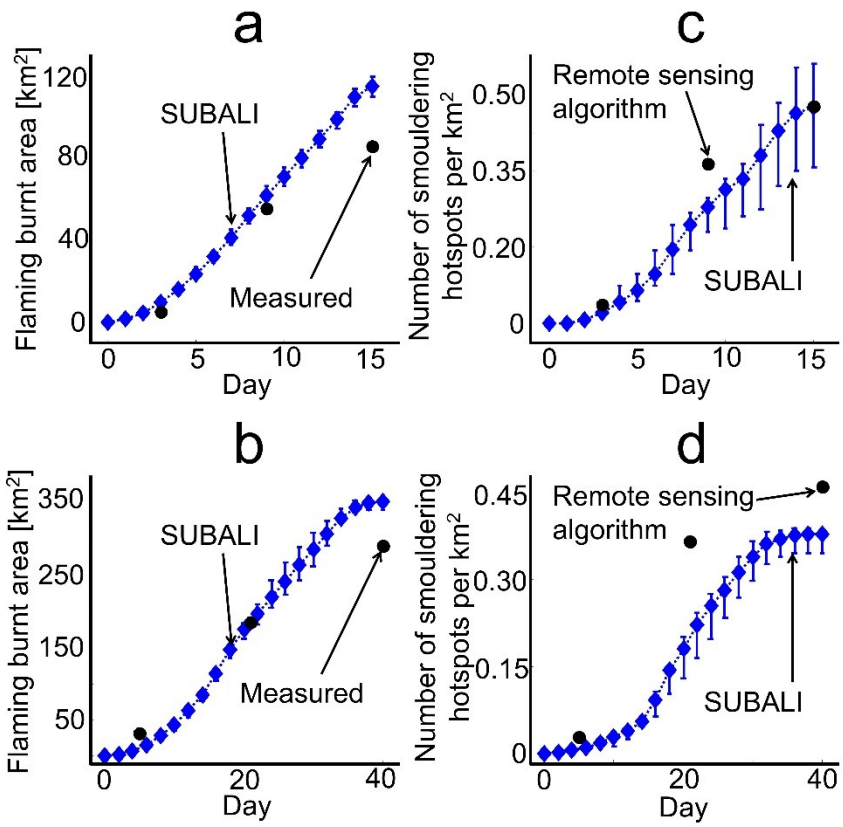

Figure 9.9. Comparison between the flaming burnt areas (areas of the exposed peat) derived from the satellite observations (based on Sentinel-2; Copernicus, 2022) and from the SUBALI predictions at different times in the (a) Central Kalimantan and (b) Jambi landscapes. Comparisons between the numbers of smouldering hotspots derived from the satellite observations (based on Sentinel-2; Copernicus, 2022) and the SUBALI predictions at different times in the (c) Central Kalimantan and (d) Jambi landscapes. The error bars represent the uncertainty of SUBALI results after 10 repetitions.

Figure 9.10 shows the evolution of burnt area of flaming and smouldering wildfires in the Central Kalimantan (a) and Jambi (b) landscapes. This figure corresponds to the simulation of SUBALI that was continued after the flames stopped, for six months of simulation time. The evolution of the burnt area of flaming and smouldering wildfires have similar pattern in the two sites. In the nucleation regime (blue symbols), both the flaming and smouldering burnt areas grow over time, which corresponds to flaming spread and smouldering hotspot nucleation (which dominates its spread), during the flaming lifespan (16 days for Central Kalimantan and 40 days for Jambi). In the growth regime (red symbols), the burnt area of flaming is plateau due to the extinction of the flames, whereas the smouldering burnt area continues to increase due to the growth of the smouldering hotspots. This phenomenon means that the smouldering was still active,

for a very long time, even after the flames were extinguished. At the end of the simulation time, 3.57 km^2 and 10.62 km^2 of peat were burnt via smouldering in Central Kalimantan and Jambi, respectively.

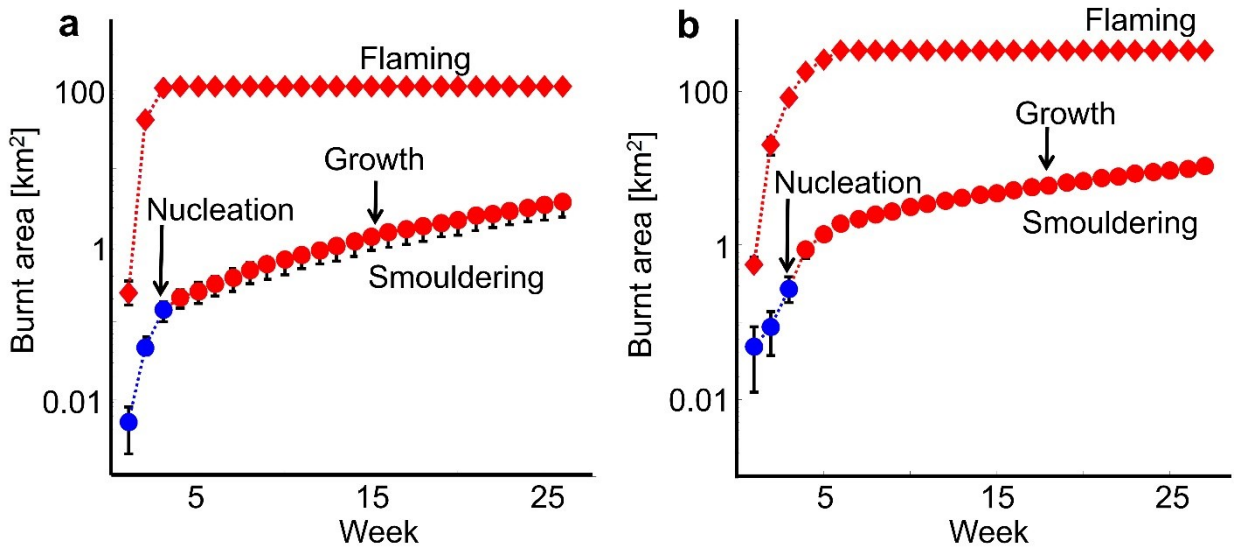

Figure 9.10. Predicted evolution of burnt area of flaming and smouldering wildfires in the (a) Central Kalimantan site and (b) Jambi landscapes. The blue symbols correspond to the smouldering hotspot nucleation regime (dominated by nucleation), whereas the red symbols correspond to the smouldering hotspot growth regime (dominated by growth). The error bar represent the uncertainty of SUBALI after 10 repetition.

The total smouldering burnt area after six months period in both sites correspond to a ratio of approximately 0.02 – 0.03 with the flaming burnt area. Here, for the first time, this ratio is quantified to enable the estimation of smouldering bunt area, given the flaming burnt area. The quantification of this ratio was performed based on the peat MC, the single most important properties of the fuel that affects smouldering. With different peat MC, the smouldering dynamics change, which causes the difference in burnt area. However, since the most important peat MC are within the nucleation regime (see Chapter 7), the peat MC that was used to quantify the ratio is the average peat MC within the nucleation regime (16 days for Central Kalimantan and 40 days for Jambi). SUBALI was further used to predict the smouldering burnt area when the flames began in different months and years from 2000 to 2019, and each individual case has a six-month simulation period. Therefore, there were a total of 480 independent cases (240 for each site), in which the first case began in January, 2000 and ended in June, 2000, whereas the last case began in December, 2019 and ended in May 2020. The ratio between the predicted smouldering and flaming burnt area of the 480 cases were collected and correlated with

the corresponding average peat MC within the nucleation regime on each case (see Figure 9.11). The ratio between smouldering and flaming burnt area has an inverse exponential correlation with the average peat MC within the nucleation regime (see Figure 9.11). Although there is deviation in this correlation, the correlation coefficient of this estimation is reasonably high (R = 0.86); thus, the correlation can be used to estimate the smouldering burnt area from the flaming burnt area. This quantification can help improve the accuracy of the smouldering burnt area estimation using data on the flaming burnt area, which are more readily available.

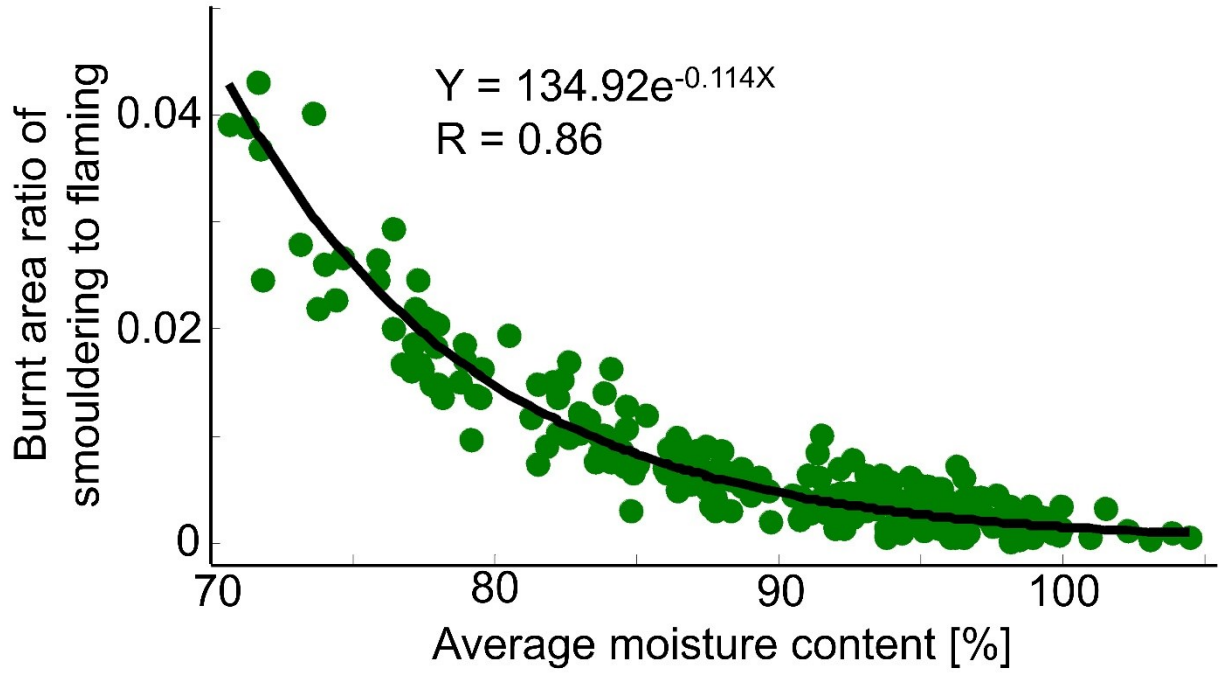

Figure 9.11. Correlation of the ratio between burnt area from flaming and smouldering with the average peat MC within the nucleation regime. The green circles represent the SUBALI predictions, and the black line represents the curve fitting of the correlation.

9.2.2. Estimation of carbon emission

With the quantification of the smouldering burnt area given the flaming burnt area (Figure 9.11), the total burnt area caused by smouldering wildfires, such as the entire country, can be estimated without significant effort, since data on flaming burnt area are usually available. Once these data are obtained, smouldering burnt area can be estimated with a simple calculation. This approach was used to estimate the smouldering burnt area from Indonesian wildfires in peatlands in each month from 2015 to 2019. The data on flaming burnt area that burned peatland regions in Indonesia were obtained from Endrawati and Yusnita (2015); Endrawati (2016, 2017, 2018, 2019). The data were

collected based on remote sensing detection (from NOAA, MODIS, VIIRS), burnt area analysis (Landsat 8 OLI/TIRS), and validation against field observations from local firefighters (Endrawati and Yusnita, 2015; Endrawati, 2016, 2017, 2018, 2019). From the data on flaming burnt area that were obtained, and on smouldering burnt areas that were calculated, the carbon emissions were estimated using a similar approach to the bottom-up approach.

The bottom-up approach estimates carbon emissions based on the product of dry matter (DM) consumed and the emission factor (EF). For flaming, the DM is the aboveground biomass that covers the flaming burnt area. While the data for flaming burnt areas were obtained from Endrawati and Yusnita (2015); Endrawati (2016, 2017, 2018, 2019), the average aboveground biomass per unit area over peatland region (based on SIPONGI, 2021) in Borneo Island in 2014 were used, which is estimated by using the remote sensing data of Ferraz *et al.* (2019). From this estimation, every km^2 of peatland in Borneo Island has approximately 22,675 tonnes of DM. By following Lohberger *et al.* (2018), one kg of DM burnt can release 0.5 kg of carbon. Therefore, in every km^2 of peatland in Indonesia burnt, 11,340 tonnes of carbon is released to the atmosphere via flaming wildfire. Since a similar value for average aboveground biomass per unit area on peatland region in one province on Sumatra Island was found (Thapa *et al.*, 2015), the aboveground biomass in other Islands is expected to be similar to Borneo.

For smouldering, the mass of DM was estimated based on the product of the volume of peat loss with its bulk density. The volume of peat loss is the product of the smouldering burnt area with DOB. From the field observations of Page *et al.* (2002), the DOB of smouldering wildfires range from 0.25 m to 0.85 m during the 1997 peatland wildfires in Borneo Island in Indonesia. Further research on 2015 peatland wildfires in Sumatera Island in Indonesia, revealed that the DOB ranges from 0 m to 1.3 m (Simpson *et al.*, 2016). This DOB range was obtained by measuring the pre burnt and post burnt peat elevation in flaming burnt areas. A DOB close to 0 m corresponds to the location where smouldering hotspots were not nucleated. This DOB range confirms with Konecny *et al.* (2016), who found the DOB range to be between close to 0 m and 1.19 m in 2011 peatland wildfires in Borneo Island, Indonesia.

Smouldering wildfire stops its vertical spread when the fire encounter mineral soil or reach a sufficiently wet peat (above the critical MC). Since the peat layer in Indonesia is relatively thick (2 m – 7 m; SIPONGI, 2021), it is assumed that the in-depth spread of smouldering stops when it reaches a sufficiently wet peat. The peat MC is higher at a deeper location, i.e., closer to GWT, thus, the DOB is highly influenced by the GWT.

Although the in-depth spread of smouldering peat can stop before reaching the GWT if the peat at a corresponding depth is higher than critical MC, in this chapter, the DOB of the smouldering wildfire was assumed to be the minimum GWT of the corresponding month in which the wildfire begins, which is a simplification of the case and can be considered a conservative approach. However, the deepest DOB is limited to be 0.85 m to avoid overestimation of the carbon emissions. The 0.85-m DOB is assumed to be the maximum DOB that the smouldering can sustain before it extinguishes due to the change of season (from dry to wet), which is the main reason for the extinction of both flaming and smouldering wildfires (Huijnen *et al.*, 2016). Therefore, smouldering can have a deeper DOB than 85 cm, but when the wet season arrives, smouldering encounters premature extinction prior reaching the GWT. A higher DOB, such as above 1 m might be possible, but it will be rarely observed and sensitive to the spatial heterogeneity, thus, this value was not considered as the limit.

The peat bulk density was estimated based on a function of peat solid density and porosity. The peat solid density was considered to be 1500 kg/m^3, following Huang and Rein (2017), whereas for the peat porosity, a varied value was used instead of constant value (such as 0.61 that was used in the validation of SUBALI and KAPAS II), since the representative porosity depends on the DOB. The representative porosity corresponds to the value of peat porosity that is used in SUBALI to estimate the smouldering burnt area and carbon emissions, in which this value was assumed to be constant in one case (e.g., in one province within one month time). The deeper the DOB, the denser the peat that is burnt, meaning the lower the representative porosity. Deep DOB corresponds to deep GWT, and deep GWT causes low peat MC; thus, peat MC was used to estimate the variation of the porosity. The minimum possible value of peat porosity is equal to the volumetric MC of the peat, meaning that the entire porosity is occupied by water instead of air, whereas the maximum porosity was assumed to be 0.68, following the value used in PEATCLSM$_{\text{Trop,Drain}}$ (Apers *et al.*, 2020). The average of these minimum and maximum porosities was used to estimate the peat porosity; thus, its value corresponded to the porosity at a depth of 0.25 m and below (peat porosity exceeds 0.8 at the surface and less than 0.5 at 0.5 m; Rezanezhad *et al.*, 2016), which is the minimum DOB reported in Page *et al.* (2002). This porosity was also used to calculate the gravimetric MC that is required for the estimation of smouldering burnt area, given the flaming burnt area.

The EF of smouldering is different from flaming, and the values reviewed in Hu *et al.* (2018) were used to estimate the EF for the smouldering. In Hu *et al.* (2018), for one kg of DM burnt, it is estimated that 1,615 g of CO_2, 248 g of CO, 12.3 g of CH_4, and a small

amount of other carbon-based gasses are released. From these values, an EF of 0.556 kg-C/kg-DM was used for smouldering, and this value was considered in the estimation of carbon emissions.

To estimate the carbon emissions from Indonesian peatland wildfires, the peat MC and GWT data were estimated, using PEATCLSM$_{Trop,Drain}$, from each province in Indonesia that has a peatland ecosystem. It is almost impossible to spatially vary the peat MC and GWT data within one province, which associate to every single wildfire; uniform values of peat MC and GWT within one province were used, and these data were selected from the middle of the peatland region in each corresponding province. Table 9.1 lists the provinces in Indonesia, and their corresponding longitude and latitude, which have peatland ecosystems, as reported by Endrawati and Yusnita (2015); Endrawati (2016, 2017, 2018, 2019); SIPONGI (2021). Figure 9.12 illustrates the locations in each province from which the data of peat MC and GWT were derived. The validation locations in this figure correspond to the exact locations of Central Kalimantan and Jambi sites used for validating SUBALI.

Table 9.1 also summarizes the total flaming burnt area of peatland in each province over one year, reported by Endrawati and Yusnita (2015); Endrawati, (2016, 2017, 2018, 2019). However, here the monthly value of the flaming burnt area was used, instead of yearly, to estimate the smouldering burnt area, since the peat MC and GWT change significantly over the months, especially when the seasons change. The exact date on which each wildfire began was not considered; thus, all wildfires within one month were assumed to begin at the beginning of each month. This method was used to estimate the average peat MC and minimum GWT for each month. The average peat MC that was used to estimate the smouldering burnt area was obtained from averaging the peat MC within one calendar month (from 1st to 28th 29th, 30th, or 31st day), which is the same as for the minimum GWT. Since the peat MC that is required to estimate the smouldering burnt area is the peat MC in the nucleation regime, which is relatively short (e.g., 16 days for Central Kalimantan and 41 days for Jambi), the assumption of the average peat MC within one month is well justified. From the estimation of peat MC and GWT in the locations listed in Table 9.1, the average porosity used in SUBALI was 0.57, which is similar to the value used for validation (0.61), and the DOB to be used ranged from 0.26 m to 0.85 m, which has a good agreement with the field observations of Page *et al.* (2002). The average of the porosity used in SUBALI has a good agreement with the field measurements of peat properties in Indonesian peatland, where porosity (with 0% MC and <5% IC) was 0.67 near the surface (Cui, 2022).

Table 9.1. Longitude and latitude of provinces in Indonesia that have peatland ecosystems and where peat MC and GWT data were obtained, and the corresponding flaming burnt area within a one year time from 2015 to 2019.

No	Province	Longitude	Latitude	Flaming burnt area (km^2)				
				2015	2016	2017	2018	2019
1	Aceh	97.758	2.528	3.58	19.73	25.21	4.48	2.02
2	North Sumatera	100.03	2.326	6.89	35.24	1.31	20.61	7.14
3	West Sumatera	100.1703	-0.2209	14.41	9.30	4.30	14.83	8.58
4	Riau	102.433	0.339	1,204.33	584.16	56.62	338.67	632.82
5	Riau Islands	103.457	0.702	0.02	0.00	0.00	0.00	1.32
6	Bengkulu	101.161	-2.585	0.23	0.00	0.31	0.00	0.00
7	Jambi	103.945	-1.305	719.76	66.38	0.00	8.01	240.45
8	Lampung	105.574	-4.146	67.86	0.62	0.00	14.10	26.95
9	South Sumatera	105.467	-3.111	4,393.82	50.64	0.00	25.86	1,368.75
10	Bangka Belitung	105.907	-2.433	21.39	0.00	0.00	2.48	5.48
11	West Kalimantan	109.4735	-0.3534	309.92	53.69	39.88	396.84	604.87
12	Central Kalimantan	113.991	-3.087	3,915.53	22.57	6.23	324.22	1,838.36
13	South Kalimantan	115.0466	-2.9161	536.08	8.42	0.40	99.02	119.50
14	East Kalimantan	116.621	0.008	82.04	84.13	0.00	39.74	56.73
15	North Kalimantan	117.061	3.768	13.50	12.19	0.00	0.00	0.05
16	West Papua	132.759	-2.081	17.98	0.54	0.81	1.48	9.51
17	Papua	139.226	-6.335	1,184.87	30.27	0.46	23.95	21.99
	Indonesia			12,492.21	977.88	135.53	1,314.29	4,944.52

In the bottom-up approach in previous works, such as in Page *et al.* (2002); Konecny *et al.* (2016); Lohberger *et al.* (2018), the smouldering burnt area is considered to be equal to the flaming burnt area, which is not the case (see Figure 1.4). The DOB used in these works varied, Page *et al.* (2002) used the average DOB of 0.51 m, whereas Konecny *et al.* (2016) and Lohberger *et al.* (2018) considered different DOB based on the distance from canals, and ranged from 0.19 m to 0.38 m. The lower value of DOB in Konecny *et al.* (2016) and Lohberger *et al.* (2018) corresponds to the general use of this DOB, since the DOB in Page *et al.* (2002) corresponds to the value in an El Niño year. The porosity considered in Page *et al.* (2002); Konecny *et al.* (2016); Lohberger *et al.* (2018) exceeded 0.9 (~ 0.92), thus, this porosity corresponds to the porosity at the surface; however, Page *et al.* (2002); Konecny *et al.* (2016); Lohberger *et al.* (2018) considered the

EF of smouldering peat to be 0.57 kg-C/kg-DM, which is similar to the value used in SUBALI.

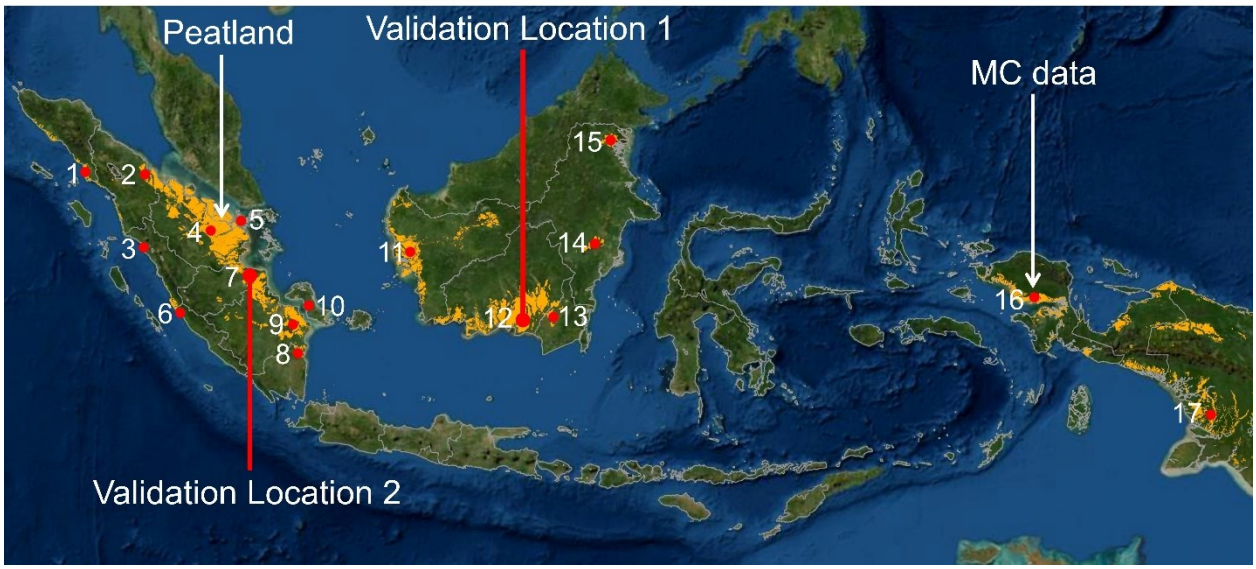

Figure 9.12. Locations (red dots) from which the data for peat MC and GWT were derived. The orange regions are peatland, and the validation locations are the Central Kalimantan and Jambi sites used for validating SUBALI.

While SUBALI used varied DOB and EF of 0.556 kg-C/kg-DM, the uncertainty of the emission estimation due to the EF and DOB uncertainties was also considered. For EF uncertainty (SUBALI EF), the range of EF of tropical peat reviewed by Hu *et al.* (2018) was considered, ranging from 0.522 and 0.604. For DOB uncertainty (SUBALI DOB), the average DOB used in Page *et al.* (2002) and Konecny *et al.* (2016), of 0.51 m and 0.27 m DOB, were considered. The use of a high representative peat porosity (above 0.8; Rezanezhad *et al.*, 2016) was not considered, since the porosity that is used in the land-surface model to simulate the peat MC is 0.68 (Apers *et al.*, 2020), and a higher porosity results in the estimation of gravimetric MC being above 300%, which is higher than critical gravimetric MC to ignite smouldering (Frandsen, 1987, 1997); thus, the smouldering burnt area could become zero and violate the observed phenomena.

Figure 9.13a shows the monthly estimation of carbon emissions from Indonesian smouldering wildfires in 2015 using different bottom-up methods: SUBALI EF, SUBALI DOB, and previous studies (Page *et al.*, 2002; Konecny *et al.*, 2016). In these estimations, the method of Page *et al.* (2002) and Konecny *et al.* (2016) considered the smouldering burnt area to be 4,700 km^2 and 4,800 km^2 in September and October, respectively, following the flaming burnt area reported in Endrawati and Yusnita (2015); Endrawati (2016, 2017, 2018, 2019). The total of 9,500 km^2 flaming burnt area in September and October 2015 reported in Endrawati and Yusnita (2015); Endrawati (2016, 2017, 2018,

2019) has a good agreement with Huijnen *et al.* (2016), who estimated 8,000 km^2 area of peatland was burnt via flaming. Prior to dry season, the emission estimate by Page *et al.* (2002) was the highest, however, during dry season, the emission estimation by SUBALI EF was the highest. This pattern is similar to the comparison between the emission estimation by Konecny *et al.* (2016) and SUBALI DOB, however, with a lower estimation than Page *et al.* (2002) and SUBALI EF, respectively. This finding shows that SUBALI emphasizes the influence of peat MC and GWT on the emission prediction, where in the wet season, smouldering hotspots are unlikely to be nucleated and the DOB is relatively shallow, whereas in the dry season, more smouldering hotspots can be nucleated and the DOB is relatively deep.

The average total emissions in Indonesian smouldering wildfires in 2015 as predicted by SUBALI EF, SUBALI DOB, and Page *et al.* (2002); Konecny *et al.* (2016) were 0.33 Gt-C, 0.22 Gt-C, 0.36 Gt-C, and 0.23 Gt-C respectively. The prediction by SUBALI EF has a good agreement with Page *et al.* (2002), although the smouldering burnt area of SUBALI EF was two order of magnitude smaller than the area used in the method of Page *et al.* (2002) (equal to flaming burnt area). This finding indicates the importance of the consideration of varied DOB and denser peat. Since smouldering burnt area is unlikely to be equal to flaming burnt area (see Figure 1.4), this finding shows the importance of the peat porosity and varied DOB, which are controlled by peat MC and GWT, for the estimation of carbon emissions. While Page *et al.* (2002) (and Konecny *et al.*, 2016), by averaging the DOB over the entire flaming burnt area, did not consider the locations with non-self-sustained smouldering (locations with DOB close to zero), SUBALI explicitly considered these locations, and considered the DOB of locations with self-sustained smouldering to be a function of GWT. With these considerations and the peat density at a deeper location, the carbon emission estimation by SUBALI was similar to the estimate made by using the method of Page *et al.* (2002). By using the same assumption of average DOB, estimates using the method of Konecny *et al.* (2016) were significantly lower than Page *et al.* (2002), since the DOB considered in Konecny *et al.* (2016) corresponds to the DOB in years without El Niño. However, 2015 was a strong El Niño year (with ONI of 2.5), similar to 1997; thus, the estimation using the DOB of Page *et al.* (2002) is argued to be more accurate, and SUBALI EF, is therefore also reasonably accurate.

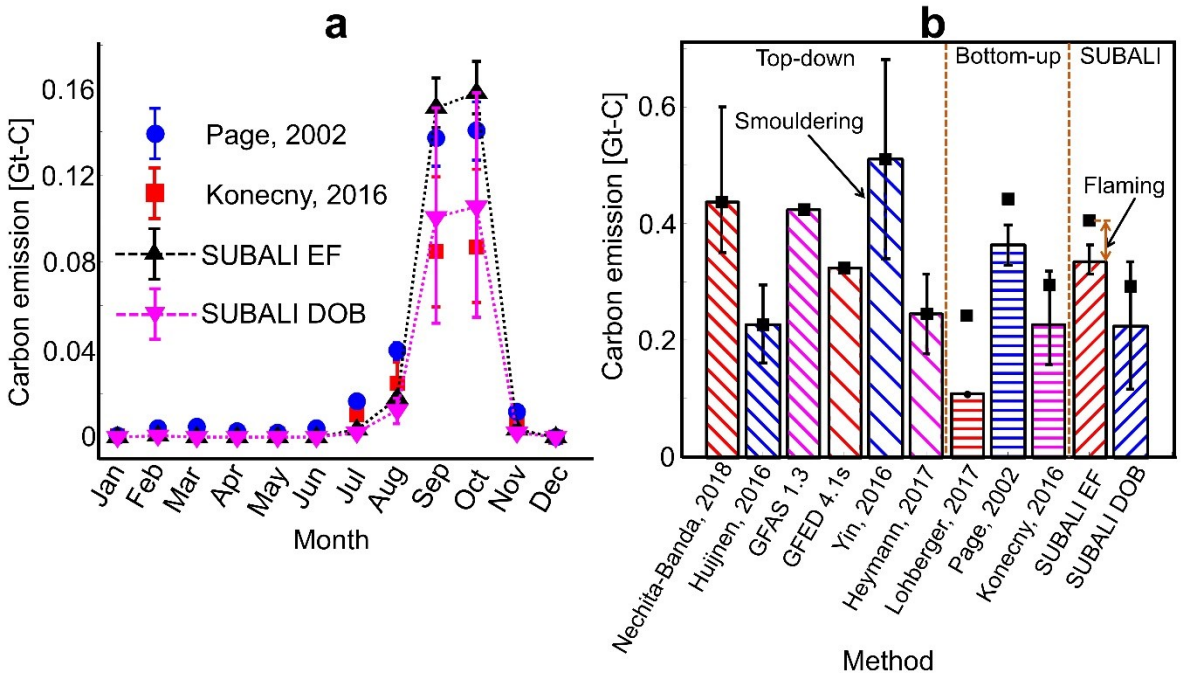

Figure 9.13. (a) Estimation of carbon emissions from Indonesian smouldering wildfires for each month in 2015 using different bottom-up methods: SUBALI with EF uncertainty (SUBALI EF), SUBALI with DOB uncertainty (SUBALI DOB), and previous studies (Page et al., 2002; Konecny et al., 2016). (b) Estimation of carbon emissions from Indonesian peatland wildfires in 2015 by using different methods: SUBALI, bottom-up, and top-down. The bar graph represents smouldering emissions, the error bar represents smouldering emission uncertainty, and the distance between the top of the bar graph and the black square represents flaming emissions. Zero flaming emissions means that the distinction between smouldering and flaming emissions was not considered in the methods.

The uncertainty because of EF (SUBALI EF) is insignificant (see Figure 9.13a), since the uncertainty of EF in smouldering is also low; the uncertainty because of DOB (SUBALI DOB) is relatively high, since there are significant difference between DOB estimation in different methods, which are also affected by various factors such as the present of El Niño. The average estimation of SUBALI DOB was similar to the estimation by Konecny *et al.* (2016), which is an underestimation; it strengthens the importance of varied DOB for carbon emission estimations of smouldering wildfires. This finding indicates that carbon emissions are not linearly correlated to the DOB, which is caused by the interconnection between DOB, GWT, and peat MC, where deeper DOB corresponds to deeper GWT and lower peat MC, and thus a larger smouldering burnt area. Here, this combined effect was quantified into a single value of carbon emission that is reasonably accurate when compared with the estimation using the method in the previous works, but

with a more realistic consideration of different burnt area between flaming and smouldering.

The method of Page *et al.* (2002) is a powerful way to estimate the carbon emissions, however, the omission of additional key factors of the smouldering dynamics (nucleation and growth), could lead to the underestimation of carbon emissions, when the smouldering goes on longer (hundreds of years; Rein and Huang, 2021) and DOB becomes deeper, which is not impossible (see Figure 1.4 and Figure 9.7d where smouldering exceeds flaming perimeter). Moreover, SUBALI can be used for different cases of peatland wildfires without additional significant efforts (only peat MC and GWT data from the $PEATCLSM_{Trop,Drain}$ model), whereas the use of the method in Page *et al.* (2002) and Konecny *et al.* (2016) requires new measurement of DOB for different cases of peatland wildfires, since the DOB varies significantly especially when El Niño is involved (0.51 m DOB in Page *et al.* (2002) and 0.27 m DOB in Konecny *et al.* (2016)).

Figure 9.13b shows the estimates of carbon emissions from flaming and smouldering wildfires by using different methods, covering both bottom-up (SUBALI EF, SUBALI DOB, and Page *et al.*, 2002; Konecny *et al.*, 2016; Lohberger *et al.*, 2018) and top-down (GFED 4.1s (Global Fire Emissions Database), GFAS 1.3 (Global Fire Assimilation Systems), and Huijnen *et al.*, 2016; Yin *et al.*, 2016; Heymann *et al.*, 2017; Nechita-Banda *et al.*, 2018) approaches. In the top-down approach, the estimation of carbon emissions was based on the remote sensing detection of the released gasses, such as CO and CO_2 (Huijnen *et al.*, 2016). Since the top-down approach is unable to distinguish between the emissions from flaming and smouldering, the estimation by the top-down approach in Figure 9.13b corresponds to the total emissions from flaming and smouldering wildfires. The prediction of SUBALI EF has a good agreement with that of the top-down approach from GFAS 1.3 and Nechita-Banda *et al.* (2018), underestimates Yin *et al.* (2016), and overestimates GFED 4.1s and Huijnen *et al.* (2016); Heymann *et al.* (2017); Lohberger *et al.* (2018). The prediction by GFED 4.1s and Huijnen *et al.* (2016); Heymann *et al.* (2017); Lohberger *et al.* (2018) are similar to Konecny *et al.* (2016) and SUBALI DOB, which are the prediction that correspond to non El Niño year, thus, these predictions potentially underestimate the actual carbon emissions. This underestimation could stem from the different input parameters and optimization techniques in the model (Nechita-Banda *et al.*, 2018). Different input parameters and optimization techniques could also cause the prediction from Yin *et al.* (2016) to overestimate the actual carbon emissions, however, due to high uncertainty of the prediction from Yin *et al.* (2016), the prediction from SUBALI EF (and the method of Page *et al.*, 2002) is within this

uncertainty, strengthening the robustness of SUBALI predictions. Therefore, SUBALI provides a tool to estimate carbon emissions from peatland wildfires with high accuracy (compared to others, both bottom-up and top-down approaches), can be used for different cases of peatland wildfires, can distinguish the sources of emissions, either flaming or smouldering wildfires, and consider the smouldering dynamics (nucleation and growth) for the estimation.

SUBALI was used to estimate the cumulative carbon emissions from Indonesian peatland wildfires in 2015, both due to flaming and smouldering wildfires. Figure 9.14a shows this estimation, where the total carbon emission from smouldering within one year period was approximately 0.33 Gt-C, whereas from flaming, it was only 0.07 Gt-C. Although the flaming burnt areas are constantly larger than smouldering burnt areas (Figure 9.14b), in wet season, the most prominent carbon emitter was flaming wildfires, whereas in dry season, it was smouldering wildfires (Figure 9.14a). While in wet season the smouldering emissions were insignificant, once the dry season arrived, the additional emissions from smouldering wildfires were dramatic and quadruple the cumulative emissions from flaming wildfires at the end of the year.

The 0.07 Gt-C emissions from flaming wildfires can be reabsorbed by the ecosystem via vegetation regrowth (Le Quéré *et al.*, 2015), whereas the 0.33 Gt-C emissions from smouldering wildfires could remain in the atmosphere and creates a positive feedback mechanism to climate change. The carbon sink does not consider the sources of the emission, however, from the estimation in Le Quéré *et al.* (2015), the carbon sink via vegetation regrowth is only ~0.5 t/ha per year, thus, with approximately 12,000 km^2 surface vegetation was burnt in Indonesian peatland wildfires in 2015 (Endrawati and Yusnita, 2015), the carbon sink via vegetation regrowth is only able to absorbs 6×10^{-4} Gt-C in one year, which is insufficient even for the flaming wildfires emission alone. The carbon neutral can still be achieved by considering the carbon sink from other sink mechanisms such as terrestrial and ocean sinks; however, since the carbon sink from the entire Earth was only ~5.6 ± 0.8 Gt-C/yr (Le Quéré *et al.*, 2015), the carbon sink near Indonesian region is significantly smaller than the carbon emitted by smouldering wildfires, unless, the carbon emission source was only from Indonesian peatland wildfires, which is impossible.

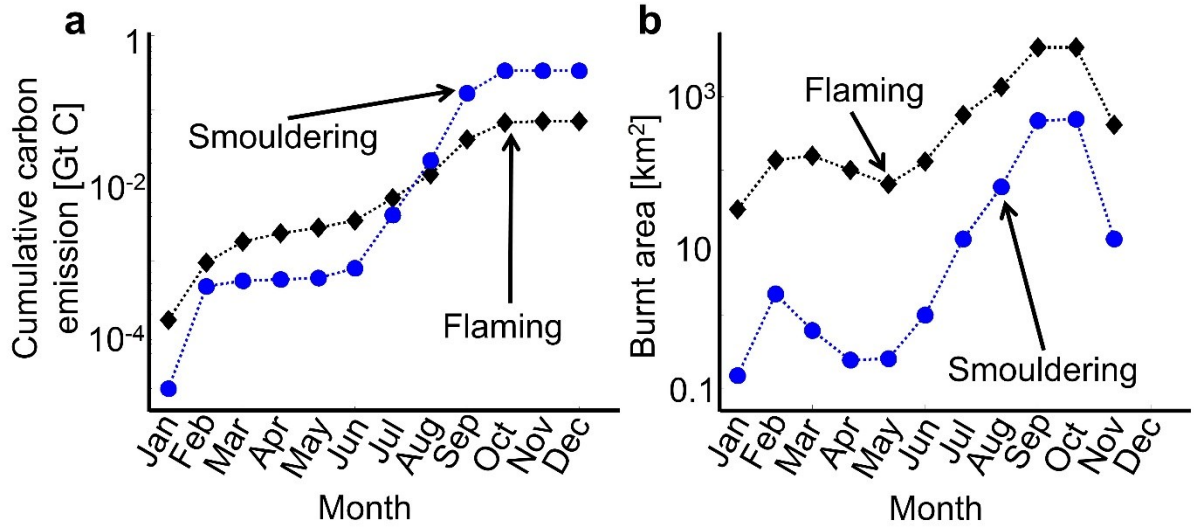

Figure 9.14. Cumulative carbon emissions from flaming and smouldering wildfires (a) and its corresponding burnt area (b) in Indonesia in 2015. The carbon emissions from smouldering wildfires correspond to carbon stored in peat and carbon emissions from flaming wildfires correspond to carbon stored in surface vegetation.

Another important finding in this chapter is the burnt area of smouldering that is around ten times smaller than flaming but emits almost five times more carbon than flaming (see Figure 9.14). This finding indicates the significant negative impact of smouldering wildfires that cannot be overlooked to maintain the inhabitability of planet Earth. Without adequate countermeasures, the carbon emitted by smouldering wildfires that has been released to the atmosphere could encourage more frequent and more severe wildfires due to the warmer and drier conditions. Since the peat becomes drier due to climate change (this already happened in Arctic that promote the overwintering smouldering wildfires; Scholten *et al.*, 2021), the smouldering burnt area becomes larger when peatland wildfires happen, even though the total of flaming burnt area is similar. The larger smouldering burnt area, coupled with the deeper DOB that is likely to happen with drier peat, could exponentially increase the carbon emissions, which again, remain in the atmosphere and cannot be reabsorbed by the ecosystem.

SUBALI was further used to estimate the cumulative carbon emissions from 2016 to 2019 to investigate the effect of El Niño to the carbon emissions (see Figure 9.15). The ONI from 2016 to 2019 are approximately -0.6 (weak La Niña), -0.7 (moderate La Niña), 0.1 (weak El Niño), and 0.7 (moderate El Niño), respectively (Null, 2021), in which negative values of ONI represent La Niña, and the greater value represent stronger El Niño. The carbon emissions from smouldering wildfires are lower than from flaming wildfires in La Niña years (2016 and 2017). The total carbon emission from both flaming

and smouldering in 2016 and 2017 are expected to be carbon neutral since their value are only 6.9×10^{-3} Gt-C and 7.6×10^{-4} Gt-C respectively (see Figure 9.15a). The low smouldering carbon emissions stems from the small smouldering area due to wetter peat, which prevents the nucleation of smouldering hotspots. In 2018, although with similar flaming burnt area as in 2016 (similar emissions from flaming wildfires), the carbon emissions from smouldering was approximately 0.008 Gt-C, which is higher than the emissions from flaming in 2018 and ten times higher than smouldering emissions in 2016 (see Figure 9.15a), The total of 0.015 Gt-C emissions from flaming and smouldering in 2018, can give a weak positive feedback to climate change since not all of these emissions can be reabsorbed by the ecosystem to create carbon neutral mechanism. This finding indicates that the peat was drier in 2018 than in 2016, which enable larger area and deeper peat to be burnt via smouldering. Therefore, in El Niño years (even in weak El Niño years), the dryness of the peat could facilitate stronger smouldering wildfires and promote carbon positive cycles.

In 2019, which was a moderately strong El Niño year, the flaming wildfires were more frequent and more severe, which is indicated by the burnt area of flaming being significantly larger than the other years in Figure 9.15b. This significant increase in flaming burnt area was accompanied with the increase of smouldering burnt area, and consequently, a significant increase in the its carbon emission. In 2019, a total of 0.11 Gt-C was released to the atmosphere via smouldering wildfires. The 0.03 Gt-C that was released via flaming wildfires can be expected to be reabsorbed by the ecosystem and create carbon neutral; however, the 0.11 Gt-C from smouldering wildfires can be assumed to remain in the atmosphere. These emissions are almost two order of magnitude greater than those in 2018, which indicates the strong influence of El Niño to the carbon emission from peatland wildfires. The carbon emissions in 2019 were concentrated in the dry season (90% of total emissions) and in this season, the carbon release rate of the smouldering wildfires was ~1.67 Mt-C/day, which is similar to the fossil fuel carbon release rate of the European Union (2.42 Mt-C/day; Huijnen *et al.*, 2016). Therefore, the carbon emissions from 2019 are alarming, although their value is only one third of those in 2015.

From 2016 to 2019, a total of 0.04 Gt-C and 0.12 Gt-C were released via flaming and smouldering wildfires, respectively. Within the first three years (2016 – 2018), the emissions from flaming wildfires were higher than emissions from smouldering wildfires. During the short time span of dry season in 2019, the emissions from smouldering wildfires overtook the emissions from flaming wildfires and become three times higher.

This finding shows the significant effect of the drier and more vulnerable peat condition in El Niño years. Combined with the carbon emissions from 2015, a total of 0.56 Gt-C has been released to the atmosphere due to Indonesian peatland wildfires, and part of these emissions are still in the atmosphere and contribute to the self-acceleration of climate change.

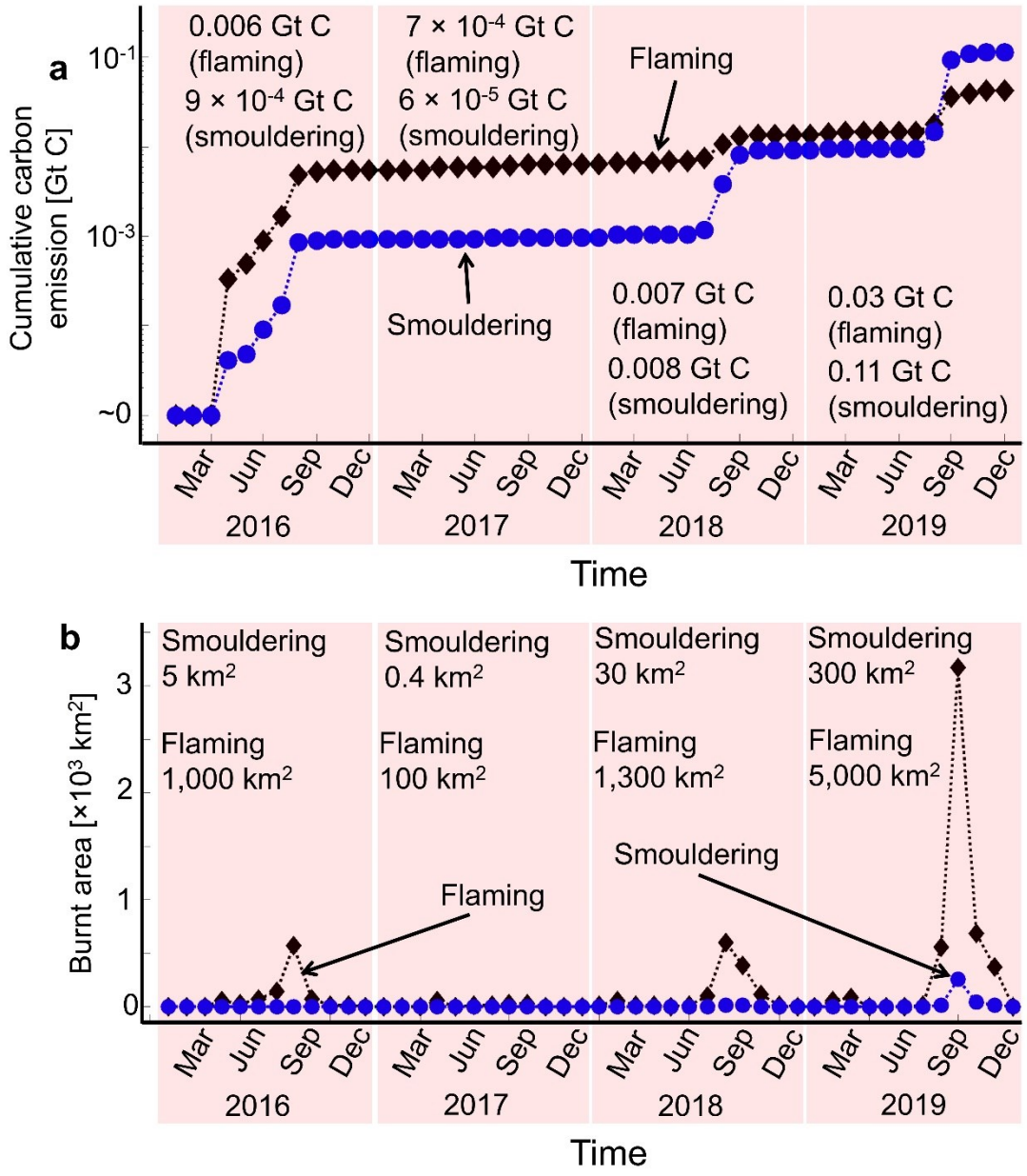

Figure 9.15. Cumulative carbon emissions from flaming and smouldering wildfires (a) and their corresponding burnt areas (b) in Indonesia in 2016 - 2019. The carbon emissions from smouldering wildfires correspond to carbon stored in peat and carbon emissions from flaming wildfires correspond to carbon stored in surface vegetation.

9.3. Conclusions

In this chapter, a cellular automata model, SUBALI, was developed based on KAPAS II (Chapter 7) and BARA (Chapter 4) to simulate 3-D peatland wildfires at the field-scale, and was used to estimate the smouldering burnt area based on the flaming burnt area and peat conditions. SUBALI was validated against two independent peatland wildfires in two different islands in Indonesia, Central Kalimantan in Borneo and Jambi in Sumatera, and was found to have a good agreement with the validation data on flaming burnt scar (79% and 86% accuracy, for Central Kalimantan and Jambi, respectively) and number of smouldering hotspots (85% and 82% accuracy, for Central Kalimantan and Jambi, respectively). SUBALI showed, from simulations over the same locations but began in different months and years from 2000 to 2019 (480 cases), that the ratio between smouldering and flaming burnt area has an inverse exponential correlation with the average peat MC within the nucleation regime.

A peat-specific land surface model was used to estimate peat MC and GWT that vary daily, and embedded these data and the data on flaming burnt area from peatland wildfires in 17 provinces in Indonesia into the flaming-smouldering burnt area correlation to estimate the smouldering burnt area and carbon emissions of Indonesian peatland wildfires from 2015 to 2019. Using this method, in 2015, a total of 0.33 Gt-C was released to the atmosphere, and this prediction was comparable with other estimations, both bottom-up and top-down approaches (GFAS 1.3 and Page *et al.*, 2002; Nechita-Banda *et al.*, 2018). The discrepancy between SUBALI estimation and some other estimations (GFED 4.1s and Huijnen *et al.*, 2016; Heymann *et al.*, 2017; Lohberger *et al.*, 2018) stems from the possible underestimation due to different input parameters and optimization techniques in the top-down approaches and the insufficient consideration of El Niño effect in the bottom-up approach. A field-scale experiment showed that the smouldering burnt area was different from the flaming burnt area (Santoso, 2021), thus, the good agreement between SUBALI estimation with the bottom-up estimation of Page *et al.* (2002) (that considers equal burnt area between flaming and smouldering), emphasizes the importance on the consideration of accurate peat MC and GWT for the estimation of carbon emissions.

In El Niño years, the carbon emissions from smouldering wildfires become significantly higher than the emission from flaming wildfires, and potentially cannot be reabsorbed by the ecosystem, thus, promoting carbon positive cycles. In 2019, a moderately strong El Niño year, the carbon emissions from smouldering wildfires were

approximately 0.11 Gt-C, whereas the emissions from flaming wildfires was only 0.03 Gt-C. Although this value is only one third of the smouldering wildfires emissions in 2015, in the dry season of 2019, the carbon release rate was approximately 1.67 Mt-C/day, which was similar to the rate of fossil fuel emissions of the European Union (2.42 Mt-C/day). From 2015 to 2019, a total of 0.56 Gt-C was released by peatland wildfires in Indonesia, and a significant fraction of this remains in the atmosphere and encourages positive feedback mechanisms to climate change. The findings and model provide knowledge and tools to predict the spread of flaming and smouldering wildfires in peatlands and its carbon emission. This can contribute to mitigating peatland wildfires and their impact on climate change, through faster-than-real-time simulations, to find the optimum firefighting strategy, and to develop better peatland management based on the vulnerability of peatland in the event of wildfires and the carbon emission estimation.

Chapter 10 – Conclusions

Peatland wildfires, wildfires that happen on peatland ecosystems, release carbon stored in peat, and can create positive feedback mechanisms to climate change. These wildfires happen all around the world: Southeast Asia, Southern Africa, Northern Europe, North America, and even in the Arctic, and could release significant amount of carbon emissions that cannot be reabsorbed by the ecosystem. However, studies on peatland wildfires are limited, since investigating peatland wildfires means investigating field-scale phenomena (thousands of hectares), which involve flaming and smouldering types of combustion, and both are affected by environmental factors that vary spatially and temporally. Moreover, understanding smouldering requires an understanding of its 3-D spread, which includes many important phenomena, such as subsurface spread. While experimental studies can be conducted at the small scale, the investigation of peatland wildfires at their actual scale can be prohibitively expensive to do in a comprehensive manner. Computational models are, therefore, the most promising route to investigate field-scale peatland wildfires. This thesis aims to computationally study field-scale peatland wildfires using cellular automata, discrete computational models that use simple rules. Figure 10.1 shows the connection between chapters in this thesis, which consist of supporting chapters (grey shade), the development of the models (green and blue shades), and the main outputs (red shade).

From the literature review in Chapter 1, field-scale studies on peatland wildfires were shown to revolve around remote sensing research, via infrared emissions, for its detection and for the estimation of its carbon emissions. However, while flaming wildfires can be detected with a reasonable level of accuracy, due to the lower temperature of smouldering, the radiation from smouldering wildfires is significantly weaker than flaming wildfires, causing the detection of smouldering become challenging, especially when subsurface spread of smouldering happens.

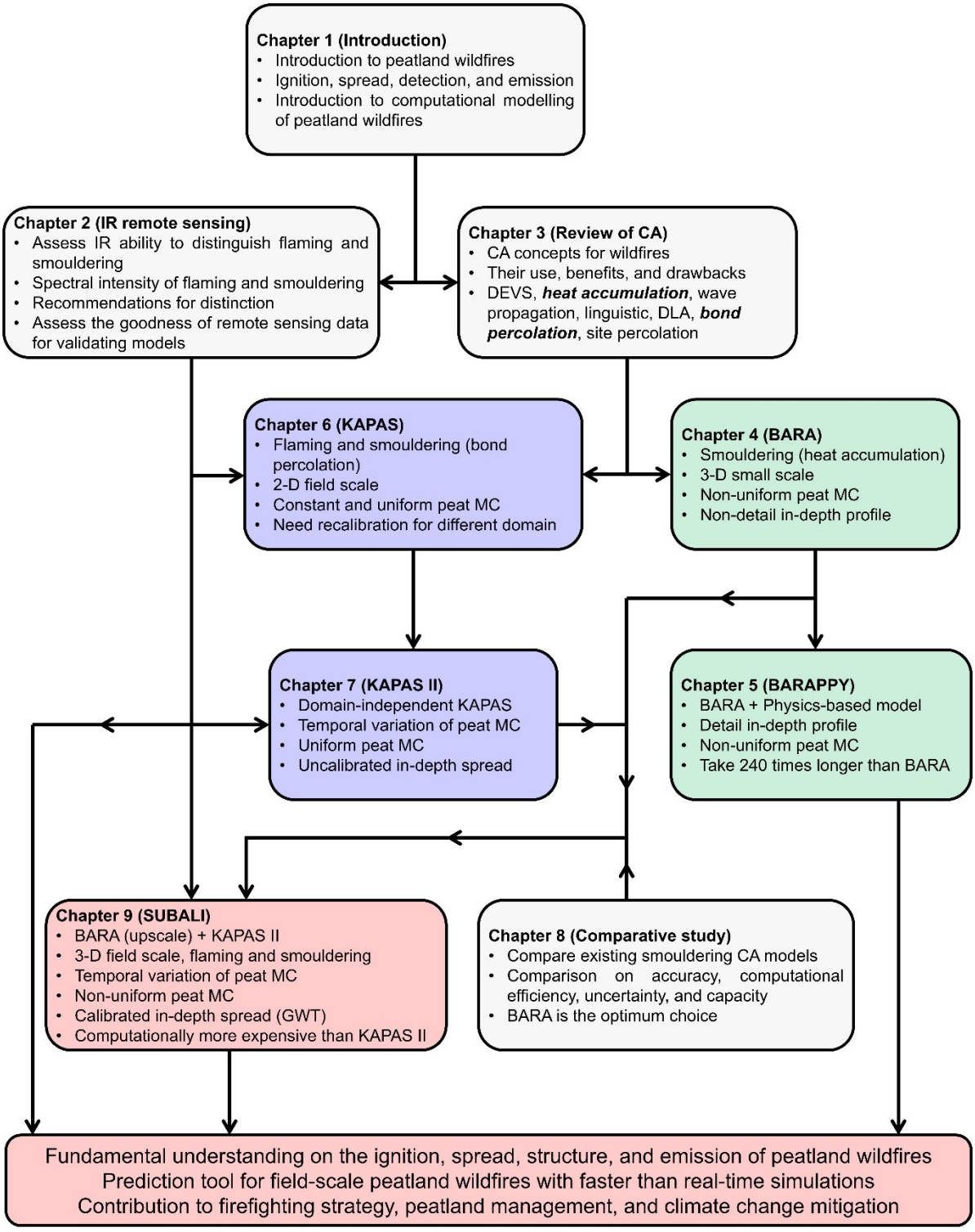

Figure 10.1 Diagram illustrating the connections between chapters in this thesis. Grey shade represents supporting chapters, green and blue shades represent chapters for the development of the models, and red shade represents main outputs and outcomes. The main outputs of this thesis are the fundamental understanding of ignition, spread, structure, and emissions (carbon and infrared) of field-scale peatland wildfires and the 3-D field-scale peatland wildfire model with faster-than-real-time simulations, which can contribute to the development of firefighting strategy, peatland management, and climate change mitigation.

From the laboratory-controlled experiments in Chapter 2, it was found that the spectral intensity of smouldering is one-sixth to half of flaming, depending on the infrared wavelength that is considered, where this ratio peaks at mid-wave range of wavelength (3 – 5 μm, with ratio between 4.4 and 6.5). While both flaming and smouldering in these experiments can be detected and distinguished, the significantly higher noise level in the actual landscape, than in the laboratory, could pose problems for detection. Moreover, none of these wavelengths could detect subsurface smouldering that are prevalent in real peatland wildfires. The detection of subsurface smouldering can be potentially performed by integrating the radiation of a wide range of wavelengths, which are not available through current satellite instruments, the most widely used method for wildfire detection. Due to these limitations, most of carbon emission estimation of peatland wildfires assume the smouldering burnt area to be equal to the flaming burnt area (Page *et al.*, 2002; Huijnen *et al.*, 2016), which is unlikely to be the case, as revealed by the field-scale observations of Grundling *et al.* (2019) and Santoso (2021). Therefore, models for peatland wildfires are needed to overcome these limitations.

In Chapter 3, cellular automata models for wildfires were reviewed, and from this review, there are seven concepts were found to be used for its rules: discrete physical event, wave propagation, heat accumulation, linguistic, diffusion limited aggregation, bond percolation, and site percolation. Each concept has different characteristics and inherent benefits and shortcomings, and have been implemented in range of applications across scales. Although cellular automata have modelled many phenomena occurring in wildfires such as crown fire and firebrand, the number of phenomena considered is limited compared to the number of phenomena emerging in real wildfires, especially in smouldering wildfires. Therefore, while the cellular automata models developed in this thesis consider flaming, the main focus of the model development is smouldering.

The aims of Chapter 4 and Chapter 5 were to develop three-dimensional (3-D) cellular automata models for smouldering at the small-scale (cm-scale). In Chapter 4, the BARA model used heat accumulation concept for its rules (Figure 10.1). BARA was calibrated against lab-scale experiments in 22 different conditions, with an error of less than 10%, then applied to blind predict different set of lab-scale experiments of smouldering fire in peat with spatially non-uniform MC. BARA accurately reproduced various phenomena observed in the experiments such as encirclement of wet peat and fire front merging, due to the changes of fire front shape and spread direction that depend on the peat moisture profile. Applied to a larger scale case (m-scale), BARA simulates the creation of patches of unburned peat for the first time, which is a common phenomenon

observed in peatland wildfires. In this large-scale simulation, the smouldering spread was found to be able to penetrate and partially burn wet peat, which implies that the horizontal layers of wet peat that discontinue smouldering spread might fail if their width or MC are insufficient, indicating the importance of peat moisture profile on the vulnerability of peatlands to fire.

Although BARA accurately simulated 3-D smouldering spread on peat with spatially non-uniform MC, the in-depth profile predicted by BARA was inadequate, due to the absence of experimental data for the calibration of the in-depth profile. In Chapter 5, BARAPPY was developed to solve this issue (Figure 10.1), by integrating BARA with a physics-based model (GPyro). BARA and GPyro were independently validated against laboratory-controlled experiments (with 12 different conditions) and found to have accuracy of spread rate higher than 90% and 70% respectively, and the average error of both models was within experimental uncertainty. The main benefit of BARA is its computational efficiency, which is 240 times higher than GPyro, whereas the main benefit of GPyro is the level of generality and detail that can be acquired such as temperature, species, and reaction profiles. The hybrid model (BARAPPY) blind predicts an experiment of smouldering peat with non-uniform MC, a half wet-half dry MC configuration, and accurately simulates the 3-D structure of the smouldering peat surface. In wet peat, the DOB is non-uniform, caused by the step profile of the leading edge. This profile also forms a step of DOB at the interface between wet and dry peat, and BARAPPY simulate the initiation of overhang phenomenon in 3-D, which conforms to Huang *et al.* (2016). The DOB step height increases linearly with the MC gradient between wet and dry peat, and overhang is initiated when the MC gradient is higher than 20%.

While BARAPPY was able to simulate the initiation overhang phenomenon, the continuation of this phenomenon to become subsurface smouldering was not considered, especially at the field-scale, and can be the direction of future works. This consideration facilitates the understanding of deep layer peat smouldering, which is the main driver of the wildfires across season, such as overwintering smouldering (Scholten *et al.*, 2021). This consideration requires understanding on natural pipe system, which facilitate the oxygen supply to sustain smouldering (Rein, 2013), thus, the integrated understanding on deep peat smouldering, natural pipe system, and oxygen supply through the pipe system, are important.

The aims of Chapter 6 and Chapter 7 are to develop 2-D cellular automata models for peatland wildfires that involve flaming and smouldering at the field-scale (km-scale). Due to its simplicity, bond percolation was used for the rules in the models in Chapter 6

(KAPAS) and Chapter 7 (KAPAS II). KAPAS II is the successor of KAPAS, in which KAPAS considers temporally constant peat MC, whereas KAPAS II considers the daily temporal variation of peat MC (Figure 10.1). Both KAPAS and KAPAS II were validated against remote sensing data on flaming burnt scar and smouldering hotspots, and were found to have high accuracy (above 80%). However, since from Chapter 2 the subsurface spread of smouldering cannot be accurately detected with the current remote sensing method, only the numbers of smouldering hotpots were considered for validation (Figure 10.1), which means considering its initiation (at the surface) but ignoring its spread (potentially subsurface). KAPAS showed how smouldering hotspots are initiated by flaming wildfires on peatland, and how these hotspots merged over time when they grow sufficiently large. KAPAS also showed the sigmoid relationship between smouldering burnt area and peat MC when flaming wildfires occur on peatland. This sigmoid relationship causes the smouldering burnt area to be reduced or increased, exponentially, by the same flaming wildfire, depending on the peat MC.

Considering peat MC temporal variation, obtained from a peat-specific land surface model, KAPAS II showed that the prediction of KAPAS could significantly underestimate the smouldering burnt area (four times smaller). Although peat MC determines the smouldering burnt area, the peat MC during the flaming lifespan (smouldering nucleation regime) governs the overall severity of smouldering wildfire, and its influence is more significant than the peat MC after the flaming wildfire are extinguished (smouldering growth regime). Due to the strong influence of peat MC temporal variation on smouldering wildfires, the peatland wildfires that start in dry season could have significantly larger smouldering burnt area than the wildfires that start in wet season (a comparison of zero with hundreds of hectares), although with equal flaming burnt area.

KAPAS and KAPAS II have considered the transition from flaming vegetation to smouldering peat, but not the reverse transition. The consideration of the transition from smouldering peat to flaming vegetation in the model is an important topic to explore in future works, since the deep layer peat smouldering could initiate new flaming wildfires at relatively distant locations from the initial flaming wildfire location, and cause new peatland wildfires without a new source of ignition (Rein, 2013; Scholten *et al.*, 2021). The relationship between smouldering to flaming transition with the vegetation root system is also an important consideration, since the interaction between flaming and smouldering wildfires are mostly through the root system (Rein *et al.*, 2008).

In Chapter 8, BARA (Chapter 4) was compared with other CA models that have been used for smouldering modelling, including bond percolation of KAPAS (Chapter 6) and KAPAS II (Chapter 7), to find the best 3-D CA model for smouldering at the field-scale. BARAPPY (Chapter 5) was not included in this comparison, since BARAPPY is unsuitable for field-scale modelling due to its two order of magnitude higher computational cost than BARA. From the comparison, it was found that BARA (see Chapter 4) is the best performer out of the CA models in the literature (Hargrove *et al.*, 2000; Belcher *et al.*, 2010; Fernandez-Anez *et al.*, 2019) to simulate 3-D smouldering. BARA has high accuracy (within 10% error) and low uncertainty when compared to experiments. This model also has the largest capacity, possible scenario can be simulated by the model, compared to other models although the model requires longest computational time to finish the simulation. Although the complexity of BARA is significantly higher than other models, it can be related to the physical terms more easily, which is beneficial to ensure the high level of generality. From this analysis, the integration of bond percolation (KAPAS II) for flaming wildfire and heat accumulation (BARA) for smouldering wildfire is the optimum model for simulating 3-D peatland wildfires at the field-scale (Figure 10.1).

Chapter 9 aims to develop the 3-D model for field-scale peatland wildfires, SUBALI, by integrating BARA and KAPAS II (Figure 10.1), which is the ultimate model in this thesis. Through this integration, SUBALI considered the temporal and horizontal variation in peat moisture content. More realistic conditions can be considered in future works, for instance, the vertical variation of peat moisture content, the spatial variation of inorganic content, and the consideration of vegetation type for the nucleation of smouldering hotspots. The considerations of these variables could significantly improve the fidelity of the peatland wildfires model.

SUBALI showed that the ratio between smouldering and flaming burnt area has an inverse exponential correlation with the average peat MC within the smouldering nucleation regime. By using this correlation, the data for the flaming burnt area, and the data of peat MC and GWT, carbon emissions from peatland wildfires can be estimated. By considering these data on 17 provinces in Indonesia, a total of 0.33 Gt-C was predicted to be released to the atmosphere in 2015 via smouldering wildfires, and this prediction was comparable with other estimations, both bottom-up and top-down approaches (GFAS 1.3 and Page *et al.*, 2002; Nechita-Banda *et al.*, 2018). Some other estimations (GFED 4.1s and Huijnen *et al.*, 2016; Heymann *et al.*, 2017; Lohberger *et al.*, 2018) potentially underestimate these emissions due to different input parameters and optimization

techniques in the top-down approaches and the inadequate consideration of the El Niño effect in the bottom-up approach. Since the smouldering burnt area is different from the flaming burnt area (Grundling *et al.*, 2019; Santoso, 2021), the good agreement between SUBALI estimation with a bottom-up estimation of Page *et al.* (2002) (that considers equal burnt area between flaming and smouldering), reveals the importance of peat MC and GWT for the carbon emission estimations.

Further estimation of carbon emissions in Indonesia from 2016 to 2019 reveals that in El Niño years, carbon emissions from smouldering wildfires are significantly higher than from flaming wildfires, and potentially cannot be reabsorbed by the ecosystem, thus, promote a carbon positive cycle. In 2019, a moderately strong El Niño year, carbon emissions from smouldering wildfires were approximately 0.11 Gt-C, whereas emissions from flaming wildfires were only 0.03 Gt-C, and in the dry season, the carbon release rate was approximately 1.67 Mt-C/day, which was similar to the rate of fossil fuel emissions of the European Union (2.42 Mt-C/day). From these estimations, a total of 0.45 Gt-C and 0.11 Gt-C were released from 2015 to 2019 by smouldering and flaming wildfires respectively, which are concentrated in 2015 and 2019 (El Niño years).

Of the potential topics for future works that are identified in this chapter (subsurface smouldering modelling, modelling of the transition from smouldering to flaming, and models with more realistic conditions such as spatially varying IC), the modelling of transition from smouldering to flaming is of utmost importance. This transition creates a significant increase of hazard, due to the significantly higher fire intensity of flaming when compared to smouldering (Santoso *et al.*, 2019), thus, this transition increase the danger level of wildfire for people and the environment. Due to the significant increase in negative impact once this transition occurs, the mitigation of smouldering wildfires becomes secondary (including the subsurface smouldering), overtaken by the urgency of the containment of flaming wildfires (Santoso *et al.*, 2019). The transition from smouldering to flaming also has a key role to understand the occurrence of new flaming wildfires without independent sources of ignition (i.e., ignited by the smouldering peat). A model with more realistic conditions, such as spatially varying IC, is also important, however, this consideration mainly affects the accuracy of the model, and has little effect on the impact on people or the environment, unlike the modelling of transition from smouldering to flaming. Meanwhile, the modelling of subsurface smouldering, while it has significant impact to the environment (by continuously releasing carbon to the atmosphere without being detected), its impact to the people is relatively low (the released smoke from smouldering is significantly reduced

when it spreads at the subsurface due to the hindrance of unburned peat above the burning peat). Only after the subsurface smouldering has resurfaced, especially when it successfully initiates new flaming wildfires, does its effect on people dramatically increase. Therefore, immediate consideration of transition from smouldering to flaming in the model is recommended.

Figure 10.2 shows the comparison between models developed in this thesis (black symbols) and the models in the previous works (blue symbols; Huang and Rein, 2015, 2017; Huang, Rein and Chen, 2015; Huang *et al.*, 2016; Widyastuti *et al.*, 2021; Yuan, Restuccia and Rein, 2021). The comparison is based on the level of detail, domain size, and computational efficiency. The level of detail comparison covers the physics and phenomena considered in the model, and is based on score. The physics consists of energy transfer, momentum transfer, mass transfer, heat transfer, and kinetics, whereas the phenomena consist of spatial non-uniformity and temporal variation of the peat physical properties (such as MC) and the consideration of flaming. The score for each physics consideration is 2 if it is from the first principle, 1 if it is from a calibration, and 1.5 if it is from calibration but based on the physical properties of peat. For each phenomenon, it is 2 if the model considers the particular phenomenon, and 0 otherwise. The domain size comparison is based on the volume of the domain considered in the model, which is the product of area and depth. If a dimension is not considered, such as 1-D or 2-D model, the corresponding dimension is assumed to be 1 mm, which is the minimum length considers in the CA models in this thesis, whereas if the model considers field-scale, the corresponding dimension is assumed to be 1 km, to ensure the comparability between models since the field-scale models can simulate a very large domain. The computational efficiency comparison is based on the inverse of computational time required by the models to finish a simulation for a certain simulation time, by using the same computer.

The models of Huang and Rein (2015, 2017); Huang, Rein and Chen (2015) have a high level of detail since these models are physics-based models and consider the first principle, but with low volume and computational efficiency, since these models are 1-D small scale models and require a relatively long time to finish a simulation. The computational efficiency of these models are, however, higher than BARAPPY (Chapter 5) and Huang *et al.* (2016); Yuan, Restuccia and Rein (2021), since BARAPPY and Huang *et al.* (2016); Yuan, Restuccia and Rein (2021) consider 2-D physics-based equation. BARAPPY and Huang *et al.* (2016); Yuan, Restuccia and Rein (2021) require 120 times more computational resources to finish a simulation, to enable the 2-D modelling. The level of detail of BARAPPY and Huang *et al.* (2016); Yuan, Restuccia and Rein (2021) are

equal, which is also equal to Huang and Rein (2015, 2017); Huang, Rein and Chen (2015), however, these models have different domain size. The difference in domain size between Huang *et al.* (2016) and Yuan, Restuccia and Rein (2021) is because of the different in size of the reactor considered, whereas the difference between BARAPPY and Huang *et al.* (2016); Yuan, Restuccia and Rein (2021) is because of the 3-D consideration of BARAPPY, but this consideration is via CA, thus, does not affect the computational efficiency. BARA has higher computational efficiency than BARAPPY and Huang and Rein (2015, 2017); Huang, Rein and Chen (2015); Huang *et al.* (2016); Yuan, Restuccia and Rein (2021) since it uses CA, but without the consideration of physics-based equation, unlike BARAPPY. This model, consequently, has a lower level of detail than BARAPPY and Huang and Rein, (2015, 2017); Huang, Rein and Chen (2015); Huang *et al.* (2016); Yuan, Restuccia and Rein (2021). The domain size of BARA is similar to BARAPPY since BARA is also a 3-D small-scale model.

KAPAS, KAPAS II, and Widyastuti *et al.* (2021) have an even higher domain size than BARA, BARAPPY, and Huang and Rein (2015, 2017); Huang, Rein and Chen (2015); Huang *et al.* (2016); Yuan, Restuccia and Rein (2021) since these models are field-scale models. However, the level of detail of KAPAS, KAPAS II, and Widyastuti *et al.* (2021) are very low since these models are based on calibration that do not consider peat physical properties, although they consider flaming combustion. This low level of detail is accompanied with a high computational efficiency since there are very few computational operation executed during a simulation. The higher level of detail of KAPAS II than KAPAS and Widyastuti *et al.* (2021) is because of the consideration of temporal variation in peat MC on top of considerations of flaming, whereas the lower computational efficiency of Widyastuti *et al.* (2021) than KAPAS and KAPAS II is because of the required optimisation process of input parameters in Widyastuti *et al.* (2021), unlike KAPAS and KAPAS II that are based on Rothermel model of flaming spread rate (Rothermel, 1972) and experiments on smouldering spread rate (Frandsen, 1997; Huang *et al.*, 2016; Prat-Guitart *et al.*, 2016b). SUBALI has the highest domain size since SUBALI is a 3-D field-scale model. This model is also a relatively high level of detail since SUBALI is based on BARA (same computational efficiency as BARA) that considers the physical properties of peat and considers the flaming wildfires and temporal variation in peat MC (based on KAPAS II).

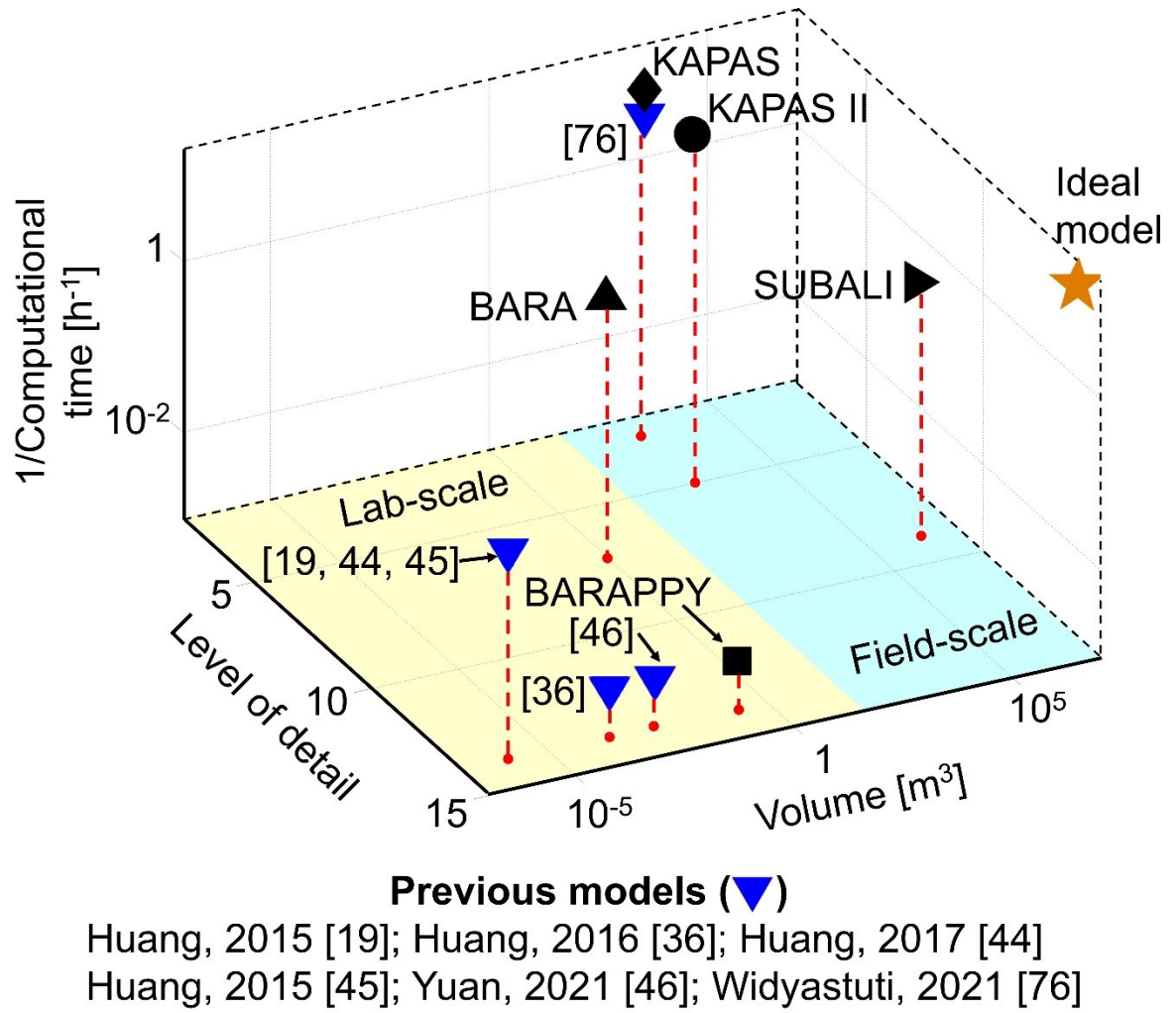

Figure 10.2 Comparison between the models developed in this thesis (black symbols) and models in the previous works (blue symbols). The comparison is based on the computational time, volume of the domain (area × depth), and the level of detail (phenomena and physics details) considered in the models. The ideal model (brown star) is the ultimate target of the modelling.

From this comparison, the main uses for each model developed in this thesis are different. The main use of BARAPPY is to simulate the 3-D smouldering spread with high detail (although it is less detail than physics-based model), where it can simulate the 3-D structure of peat during smouldering, however, BARAPPY cannot be used to aid with the development of firefighting strategy since it is significantly slower than real-time. The main use of BARA is to simulate the 3-D spread of smouldering but with limited accuracy in the in-depth profile; however, it can perform faster-than-real-time simulations, thus, this model can be used to aid with the firefighting attempts, although the insights from BARA cannot be directly used since BARA is a small-scale model. KAPAS and KAPAS II can be considered to have the same uses, since KAPAS II is developed based on KAPAS (with several modifications), but it is integrated with peat-specific land surface model to

estimate the temporally varying peat MC. The main use of KAPAS (and KAPAS II) is to simulate peatland wildfires at the field-scale that involve flaming and smouldering multiple times (due to its faster-than-real-time simulations, even faster than BARA), which can be used to optimise the firefighting strategy of peatland wildfire based on the predictions of the wildfire spread in different fire (e.g., weather and ignition location) and firefighting (by improving things such as resources allocation and evacuation routes) scenarios. KAPAS and KAPAS II can also be used to assist peatland management, for instance, by developing a strategy for rewetting treatment (e.g., which location and how wet) of peatland based on the wildfire impacts on the peatland (e.g., smouldering burnt area) in different wildfire scenarios, which are simulated using the model. SUBALI has similar use to KAPAS and KAPAS II, i.e., to optimise the firefighting strategy and to assist peatland management, although with slower simulations, thus, fewer scenarios can be considered. However, SUBALI considers the 3-D spread of smouldering peat, thus, this model also has the ability to estimate the carbon emission from the wildfires, unlike KAPAS and KAPAS II. This additional ability has main uses to assist the peatland restoration, i.e., by estimating the peat loss and optimising the peat condition (based on faster-than-real-time simulations) to minimise the peat loss in the event of wildfires, and to provide carbon emission estimation that can contribute to the climate change mitigation, for instance, based on the carbon emission estimation from SUBALI, the amount of carbon sink that is required to minimize the climate change can be approximated.

In summary, this thesis provides results to fundamentally understand peatland wildfires and phenomena that are involved. Both small and field-scale models in this thesis reveal the 3-D smouldering spread and its 3-D structure, the initiation and progression of field-scale smouldering wildfires and the factors that influence it, and the importance of these factors for the carbon emission estimation (Figure 10.1). The models and methodology presented here, represent a significant advancement on the understanding of peatland wildfires, from its initiation, spread, structure, and carbon emission. By using the models developed in this thesis, the spread of flaming and smouldering wildfires in peatland can be predicted in a faster-than-real-time simulation and its emission can be estimated, allowing for the better mitigation of peatland wildfires through multiple simulations to find the optimum firefighting strategy and to assess the vulnerability of peatlands in the event of wildfires. Through understandings and models presented in this thesis, improved firefighting strategy and management in the peat-rich

landscapes can be developed, which can contribute to mitigating climate change and adversities of haze from smouldering peatlands.

References

Achtemeier, G.L. (2003) '"Rabbit Rules" - An application of Stephen Wolfram's "New Kind of Science" to fire spread modeling', *The 5th Symposium on Fire and Forest Meteorology and the 2nd International Wildland Fire Ecology and Fire Management Congress* [Preprint].

Achtemeier, G.L. (2013) 'Field validation of a free-agent cellular automata model of fire spread with fire-atmosphere coupling', *International Journal of Wildland Fire*, 22(2), pp. 148–156. doi:10.1071/WF11055.

Adou, J.K. *et al.* (2010) 'Simulating wildfire patterns using a small-world network model', *Ecological Modelling*, 221(11), pp. 1463–1471. doi:10.1016/j.ecolmodel.2010.02.015.

Albinet, G., Searby, G. and Stauffer, D. (1986) 'Fire propagation in a 2-D random medium', *Journal de Physique*, 47(1), pp. 1–7. doi:10.1051/jphys:019860047010100.

Albini, F.A. and Brown, J.K. (1996) 'Mathematical modelling and predicting wildland fire effects', *Combustion, Explosion and Shock Waves*, 32, pp. 520–533. doi:10.1007/BF01998574.

Alexander, M.E. (1985) 'Estimating the length-to-breadth ratio of elliptical forest fire patterns', in *Eighth Conference on Fire and Forest Meteorology*. Detroit, Michigan: Society of American Foresters, pp. 287–304.

Alexandridis, A. *et al.* (2008) 'A cellular automata model for forest fire spread prediction: The case of the wildfire that swept through Spetses Island in 1990', *Applied Mathematics and Computation*, 204(1), pp. 191–201. doi:10.1016/j.amc.2008.06.046.

Alexandridis, A. *et al.* (2011) 'Wildland fire spread modelling using cellular automata: Evolution in large-scale spatially heterogeneous environments under fire suppression tactics', *International Journal of Wildland Fire*, 20(5), pp. 633–647. doi:10.1071/WF09119.

Almeida, R.M. and Macau, E.E.N. (2011) 'Stochastic cellular automata model for wildland fire spread dynamics', *Journal of Physics: Conference Series*, 285(1). doi:10.1088/1742-6596/285/1/012038.

Amin, H.M.F., Hu, Y. and Rein, G. (2020) 'Spatially resolved horizontal spread in smouldering peat combining infrared and visual diagnostics', *Combustion and Flame*, 220, pp. 328–336. doi:10.1016/j.combustflame.2020.06.039.

Andrews, P.L. (2008) 'BehavePlus fire modeling system, version 5.0: variables', *USDA Forest Service, Rocky Mountain Research Station, Report RMRS-GTR-*, 213. doi:10.2737/RMRS-GTR-213.

Apers, S. *et al.* (2020) *Extending the PEATCLSM Framework to Tropical Peatlands: Model*

Evaluation for the Major Tropical Peatland Areas. Fall Meeting: American Geophysical Union.

Asmuß, T., Bechtold, M. and Tiemeyer, B. (2019) 'On the potential of Sentinel-1 for high resolution monitoring of water table dynamics in grasslands on organic soils', *Remote Sensing*, 11(14), pp. 1659–1677. doi:10.3390/rs11141659.

Atwood, E.C. *et al.* (2016) 'Detection and characterization of low temperature peat fires during the 2015 fire catastrophe in Indonesia using a new high-sensitivity fire monitoring satellite sensor (FireBird)', *PLoS ONE*, 11(8). doi:10.1371/journal.pone.0159410.

Avolio, M. V *et al.* (2012) 'Simulation of Wildfire Spread Using Cellular Automata with Randomized Local Sources', in Greece, S.I. (ed.) *International Conference on Cellular Automata*. doi:10.1007/978-3-642-33350-7_29.

Bak, P., Chen, K. and Tang, C. (1990) 'A forest-fire model and some thoughts on turbulence', *Physics Letters A*, 147(5–6), pp. 297–300. doi:10.1016/0375-9601(90)90451-S.

Baker, W.L., Egbert, S.L. and Frazier, G.F. (1991) 'A spatial model for studying the effects of climatic change on the structure of landscapes subject to large disturbances', *Ecological Modelling*, 56(C), pp. 109–125. doi:10.1016/0304-3800(91)90195-7.

Bal, N. and Rein, G. (2013) 'Relevant model complexity for non-charring polymer pyrolysis', *Fire Safety*, 61, pp. 36–44.

Ball, P. (2001) *Fire's spread looks fractal*. Nature. doi:10.1038/news010816-5.

Bechtold, M. *et al.* (2018) 'Inferring water table depth dynamics from ENVISAT-ASAR C-band backscatter over a range of peatlands from deeply-drained to natural conditions', *Remote Sensing*, 10(4), pp. 536–556. doi:10.3390/rs10040536.

Bechtold, M. *et al.* (2019) 'PEAT-CLSM: A Specific Treatment of Peatland Hydrology in the NASA Catchment Land Surface Model', *Journal of Advances in Modeling Earth Systems*, 11(7), pp. 2130–2162. doi:10.1029/2018MS001574.

Bechtold, M. *et al.* (2020) 'Improved groundwater table and L-band brightness temperature estimates for Northern Hemisphere peatlands using new model physics and SMOS observations in a global data assimilation framework', *Remote Sensing of Environment*, 246. doi:10.1016/j.rse.2020.111805.

Belcher, C.M. *et al.* (2010) 'Baseline intrinsic flammability of Earth's ecosystems estimated from paleoatmospheric oxygen over the past 350 million years', *Proceedings of the National Academy of Sciences of the United States of America*, 107(52), pp. 22448–22453. doi:10.1073/pnas.1011974107.

Bendicenti, E. *et al.* (2002) 'Simulations of Forest Fires by Cellular Automata Modelling', *Emergence in Complex, Cognitive, Social, and Biological Systems*, (December), pp. 31–40.

doi:10.1007/978-1-4615-0753-6_3.

Berjak, S.G. and Hearne, J.W. (2002) 'An improved cellular automaton model for simulating fire in a spatially heterogeneous Savanna system', *Ecological Modelling*, 148(2), pp. 133–151. doi:10.1016/S0304-3800(01)00423-9.

Block, W.M. *et al.* (2016) *Effects of Prescribed Fire on Wildlife and Wildlife Habitat in Selected Ecosystems of North America*. Maryland, USA.

BMKG (2018) *DATA ONLINE - PUSAT DATABASE*. Available at: https://dataonline.bmkg.go.id/data_iklim.

Boelter, D.H. (1968) 'Important Physical Properties of Peat Materials', in *Proceedings of the 3rd International Peat Congress*, pp. 150–154.

Bogdos, N. and Manolakos, E.S. (2013) 'A tool for simulation and geo-animation of wildfires with fuel editing and hotspot monitoring capabilities', *Environmental Modelling and Software*, 46, pp. 182–195. doi:10.1016/j.envsoft.2013.03.009.

Boulet, P. *et al.* (2009) 'Spectral emission of flames from laboratory-scale vegetation fires', *International Journal of Wildland Fire*, 18(7), pp. 875–884. doi:10.1071/WF08053.

Boulet, P. *et al.* (2011) *Experimental investigation of radiation emitted by optically thin to optically thick wildland flames*, *Journal of Combustion*. Journal of Combustion. doi:10.1155/2011/137437.

Bowman, D.M.J.S. (2009) 'Fire in the Earth system', *Science*, 324(5926), pp. 481–484. doi:10.1126/science.1163886.

Braun, J. and Sambridge, M. (1995) 'A numerical method for solving partial differential equations on highly irregular evolving grid', *Nature*, 376, pp. 655–660. doi:10.1038/376655A0.

Buchhorn, M. *et al.* (2020) 'Copernicus Global Land Service: Land Cover 100m: collection 3: epoch 2019: Globe', *Copernicus* [Preprint].

Bump, P. (2018) *The staggering scale of California's wildfires*. Washington: The Post.

Burdun, I. *et al.* (2020) 'Satellite determination of peatland water table temporal dynamics by localizing representative pixels of A SWIR-Based Moisture Index', *Remote Sensing*, 12(18). doi:10.3390/RS12182936.

Burke, C. *et al.* (2019) 'Thermal-drones as a safe and reliable method for detecting subterranean peat fires', *Drones*, 3(1), pp. 1–16. doi:10.3390/drones3010023.

Camps-Valls, G. *et al.* (2021) 'A unified vegetation index for quantifying the terrestrial biosphere', *Science Advances*, 7(9), pp. 1–11. doi:10.1126/sciadv.abc7447.

Cancellieri, D. *et al.* (2012) 'Kinetic investigation on the smouldering combustion of boreal peat',

Fuel, 93, pp. 479–485. doi:10.1016/j.fuel.2011.09.052.

Cao, C. *et al.* (2017) *Visible Infrared Imaging Radiometer Suite (VIIRS) Sensor Data Record (SDR) User's Guide*, *NOAA Technical Report NESDIS 142*. Available at: https://ncc.nesdis.noaa.gov/documents/documentation/viirs-users-guide-tech-report-142a-v1.3.pdf.

Carvalho, J.P., Carola, M. and Tomé, J.A.B. (2006) 'Forest fire modelling using Rule-Based Fuzzy Cognitive Maps and voronoi based cellular automata', *Annual Conference of the North American Fuzzy Information Processing Society - NAFIPS*, pp. 217–222. doi:10.1109/NAFIPS.2006.365411.

Catchpole, T., Hatton, T.J. and Catchpole, W.R. (1989) 'Fire spread through non-homogeneous fuel modelled as a {M}arkov process', *Ecological Modelling*, 48, pp. 101–112. doi:10.1016/0304-3800(89)90062-8.

Chen, K., Bak, P. and Jensen, M.H. (1990) 'A deterministic critical forest fire model', *Physics Letters A*, 149(4), pp. 207–210. doi:10.1016/0375-9601(90)90328-L.

Christensen, E. (2021) *Experimental investigation of environmental and solid conditions on smouldering spread*. London: Imperial College London.

Christensen, E.G., Fernandez-Anez, N. and Rein, G. (2020) 'Influence of soil conditions on the multidimensional spread of smouldering combustion in shallow layers', *Combustion and Flame*, 214, pp. 361–370. doi:10.1016/j.combustflame.2019.11.001.

Clar, S., Drossel, B. and Schwabl, F. (1994) 'Scaling laws and simulation results for the self--organized critical forest--fire model', *Physical Review E*, 50(2), pp. 1009–1018. doi:10.1103/PhysRevE.50.1009.

Clarke, K.C., Brass, J.A. and Riggan, P.J. (1994) 'A cellular automaton model of wildfire propagation and extinction', *Photogrammetric Engineering & Remote Sensing*, 60(11), pp. 1355–1367.

Collin, A., Bernardin, D. and Sero-Guillaume, O. (2011) 'A physical-based cellular automaton model for forest-fire propagation', *Combustion Science and Technology*, 183(4), pp. 347–369. doi:10.1080/00102202.2010.508476.

Copernicus (2022) 'Sentinel data, processed by ESA'.

Couce, E. and Knorr, W. (2010) 'Statistical parameter estimation for a cellular automata wildfire model based on satellite observations', *WIT Transactions on Ecology and the Environment*, 137, pp. 47–55. doi:10.2495/FIVA100051.

Cousins, W.J., Heron, D.W. and Mazzoni, S. (2002) *Estimating risks from fire following earthquake*, *Bull. Seism. Soc. Am.* New Zealand: Institute of Geological & Nuclear Sciences.

Cui, W. (2022) *Laboratory Investigation of Ignition, SPread, and Emission of Smouldering Peat*

with Field Samples. London: Imperial College London.

Curiac, D.I. *et al.* (2010) 'Cellular automata based simulation for smoke and fire spreading in large buildings', in *International Conference on Development, Energy, Environment, Economics - Proceedings*. Tenerife, pp. 89–94.

D'Ambrosio, D. *et al.* (2006) *A model for the simulation of forest fire dynamics using Cellular Automata*, *Proceedings of the iEMSs 3rd Biennial Meeting," Summit on Environmental Modelling and Software"*. in Proceeding of Summit on Environmental Modelling and Software 2006.

Dadap, N. (2020) 'Drainage Canals in Southeast Asian Peatland, Index Map'. Stanford Digital Repository. Available at: https://earthworks.stanford.edu/catalog/stanford-zy089tj2215.

Dettmann, U. and Bechtold, M. (2016) 'Deriving Effective Soil Water Retention Characteristics from Shallow Water Table Fluctuations in Peatlands', *Vadose Zone Journal*, 15(10), p. vzj2016.04.0029. doi:10.2136/vzj2016.04.0029.

Dozier, J. (1981) 'A method for satellite identification of surface temperature fields of subpixel resolution', *Remote Sensing of Environment*, 11(C), pp. 221–229. doi:10.1016/0034-4257(81)90021-3.

Drossel, B. and Schwabl, F. (1992) 'Self-Organized Critical Forest-Fire Model', *Physical Review Letter*, 69(11), pp. 1629–1632. doi:10.1103/PhysRevLett.69.1629.

Drossel, B. and Schwabl, F. (1993) 'Forest-fire model with immune trees', *Physica A: Statistical Mechanics and its Applications*, 199(2), pp. 183–197. doi:10.1016/0378-4371(93)90001-K.

Dunn, A. and Milne, G. (2004) 'Modelling Wildfire Dynamics via Interacting Automata', *In Proceedings of ACRI*, 2004, pp. 395–404. doi:10.1007/978-3-540-30479-1_41.

Elvidge, C.D. *et al.* (2013) 'VIIRS nightfire: Satellite pyrometry at night', *Remote Sensing*, 5(9), pp. 4423–4449. doi:10.3390/rs5094423.

Elvidge, C.D. *et al.* (2015) 'Long-wave infrared identification of smoldering peat fires in Indonesia with nighttime Landsat data', *Environmental Research Letters*, 10(6). doi:10.1088/1748-9326/10/6/065002.

Encinas, A.H. *et al.* (2007) 'Simulation of forest fire fronts using cellular automata', *Advances in Engineering Software*, 38(6), pp. 372–378. doi:10.1016/j.advengsoft.2006.09.002.

Encinas, L.H. *et al.* (2007) 'Modelling forest fire spread using hexagonal cellular automata', *Applied Mathematical Modelling*, 31(6), pp. 1213–1227. doi:10.1016/j.apm.2006.04.001.

Endrawati (2016) 'Analisis Data Titik Panas (Hotspot) dan Areal Kebakaran Hutan dan Lahan tahun 2016'. Kementrian Lingkungan Hidup & Kehutanan, p. 37. Available at: https://rfmrc-sea.org/wp-content/uploads/2015/01/Analisis-Data-Titik-Panas-Hotspot-dan-Areal-Kebakran-

Hutan-dan-Lahan-Tahun-2016.pdf.

Endrawati (2017) 'Analisis Data Titik Panas (Hotspot) dan Areal Kebakaran Hutan dan Lahan tahun 2017'. Kementrian Lingkungan Hidup & Kehutanan.

Endrawati (2018) 'Analisis Data Titik Panas (Hotspot) dan Areal Kebakaran Hutan dan Lahan tahun 2018'. Kementrian Lingkungan Hidup & Kehutanan.

Endrawati (2019) 'Analisis Data Titik Panas (Hotspot) dan Areal Kebakaran Hutan dan Lahan tahun 2019'. Kementrian Lingkungan Hidup & Kehutanan. Available at: https://geoportal.menlhk.go.id.

Endrawati and Yusnita, R. (2015) 'Analisis Data Titik Panas (Hotspot) dan Areal Kebakaran Hutan dan Lahan tahun 2015'. Kementrian Lingkungan Hidup & Kehutanan, pp. 1–84.

ESA (2015) *SENTINEL-2 User Handbook*. doi:10.1021/ie51400a018.

Eyal, W. *et al.* (2017) *Ecocide in Indonesia*. Forensic Architecture [Online]. Available. Available at: https://forensic-architecture.org/investigation/ecocide-in-indonesia.

Favier, C. (2004) 'Percolation model of fire dynamic', *Physics Letters, Section A: General, Atomic and Solid State Physics*, 330(5), pp. 396–401. doi:10.1016/j.physleta.2004.07.053.

Fernandez-Anez, N. *et al.* (2019) 'Simulation of fingering behavior in smoldering combustion using a cellular automaton', *Physical Review E*, 99(2), pp. 1–13. doi:10.1103/PhysRevE.99.023314.

Fernandez-Anez, N., Christensen, K. and Rein, G. (2017) 'Two-dimensional model of smouldering combustion using multi-layer cellular automaton: The role of ignition location and direction of airflow', *Fire Safety Journal*, 91, pp. 243–251. doi:10.1016/j.firesaf.2017.03.009.

Ferraz, A. *et al.* (2019) *Aboveground Biomass, Landcover, and Degradation, Kalimantan Forests, Indonesia, 2014*. Oak Ridge, Tennessee, USA: ORNL DAAC. doi:10.3334/ORNLDAAC/1645.

Finney, M.A. (1998) *FARSITE: Fire Area Simulator - Model Development and Evaluation*, *USDA Forest Service - Research Papers RMRS*. Montana: USDA Forest Service.

Finney, M.A. *et al.* (2015) 'Role of buoyant flame dynamics in wildfire spread', *Proceedings of the National Academy of Sciences of the United States of America*, 112(32), pp. 9833–9838. doi:10.1073/pnas.1504498112.

Frandsen, W.H. (1987) 'The influence of moisture and mineral soil on the combustion limits of smoldering forest duff', *Canadian Journal of Forest Research*, 17(12), pp. 1540–1544. doi:10.1139/x87-236.

Frandsen, W.H. (1997) 'Ignition probability of organic soils', *Canadian Journal of Forest Research*, 27(9), pp. 1471–1477. doi:10.1139/x97-106.

Freire, J.G. and Dacamara, C.C. (2019) 'Using cellular automata to simulate wildfire propagation and to assist in fire management', *Natural Hazards and Earth System Sciences*, 19(1), pp. 169–179. doi:10.5194/nhess-19-169-2019.

Gazmeh, H. *et al.* (2013) 'Spatio-Temporal Forest Fire Spread Modeling Using Cellular Automata, Honey Bee Foraging and GIS', *Bulletin of Environment, Pharmacology and Life Sciences*, 3(1), pp. 201–214.

Ghisu, T. *et al.* (2015) 'An improved Cellular Automata for wildfire spread', *Procedia Computer Science*, 51(1), pp. 2287–2296. doi:10.1016/j.procs.2015.05.388.

Giannino, F. *et al.* (2017) 'Cellular automata simulation of forest fire behavior on Italian landscape: The case of Sardinia', *AIP Conference Proceedings*, 1906(November). doi:10.1063/1.5012376.

Gibbons, P. *et al.* (2012) 'Land Management Practices Associated with House Loss in Wildfires', *PLoS ONE*, 7(1). doi:10.1371/journal.pone.0029212.

Giglio, L., Schroeder, W. and Justice, C.O. (2016) 'The collection 6 MODIS active fire detection algorithm and fire products', *Remote Sensing of Environment*, 178, pp. 31–41. doi:10.1016/j.rse.2016.02.054.

Gohnai, Y. *et al.* (2005) *Development of WebGIS Supporting Community-Based Planning for Disaster Mitigiation Integrated with a Fire Spread Simulation Model using CA*. Computer in Urban Planning and Urban Management, London: in 9th International Conference. doi:10.13140/2.1.4228.5123.

Graham, I. and Matthai, C.C. (2003) 'Investigation of the forest-fire model on a small-world network', *Physical Review E - Statistical, Nonlinear, and Soft Matter Physics*, 68(3), pp. 361091–361097. doi:10.1103/PhysRevE.68.036109.

Grassberger, P. (1993) 'On a self-organized critical forest-fire model', *Journal of Physics A: Mathematical and General*, 26(9), pp. 2081–2089. doi:10.1088/0305-4470/26/9/007.

Grassberger, P. (2002) 'Critical behaviour of the Drossel-Schwabl forest fire model', *New Journal of Physics*, 4. doi:10.1088/1367-2630/4/1/317.

Green, D.G. (1983) 'Shapes of simulated fires in discrete fuels', *Ecological Modelling*, 20(1), pp. 21–32. doi:10.1016/0304-3800(83)90029-7.

Green, D.G. (1989) 'Simulated effects of fire, dispersal and spatial pattern on competition within forest mosaics', *Vegetatio*, 82(2), pp. 139–153. doi:10.1007/BF00045027.

Di Gregorio, S. *et al.* (2013) 'Accelerating wildfire susceptibility mapping through GPGPU', *Journal of Parallel and Distributed Computing*, 73(8), pp. 1183–1194. doi:10.1016/j.jpdc.2013.03.014.

Grundling, P.L. *et al.* (2019) 'Extinguishing subsurface fires in peatlands with the sprouting water

pressure method', *Water Wheel*, 18(5), pp. 38–41.

Hargrove, W.W. *et al.* (2000) 'Simulating fire patterns in heterogeneous landscapes', *Ecological Modelling*, 135(2–3), pp. 243–263. doi:10.1016/S0304-3800(00)00368-9.

Harris, A. and Bryant, R.G. (2009) 'A multi-scale remote sensing approach for monitoring northern peatland hydrology: Present possibilities and future challenges', *Journal of Environmental Management*, 90(7), pp. 2178–2188. doi:10.1016/j.jenvman.2007.06.025.

Hayasaka, H., Usup, A. and Naito, D. (2020) 'New Approach Evaluating Peatland Fires in Indonesian Factors', *Remote Sensing*, 12. doi:10.3390/rs12122055.

Hermans, L.D. (2021) *Simulating smoldering and flaming combustion spread in wildfires through cellular automata modelling: the case of the 2020 Peel region wildfire*. Amsterdam: Utrecht University.

Heymann, J. *et al.* (2017) 'CO2 emission of Indonesian fires in 2015 estimated from satellite-derived atmospheric CO2 concentrations', *Geophys. Res*, 44, pp. 1537–1544. doi:10.1002/2016GL072042.

Hu, Y. *et al.* (2018) 'Review of emissions from smouldering peat fires and their contribution to regional haze episodes', *International Journal of Wildland Fire*, 27(5), pp. 293–312. doi:10.1071/WF17084.

Hu, Y. *et al.* (2019) 'Transient gas and particle emissions from smouldering combustion of peat', in *Proceedings of the Combustion Institute*. no. 3: vol. 37, pp. 4035–4042. doi:10.1016/j.proci.2018.06.008.

Huang, X. *et al.* (2016) 'Experimental study of the formation and collapse of an overhang in the lateral spread of smouldering peat fires', *Combustion and Flame*, 168, pp. 393–402. doi:10.1016/j.combustflame.2016.01.017.

Huang, X. and Rein, G. (2015) 'Computational study of critical moisture and depth of burn in peat fires', *International Journal of Wildland Fire*, 24(6), pp. 798–808. doi:10.1071/WF14178.

Huang, X. and Rein, G. (2017) 'Downward spread of smouldering peat fire: The role of moisture, density and oxygen supply', *International Journal of Wildland Fire*, 26(11), pp. 907–918. doi:10.1071/WF16198.

Huang, X., Rein, G. and Chen, H. (2015) 'Computational smoldering combustion: Predicting the roles of moisture and inert contents in peat wildfires', in *Proceedings of the Combustion Institute*. p: Volume 35, pp. 2673–2681. doi:10.1016/j.proci.2014.05.048.

Huggett, C. (1980) 'Estimation of rate of heat release by means of oxygen consumption measurements', *Fire and Material*, 4, pp. 61–65.

Huijnen, V. *et al.* (2016) 'Fire carbon emissions over maritime southeast Asia in 2015 largest since 1997', *Scientific Reports*, 6. doi:10.1038/srep26886.

Ichoku, C. *et al.* (2016) 'Fire and Smoke Remote Sensing and Modeling Uncertainties: Case Studies in Northern Sub-Saharan Africa', *Natural Hazard Uncertainty Assessment: Modeling and Decision Support*, 495, pp. 215–230. doi:10.1002/9781119028116.ch14.

Innocenti, E. *et al.* (2009) 'A software framework for fine grain parallelization of cellular models with OpenMP: Application to fire spread', *Environmental Modelling and Software*, 24(7), pp. 819–831. doi:10.1016/j.envsoft.2008.11.014.

Islami, N. *et al.* (2018) 'Geophysical survey for groundwater potential investigation in peat land area, Riau, Indonesia', *IOP Conference Series: Earth and Environmental Science*, 144(1). doi:10.1088/1755-1315/144/1/012001.

Ito, A. (2005) 'Modelling of carbon cycle and fire regime in an east Siberian larch forest', *Ecological Modelling*, 187(2–3), pp. 121–139. doi:10.1016/j.ecolmodel.2005.01.037.

Johnston, F.H. *et al.* (2012) 'Estimated global mortality attributable to smoke from landscape fires', *Environmental Health Perspectives*, 120(5), pp. 695–701. doi:10.1289/ehp.1104422.

Johnston, P., Kelso, J. and Milne, G.J. (2008) 'Efficient simulation of wildfire spread on an irregular grid', *International Journal of Wildland Fire*, 17(5), pp. 614–627. doi:10.1071/WF06147.

de Jonge, H. and Mittelmeijer-Hazeleger, M.C. (1996) 'Adsorption of CO2 and N2 on Soil Organic Matter: Nature of Porosity, Surface Area, and Diffusion Mechanisms', *Environ. Sci*, 30(2), pp. 408–413.

Karafyllidis, I. (1999) 'Acceleration of cellular automata algorithms using genetic algorithms', *Advances in engineering software*, 30(6), pp. 419–437. doi:10.1016/S0965-9978(98)00091-X.

Karafyllidis, I. (2004) 'Design of a dedicated parallel processor for the prediction of forest fire spreading using cellular automata and genetic algorithms', *Engineering Applications of Artificial Intelligence*, 17(1), pp. 19–36. doi:10.1016/j.engappai.2003.12.001.

Karafyllidis, I. and Thanailakis, A. (1997) 'A model for predicting forest fire spreading using cellular automata', *Ecological Modelling*, 99(1), pp. 87–97. doi:10.1016/S0304-3800(96)01942-4.

Khayal, M.S.H. *et al.* (2011) 'Modified new algorithm for seed filling', *Journal of Theoretical and Applied Information Technology*, 26(1), pp. 28–32.

Kolden, C. and Rogan, J. (2013) 'Mapping wildfire burn severity in the arctic tundra from downsampled MODIS data', *Arctic, Antarctic, and Alpine Research*, 45(1), pp. 64–74. doi:10.1657/1938-4246-45.1.64.

Konecny, K. *et al.* (2016) 'Variable carbon losses from recurrent fires in drained tropical peatlands',

Global Change Biology, 22(4), pp. 1469–1480.

Kourtz, P. and O'Regan, W. (1971) 'A Model a Small Forest Fire... to Simulate Burned and Burning Areas for Use in a Detection Model', *Forest Science*, 17(2), pp. 163–169. Available at: http://www.ingentaconnect.com/content/saf/fs/1971/00000017/00000002/art00005?crawler=true.

Kramer, H.J. (1996) 'Observation of the Earth and its environment: survey of missions and sensors. 3rd edition', *Observation of the Earth and its environment: survey of missions and sensors. 3rd edition*, 2002. doi:10.1029/96eo00211.

Lautenberger, C. and Fernandez-Pello, C. (2009) 'Generalized pyrolysis model for combustible solids', *Fire Safety Journal*, 44(6), pp. 819–839.

Li, D., Cova, T.J. and Dennison, P.E. (2019) 'Setting Wildfire Evacuation Triggers by Coupling Fire and Traffic Simulation Models: A Spatiotemporal GIS Approach', *Fire Technology*, 55(2), pp. 617–642. doi:10.1007/s10694-018-0771-6.

Li, X. and Magill, W. (2001) 'Modeling fire spread under environmental influence using a cellular automaton approach', *Complexity*, 8, pp. 1–14.

Li, X. and Magill, W. (2003) 'Critical density in a fire spread model with varied environmental conditions', *International Journal of Computational Intelligence and Applications*, 3(2), pp. 145–155.

Lin, S., Liu, Y. and Huang, X. (2021) 'How to build a firebreak to stop smouldering peat fire: Insights from a laboratory-scale study', *International Journal of Wildland Fire*, 30(6), pp. 454–461. doi:10.1071/WF20155.

Lohberger, S. *et al.* (2018) 'Spatial evaluation of Indonesia's 2015 fire-affected area and estimated carbon emissions using Sentinel-1', *Global Change Biology*, 24, pp. 644–654. doi:10.1111/gcb.13841.

Malamud, B.D., Morein, G. and Turcotte, D.L. (1998) 'Forest fires: An example of self-organized critical behavior', *Science*, 281(5384), pp. 1840–1842. doi:10.1126/science.281.5384.1840.

Malamud, B.D. and Turcotte, D.L. (1999) 'Self-organized criticality applied to natural hazards', *Natural Hazards*, 20(2–3), pp. 93–116. doi:10.1023/a:1008014000515.

Malamud, B.D. and Turcotte, D.L. (2000) 'Cellular-Automata Models Applied to Natural Hazards', *Computer in Science and Engineering*, 2, pp. 42–51. doi:10.1109/5992.841795.

Mandelbrot, B. (1974) 'The Fractal Geometry Of Nature', *Journal of Fluid Mechanics*, 62. doi:10.2307/2323761.

Maranghides, A. *et al.* (2013) 'A Case Study of a Community Affected by the Witch and Guejito Fires: Report #2 -- Evaluating the Effects of Hazard Mitigation Actions on Structure Ignitions', *NIST Technical Note*, 1796. doi:10.6028/NIST.TN.1796.

McRae, R.H.D. (1990) 'Use of digital terrain data for calculating fire rates of spread with the PREPLAN computer system', *Mathematical and Computer Modelling*, 13(12), pp. 37–48. doi:10.1016/0895-7177(90)90097-7.

Meingast, K.M. *et al.* (2014) 'Spectral detection of near-surface moisture content and water-table position in northern peatland ecosystems', *Remote Sensing of Environment*, 152, pp. 536–546. doi:10.1016/j.rse.2014.07.014.

Mooney, S.J. *et al.* (2001) 'A comparison of morphological data and physical measurements of pore structures in milled peat stockpiles', *Geoderma*, 104(1–2), pp. 61–73. doi:10.1016/S0016-7061(01)00056-8.

Mraz, M., Zimic, N. and Virant, J. (1999) 'Intelligent bush fire spread prediction using fuzzy cellular automata', *Journal of Intelligent and Fuzzy Systems*, 7(2), pp. 203–207.

Muzy, A. *et al.* (2002) 'Cell-DEVS quantization techniques in a fire spreading application', *Winter Simulation Conference Proceedings*, 1(January), pp. 542–549. doi:10.1109/wsc.2002.1172929.

Muzy, A. *et al.* (2003) 'Optimization of cell spaces simulation for the modeling of fire spreading', in *Proceedings of the 36th Annual Symposium on Simulation*. FL, USA: Orlando, pp. 289–296. doi:10.1109/SIMSYM.2003.1192825.

Muzy, A. *et al.* (2005a) 'Modelling and simulation of ecological propagation processes: Application to fire spread', *Environmental Modelling and Software*, 20(7), pp. 827–842. doi:10.1016/j.envsoft.2004.04.011.

Muzy, A. *et al.* (2005b) 'Specification of discrete event models for fire spreading', *Simulation*, 81(2), pp. 103–117. doi:10.1177/0037549705052230.

Muzy, A. *et al.* (2006) 'Dynamic Structure Cellular Automata in a Fire Spreading Application', *Informatics in Control, Automation and Robotics I*, pp. 247–254. doi:10.1007/1-4020-4543-3_30.

Nahom, D. (2016) *Forecasting building fires using cellular automata, sensor data and building information models*. Gaithersburg, MD, USA: Society of Fire Protection Engineers.

NASA (2020) *MODIS Collection 6 (C6) LAI / FPAR Product User's Guide*.

Nechita-Banda, N. *et al.* (2018) 'Monitoring emissions from the 2015 Indonesian fires using CO satellite data', *Phil. Trans. R. Soc. B*, 373(20170), p. 307. doi:10.1098/rstb.2017.0307.

von Neumann, J. (1967) *Theory of Self-Reproducing Automata*, *Mathematics of Computation*. Edited by A.W. Burks. Urbana: University of Illinois Press. doi:10.2307/2005041.

von Niessen, W. and Blumen, A. (1986) 'Dynamics of forest fires as a directed percolation model', *Journal of Physics A*, 19, pp. L289–L293.

Noble, A. *et al.* (2018) 'Impacts of prescribed burning on Sphagnum mosses in a long-Term peatland field experiment', *PLoS ONE*, 13(11), p. 11. doi:10.1371/journal.pone.0206320.

Nowzad, A. (2019) 'Airborne-Based Fire Detection', in Manzello, S.L. (ed.) *Encyclopedia of Wildfires and Wildland-Urban Interface (WUI) Fires*. Springer Nature: Switzerland, pp. 1–5. doi:10.1007/978-3-319-51727-8_146-1.

Ntinas, V.G. *et al.* (2017) 'Parallel fuzzy cellular automata for data-driven simulation of wildfire spreading', *Journal of Computational Science*, 21, pp. 469–485. doi:10.1016/j.jocs.2016.08.003.

Null, J. (2021) *El Niño and La Niña Years and Intensities*. Golden Gate Weather Service.

Nusantara, R.W., Hazriani, R. and Suryadi, U.E. (2018) *Water-table Depth and Peat Subsidence Due to Land-use Change of Peatlands*. in IOP Conference Series: Earth and Environmental Science. doi::10.1088/1755-1315/145/1/012090.

Ohgai, A. *et al.* (2004) *Cellular Automata Modeling For Fire Spreading As a Tool to Aid Community-Based Planning for Disaster Mitigation*. Dordrecht: in Recent Advances in Design and Decision Support Systems in Architecture and Urban Planning. doi:10.1007/1-4020-2409-6_13.

Packalen, M.S. and Finkelstein, S.A. (2014) 'Quantifying Holocene variability in carbon uptake and release since peat initiation in the Hudson Bay Lowlands, Canada', *Holocene*, 24(9), pp. 1063–1074. doi:10.1177/0959683614540728.

Page, S.E. *et al.* (2002) 'The amount of carbon released from peat and forest fires in Indonesia during 1997', *Nature*, 420(6911), pp. 61–65. doi:10.1038/nature01131.

Page, S.E. *et al.* (2004) 'A record of Late Pleistocene and Holocene carbon accumulation and climate change from an equatorial peat bog (Kalimantan, Indonesia): Implications for past, present and future carbon dynamics', *Journal of Quaternary Science*, 19(7), pp. 625–635. doi:10.1002/jqs.884.

Pak, S. Il and Hayakawa, T. (2011) 'Forest fire modeling using cellular automata and percolation threshold analysis', *Proceedings of the American Control Conference*, pp. 293–298. doi:10.1109/acc.2011.5991603.

Pastor-Satorras, R. and Vespignani, A. (2000) 'Corrections to scaling in the forest-fire model', *Physical Review E - Statistical Physics, Plasmas, Fluids, and Related Interdisciplinary Topics*, 61(5), pp. 4854–4859. doi:10.1103/PhysRevE.61.4854.

Pastor, E. *et al.* (2003) 'Mathematical models and calculation systems for the study of wildland fire behaviour', *Progress in Energy and Combustion Science*, 29(2), pp. 139–153. doi:10.1016/S0360-1285(03)00017-0.

Perry, G.L.W. (1998) 'Current approaches to modelling the spread of wildland fire: a review', *Progress in Physical Geography: Earth and Environment*, 22(2), pp. 222–245.

doi:10.1177/030913339802200204.

Peterson, S.H. *et al.* (2009) *Using HFire for spatial modeling of fire in shrublands*, *Res. Pap. PSW-RP-259. Department of Agriculture, Forest Service, Pacific Southwest Research Station*. Albany, CA: U.S. doi:10.2737/PSW-RP-259.

Porterie, B. *et al.* (2007) 'Modeling forest fire spread and spotting process with small world networks', *Combustion and Flame*, 149(1–2), pp. 63–78. doi:10.1016/j.combustflame.2006.12.008.

Prat-Guitart, N. *et al.* (2016a) 'Effects of spatial heterogeneity in moisture content on the horizontal spread of peat fires', *Science of the Total Environment*, 572, pp. 1422–1430. doi:10.1016/j.scitotenv.2016.02.145.

Prat-Guitart, N. *et al.* (2016b) 'Propagation probability and spread rates of self-sustained smouldering fires under controlled moisture content and bulk density conditions', *International Journal of Wildland Fire*, 25(4), pp. 456–465. doi:10.1071/WF15103.

Prat-Guitart, N. *et al.* (2017) 'Fine-scale distribution of moisture in the surface of a degraded blanket bog and its effects on the potential spread of smouldering fire', *Ecohydrology*, 10(8). doi:10.1002/eco.1898.

Progias, P. and Sirakoulis, G.C. (2013) 'An FPGA processor for modelling wildfire spreading', *Mathematical and Computer Modelling*, 57(5–6), pp. 1436–1452. doi:10.1016/j.mcm.2012.12.005.

Pruessner, G. and Jensen, H.J. (2002) 'Broken scaling in the forest-fire model', *Physical Review E - Statistical Physics, Plasmas, Fluids, and Related Interdisciplinary Topics*, 65(5), p. 8. doi:10.1103/PhysRevE.65.056707.

Purnomo, D.M.J. *et al.* (2021) 'Using cellular automata to simulate field-scale flaming and smouldering wildfires in tropical peatlands', in *Proceedings of the Combustion Institute*, pp. 5119–5127. doi:10.1016/j.proci.2020.08.052.

Quah, E. and Johnston, D. (2001) 'Forest fires and environmental haze in Southeast Asia: Using the "stakeholder" approach to assign costs and responsibilities', *Journal of Environmental Management*, 63(2), pp. 181–191. doi:10.1006/jema.2001.0475.

Quartieri, J. *et al.* (2010) 'A Cellular Automata Model for Fire Spreading Prediction', in *Proceeding of 3rd WSEAS International Conference on Urban Planning and Transportation*. Greece: Corfu Island.

Le Quéré, C. *et al.* (2015) 'Global Carbon Budget 2015', *Earth System Science Data*, 7(2), pp. 349–396. doi:10.5194/essd-7-349-2015.

Rein, G. *et al.* (2008) 'The severity of smouldering peat fires and damage to the forest soil', *Catena*, 74(3), pp. 304–309. doi:10.1016/j.catena.2008.05.008.

Rein, G. (2013) 'Smouldering Fires and Natural Fuels', in *Fire Phenomena and the Earth System: An Interdisciplinary Guide to Fire Science*. s.l.: Wiley and Sons, pp. 15–33. doi:10.1002/9781118529539.ch2.

Rein, G. (2016) 'Smoldering combustion', *SFPE Handbook of Fire Protection Engineering, Fifth Edition*, pp. 581–603. doi:10.1007/978-1-4939-2565-0_19.

Rein, G. and Huang, X. (2021) *Smouldering wildfires in peatlands, forests and the arctic: Challenges and perspectives*, *Current Opinion in Environmental Science and Health*. Curr Opin Environ Sci Health. doi:10.1016/j.coesh.2021.100296.

Restuccia, F., Huang, X. and Rein, G. (2017) 'Self-ignition of natural fuels: Can wildfires of carbon-rich soil start by self-heating?', *Fire Safety Journal*, 91, pp. 828–834. doi:10.1016/j.firesaf.2017.03.052.

Rezanezhad, F. *et al.* (2016) 'Structure of peat soils and implications for water storage, flow and solute transport: A review update for geochemists', *Chemical Geology*, 429, pp. 75–84. doi:10.1016/j.chemgeo.2016.03.010.

Ritzema, H. *et al.* (2014) 'Canal blocking strategies for hydrological restoration of degraded tropical peatlands in Central Kalimantan, Indonesia', *Catena*, 114, pp. 11–20. doi:10.1016/j.catena.2013.10.009.

Rothermel, R.C. (1972) *A Mathematical Model for Predicting Fire Spread in Wildland Fuels*. Available at: https://www.fs.usda.gov/treesearch/pubs/32533.

Rui, X. *et al.* (2018) 'Forest fire spread simulation algorithm based on cellular automata', *Nat Hazards*, 91, pp. 309–319. doi:10.1007/s11069-017-3127-5.

Russo, L. *et al.* (2014) 'Detecting weak points of wildland fire spread: A cellular automata model risk assessment simulation approach', *Chemical Engineering Transactions*, 36(June), pp. 253–258. doi:10.3303/CET1436043.

Russo, L., Vakalis, D. and Siettos, C. (2013) 'Simulating the wildfire in rhodes in 2008 with a cellular automata model', *Chemical Engineering Transactions*, 35(1946), pp. 1399–1404. doi:10.3303/CET1335233.

Santoso, M.A. *et al.* (2019) 'Review of the Transition From Smouldering to Flaming Combustion in Wildfires', *Frontiers in Mechanical Engineering*, 5, p. 49. doi:10.3389/fmech.2019.00049.

Santoso, M.A. (2021) *Experimental study of smouldering wildfire mitigation: spread, suppression and transition to flaming*. London: Imperial College London. Available at: http://spiral.imperial.ac.uk/handle/10044/1/91115.

Santoso, M.A. *et al.* (2021) 'Laboratory study on the suppression of smouldering peat wildfires:

effects of flow rate and wetting agent', *International Journal of Wildland Fire*, 30(5), pp. 378–390. doi:10.1071/WF20117.

Schenk, K. *et al.* (2000) 'Finite-size effects in the self-organized critical forest-fire model', *The European Physical Journal B*, 15(1), pp. 177–185. doi:10.1007/s100510051113.

Schenk, K., Drossel, B. and Schwabl, F. (2002) 'Self-organized critical forest-fire model on large scales', *Physical Review E - Statistical Physics, Plasmas, Fluids, and Related Interdisciplinary Topics*, 65(2), pp. 1–8. doi:10.1103/PhysRevE.65.026135.

Scholten, R.C. *et al.* (2021) 'Overwintering fires in boreal forests', *Nature*, 593(7859), pp. 399–404. doi:10.1038/s41586-021-03437-y.

Séro-Guillaume, O. *et al.* (2008) 'On large scale forest fires propagation models', *International Journal of Thermal Sciences*, 47(6), pp. 680–694. doi:10.1016/j.ijthermalsci.2007.06.016.

Siegert, F. *et al.* (2004) 'Peat fires detected by the BIRD satellite', *International Journal of Remote Sensing*, 25(16), pp. 3221–3230. doi:10.1080/01431160310001642377.

Simpson, J.E. *et al.* (2016) 'Tropical Peatland Burn Depth and Combustion Heterogeneity Assessed Using UAV Photogrammetry and Airborne LiDAR', *Remote Sensing*, 8. doi:10.3390/rs8121000.

SIPONGI (2021) *Sipongi Karhutla Monitoring System*. Available at: http://sipongi.menlhk.go.id (Accessed: 20 January 2021).

Sofan, P. *et al.* (2019) 'Detection and validation of tropical Peatland flaming and smouldering using Landsat-8 SWIR and TIRS bands', *Remote Sensing*, 11(4), p. 4. doi:10.3390/rs11040465.

Sofan, P. *et al.* (2020) 'Applying the tropical peatland combustion algorithm to landsat-8 operational land imager (OLI) and sentinel-2 multi spectral instrument (MSI) imagery', *Remote Sensing*, 12(23), pp. 1–37. doi:10.3390/rs12233958.

Sousa, F.A., dos Reis, R.J.N. and Pereira, J.C.F. (2012) 'Simulation of surface fire fronts using fireLib and GPUs', *Environmental Modelling and Software*, 38, pp. 167–177. doi:10.1016/j.envsoft.2012.06.006.

Spyratos, V., Bourgeron, P.S. and Ghil, M. (2007) 'Development at the wildland-urban interface and the mitigation of forest-fire risk', *Proceedings of the National Academy of Sciences of the United States of America*, 104(36), pp. 14272–14276. doi:10.1073/pnas.0704488104.

Stavrakoudis, D. *et al.* (2020) 'Automated Burned Scar Mapping Using Sentinel-2 Imagery', *Journal of Geographic Information System*, 12(03), pp. 221–240. doi:10.4236/jgis.2020.123014.

Sullivan, A.L. (2009a) 'Wildland surface fire spread modelling, 1990--2007. 1: Physical and quasi-physical models', *International Journal of Wildland Fire*, 18(4), pp. 349–368. doi:10.1071/WF06143.

Sullivan, A.L. (2009b) 'Wildland surface fire spread modelling, 1990 - 2007. 2: Empirical and quasi-empirical models', *International Journal of Wildland Fire*, 18(4), p. 369. doi:10.1071/wf06142.

Sullivan, A.L. (2009c) 'Wildland surface fire spread modelling, 1990 - 2007. 3: Simulation and mathematical analogue models', *International Journal of Wildland Fire*, 18(4), p. 387. doi:10.1071/wf06144.

Sullivan, A.L. and Knight, I.K. (2004) 'A hybrid cellular automata/semi-physical model of fire growth', *Complexity International*, 12(December), pp. 1–10.

Sun, H. *et al.* (2006) *Spectral characteristics of infrared radiation from forest fires*, *Remote Sensing and Modeling of Ecosystems for Sustainability III*. San Diego: in Remote Sensing and Modeling of Ecosystems for Sustainability III. doi:10.1117/12.679775.

Sun, T. *et al.* (2013) 'Mountains forest fire spread simulator based on geo-cellular automaton combined with Wang Zhengfei velocity model', *IEEE Journal of Selected Topics in Applied Earth Observations and Remote Sensing*, 6(4), pp. 1971–1987. doi:10.1109/JSTARS.2012.2231956.

Takizawa, A. *et al.* (2000) *Simulation of Spreads of Fire on City Site by Stochastic Cellular Automata*. New Zealand: Auckland.

Tambunan, L., Salamah, H. and Asriana, N. (2017) *Analysis of Architectural Building Design Influences on Fire Spread in Densely Urban Settlement using Cellular Automata*.

Thapa, R.B. *et al.* (2015) 'Time-series maps of aboveground carbon stocks in the forests of central Sumatra', *Carbon Balance Management*, 10, p. 23.

Trunfio, G.A. (2004) 'Predicting Wildfire Spreading Through a Hexagonal Cellular Automata Model', *Lecture Notes in Computer Science (including subseries Lecture Notes in Artificial Intelligence and Lecture Notes in Bioinformatics)*, 3305, pp. 385–394. doi:10.1007/978-3-540-30479-1_40.

Trunfio, G.A. *et al.* (2011) 'A new algorithm for simulating wildfire spread through cellular automata', *ACM Transactions on Modeling and Computer Simulation*, 22(1), pp. 1–26. doi:10.1145/2043635.2043641.

Turetsky, M.R. *et al.* (2015) 'Global vulnerability of peatlands to fire and carbon loss', *Nature Geoscience*, 8(1), pp. 11–14. doi:10.1038/ngeo2325.

Urbanski, S. (2014) 'Wildland fire emissions, carbon, and climate: Emission factors', *Forest Ecology and Management*, 317, pp. 51–60. doi:10.1016/j.foreco.2013.05.045.

USGS (2019) *Landsat 8 Data Users Handbook*. Available at: https://landsat.usgs.gov/documents/Landsat8DataUsersHandbook.pdf.

Usup, A. *et al.* (2004) 'Combustion and thermal characteristics of peat fire in tropical peatland in

Central Kalimantan, Indonesia', *Tropics*, 14, pp. 1–19. doi:10.3759/tropics.14.1.

Valdivieso, J.P. and Rivera, D. (2014) 'Effect of Wind on Smoldering Combustion Limits of Moist Pine Needle Beds', *Fire Technology*, 50, pp. 1589–1605. doi:10.1007/s10694-013-0357-2.

van Wagner, C. (1977) 'Conditions for the start and spread of crown fire', *Canadian Journal of Forest Research*, 7, pp. 23–34. doi:10.1139/x77-004.

van Wagner, C. (1993) 'Prediction of crown fire behavior in two stands of jack pine', *Canadian Journal of Forest Research*, 23, pp. 442–449. doi:10.1139/x93-062.

Waldrop, A.T. and Goodrick, L.S. (2018) *Introduction to Prescribed Fire in Southern Ecosystems*. Asheville, NC: US Department of Agriculture Forest Service, Southern Research.

Wang, H. and Zhou, H. (2014) *A Fire Spread Model Based on Cellular Automaton*.

Wang, S. *et al.* (2017) 'Interaction between flaming and smouldering in hot-particle ignition of forest fuels and effects of moisture and wind', *International Journal of Wildland Fire*, 26(1), pp. 71–81. doi:10.1071/WF16096.

Wang, Z.F. (1992) 'General forest fire weather ranks system', *Journal of Natural Disasters*, 1(3), pp. 39–45.

Watson, A., Lovelock, J.E. and Margulis, L. (1978) 'Methanogenesis, fires and the regulation of atmospheric oxygen', *Biosystems*, 10(4), pp. 293–298. doi:10.1016/0303-2647(78)90012-6.

Weber, R. (1990) 'A model for fire propagation in arrays', *Mathematical and Computer Modelling*, 13, pp. 95–102. doi:10.1016/0895-7177(90)90103-T.

Widyastuti, K. *et al.* (2021) 'PeatFire: An agent-based model to simulate fire ignition and spreading in a tropical peatland ecosystem', *International Journal of Wildland Fire*, 30(2), pp. 71–89. doi:10.1071/WF19213.

Wolfram, S. (1984) 'Cellular automata as models of complexity', *Nature*, 311(5985), pp. 419–424. doi:10.1038/311419a0.

Wolfram, S. (2002) *A New Kind of Science*. Illinois: Wolfram Media, Inc.

Wooster, M.J. *et al.* (2021) 'Satellite remote sensing of active fires: History and current status, applications and future requirements', *Remote Sensing of Environment*, 267. doi:10.1016/j.rse.2021.112694.

Wooster, M.J., Zhukov, B. and Oertel, D. (2003) 'Fire radiative energy for quantitative study of biomass burning: Derivation from the BIRD experimental satellite and comparison to MODIS fire products', *Remote Sensing of Environment*, 86(1), pp. 83–107. doi:10.1016/S0034-4257(03)00070-1.

Xuehua, W. *et al.* (2016) 'A cellular automata model for forest fire spreading simulation', in *2016 IEEE Symposium Series on Computational Intelligence, SSCI 2016*. Athens, Greece. doi:10.1109/SSCI.2016.7849971.

Yassemi, S., Dragićević, S. and Schmidt, M. (2008) 'Design and implementation of an integrated GIS-based cellular automata model to characterize forest fire behaviour', *Ecological Modelling*, 210(1–2), pp. 71–84. doi:10.1016/j.ecolmodel.2007.07.020.

Yin, Y. *et al.* (2016) 'Variability of fire carbon emissions in equatorial Asia and its nonlinear sensitivity to El Ni{\ n}o', *Geophysical Research Letters*, 43, pp. 10472–10479. doi:10.1002/2016GL070971.

Yongzhong, Z. *et al.* (2004) 'Simulating wildfire spreading processes in a spatially heterogeneous landscapes using an improved cellular automaton model', *International Geoscience and Remote Sensing Symposium (IGARSS)*, 5(1), pp. 3371–3374. doi:10.1109/igarss.2004.1370427.

Yongzhong, Z. *et al.* (2005) 'A CA-Based Information System For Surface Fire Spreading Simulation', *IEEE, IGARSS'0*, 5, pp. 3484–3487. doi:10.1109/IGARSS.2005.1526595.

Yu, Z.C. (2012) 'Northern peatland carbon stocks and dynamics: A review', *Biogeosciences*, 9(10), pp. 4071–4085. doi:10.5194/bg-9-4071-2012.

Yuan, H., Restuccia, F. and Rein, G. (2021) 'Spontaneous ignition of soils: A multi-step reaction scheme to simulate self-heating ignition of smouldering peat fires', *International Journal of Wildland Fire*, 30(6), pp. 440–453. doi:10.1071/WF19128.

Zhao, S. (2011) 'Simulation of Mass Fire-Spread in Urban Densely Built Areas Based on Irregular Coarse Cellular Automata', *Fire Technology*, 47, pp. 721–749. doi:10.1007/s10694-010-0187-4.

Zheng, Z. *et al.* (2017) 'Forest fire spread simulating model using cellular automaton with extreme learning machine', *Ecological Modelling*, 348, pp. 33–43. doi:10.1016/j.ecolmodel.2016.12.022.

Zik, O. and Moses, E. (1999) 'Fingering instability in combustion: an extended view', *PHYSICAL REVIEW E, pp*, pp. 518–531. doi:10.1103/physreve.60.518.

Appendix

Appendix Chapter 2

Table S2.1. The abbreviations and its meaning that are used in the satellite and its instruments naming.

Satellite abbreviation	Meaning	Instrument abbreviation	Meaning
Landsat 8	N/A	OLI	Operational Land Imager
	N/A	TIRS	Thermal Infrared Sensor
Sentinel-2	30	MSI	Multispectral Instrument
NASA Terra & Aqua	N/A	MODIS	Moderate Resolution Imaging Spectroradiometer
Suomi NPP	Suomi National Polar-orbiting Partnership	VIIRS	Visible Infrared Imaging Radiometer Suite
NOAA	National Oceanic and Atmospheric Administration	AVHRR	Advanced Very High Resolution Radiometer
BIRD	Bispectral and Infrared Remote Detection	HSRS	Hot Spot Recognition Sensor
TET-1	Technologie Erprobungs Träger-1	BIROS	Bispectral Infrared Optical System

Appendix Chapter 4

A. Supplementary figures

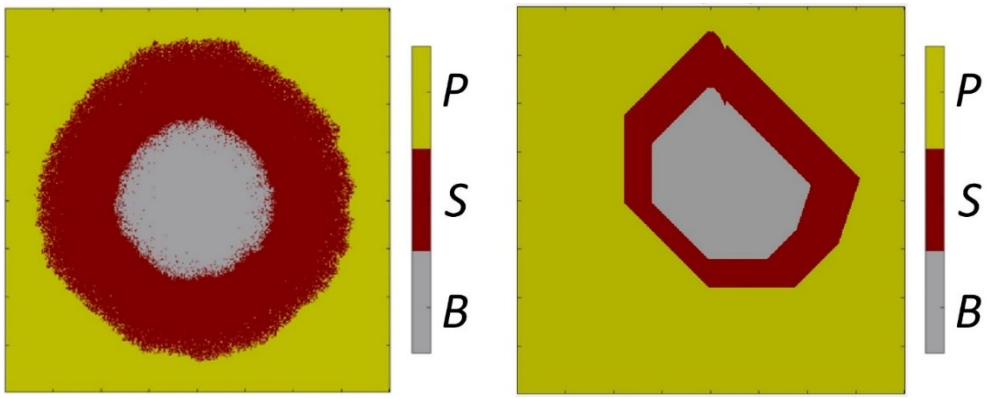

Figure S4.1. Results from BARA simulation of smouldering peat, with 20%MC and 20%IC, both the expected circular ring result (left) and the unexpected polygon result (right).

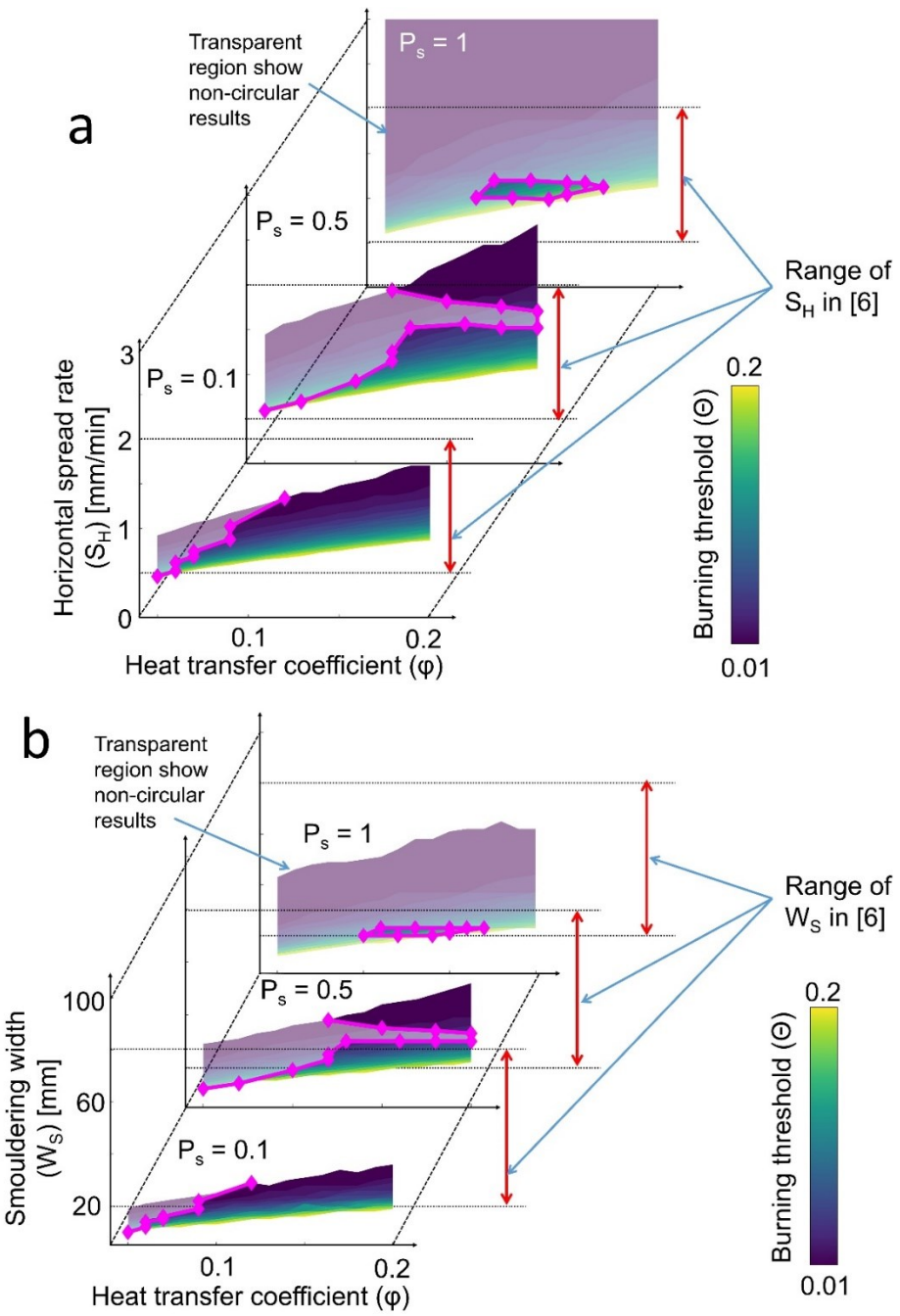

Figure S4.2. Sensitivity analysis of P_s on different Θ and φ based on (a) horizontal spread rate (S_H) and (b) smouldering width (W_S). The magenta lines represent the boundary between simulation results with circular and non-circular (transparent) shapes.

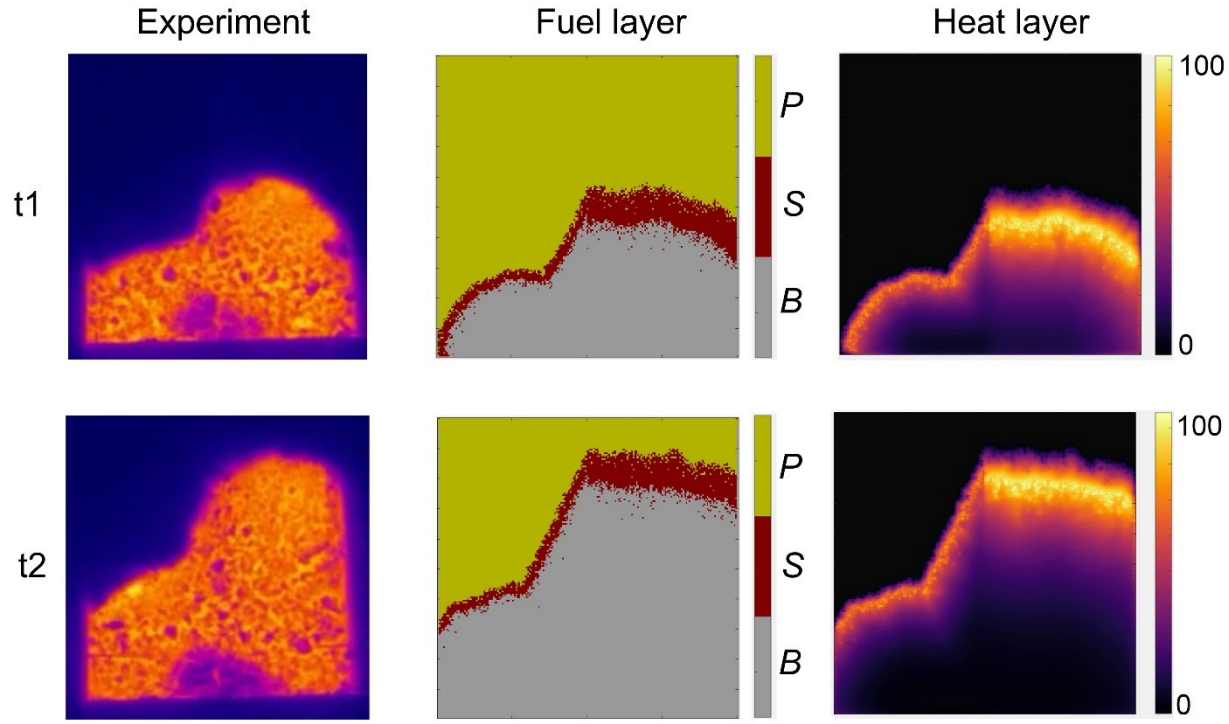

Figure S4.3. Comparison between BARA predictions with experiments of smouldering fire in peat with heterogeneous MC with halftone configuration. The comparison is focused at two different times after ignition which show significant differences. The full comparison can be found in supplementary material.

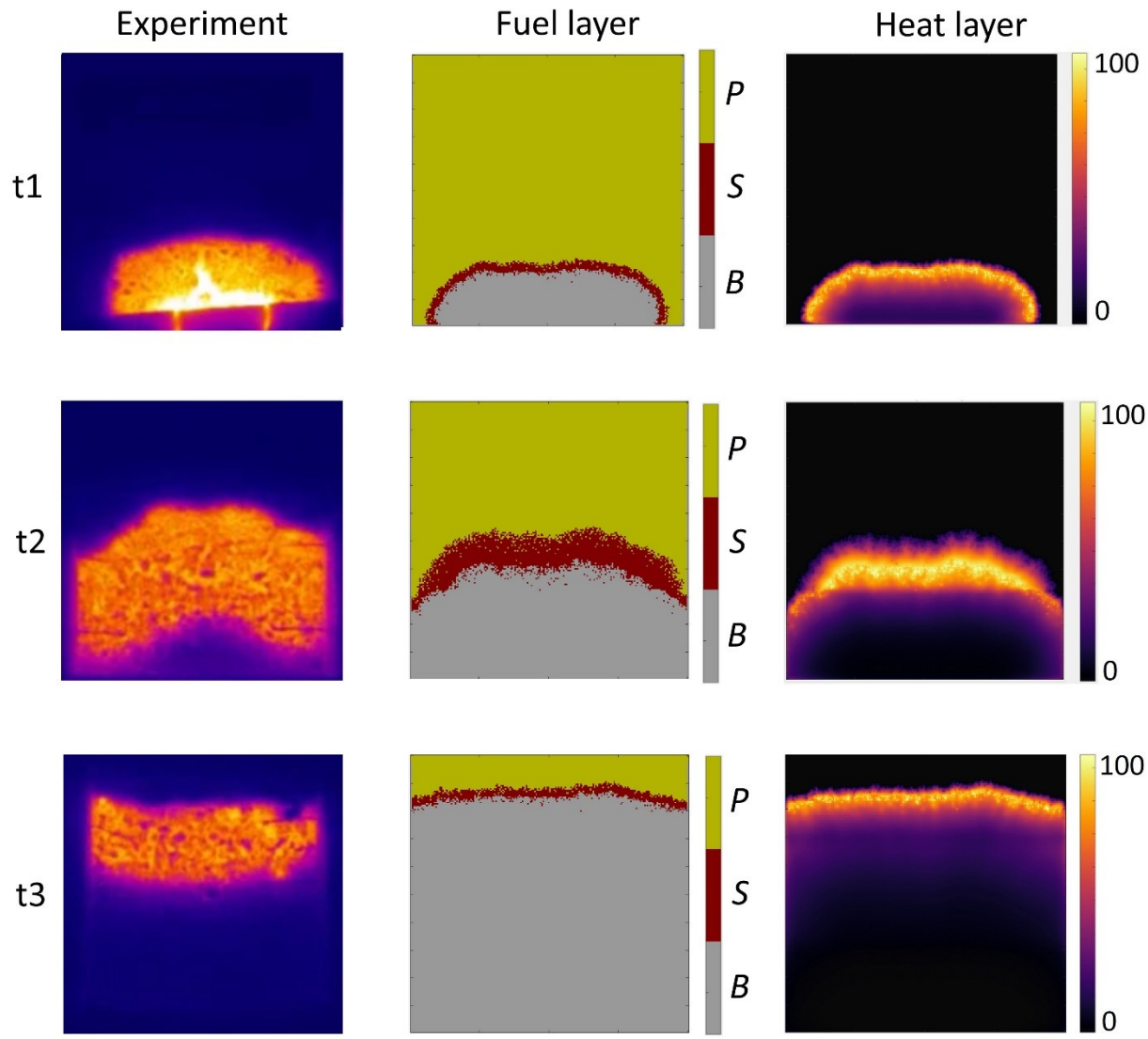

Figure S4.4. Comparison between BARA simulations with experiments smouldering fire in peat with heterogeneous MC with stripes configuration. The comparison is focused at three different times after ignition which show significant differences. The full comparison can be found in supplementary material.

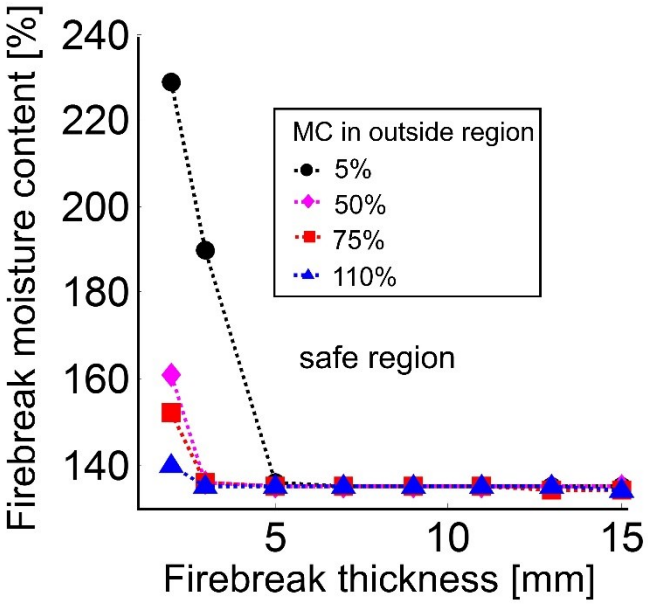

Figure S4.5. The thickness and MC of firebreak (layers of wet peat) that lead to failure of the firebreak in different MC of outside region (see Figure 4.12 (right)). The region above the lines are the safe region where the firebreak successfully discontinue the smouldering spread.

B. Derivation from first principle

Heat release rate

Figure 4.2 illustrates consumed peat at one time-step and its components. In consumed peat with the volume of ($\delta V = \Delta x^2 \delta$), it contains water with a volume of δV_{w}, inorganic content with a volume of δV_{i}, air with a volume of δV_{a}, and organic content with a volume of δV_{o}. The heat release rate (Q_{R}) depends on the heat generation per m^3 (ΔH_{c}) and δV_{o} as shown in Eq. S4.1. By using mathematical operations, δV_{o} can be formulated as a function of organic density (ρ_{o}), particle density of the peat (ρ'_{o}), and δV. The thickness of the consumed peat is a function of in-depth spread rate (S_{d}), therefore, Q_{R} can be formulated as shown in Eq. S4.6 where b_1 is a constant. By assuming constant ΔH_{c}, ρ'_{o} and Δx, Eq. S4.6 can be simplified to become Eq. 4.3.

$$Q_{\mathrm{R}} = \Delta H_{\mathrm{c}} \delta V_{\mathrm{o}} \tag{S4.1}$$

$$\frac{\delta V_{\mathrm{o}}}{\delta V} = \frac{\rho_{\mathrm{b}}}{\rho'_{\mathrm{o}}} \cdot \frac{m_{\mathrm{o}}}{m_{\mathrm{b}}} = \frac{1}{\rho'_{\mathrm{o}}} \cdot \frac{m_{\mathrm{o}}}{\delta V} \tag{S4.2}$$

$$\frac{\delta V_{\mathrm{o}}}{\delta V} = \frac{\rho_{\mathrm{o}}}{\rho'_{\mathrm{o}}} \tag{S4.3}$$

$$Q_{\mathrm{R}} = \Delta H_{\mathrm{c}} \frac{\rho_{\mathrm{o}}}{\rho'_{\mathrm{o}}} \delta V \tag{S4.4}$$

$$Q_{\mathrm{R}} = \frac{\Delta H_{\mathrm{c}}}{\rho'_{\mathrm{o}}} \rho_{\mathrm{o}} \Delta x^2 \delta \tag{S4.5}$$

$$Q_{\mathrm{R}} = \left(b_1 \Delta x^2 \frac{\Delta H_{\mathrm{c}}}{\rho_{\mathrm{o}}'}\right) \rho_{\mathrm{o}} S_{\mathrm{d}} \tag{S4.6}$$

Heat transfer coefficient

Figure S4.6 shows the physical analogy of heat transfer in BARA and heat transfer in physical realm. If two adjacent cells have different heat value (U), this condition is analogous to have different temperature (T) in physical meaning. Due to the temperature difference (ΔT), there is heat transfer (Q) from the cell with higher temperature (red) to the cell with lower temperature (blue). By assuming a 1-D transient conduction heat transfer (Eq. S4.7) with effective thermal conductivity, k_{e} (see Eq. S4.8) for porous media following (Huang, Rein and Chen, 2015), a finite difference method is applied to the Eq. S4.7 which resulting in Eq. S4.9. In these equations, T is temperature, t is time, ρ_{b} is bulk density, c is specific heat, x is distance, k is material thermal conductivity, Φ is porosity, γ is radiative conductivity coefficient, and σ is Stefan–Boltzmann constant. Meanwhile, ΔT_{1-2} is temperature difference between cell 1 (west neighbour) and cell 2 (centre cell) and ΔT_{3-2} is temperature difference between cell 2 and cell 3 (east neighbour). These equation are implemented in BARA where the heat transfer is discretized to one time step and to one neighbour (the other three sides of the cell are assumed to be insulated). Therefore, in Eq. S4.9, $\Delta t = 1$ and $\Delta T_{3-2} = 0$, resulting in Eq. S4.10 when the temperature is translated to heat value. These processes are repeated independently for the other three neighbours (in this example North, East, South), therefore, although the heat transfer between a centre cell with each neighbour is not directly connected, eventually they are affecting one another. This neighbourhood concept is one of the reason CA become computationally efficient. To further simplify the model, k_e is set to be constant resulting in Eq. S4.11 where b_2 is a constant. In BARA, the heat value transferred to the neighbour (Q) is $\delta U / \Delta l$, where Δl is the number of cells that separate the two cells which are interacting. Therefore, Eq. S4.11 can be further modified to be Eq. S4.12 where φ is heat transfer coefficient in BARA which depends on the ρ_b and c of the sample.

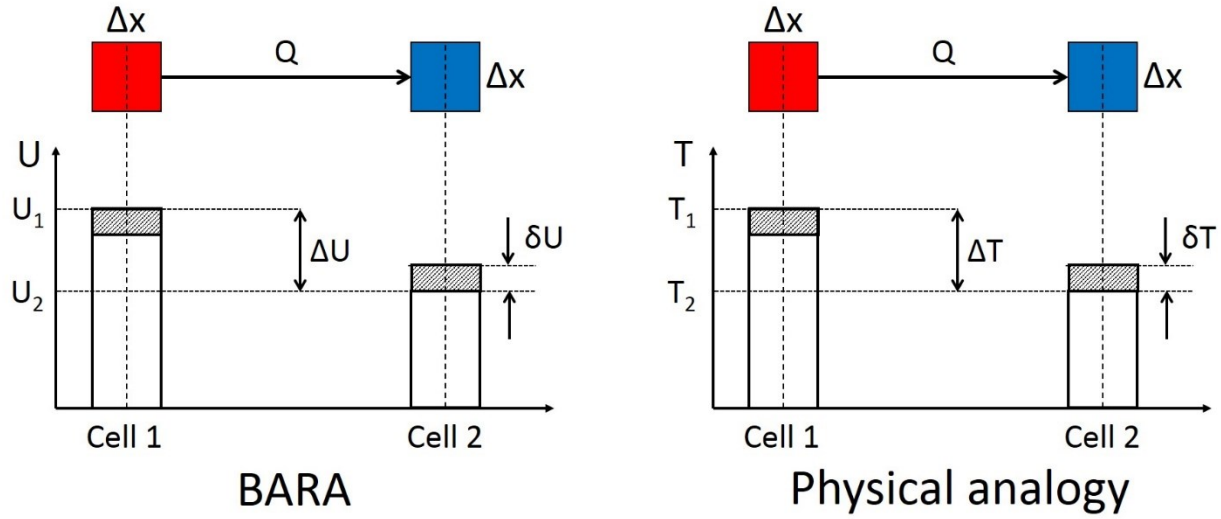

Figure S4.6. Schematic of analogy of heat transfer in BARA and physical analogy.

$$\frac{\partial T}{\partial t} = \frac{k_e}{\rho_b c} \cdot \frac{\partial^2 T}{\partial x^2} \tag{S4.7}$$

$$k_e = k(1-\Phi) + \gamma\sigma T^3 \tag{S4.8}$$

$$\frac{\Delta T}{\Delta t} = \frac{k_e}{\rho_b c} \cdot \frac{\Delta T_{1-2} + \Delta T_{3-2}}{\Delta x^2} \tag{S4.9}$$

$$\delta U = \frac{k_e}{\Delta x^2} \frac{\Delta U}{\rho_b c} \tag{S4.10}$$

$$\delta U = \frac{b_2}{\rho_b c} \Delta U \tag{S4.11}$$

$$Q = \varphi \frac{\Delta U}{\Delta l} \tag{S4.12}$$

Appendix Chapter 7

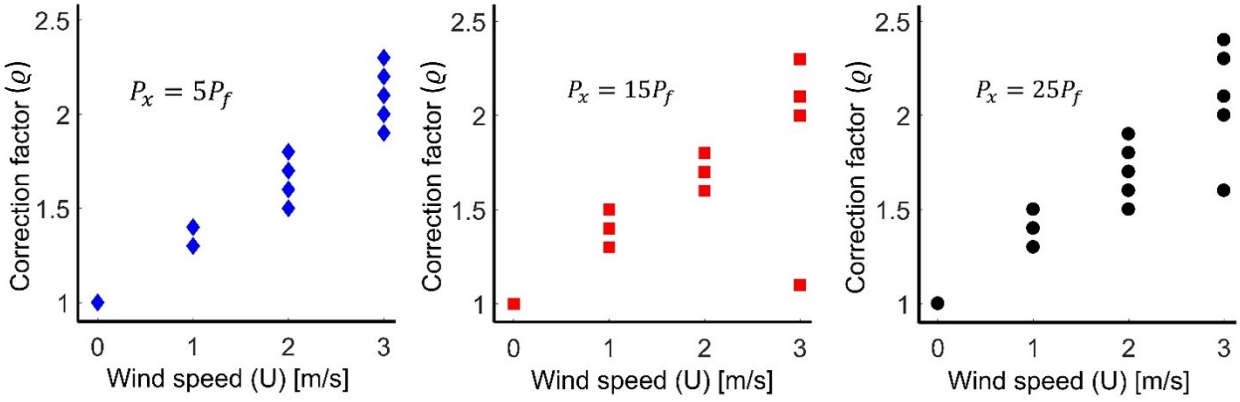

Figure S7.1. The correction factor (ϱ) for the simulation with different flaming extinction probability (P_x) which is formulated as a function of flaming spread probability (P_f). The variation of ϱ in one wind speed (V) is due to the variation of spatiotemporal resolution (λ).

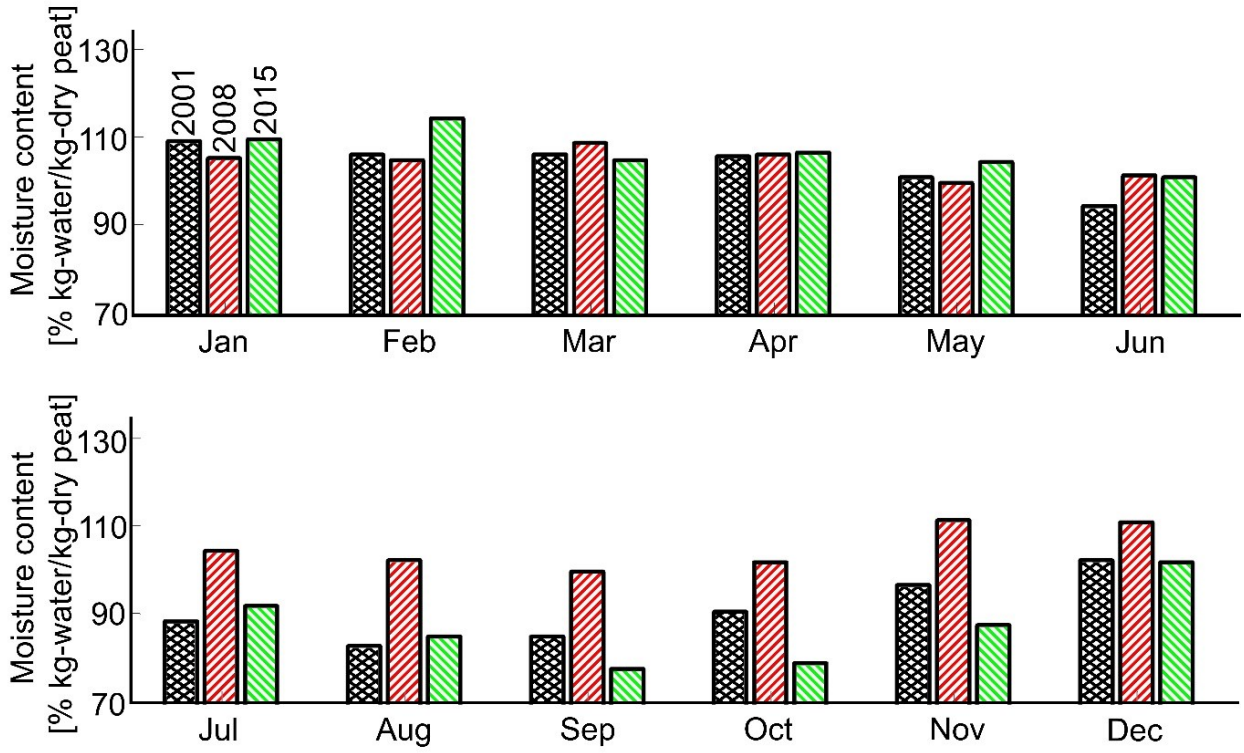

Figure S7.2. Gravimetric MC of the peat in the peatland in Borneo over many years, simulated by using the model of (Apers et al.*, 2020). Each bar represents the average peat MC in one month. The El Niño year in 2015 is clearly shown in the low MC during the dry season of the green bars.*

Appendix Chapter 9

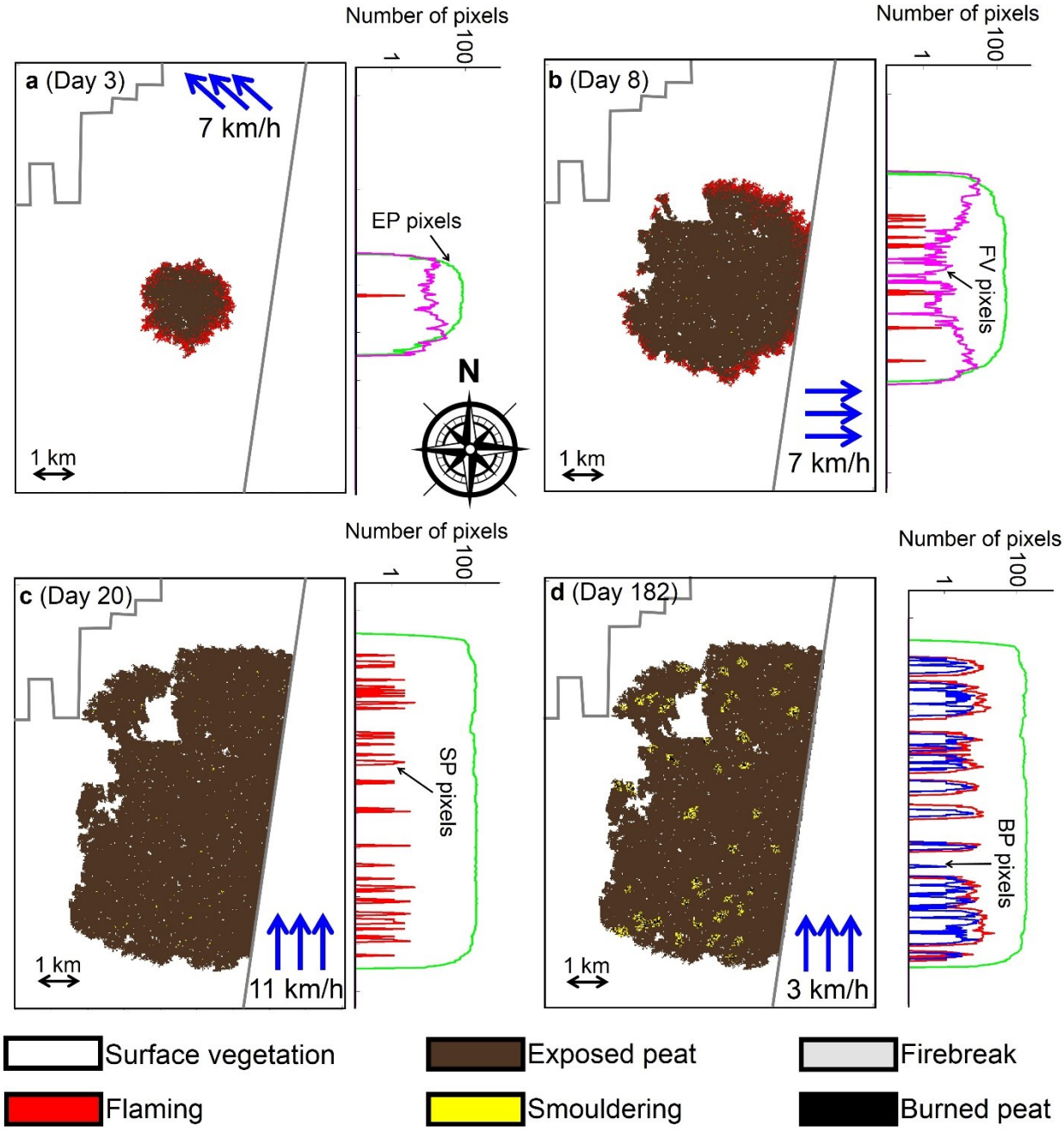

Figure S9.1. Snapshots of a simulation of the peatland wildfire in Central Kalimantan site taken at different times and its corresponding number of pixels of different states (EP, FV, SP, and BP). (a) The early stage of the surface flaming (day 3), (b) the spread of surface flaming and the nucleation of smouldering hotspots (day 8), (c) surface flaming extinguish and the smouldering hotspots nucleation stops (day 20), and (d) the end of simulation (day 182) where the smouldering hotspots have spread and grown bigger. The surface vegetation (white) corresponds to the three different vegetation type in Figure 7.2. The blue arrows show the wind direction and their values (km/h) correspond to wind speed. Firebreak (grey) stops the spread of flaming.

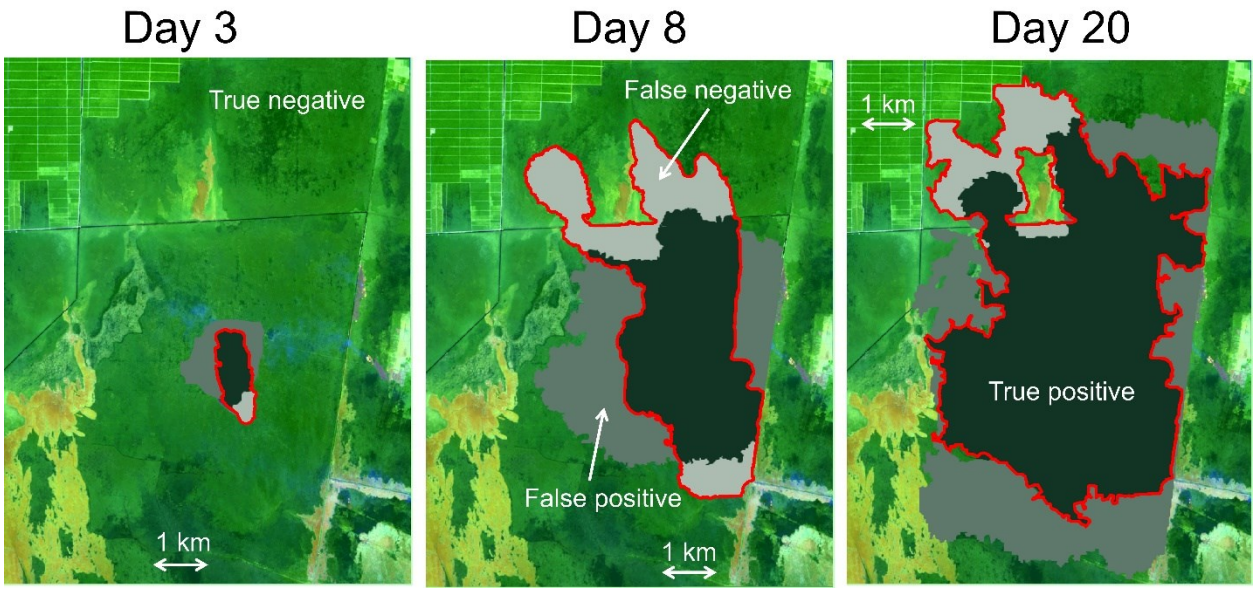

Figure S9.2. The comparison of burnt scar between satellite detection and SUBALI prediction of Central Kalimantan site at three different times. This compares the burnt scar in Figure 7.1b and Figure S9.1a – Figure S9.1c. The red lines represent the perimeter of the actual burnt scar detected by satellite. True negative and true positive are the accurate predictions which mean that the prediction and the satellite detection are both not burn and both are burn respectively. False positive corresponds to the predicted burn region which is not burn in the satellite detection, whereas false negative is the predicted not burn region which is burn in the satellite detection.